Energy Transport in Organic Photovoltaics

by

Kevin J. Bergemann

A dissertation submitted in partial fulfillment
of the requirements for the degree of
Doctor of Philosophy
(Physics)
in the University of Michigan
2015

Doctoral Committee:

Professor Stephen Forrest, Chair
Professor Roy Clarke
Professor Cagliyan Kurdak
Associate Professor Max Shtein
Assistant Professor Kai Sun

2015

Science!!!
-Unattributed

Acknowledgments

I'd like to thank everyone in OCM for your help getting me to this point. Special thanks go to Brian, Panda, Greg, Guodan, Quinn and Xin. And I especially must thank Olga and Jeramy, who helped me out of so many dead ends. And of course, my advisor Professor Forrest as well.

To all the friends I've made here and those I had before, thank you. Matt, Amanda, Michelle, Sandor, Katie, Mark, Dan, Craig, Kevin, Deb, and Sara, you're awesome. Frances, Jonathan, Steph, Will, Julie, Adrian, MacKenzie and everyone else, you're also pure amazing. Thanks to all of you for keeping me sane. Well, arguably sane. No comments from the peanut gallery please.

Also, Matt, Carric. And Kaz and Nalrin. It's a tie!

I also couldn't have done it without support from my family. Thank you to all of you, Mom, Dad, Eric, Patrick, Jeff, Melissa and Rachel. I don't know where I'd be without you.

And now I'm going to sleep for a week.

TABLE OF CONTENTS

LIST OF FIGURES

LIST OF TABLES

LIST OF APPENDICES

LIST OF ABBREVIATIONS

1-NPSQ 2-[4-(N-phenyl-N-1-naphthylamino)-2,6-dihydroxyphenyl]-4-[(4-(N-phenyl-N-1-naphthyliminio)-2,6-dihydroxyphenyl)-2,5-dien-1-ylidene]-3-oxocyclobut-1-en-1-olate

AFM atomic force microscopy

AIST National Institute of Advanced Industrial Science and Technology

Alq_3 tris-(8-hydroxyquinoline)aluminum

APD avalanche photodiode

ASSQ 2-[4-(N,N-diisobutylamino)-2,6-dihydroxyphenyl]-4-(4-diphenyliminio)-2,5-dien-1-ylidene-3-oxocyclobut-1-en-1-olate

BCP bathocuproine

BGR bandgap renormalization

BPhen bathophenanthroline

cAFM conductive-tip atomic force microscopy

CELIV charge extraction through linearly increasing voltage

ClAlPc chloro-aluminum phthalocyanine

CNT carbon nanotube

CT charge-transfer

CuPc copper phthalocyanine

DBP tetraphenyldibenzoperiflanthene

DPASQ 2-[4-(N,N-diphenylamino)-2,6-dihydroxyphenyl]-4-(4-diphenyliminio)-2,5-dien-1-ylidene-3 oxocyclobut-1-en-1-olate

DPSQ 2,4-bis[4-(N,N-diphenylamino) 2,6-dihydroxyphenyl] squaraine

EML emissive layer

EQE external quantum efficiency

ETL electron transport layer

eV electon volt

FF fill factor

FIB focused ion beam

GaAs gallium arsenide

HOMO highest occupied molecular orbital

HPLC high pressure liquid chromatography

HTL hole transport layer

IMPS intensity-modulated photocurrent spectroscopy

IQE internal quantum efficiency

IR infrared

Ir(ppy)$_3$ tris[2-phenylpyridinato-C^2,N]iridium(III)

ISC intersystem crossing

ITO indium tin oxide

IV current-voltage

J$_{SC}$ short-circuit current

L_D exciton diffusion length

LCD liquid-crystal display

LED light-emitting diode

LUMO lowest unoccupied molecular orbital

MoOx molybdenum oxide

NIR near infrared

NIST National Institute of Standards and Technology

NPD N,N-Di-[(1-naphthyl)-N,N-diphenyl]-1,1-biphenyl)-4,4-diamine

NREL National Renewable Energy Laboratory

NTCDA 1,4,5,8-napthalene-tetracarboxylic-dianhydride

OLED organic light-emitting diode

OPV organic photovoltaic

OSL organic semiconductor laser

OTFT organic thin film transistor

OVJP organic vapor jet printing

OVPD organic vapor phase deposition

P3HT poly(3-hexylthiophene-2,5-diyl)

PC60BM [6,6]-phenyl-C_{60}-butyric acid methyl ester

PC70BM [6,6]-phenyl-C_{70}-butyric acid methyl ester

PCE power conversion efficiency

pDPP5T-2 a diketopyrrolopyrrole-quinquethiophene alternating copolymer

PEIE polyethylenimine, ethoxylated

PHOLED phosphorescent OLED

PL photoluminescence

PLE photoluminescence excitation

PMT photomultiplier tube

PP polaron-pair

ppm parts per million

PTCBI 3,4,9,10 perylenetetracarboxylic bisbenzimidazole

PTCDA 3,4,9,10-perylenetetracarboxylic dianhydride

QCM quartz crystal monitor

RISC reverse intersystem crossing

RPM revolutions per minute

SEM scanning electron microscopy

Si silicon

SQ Shockley-Queisser

SR-PLQ spectrally-resolved photoluminescence quenching

SubPc boron subphthalocyanine chloride

TADF thermally-activated delayed fluorescence

TAPC 1-bis[4-[N,N-di(4-toyl)amino]phenyl]-cyclohexane

TCO transparent conductive oxide

TD-PLQ thickness-dependent photoluminescence quenching

TEM transmission electron microscopy

UV ultraviolet

V$_{OC}$ open-circuit voltage

VTE vacuum thermal evaporation

XRD X-ray diffraction

ZnPc zinc phthalocyanine

ABSTRACT

Organic photovoltaics (OPV) have the potential to be a flexible and low-cost form of carbon-neutral energy production. However, many of the underlying physical mechanisms that dictate the behavior of OPVs remain frustratingly obscure in comparison to the well-understood physics of inorganic semiconductors. This dissertation centers around the development of new techniques to characterize the behavior of excitons in organic semiconductors, both in the bulk and at interfaces. We first examine the method of spectrally-resolved photoluminescence quenching (SR-PLQ), the most convenient and powerful current technique for measuring the exciton diffusion length (L_D) of organic semiconductors, and extend it to work with optically thin films. This allows for its application to a much wider range of materials and physical systems. The second part of the dissertation presents a further extension of the method of PL quenching to characterize non-ideal interfaces, those which block or quench only a fraction of incident excitons. This is used to understand the operation of a novel fullerene:wide energy gap material buffer in OPVs. In combination with charge transport and morphological studies, it is shown that the mixed buffer shows disproportionate benefits from the two materials; blocking excitons superlinearly with wide energy gap material concentration and still conducting charges efficiently even at very small (10%) fullerene concentration. Finally, we extend the principles of PL quenching to characterize arbitrary interfaces, including those between materials with identical energy levels but different L_D and exciton lifetime, and those between materials with small ($\sim$20 meV) energy offsets. These techniques allow us to finally resolve the ambiguity in the spin state of the exciton which serves as the primary source of photocurrent in C_{60}, one of the most important materials in current efficient OPVs.

CHAPTER 1

Introduction to Organic Semiconductors

Here we give a brief introduction to the field of organic semiconductors. We begin with a discussion of the unique properties of organic semiconductors, what distinguishes them from inorganics and makes them interesting subjects for research. We continue with a discussion of the technical advantages and disadvantages of organics, with an eye towards explaining why one would consider using them in place of already-mature inorganic technologies. We also cover some of the obstacles that must be overcome to successfully utilize organic semiconductors, many but not all of them inherent features of the materials. A summary of the processing techniques of organics is next, looking both at purification methods and at the deposition techniques used to form the organics into devices. We conclude with a brief discussion of the major applications of organic semiconductors in development. Only one application, organic light-emitting diodes (OLEDs), has penetrated significantly into the marketplace, but a large range of organic devices is being researched.

1.1 Introduction to Organic Semiconductors

Ever since the invention of the transistor in 1947, an achievement honored with the 1956 Nobel Prize in Physics, electronics have been based on inorganic semiconductors such as silicon and gallium arsenide (GaAs). An enormous range of mature industries, from light-emitting diodes (LEDs) to solar cells to microchips, are based on inorganic materials, characterized by strong covalent bonds between atoms (on the order of electon volt (eV)). Inorganic materials are generally crystalline with high melting points ($\sim 1000°$C), and their strong bonds make them hard and brittle.

Organic semiconductors are a relatively young field with only one truly mature technology, OLEDs. In contrast to inorganic semiconductors, the individual molecules in organic semiconductors are held together by relatively weak van der Waals bonds with binding energy on the order of meV. These weak intermolecular forces give rise to a host of intriguing

and potentially useful properties in organics and are at the root of the majority of their differences from inorganics.

The definition of 'organic' is somewhat of a historical artifact and is acknowledged to be reasonably arbitrary.[1] It arose in the time of vitalism theory which stated that living beings and the compounds derived from them were qualitatively different from nonliving inorganic materials making it impossible to produce organic materials from inorganic precursors. In this context 'organic' simply meant 'made by a living being.' Modern usage varies, but generally falls into one of three categories. Some define an organic compound as one that contains carbon-carbon bonds, some as a compound containing carbon-hydrogen bonds, and some simply state that any compound that contains carbon is organic. These definitions are further muddied by historical reasons for classifying some molecules that are inorganic by one of these definitions as organic* or for classifying molecules that should be organic by these definitions as inorganic.†

What truly distinguishes organic chemistry as a whole from inorganic chemistry is the ability of carbon to bond with itself to form structures of arbitrary size. This makes the number of possible organic molecules practically infinite. In practice, organic molecules used as semiconductors are divided into two categories, small molecules and polymers. Small molecules have well-defined molecular structures with a molecular weight typically below 1000, while polymers are arbitrarily long chains of repeating subunits with no defined molecular weight. Characteristic inorganic and organic materials are shown in Fig. 1.1.

*Urea ($CO(NH_2)_2$) and oxalic acid ($H_2C_2O_4$) are both compounds that contain no carbon-carbon or carbon-hydrogen bonds. They were originally classified as organic because they both were derived from organic sources. They continue to be classified as organic due to historical reasons, as they were the first 'organic' molecules to be synthesized from purely inorganic sources and therefore served as an important disproof of vitalism.

†For example, carbon-containing steels are considered inorganic, as are allotropes of carbon such as diamond or graphite. This is relevant as the fullerenes C_{60} and C_{70} are common components in organic photovoltaics, while nanotubes have been considered as absorbers or contacts. Neither of these are considered organic by many definitions. This has led some to propose 'a fully inorganic organic solar cell,' one made entirely out of these allotropes of carbon.

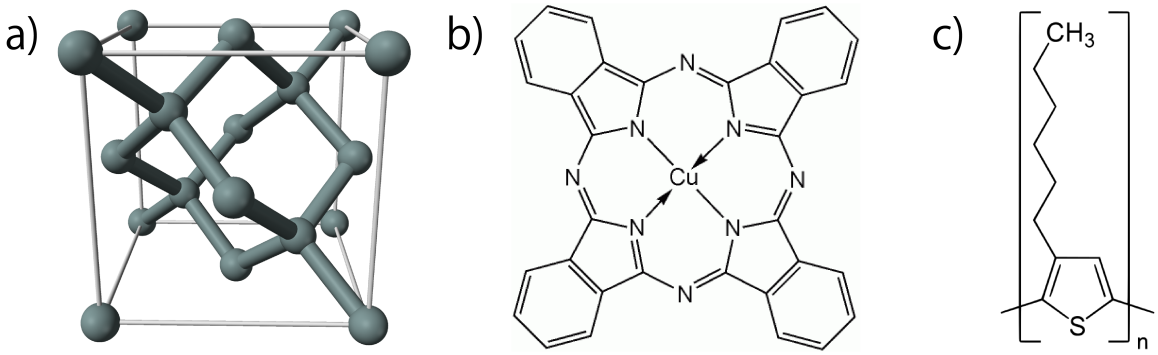

Figure 1.1: a) The 8-atom diamond cubic unit cell of crystalline silicon. b) copper phthalocyanine (CuPc), a classic small-molecule organic semiconductor. c) The monomer of poly(3-hexylthiophene-2,5-diyl) (P3HT), a common polymer organic semiconductor.

1.2 Unique Features of Organic Semiconductors

Most inorganic semiconductors are crystalline with a repeating, regularly spaced chemical structure. Most organic semiconductors, in contrast, are amorphous with the molecules randomly distributed and randomly oriented. Combined with the weak bonding between organic molecules, this means organic semiconductors lack many of the aggregate behaviors that crystalline inorganic semiconductors exhibit, especially the delocalization of electrons and holes that leads to band transport.[2]

Band structure in crystalline semiconductors arises from the periodic crystalline structure represented as a periodic potential.[3] Bloch's theorem states that a charge* traveling in a periodic potential† can be represented as a Bloch state:[2,4]

$$\Psi(r) = e^{ikr}u(r) \tag{1.1}$$

where Ψ is the total wavefunction of the charge, r is the position coordinate, k is the wavenumber, and u is a periodic function with the same period as the potential. Note that Ψ exists over all position space (r), indicating a very delocalized charge. Charge wavefunctions in inorganic materials are therefore characterized by the energy E and the wavenumber k of the electron. The highly delocalized nature of the charges also results in aggregate behaviors with the individual orbitals of the constituent atoms of the substance spreading out to form bands.

Amorphous materials such as most organic semiconductors, in contrast, almost entirely

*''Charge" indicates either a hole or an electron.

†Here we only apply Bloch's theorem to charges traveling through a crystal lattice but it is generally applicable to any problem featuring periodic potentials such as photons in photonic crystals.

lack band structure*. As mentioned above, the molecules in amorphous materials are randomly distributed and cannot be represented with a periodic potential, which means Bloch's theorem cannot be used. The constant scattering of charges causes large uncertainty in k, meaning that it is no longer a good description of the charge state. By the Heisenberg uncertainty principle, this is equivalent to saying that the charges can have low uncertainty in position r and charges are indeed found to be highly localized in amorphous materials. Instead of band theory, conduction through organics is generally represented as a hopping process with charge carriers localized on individual molecules and conducting through a series of hops from molecular site to adjacent molecular site.[6–8]

Organic semiconductors are semiconductors and therefore characterized by an energy gap between filled and empty electronic states. Unlike inorganic semiconductors, this is a property of the individual molecules instead of an aggregate characteristic of the material. The equivalent to the edge of the filled valence band in organics is known as the highest occupied molecular orbital (HOMO) and the equivalent to the edge of the empty conduction band is the lowest unoccupied molecular orbital (LUMO). A given organic molecule in isolation will always have the same HOMO-LUMO energy gap, but this is influenced by the energetic environment. The random disorder in an organic amorphous film means that each molecule is in a slightly different energetic environment which leads to a spread in the aggregate HOMO-LUMO energy gap of the bulk material.

Care must be taken to avoid a false analogy to band theory. The broadened HOMO-LUMO energy gap of organic materials due to disorder is not due to a spread of band energies, but is instead a function of the statistical spread of individual HOMO-LUMO energy gaps in the material. There is a certain population of individual molecules in the film with a given deviation from the innate HOMO-LUMO energy gap of the molecule due to the energetic environment and the population decreases as the deviation from the innate HOMO-LUMO energy gap increases. The absorption peak of the organic bulk is then the sum of the individual narrow absorption lines of the separate organic molecules. This gives rise to the different absorption profiles of organics versus crystalline inorganics. Crystalline inorganics possess a characteristic band absorption where light with energy above the bandgap is strongly absorbed and light with energy below the bandgap is transmitted. Organics, in contrast, possess a molecular absorption where the peaks correspond to energetic transitions in the molecules themselves, broadened by disorder. Organic semiconductor absorption is therefore much narrower than crystalline inorganics but is also much stronger, as all molecules absorb around the peak.[9,10] This is shown in Fig. 1.2.

*Quasi-band-transport has been observed in some crystalline organic materials such as 3,4,9,10-perylenetetracarboxylic dianhydride (PTCDA),[5] but most materials under study lack this characteristic.

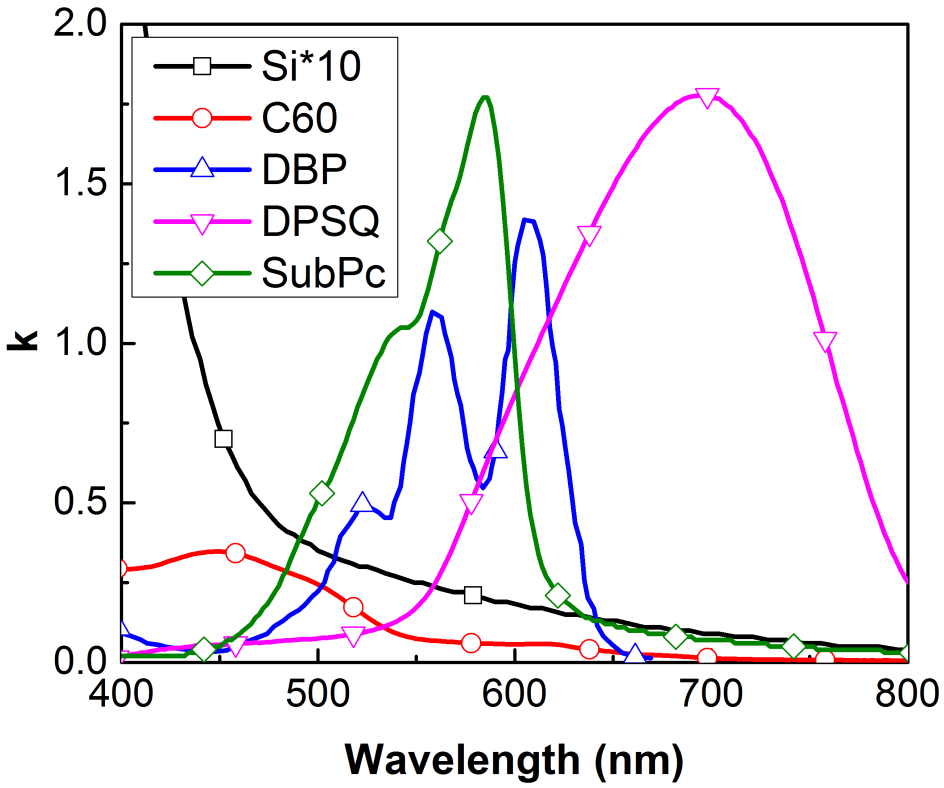

Figure 1.2: A comparison of the imaginary portion k of the complex index of refraction of several common organics and silicon. The silicon value is multiplied by a factor of 10 while the organics are shown as-is. Organics have significantly higher absorption in the visible than silicon, allowing organic photovoltaics (OPVs) to be substantially thinner, on the order of 100 nm. Organics also display spectrally resolved absorption features in comparison to inorganics which absorb all light with energy above the bandgap energy.

The weak van der Waals bonding of organic semiconductors gives rise to a marked change in the primary form of photoexcitation in these materials compared to crystalline inorganics. The primary photoexcited species in amorphous organic semiconductors are strongly-bound Frenkel and charge-transfer excitons, a bound electron-hole pair.[12] The physics of excitons will be covered in detail in Chapter 2.

The weak van der Waals bonding of organic semiconductors causes many other differences between their physical properties and those of crystalline inorganics, as shown in Table 1.1. Organics are much softer, a function both of their weaker intermolecular bonds and their amorphous nature, and much more tolerant of bending and strain. They are also significantly easier both to melt and to dissolve, allowing for much easier processing and

Property	Si[11]	C_{60}[12]	Anthracene[13]
Density (g/cm^3)	2.33	1.72	1.25
Atomic or molecular weight (g/mol)	28.09	720.77	178.22
Crystal structure	diamond	face-centered cubic	monoclinic
Lattice constant (nm)	0.543	1.42	0.60(b)
			1.11(c)
Melting point (K)	1685	1453*	217
Thermal expansion coefficient (K^{-1})	2.5 x 10^{-6}	6.1 x 10^{-5}	1.45 x 10^{-4}
Thermal conductivity [W/(cm K)]	1.412	4 x 10^{-3}	1 x 10^{-3}
Relative permittivity	11.7	4.0-4.5	3.4
Electron mobility [cm^2/(V s)]	1420	1.0	0.88
Hole mobility [cm^2/(V s)]	470	1.0	17
Ionization potential (eV)	5.2	6.2	5.8

Table 1.1: Comparison of selected physical properties of Si, C_{60}, and anthracene.

deposition. The weak bonding and disorder of organics also leads to low charge mobility, 3-5 orders of magnitude less than that of crystalline silicon and low indices of refraction as shown in Fig. 1.3, and makes them much softer than inorganic semiconductors whose strong bonding and crystalline nature makes them hard and brittle. As the amorphous nature of organic semiconductors also renders them insensitive to molecular dislocations caused by strain or impact, organic semiconductors display much better resistance to bending and impact. This allows organics to be used in curved or flexible configurations.[14–19]

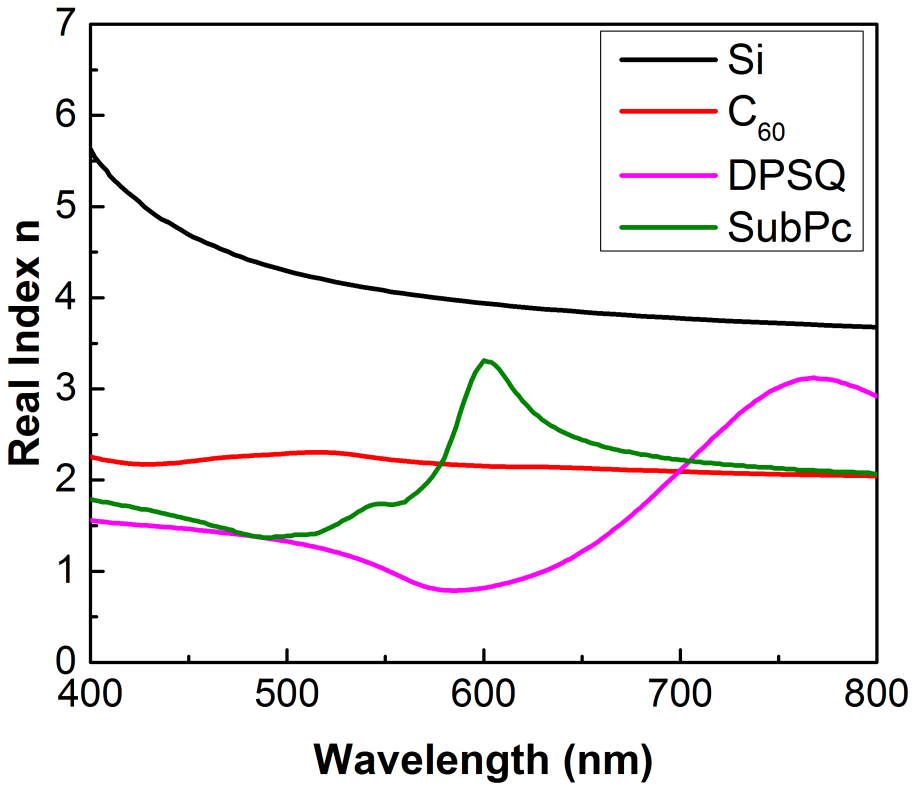

Figure 1.3: A comparison of the real portion n of the complex index of refraction of several common organics and silicon. The lower n in organics is caused by weak intermolecular bonding in these materials and is the source of the different behavior of organic semiconductors.

1.3 Technical Advantages and Disadvantages of Organic Semiconductors

The low bonding strength and amorphous structure of organic semiconductors leads to a range of differences from crystalline inorganics, both good and bad. One such feature is the comparative "softness" of organic materials. For example, the Young's modulus for crystalline Si is ~ 180 GPa compared to ~ 1 GPa for tris-(8-hydroxyquinoline)aluminum (Alq_3).[20–22] This allows organics to be used in unique curved, flexible and stretchable electronic and optoelectronic configurations.[23,24] It also renders organic devices much more resistant to stress and impact.[25,26]

The softness of organics also allows a range of stamping and transfer processing techniques that cannot be performed with inorganics.[27–30] However, the weak chemical bonds between organic molecules makes them much more vulnerable to chemical damage. The

standard techniques of photolithography and wet-etching used on inorganic semiconductors therefore cannot be applied to organics as the solvents and acids required for masking and etching can degrade or dissolve organic materials.[31,32] Patterning of organic devices is currently restricted to much larger length scales than inorganic devices and is an active area of current research.

As mentioned above, the weak intermolecular bonds between organics also results in a low melting point, as well as high solubility in many common organic solvents.[12] This allows a wider range of processing methods to be used than for inorganics, which cannot easily be dissolved in a carrier solvent and require very high temperatures to break the strong covalent bonds between molecules.[2] Small-molecule organics are commonly sublimed in vacuum at a few hundred degrees Celsius, with a substrate near room temperature or below. In comparison, GaAs is often grown at a substrate temperature of 600° C.[33,34] It is hoped that organics can one day be printed like ink on a variety of substrates, allowing for extremely low cost and environmentally friendly manufacturing.[35,36] This is further enhanced by the fact that most organic semiconductors are mostly or entirely composed of earth-abundant materials which has the potential to cut down substantially on costs.

The relatively low deposition temperature of organics (room temperature for most solvent processes) also allows a wider range of substrates. Organics may be deposited directly on thin plastic substrates such as Kapton or transferred via stamping.[27–30] These materials could not stand up to the high temperatures and caustic chemicals required to break the strong covalent bonds between inorganics during fabrication. Organics can therefore be deposited directly on thin flexible substrates, allowing for easier fabrication of lightweight flexible devices.[23,24]

Organics are easier to process than inorganics, but they are also more vulnerable to degradation by oxygen and water.[37–39] All organic devices currently require packaging to seal them away from atmosphere. This generally takes the form of a glass or quartz sandwich sealed with epoxy on the edges which increases the cost and weight of the devices. Even packaged organic devices are generally not as long-lived as equivalent inorganic devices. However, there is no inherent reason why organic materials should be short-lived. Great strides have been made recently in lifetime of organic devices with appropriate choice of materials and deposition techniques resulting in a 10X improvement in blue OLED lifetime.[40] Similar advances have been made recently in OPVs, and the search for more stable highly-efficient materials continues.

As mentioned in the previous section, many organic semiconductors have very high absorption coefficients in comparison to inorganics, with common OPV materials having an absorption coefficient as high as $5 \cdot 10^5$ cm^{-1}.[12] These materials are optically thick at

the peak with as little as $10 - 20$ nm of material. Similarly, emission from OLEDs can have 100% internal quantum efficiency (IQE), allowing emission layers also on the order of $10 - 20$ nm.[41] Organic devices are therefore generally very thin, on the order of 100 nm.

The thinness of most organic devices helps counteract one of their major disadvantages, the comparatively low charge mobility of organic semiconductors.[7,12] Crystalline silicon has an electron mobility of 1420 cm^2/V s at 300 K,[11] whereas relatively high-mobility organics such as anthracene or C_{60} may reach 1 cm^2/V s when fully crystalline.[12] Most organic semiconductors have a mobility on the order of $10^{-3} - 10^{-5}$ cm^2/V s. Organic devices are therefore more resistive than equivalent inorganic devices, even when the inorganic devices are thicker. This is also one factor putting an upper limit on how thick organic devices may be made without becoming infeasibly resistive.

Organic absorption is also relatively spectrally resolved as opposed to the broad-band absorption of inorganic semiconductors.[12] This can be both an advantage and a disadvantage. It allows for the creation of novel technologies such as power windows, OPV meant to be placed on building windows which absorb the infrared and ultraviolet portions of the solar spectrum but are transparent in the visible.[42,43] However, it is difficult to find organic materials that can absorb over the entire solar spectrum. Inorganics such as silicon and GaAs can absorb into the near infrared (NIR), while small-molecule organics that both make efficient devices and absorb above 900 nm are rare.[2] Research continues to synthesize and test such materials, which would be able to improve OPV efficiency significantly.

1.4 Processing techniques

1.4.1 Purification

As with all semiconductors, the purity of materials is directly correlated with device performance. Chemical impurities in organic semiconductors generally have different energy levels than the surrounding material which can form charge traps, lowering the charge mobility and therefore the performance of the material. If the impurities are numerous and the traps are deep enough, this can cause significant hysteresis in device electrical characteristics. Smaller gap contaminants can also trap excitons and, if they possess an optical transition resonant with the surrounding material, it will also serve as an efficient recombination site, thereby quenching emission.

The possible types of contaminants are varied. Uncatalyzed reactants or residual solvent from material synthesis can contaminate organic materials, as can environmentally introduced impurities. Atmospheric exposure is a known source of contamination as well, as

many organics undergo photo-oxidation reactions which form undesired chemical species and oxygen itself can dope films with recombination sites. Degradation can also occur during deposition of the organic semiconductor as excessive heat can break chemical bonds and form impurities.

As effects on device efficiency can be observed even at ppm concentrations of contaminants, materials must be purified before they can be used. After synthesis, chemists will generally employ techniques such as solvent recrystallization or high pressure liquid chromatography (HPLC) to purify material. Most commercial materials intended for electronics use have been purified in this manner to $> 99\%$ purity*. In practice, this purity is insufficient and further purification leads to a marked increase in device quality.

Thermal gradient sublimation is a widely used technique to further purify organic molecules. The basic setup for thermal gradient sublimation is shown in Fig. 1.4. A zone furnace is used to set up a thermal gradient across an evacuated ($\sim 10^{-6}$ torr) quartz tube, with the starting material in the hot zone. The material is then heated to the sublimation point and allowed to sit for several days. Materials with different sublimation temperatures will deposit at different points in the zone furnace, spatially separating the pure material from low- and high-temperature impurities. The pure material is generally visibly distinct from the impurities, allowing it to be removed from one region of the tube. This can be a time consuming process, as care must be taken not to ramp up the temperature too quickly or to halt the purification before all available material has diffused out from the source boat. A single cycle of purification takes approximately a week and can be repeated multiple times for further purity. In practice, however, most commercial materials require only a single cycle of thermal gradient purification to reach acceptable device performance.

One of the advantages small molecule organic semiconductors possess over polymers is their ability to be purified through thermal gradient sublimation. Polymers cannot be sublimed, as they degrade under the required temperatures. Therefore they can only be purified using solution-based methods as described above.

1.4.2 Deposition

Deposition techniques for organic semiconductors can be roughly separated into two families: evaporative techniques and solvent-based techniques. In general, polymers are restricted to solvent-based techniques as they cannot be evaporated without damage. Small molecules, in contrast, can usually be deposited with either method. There do exist some

*Thermal gradient sublimation purification of such $> 99\%$ pure materials usually has a yield of 40-60%. This suggests the manufacturer's numbers may be overly optimistic and illustrates the necessity of further purification.

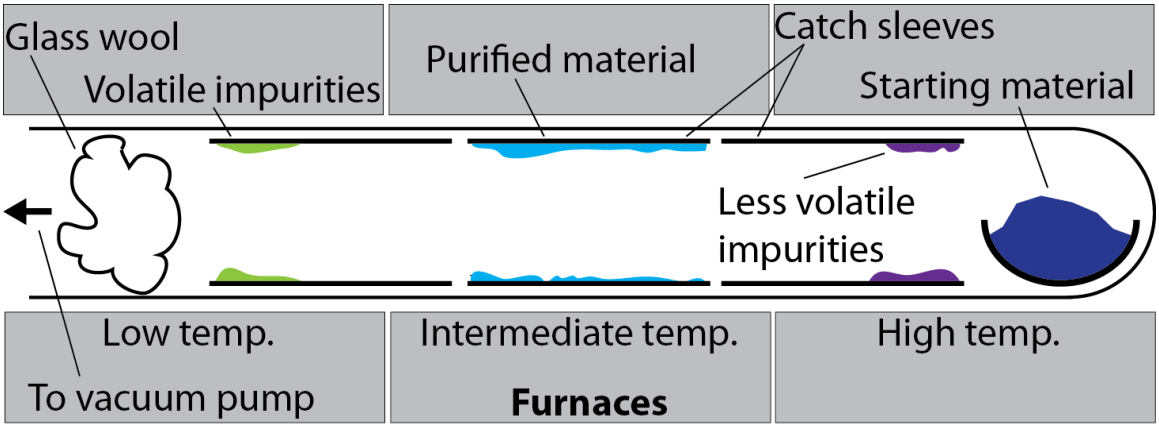

Figure 1.4: Setup of the thermal gradient sublimation purification method. The starting material is placed in the hot zone of an evacuated ($\sim 10^{-6}$ torr) quartz tube inside a zone furnace. The material is then heated to the sublimation point. Any impurities with a different sublimation temperature from the pure material will deposit in a different region of the furnace, allowing the pure material to be removed from a single section of the quartz tube.

small molecules of interest which degrade at lower temperatures than they sublime, which are then also restricted to solvent-based techniques only.

1.4.2.1 Solvent Deposition

Solvent-based deposition techniques are one of the most promising avenues for low-cost fabrication of organic devices. The hope is that it will eventually be possible to print organic circuits in a cheap roll-to-roll process like a newspaper, with equivalent processing costs. Research continues on such methods.[44–48]

One of the most widely-used solvent-based deposition methods for research is spin-coating, as shown in Fig. 1.5. In spin-coating, an organic material is dissolved in a solvent, typically an organic solvent such as toluene, chloroform, or chlorobenzene, at mass concentrations ranging from $\rho = 0.3 - 3\%$ weight/volume. The solution is filtered to remove particles, then a small volume (~ 75 μL for a ~ 2 cm^2 substrate) is deposited on the center of the substrate. The substrate is then spun at $\omega = 0.5 - 5$ kRPM to evenly distribute the solution and evaporate the solvent. Spin-coating is often followed by a thermal anneal to evaporate trapped residual solvent and produce desirable film morphology. The final thickness of a spincoated film has been shown to be approximately[49]

$$h_f = KC_0(\nu_0 D_0)^{1/4}/\Omega^{1/2} \tag{1.2}$$

where h_f is the final thickness, K is a number of order unity, C_0 is the initial solute concen-

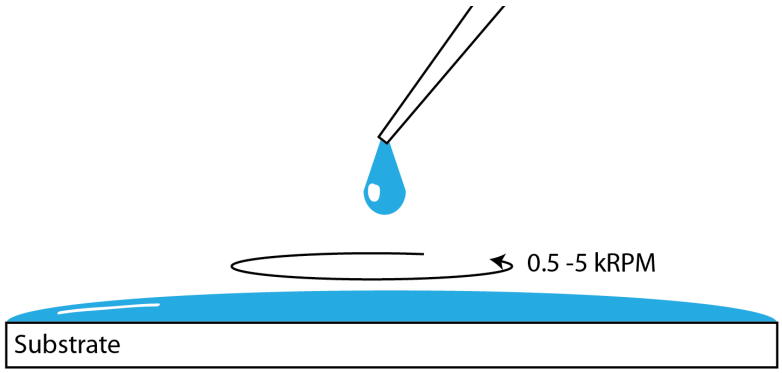

Figure 1.5: Standard setup for spincoating of substrates. A solution of the desired organic molecule in solvent is deposited on the substrate and the substrate is spun (generally at 0.5 - 5 kRPM) while the solution dries, leaving behind a uniform thin coat of material. The thickness of the film depends on the material concentration in solution and inversely on the speed at which the substrate is spun.

tration, ν_0 is the kinematic viscosity, D_0 is the solute diffusivity, and Ω is the spin speed. Typical solubility of organics in the solvents used restricts film thicknesses to between 10 nm and 10 μm.

It can be difficult to deposit multilayer structures through spin-coating as the solution tends to redissolve the underlying layers. This can be avoided through the use of perpendicular solvents, where the solvent in each successive solution is chosen so that the material in the previous layer is insoluble in it. However, it can be difficult to find such materials systems and the total number of layers is limited by the number of available perpendicular solvents. The use of crosslinked polymers have also been explored, where the film is exposed to heat or ultraviolet (UV) light after deposition to create chemical bonds between the polymer chains. This essentially "cures" the material, rendering it impervious to further solvent applications. It is also possible to reduce or eliminate the need for multiple solvent depositions in some applications by depositing a single blended layer containing all of the desired organic materials instead of successive neat layers.

The choice of solvents is known to affect the final morphology of the film as polymer chains may coil or aggregate in some solvents but not in others. This is even more pronounced in blended layers where the choice of solvent can also affect the clustering or mixing of the two component materials. The technique of binary solvents takes advantage of this phenomenon, using two solvents with different volatility, one that preferentially dissolves one material and one that preferentially dissolves the other.[50,51] When spun on a substrate, the two solvents will take different amounts of time to evaporate, leaving behind a layer rich in the material corresponding to the more volatile solvent on the bottom and

the less volatile solvent on the top. Such a gradient morphology can improve the charge generation and extraction characteristics of OPVs.[52,53]

Most solvent-processed devices must then be finished with the vacuum deposition of an evaporated or sputtered top metal contact. This can be expensive and unwieldy, and research continues on top contacts that may be sprayed on or stamped.[54–56] Generally the top contact is used to define the device area, as organics possess such low charge mobility that there is essentially no effect from any of the organic layer except that directly below the contact. However, research continues on methods such as organic vapor jet printing (OVJP) which allow for direct printing of organic devices and therefore do not require an additional patterning step.[57–59]

Spin-coating is only useful for small substrates and is therefore unsuitable for mass production of organic devices.[60] Other methods exist that can be applied to substrates of arbitrary size. In addition to the previously mentioned printing techniques, these include doctor-blading where a razor blade is swept across the substrate leaving a film of set thickness,[61–63] and spraycoating where the solution is sprayed directly on the substrate.[64–66]

1.4.2.2 Evaporation

Multiple methods to evaporate organics exist but by the far the most widely used for both research and commercial purposes is vacuum thermal evaporation (VTE). The basic setup of a VTE system is shown in Fig. 1.6. The organic source material is loaded in a baffled boat, often made of tungsten or molybdenum, and current is run through the boat to resistively heat the source. The organic material sublimes and is deposited on the substrate suspended face-down at the top of the chamber, with the substrate generally rotated to increase film uniformity. The film thickness and deposition rate is monitored in real time by quartz crystal monitors (QCMs) inside the chamber which are also used to keep the deposition rate constant. In general, materials are deposited at a rate of $0.5 - 2$ Å/s, as depositing materials at too high a rate (and, therefore, too high a temperature) can lead to material degradation. Pressure in the system is held at $10^{-6} - 10^{-7}$ torr during deposition to reduce impurity levels.

The technique of VTE allows greater control of film structure than solvent-based techniques. One of the main advantages of VTE is the ability to dope films. More than one source can be simultaneously evaporated in a VTE system, easily allowing for blended or doped layers without having to deal with the relative solubility of the two materials in the same solvent. The real-time independent control of the sources also allows for composition changes throughout the film such as the graded structures that have been shown to increase efficiency and lifetime in organic devices.[53,67–69] There is also no limit to how

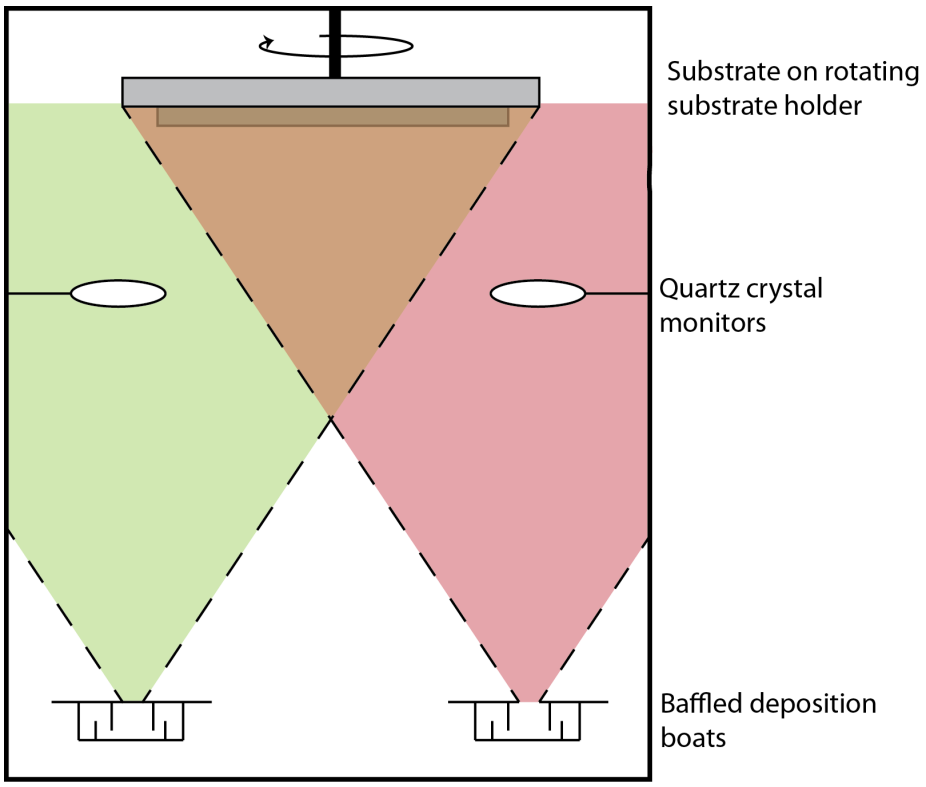

Figure 1.6: Standard setup of a VTE system. Organics are placed in baffled boats at the bottom of the chamber while the substrate is placed at the top.

thick VTE-grown films can be made, in contrast to solvent-based methods, and the real-time monitoring of the deposition rate allows for monolayer control over the film thickness.

Material utilization in VTE depends on the geometry of the chamber. In a research chamber such as that shown in Fig. 1.6, where a small ($\sim$ 10 cm diameter) substrate is suspended 60 cm above the boat, the material utilization efficiency is only $\sim$ 1%. For this setup, the material utilization may be increased by bringing the substrate closer to the source, but this comes at the cost of decreased uniformity. In a manufacturing environment this problem is addressed by using linear sources instead of the point sources shown here.[70]

A less common but promising evaporative technique is organic vapor phase deposition (OVPD), with the basic setup shown in Fig. 1.7.[10,71–73] In OVPD, the organics are evaporated into a hot carrier gas which flows through a heated chamber before reaching a cooled substrate at the end where the material recondenses. As the heated chamber walls prevent deposition of material, the material utilization efficiency can be much higher than that achievable with VTE. Deposition can occur in a range of regimes, as chamber pressure, source evaporation temperature, carrier gas flow rate, and substrate temperature can all be independently adjusted. This gives significant control over the final morphology of

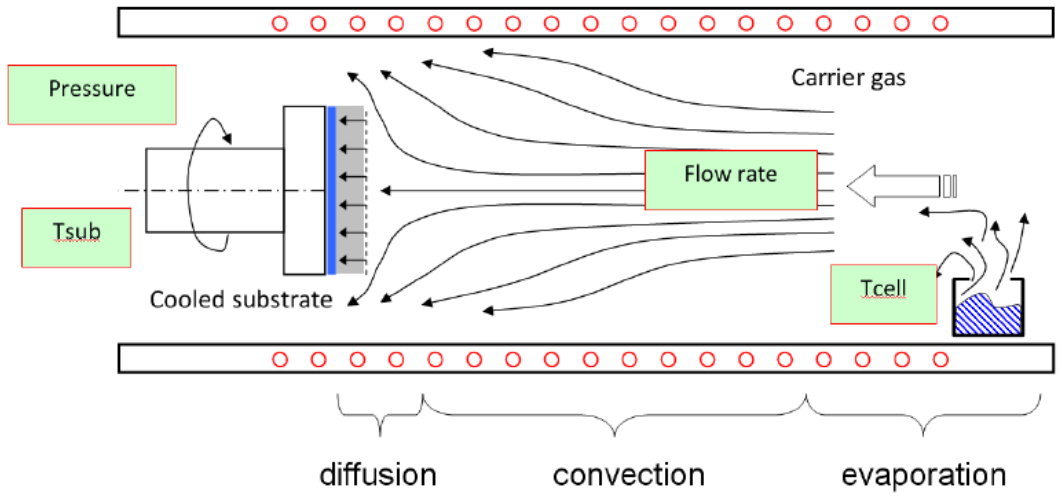

Figure 1.7: Setup of an OVPD system. Figure courtesy of Richard Lunt.

the film, more than that achievable with VTE.

In contrast to VTE, material transport in OVPD is not ballistic which makes it much better at filling in holes and roughness in underlying films. Films grown by VTE can suffer from a self-shadowing effect. With ballistic transport the substrate must have line-of-sight to the source in order for material to be deposited, so small peaks that develop on the film can block the region behind and increase the roughness of the film. This also makes VTE poor at filling in gaps in rough films as the peaks will tend to shadow portions of the substrate and leave voids. In contrast, the carrier gas in OVPD gives the molecules much higher surface mobility, allowing them to easily fill in rough spots in the underlying films.

One disadvantage of OVPD, however, is that material compatibility can be an issue. The walls of an OVPD chamber must be heated to the point where organic materials will not condense on them, but not so hot that they will degrade the organic materials. This is relatively easily achieved for single materials but blended films, important for many different organic devices, can be difficult to deposit if the two materials differ significantly in evaporation temperature. A wall temperature high enough to prevent the high-temperature material, such as the fullerene C_{60}, from condensing can then be so high as to degrade the low temperature material, such as bathophenanthroline (BPhen). This is not an issue in VTE where the different sources are shielded from each other and the walls are not heated. Device architecture for OVPD-grown devices must be carefully chosen to avoid mixed layers of incompatible materials, though research continues on methods to protect materials from interactions with the walls.

Device area for organic semiconductors is generally defined by shadow masking as

the chemicals used in conventional photolithography degrade or dissolve organic films. Shadow masking, unfortunately, has much lower resolution than the feature sizes possible with photolithography. However, the soft nature of organic semiconductors does allow for other processing techniques difficult or impossible in inorganics. Nanoimprint lithography uses a hard preformed stamp to physically imprint a pattern into the soft organic and is capable of creating sub-10 nm feature sizes.[74–76] Roll-to-roll stamping processes have also been demonstrated where organic layers are transferred from one substrate to another.[27–30] These are further pathways that may someday lead to realizing the dream of large-scale printed electronics using organic semiconductors.

1.4.3 Annealing

Annealing is the process of adding energy to a solid to allow the molecules to reorganize. In organics, this is often performed to increase crystallinity of the layer and improve the electrical and excitonic properties of the film.[77–80] Multiple annealing methods exist. In thermal annealing,[81] the film is heated to increase the thermal energy and therefore the mobility of the constituent molecules of the film, while in solvent annealing[82–84] the film is exposed to solvent vapor for a set period of time.

Both individual films and full devices may be annealed. In general, an annealed individual film will have both increased crystallinity and increased roughness. Some roughness can be advantageous; a jagged interface has a larger surface area which can improve exciton harvesting efficiency. Increased crystallinity has also been shown to improve the charge transport properties and exciton lifetime of organic materials.[82,85–88] However, care must be taken to optimize the amount of time the film is annealed. If it is annealed for too long, the material may degrade or the film might become so rough that it will cause shorts in the finished device.

Annealing of full devices tends to have a slightly different effect. The top layers tend to confine the underlying layers, especially if the top layer is a material that is relatively insensitive to the effects of annealing.[85,89] This allows for greater crystallinity in the underlying films without a corresponding increase in roughness. It has also been shown that annealing multilayer films can also cause the interpenetration of the layers with the separate materials diffusing into each other.[89] This can be highly valuable for applications such as blended heterojunctions in OPVs.[84–86,90–92]

1.5 Applications

1.5.1 Organic Photovoltaic (OPV) Cells

Like all photovoltaics, OPVs take in light and produce power in a load. The first efficient OPV (approximately 1% power conversion efficiency (PCE), defined as the ratio of the maximum generated electrical power to the incident illumination power) was developed by C. W. Tang in 1986.[93] Tang's device used an organic donor-acceptor heterojunction, an interface between two materials with a HOMO-LUMO energy offset between them where excitons can be efficiently split into free charges. Due to the energy offset, such dissociation is significantly more efficient than is possible in the bulk material.[94–98] Decades later, the heterojunction concept is still used in all OPVs while efficiency has increased to above 12%.[99] The physics of heterojunctions will be further covered in Chapter 3.

The basic structure of an OPV is shown in Fig. 1.8. In the bottom-illuminated architecture shown, the cell is illuminated through a transparent substrate (quartz or glass) and a transparent anode.* The light is then absorbed in the donor and acceptor materials forming the active layers of the device, generating excitons. The excitons diffuse to the heterojunction, the interface between the donor and acceptor, where they dissociate into free charges. The donor is labeled such as it donates an electron which is accepted by the acceptor. The charge carriers are then extracted through the anode and cathode. The buffer layers shown serve a variety of functions. The cathode contact is generally a blocking material, confining excitons to the active layers, and also serves as an optical spacer which better aligns the peaks of the optical field to the active layers. It also protects the underlying organic layers from damage during the relatively high-temperature metal deposition as well as providing a conductive pathway for electron extraction. The anode buffer does not have to serve all these functions as its position underneath the active layers means that it is much less effective as an optical spacer and does not have to deal with metal deposition. Instead, it serves as an efficient pathway for charge extraction and as a planarization layer for the rough ITO. Common anode buffer materials have been recently shown to quench excitons, though less efficiently than a metal in the same position.[100]

The structure shown in Fig. 1.8 is a planar device, named for the planar layers of donor and acceptor. To dissociate the majority of generated excitons at the heterojunction, the planar layers cannot be significantly thicker than the exciton diffusion length (L_D), the average distance an exciton travels in a material before recombining. For most organic materials, $L_D \sim 10$ nm, with the fullerene C_{60} a notable exception with $L_D \sim 40$ nm.

*The transparent contact of an OPV is often a transparent conductive oxide (TCO) such as indium tin oxide (ITO), though the rising price of indium means indium-free contacts are a region of active research.

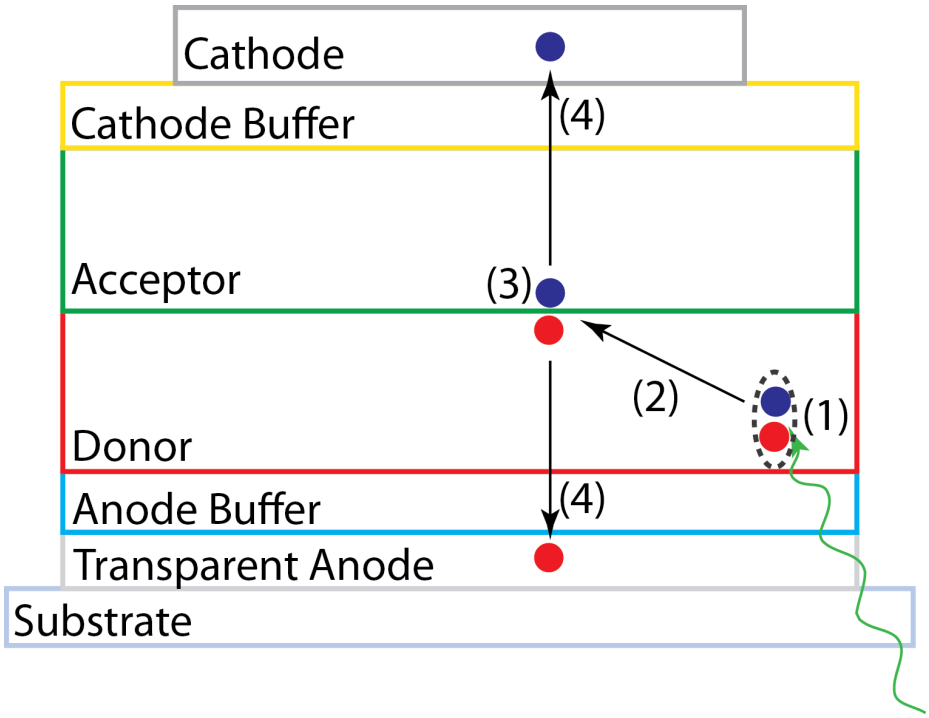

Figure 1.8: Structure and operation of an OPV. Absorption of a photon in the donor or acceptor generates an exciton(1), which then diffuses to the donor-acceptor interface(2). The energy offset between the donor and acceptor (the heterojunction) provides the energy gradient necessary to dissociate the exciton into free charges (3), with the electron on the acceptor and the hole on the donor. The charges are then extracted through the electrodes (4). The two transparent buffer layers provide better electrical contact with the electrodes. The cathode buffer also protects the organic layers from damage during the deposition of the metal top electrode and serves as an optical spacer.

Planar devices therefore have difficulty reaching high efficiencies, as absorption is limited in such thin layers.

Additional architectures have been developed to address the problems with the planar structure, shown in Fig. 1.9. The most effective in small-molecule and polymer OPV is known as the mixed heterojunction, sometimes combined with planar layers to form a planar-mixed heterojunction. A mixed heterojunction consists of a single layer blend of the donor and acceptor materials, greatly increasing the surface area of the interface. Assuming a homogeneous blend, an exciton formed in this layer will be adjacent to an interface and immediately dissociated, allowing the layers to be made arbitrarily thick and therefore arbitrarily absorptive without losing excitons. In practice, charge extraction efficiency is the limiting factor for mixed heterojunctions, as blending the materials results in narrow and circuitous pathways for charge extraction from the center of the layer. Charge extraction efficiency is highly dependent on the layer morphology which is amenable to change

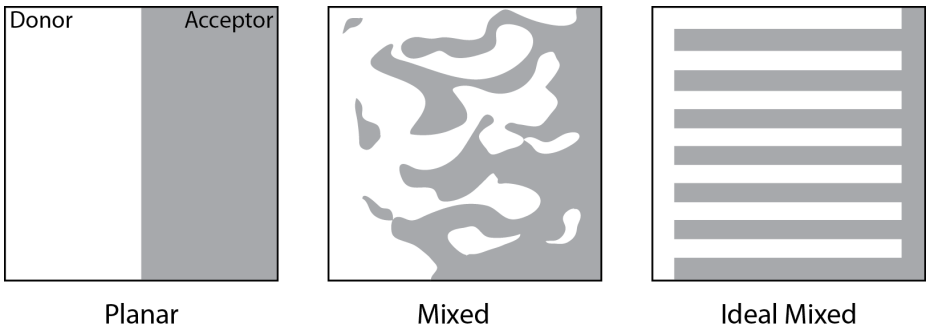

Figure 1.9: Standard OPV structures. Disorder in the mixed heterojunction (middle) can lead to charge trapping in isolated islands of donor or acceptor, as shown. The ideal structure for a mixed heterojunction is shown on the right, where long fingers of material provide wide conductive pathways for all charges to be extracted, while still remaining narrow enough that nearly all excitons reach the donor-acceptor interface and dissociate into free charges.

through appropriate choice of processing techniques. This makes it much easier to optimize mixed devices than planar devices, as L_D is an intrinsic materials property, and is the reason high-efficiency OPVs use the mixed heterojunction architecture.[85,101,102]

Further developments in heterojunction design have involved different methods of ordering the mixed layer. The ideal structure for a mixed heterojunction is a "finger" structure, with the fingers approximately L_D wide, ensuring that all excitons are dissociated while providing broad conductive pathways for charge extraction. Techniques attempting to obtain this structure have included alternating deposition of thin layers of donor and acceptor[71] (the controlled bulk heterojunction) and growth of columns of the donor through oblique angle deposition followed by infilling of the acceptor.[103]

Planar-mixed heterojunctions, a combination of the planar and mixed structures, have also been shown to improve efficiency, absorption, and reliability in devices.[69,100,104] In this structure a mixed layer is sandwiched between a planar layer of donor and acceptor. As the limiting factors for planar layer thickness and mixed layer thickness are different, this allows for a larger total thickness of the active layers and therefore more absorption. In practice, it is often only the higher mobility material, generally the acceptor, which benefits from this treatment. Low-mobility planar layers of the donor can reduce the device efficiency such that the additional absorption cannot compensate.

It is widely agreed that lab devices must exceed an efficiency of $10 - 12\%$ to be viable for large-scale power generation, and this milestone has essentially been reached.[105] As shown in Fig. 1.10, however, there is still significant room for improvement to reach inorganic cell efficiencies. As will be covered in more detail in section 3.3, the theoretical maximum power conversion efficiency for a single-junction OPV is $\sim$22%,[106] lower than

the maximum single-cell inorganic cell efficiency of 31%. This leaves room for a $\sim$ 2x improvement in single-cell efficiency, with further improvements possible with multi-junction devices.

The lifetime of OPV is still a significant obstacle to commercialization but has been making strides in recent years. A polymer tandem OPV using P3HT, [6,6]-phenyl-C_{60}-butyric acid methyl ester (PC60BM), a diketopyrrolopyrrole-quinquethiophene alternating copolymer (pDPP5T-2) and [6,6]-phenyl-C_{70}-butyric acid methyl ester (PC70BM) was recently reported with an 8 year T80 * lifetime.[107] However, such long lifetimes have not been observed for highly efficient cells, with the 8 year device having a peak efficiency of only 4.4%. Lifetime testing on most cells in the literature is rare, and this must be addressed if OPVs are to prove truly useful. Despite the high sensitivity of organics to oxygen and water, there is no intrinsic reason known why organic devices should have a lifetime less than that of silicon. More work must be done on materials and encapsulation techniques to find stable, high-efficiency organic materials, but long-lived organic devices should be an achievable goal.

The area of OPVs will also need to be increased for commercialization. Most research devices are between 1 mm^2 and 1 cm^2, significantly smaller than will be needed for large-scale power generation. Increasing the area is known to decrease yield as well as increase the series resistance due to the comparatively high resistance of the transparent ITO contact compared to metals such as silver or aluminum. Yield of devices can be improved by better contamination control as well as by improved cleaning of the cell substrate before fabrication, such as was recently demonstrated using snow cleaning.[108–110] Snow cleaning uses a jet of supercritical carbon dioxide to both blast particles off the substrate surface and dissolve chemical residues, and has been shown to significantly improve the yield of large area ($\geq$1 cm^2) devices.[111]

1.5.2 Organic Light-Emitting Diodes (OLED)

The basic operating principle of organic light-emitting diodes (OLEDs) is the opposite of OPV. In OPV, light is absorbed in the active layer and charge carriers are extracted as current, whereas in OLEDs electrons and holes are injected into a device and recombine to produce light. Research on OLEDs began with the observation of electroluminescence in organic crystals in the middle of the 20th century. One notable observation was performed by Pope, Kallmann and Magnante in 1963 on tetracene-doped anthracene crystals.[112] These devices were infeasible for commercialization as they required extremely

*T80 is the time it takes for the efficiency of a device to drop to 80% of its starting value.

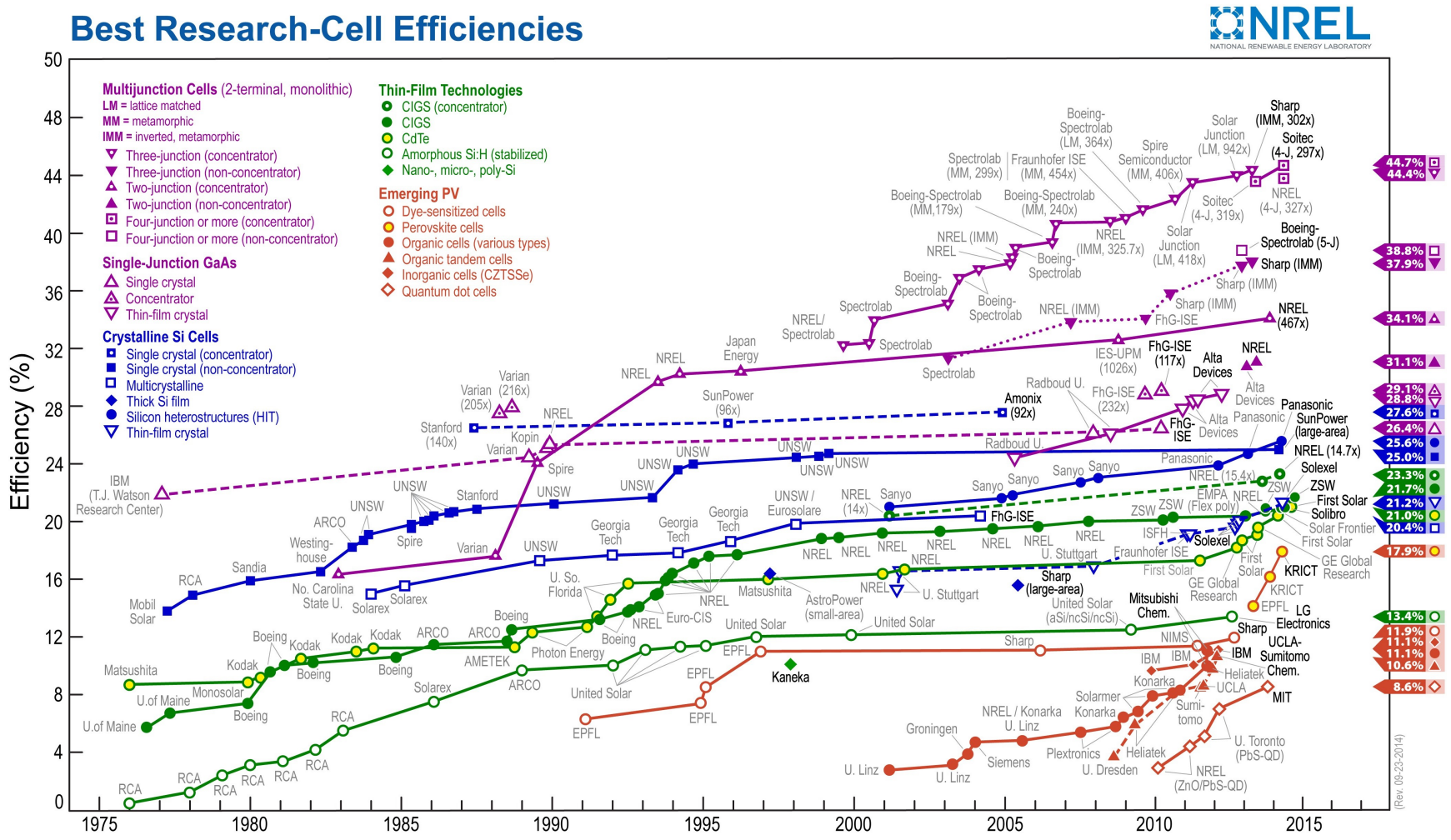

Figure 1.10: Current National Renewable Energy Laboratory (NREL) plot of research solar cell efficiency over time. All cell efficiencies were confirmed through standardized measurements by independent recognized test labs such as NREL, National Institute of Advanced Industrial Science and Technology (AIST), or Fraunhofer. Device efficiency was measured with respect to Standard Test or Reporting Conditions with a reference temperature of 25° C. Bold labels on the plot correspond to the most recent world-record efficiency for that technology, with the record efficiencies and the device type highlighted in flags on the right. This plot is courtesy of the National Renewable Energy Laboratory, Golden, CO.

high voltages exceeding 400 V to luminesce. One of the first practical OLEDs was demonstrated by Tang and Van Slyke[113] in 1987 with external quantum efficiency (EQE) $> 1\%$ at a driving voltage of < 10 V. This bilayer Alq_3 and 1-bis[4-[N,N-di(4-toyl)amino]phenyl]-cyclohexane (TAPC) device introduced the concept of the electron transport layer and the hole transport layer, an architecture still used today.

Further improvements to OLEDs required the development of phosphorescent emitters. One-quarter of excitons generated in OLEDs are singlets with spin quantum number $S = 0$, with the remaining three-quarters $S = 1$ triplets, as the spin of the charge carriers is random upon recombination (see section 2.1.1). In most materials, singlets are the only photoactive species of exciton, the only species that can be optically excited* and that can release light upon recombination, known as fluorescence. Before the work of Baldo, Forrest and Thompson in the 1990s, fluorescent OLEDs could only reach an IQE $= 25\%$ as they could only use singlet excitons.[41] Phosphorescent emitters, molecules that can emit radiation from the triplet state, allowed for OLEDs with IQE $= 100\%$. These molecules generally rely on the heavy-atom effect, where a heavy metal atom such as the iridium in the common phosphor tris[2-phenylpyridinato-C^2,N]iridium(III) ($Ir(ppy)_3$) is responsible for a high degree of spin-orbit coupling in the molecule. This mixes the singlet and triplet states, allowing 100% emission via triplet excitons.

The basic structure of a bottom-emitting OLED is shown in Fig. 1.11. Bottom-emitting devices are grown on a substrate such as glass or plastic coated with a transparent anode such as ITO. The organic layers themselves are generally $100 - 200$ nm thick, with an opaque metal cathode such as aluminum on top. Holes are injected into the hole transport layer (HTL) from the anode, and electrons into the electron transport layer (ETL) from the cathode. The charge carriers then recombine to form excitons in the emissive layer (EML). In a fluorescent device, the singlet excitons then recombine radiatively on the EML material while the triplets recombine non-radiatively and are lost. In phosphorescent devices, the EML is composed of a non-phosphorescent material (the host) doped with a phosphorescent emitter (the guest). Both singlet and triplet excitons form on the host material and transfer to the guest triplet state where they are emitted as phosphorescence.

All commercial OLEDs are currently made exclusively from small molecules. As polymers cannot be evaporated, it is difficult to dope them in the small but controlled quantities required for maximum efficiency. This bars most polymer OLEDs from the other advantages of a doped EML as well. Doping improves the color tunability of devices, and the doping profile of the layer can be freely modified. Applications of modified doping profiles include improvement of OLED lifetime by more evenly distributing the exciton profile

*Photogenerated excitons in OPV are therefore exclusively singlets.

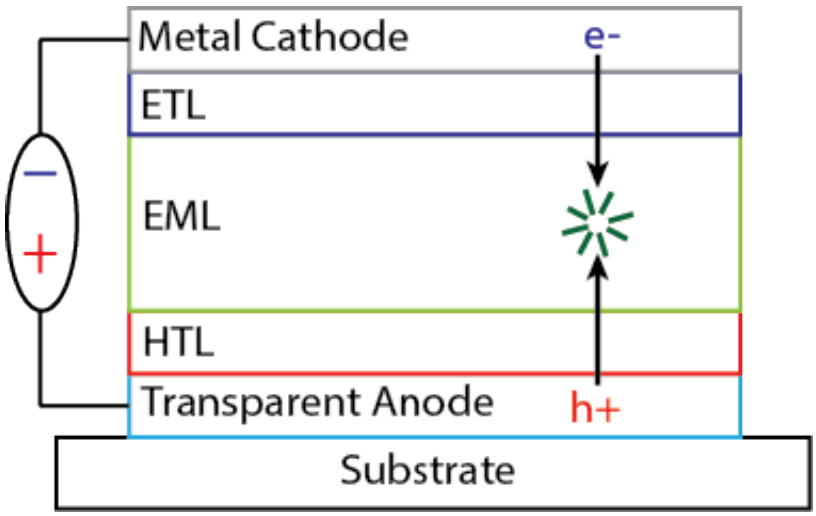

Figure 1.11: Structure and operation of an organic light-emitting diode (OLED). Electrons are injected into the electron transport layer (ETL) and holes into the hole transport layer (HTL) and recombine in the emissive layer (EML), producing light. The energy levels of the ETL and HTL are chosen to prevent transfer of holes and electrons, respectively, out of the EML, confining the charge carriers to the EML and improving efficiency. The OLED shown is a bottom-emitting structure, with light emitted through the transparent anode and substrate.

in the EML, as well as adjusting the orientation of the guest molecules to improve out-coupling of the emitted light. Diluting the luminescent guest in the host molecule also reduces concentration quenching, the tendency of excitons in close proximity to annihilate, by physically separating the molecules.[114,115] The differing HOMO/LUMO levels of the host and guest also tend to lead to charge trapping on the guest molecule which reduces recombination in the EML.

Without question, the current most successful organic semiconductor technology is in OLEDs for displays. A wide range of devices incorporate OLEDs, from smartphones, to watches, to televisions. The most well-known OLED displays are those incorporated in Samsung smartphones, with mobile displays making up more than half of the $15 billion global OLED market in 2015. Displays made from OLEDs have many advantages over conventional liquid-crystal displays (LCDs) including a high contrast ratio, fast response, light weight, large color gamut, low power consumption, and high mechanical flexibility. Similar to OPVs, however, lifetime can be an issue for OLEDs. The lifetime issue is worse for the highest-emitted-photon-energy blue phosphors, as the probability of an exciton breaking a chemical bond and degrading the film is directly related to its energy. As singlets are higher-energy than triplets, a phosphorescent material will always have higher-energy singlets than a fluorescent material emitting at the same wavelength, speeding the rate of degradation. This is the reason commercial OLED displays use fluorescent blue

emitters despite their lower efficiency. Recent work, however, has shown that changes in device structure can improve the lifetime of blue phosphorescent OLEDs by a factor of 10 with further improvements expected from additional optimization of the structure.[40]

Additional research has focused on ways to reach IQE $> 25\%$ with fluorescent emitters allowing them to be used in highly-efficient long-lived devices. One such technique is thermally-activated delayed fluorescence (TADF), where triplets are converted to singlets by ambient thermal energy.[116–118] This requires molecules with extremely close singlet and triplet energy levels, as molecules at room temperature (~ 300 K) only possess a thermal energy of approximately 25 meV. Such a device can have singlet yield of greater than 25%, as triplets are up-converted into luminescent singlets.

The other major focus of current OLED research is outcoupling. Luminscent molecules in the EML of an OLED are generally randomly oriented, meaning the radiation from the layer is isotropic in aggregate. Most of the light from the device is therefore lost into polaron modes in the metal cathode or waveguide modes in the device layers, with only $\sim 20\%$ escaping the device. Perfect outcoupling could therefore lead to a five-fold increase in efficiency. Multiple methods to improve outcoupling have been proposed including molecular alignment of emitters in the EML to preferentially emit out of the device, and low-index grids in the substrate to disrupt the waveguide mode.[119–121]

A less-mature application of OLEDs, subject to the same limitations, is lighting. Although multiple companies have demonstrated OLED luminaires, the technology involved is still less than mature. However, the market for OLED lighting is expected to grow as OLEDs have multiple advantages over competing technologies, including extremely high luminescence efficiency. Incandescent lightbulbs are extremely inefficient (approximately 15 lm/W), while the fluorescent fixtures that are replacing them range from $60 - 90$ lm/W. In contrast, OLED lighting is expected to have an efficiency of > 120 lm/W.[122] The disposal of fluorescent lights also can be difficult as they contain mercury, which is not an issue with OLEDs, and OLEDs lack the long warm-up time (~ 1 minute) of fluorescent lights.

Inorganic LED lighting has also been shown to possess efficiency on the order of > 120 lm/W and is a strong competitor with OLEDs. However, inorganic LED lighting often has problems with heat dissipation that requires active cooling, which increases the cost and the noise background of devices. It also cannot be incorporated into novel flexible or large-area substrates as is the case for OLED lighting. It is therefore expected that OLED lighting will become a leading technology in this market in the years to come.

1.5.3 Organic Semiconductor Lasers (OSL)

Lasers based on organic materials have existed almost since their invention, with the first being demonstrated in 1966 using chloro-aluminum phthalocyanine (ClAlPc) at the IBM Watson Research Center.[123] More recent work has moved from the original liquid dye lasers to thin films, with lasing in an optically-pumped organic thin film first demonstrated in 1997.[124] It was hoped that electrically-pumped organic semiconductor lasers (OSLs) would soon follow, as optical pumping is unsuited for integration into electronic devices. The rapid progress in OLEDs over the past two decades was promising as they themselves are electrically-pumped luminescent organic devices, but this has failed to extend to OSLs.

Recent work has illuminated the origins of the difficulties in creating electrically pumped OSLs. Current OSLs emit from the singlet state. As discussed in Section 1.5.2, optical excitation of organic semiconductors produces only singlets while electronic excitation produces 25% singlets and 75% triplets. As triplet lifetimes are characteristically $10^3 - 10^9$ times longer than that of singlets, an electronically pumped OSL will have an enormous triplet background compared to an equivalent optically pumped device. At such high triplet concentrations, there is a large loss of singlets due to singlet-triplet interactions making it difficult to reach the singlet concentrations required for lasing.[125]

One strategy to overcome this limitation has involved the use of a triplet manager doped into the emissive layer of the laser.[125] A triplet manager is a material with higher singlet energies and lower triplet energies than those of the emissive material. This results in transfer of triplets from the emitter to the lower energy level of the manager, separating them from the singlets which cannot transfer to the higher energy singlet of the manager. This reduces the population of triplets in the emissive material and has been used to develop steady-state optically-pumped OSLs in comparison to previous work which was only able to show pulsed lasing before the growing population of triplets quenched emission.[125] However, it remains an open question whether electrically pumped OSL will ever be possible due to the difficulties of minimizing triplet losses.

Some research has turned to indirect methods of excitation such as optically exciting the OSL with an adjacent electrically triggered LED or inorganic laser,[126,127] as organic lasers possess a variety of useful features that cannot be achieved with current inorganic technology. Organic lasers are expected to be cheap to manufacture and are broadly tuneable. The thermal stability of OSLs is substantially better than that of inorganic diode lasers,[128–130] showing little change in the emission wavelength and lasing threshold over a large temperature range ($0 - 140°$C).

1.5.4 Thin Film Transistors

The operation of organic thin film transistors (OTFTs) is analogous to that of conventional inorganic transistors. However, they share the advantages and disadvantages of all organic devices discussed. The soft organic materials of OTFTs make them flexible and relatively cheaper to deposit. However, most molecules used are air-sensitive, and air-stable materials are still in development.

There are also several characteristics unique to OTFTs. The switching speed of the OTFT is orders of magnitude slower than that of inorganic field-effect transistors, on the order of KHz instead of GHz. This is caused by the low charge mobility of organics, typically less than 1 $cm^2V^{-1}s^{-1}$, due to the weak intermolecular bonds between organic molecules.[131,132] It is therefore unlikely that organics will replace inorganics in most applications, but some possibilities remain. In particular, applications that require low cost, flexibility, and mechanical robustness but lack stringent size or switching speed requirements are ideal for organics.

CHAPTER 2

Physics of Organic Semiconductors

In contrast to inorganic semiconductors, the constituent molecules of an organic semiconductor film are held together by weak van der Waals bonds instead of strong covalent or ionic bonds. This leads to drastically different physical properties including a comparatively low index of refraction, lack of band structure, and highly localized charges. In this chapter we examine the physics of organic films including those that govern exciton generation and transport, charge transport, and fluorescence.

2.1 Excitons

Excitons are the primary carrier of energy in organic semiconductors. Excitation of the material results in the promotion of an electron from the LUMO to the HOMO, leaving behind a positively charged hole.* Coulumbic attraction between the electron and hole then results in a relaxed, charge-neutral bound state known as an exciton.

There are three categories of exciton, distinguished by their spatial extent. The largest, Wannier-Mott excitons, have a radius of 4-10 nm and are most prevalent in inorganic semiconductors. The highly delocalized wavefunctions of electrons and holes result in a weakly bound state (on the order of meV) that is spread over multiple lattice sites. In such materials with a high dielectric constant that provides significant charge screening, these weakly bound states are thermally dissociated into free charge carriers at room temperature.

In contrast, the low dielectric constant in organic semiconductors leads to reduced charge screening and more strongly bound excitons. The smallest and most strongly bound species are Frenkel excitons, common in organics. Frenkel excitons can have binding energies of up to 1 eV and are generally localized on a single molecule. Frenkel excitons are

*Excitation is commonly caused by absorption of a photon or by injection of electrons and holes which recombine into excitons. It is possible but more unusual to generate excitons through chemical reactions, transfer from another excited state, or bombardment with high energy radiation.

distinguished by their mobility, with excitons in some materials traveling over hundreds of lattice sites before recombining.

Organic semiconductors can also display charge-transfer (CT) excitons with size intermediate between the Frenkel and Wannier-Mott exciton. Such CT excitons are distributed across two or more adjacent molecules or next-nearest-neighbor molecules, with a binding energy close to, but generally less than, that of Frenkel excitons. The primary absorption in organic semiconductors is by Frenkel excitons, or more rarely, CT excitons.*

2.1.1 Spin and Excitation

Under Born-Oppenheimer separability conditions, the total wavefunction of a molecule may be written as[12]

$$\psi_t = \psi'_e \chi_v \psi_r \tag{2.1}$$

where e, v, and r refer to the electronic, vibrational, and rotational components of the wavefunction, respectively. To first order, we may further divide the electronic component of the wavefunction into two terms

$$\psi'_e = \psi_e \psi_s \tag{2.2}$$

depending only on the spatial coordinates of the electron and the spin coordinates.

The probability of exciting a molecule, R^2_{lu} is given by

$$R^2_{lu} \propto |\langle \psi'_l | \hat{M} | \psi'_u \rangle|^2 \tag{2.3}$$

where the subscripts indicate the initial and final state and the operator $\hat{M}$ is the dipole moment operator $\hat{M} = -e\hat{r}$, where $\hat{r}$ is the distance vector between the positive and negative charge of the dipole of the molecule. We may now write the expression for optical excitation of a molecule, assuming an incident plane wave

$$R^2_{lu} \propto |\langle \psi_{el} | \hat{M} | \psi_{eu} \rangle|^2 |\langle \chi_{vl} | \chi_{vu} \rangle|^2 |\langle \psi_{sl} | \psi_{su} \rangle|^2 \tag{2.4}$$

Here we neglect the magnetic component of the incident radiation and the rotational component of the molecular wavefunction. If any of the three components of R^2_{lu} are zero, then the transition is disallowed in the dipole approximation. This gives us our selection rules

*An example of a material with significant CT exciton absorption is the lowest-energy absorption peak of the fullerene C_{60}. This is due to molecular symmetries that suppress the transition between the ground state and the lowest energy Frenkel state. In general, the CT state is less tightly bound and therefore higher-energy than the lowest energy Frenkel state.

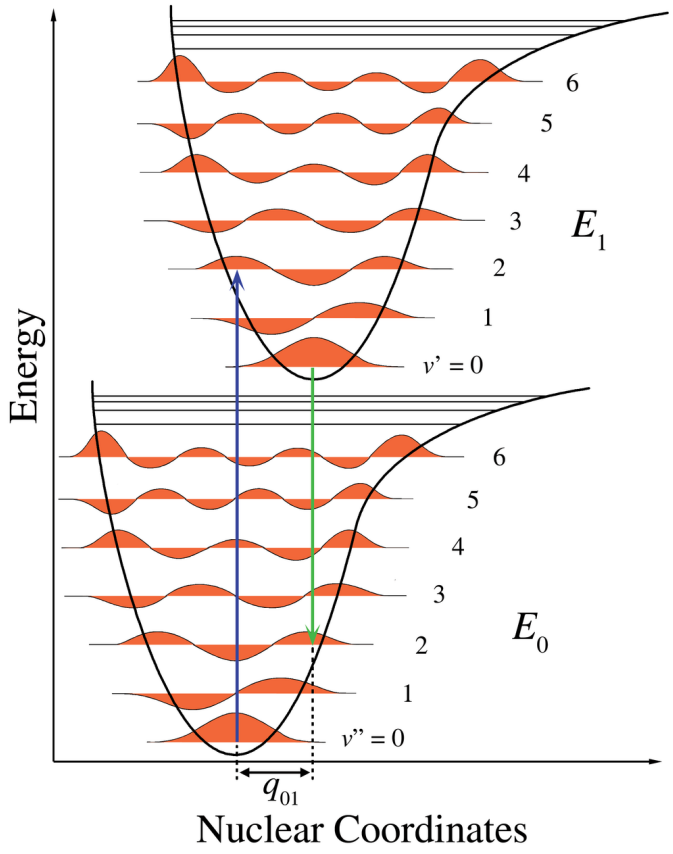

Figure 2.1: Two electronic states and their associated vibrational states. The arrows indicate absorption and emission, with both being direct Franck-Codon transitions. The horizontal offset between the two electronic manifolds indicates the configurational coordinate displacement of the excited state relative to the ground state. Image is from.[133]

for optical excitation.

Let us first consider the transition moment T of the electron spatial coordinate component of the molecular wavefunction,

$$T_e = |\langle \psi_{el} | \hat{M} | \psi_{eu} \rangle|^2 = |\langle \psi_{el} | e\hat{r} | \psi_{eu} \rangle|^2 \tag{2.5}$$

As $\hat{r}$ is an odd operator, T_e is only non-zero when the initial and final state are of opposite parity. Transitions for which $T_e = 0$ are known as dipole-forbidden. The ground state in most molecules has even parity and can only be excited to odd states by a single photon. This rule requires that the molecules in question possess at least inversion symmetry, generally true for the molecules used in organic devices.

Next let us look at the vibrational component of the transition moment,

$$T_v = \langle \chi_{vl} | \chi_{vu} \rangle \tag{2.6}$$

whose absolute square is also known as the Franck-Condon factor.

A standard representation of the ground and first excited state manifolds of a molecule is shown in Figure 2.1. Here the horizontal axis indicates the configurational coordinate displacement the molecule undergoes upon excitation. However, since nuclear motions take about 10^{-13} seconds and electronic transitions take less than 10^{-15} s, electronic transitions are completed before the nuclei can move. This vertical transition is known as a direct Franck-Condon transition and the probability is given by the Franck-Condon factor, the wavefunction overlap between the initial and excited state. After electronic excitation, the electron then thermalizes, relaxing non-radiatively to the lowest vibrational state in the manifold. The electron can then return to the ground state through radiative or non-radiative channels.

Most materials follow Kasha's rule: radiative and non-radiative transitions all occur from the lowest excited state in a given manifold.[134,135] This is because the process of thermalization, where the excited state relaxes to the lowest energy state in the manifold, is generally much faster then transitions between manifolds. This also gives rise to the mirror symmetry between absorption and emission seen in most materials, as shown in Fig. 2.2 for Rhodamine 6G. The Franck-Condon factor between two given vibrational states is the same regardless of the electronic manifold of each state. This means that absorption and emission spectra will be mirror images of the same characteristic peaks, as the $0 \rightarrow 1$ transition has the same probability and therefore the same relative peak height whether it is absorption or emission, but the transition from the 0 state of the excited manifold to the 1 state of the ground manifold will be lower energy than the corresponding transition from the ground manifold to the first excited manifold. Kasha's rule is required for this mirroring to occur; if absorption occurred from the ground vibrational state but emission occurred from a higher-order vibrational state, the Franck-Condon factors would no longer be identical.

The offset between the emission and absorption spectra is known as the Stokes shift. This corresponds to the configurational coordinate displacement between the ground and excited electronic manifold. The larger the displacement, the more energy is expended in reorganizing the molecule and the less in luminescence.

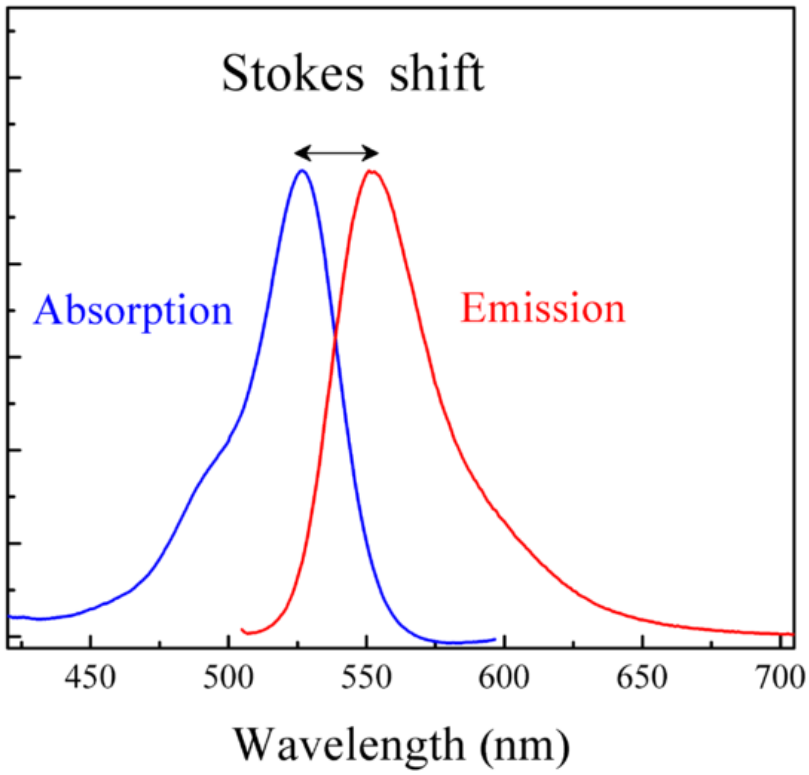

Figure 2.2: Absorption and emission of Rhodamine 6G, a common fluorescent dye. Rhodamine 6G has approximately a 25 nm Stokes shift, the offset between the absorption and emission peak. It also displays the mirror symmetry between emission and absorption expected from Kasha's rule.

Finally, let us consider the spin component of the transition moment,

$$T_s = \langle \psi_{sl} | \psi_{su} \rangle \tag{2.7}$$

As discussed in 2.1, absorption of a photon in an organic semiconductor gives rise to an exciton. As excitons are a bound state of two spin $1/2$ particles, an electron and a hole, they have four possible spin states.[136,137] These include one $S = 0$ state

$$|0,0\rangle = 1/\sqrt{2}(|\uparrow\downarrow\rangle - |\downarrow\uparrow\rangle) \tag{2.8}$$

and three $S = 1$ states,

$$\begin{aligned} |1,1\rangle &= |\uparrow\uparrow\rangle \\ |0,0\rangle &= 1/\sqrt{2}(|\uparrow\downarrow\rangle + |\downarrow\uparrow\rangle) \\ |1,-1\rangle &= |\downarrow\downarrow\rangle \end{aligned} \tag{2.9}$$

where the left side of the equations corresponds to $|S, S_z\rangle$ and the arrows correspond to the S_z states of the individual hole or electron. The single spin zero state is known as the singlet exciton and the three spin one states are collectively known as the triplet exciton.

The ground state of a molecule is generally $S = 0$. This means that optical excitation, which does not change the spin state, can only generate singlet excitons. Electronic excitation, in contrast, injects charge carriers with randomized spin into the organic layer, which then recombine to form excitons. The resulting excitons are therefore equally distributed among the four possible spin states, with one-fourth of them singlets and three-fourths triplets.

The singlet and triplet states, however, are not as distinct as has been presented so far. Spin-orbit coupling, which is present to some degree in every molecule, mixes the triplet and singlet states. This allows for a non-zero probability of transitions between the two states, enhanced in molecules incorporating heavy elements. This ''heavy atom effect" causes enhanced spin-orbit coupling and therefore an increased probability of transitions.

Exciton decay pathways follow the same spin selection rules as excitation. A singlet exciton may decay radiatively, non-radiatively through the release of phonons, or may undergo intersystem crossing (ISC) and become a triplet by interactions with phonons. As radiative decay is spin-allowed for a singlet, these excitons tend to have lifetimes on the order of nanoseconds. Triplets may also undergo radiative or nonradiative decay, as well as reverse intersystem crossing (RISC) to become a singlet. Due to the Pauli exclusion principle, the first singlet excited state is always higher energy than the first triplet excited state. For RISC to be significant, the singlet and triplet state must be close enough in energy for phonons to provide enough energy to transition.

As discussed above, in materials with no spin-orbit coupling, both radiative and non-radiative transitions for the triplet state to the ground state are spin-forbidden. This leads to characteristic long lifetimes, on the order of 10^{-6} to 10^{1} s. Depending on the strength of the spin-orbit coupling, triplets can radiatively decay, with the resulting luminescence known as phosphorescence. Phosphorescence is vital to OLEDs, as it allows 100% utilization of the $S = 0$ and $S = 1$ states.

2.1.2 Energy Transport

The regular lattice of crystalline inorganic semiconductors leads to delocalization of charge carriers, equivalent to a high uncertainty Δx in its position. By the Heisenberg uncertainty principle, $\Delta x \Delta p \geq \hbar/2$, where Δp is the uncertainty in the momentum, a delocalized charge carrier may have very well-defined momentum p. This is the origin of the well-known energy-momentum representation of inorganic semiconductor band structure.

In contrast, materials such as amorphous silicon and most organic semiconductors have highly localized charge carriers. This can be explained in an equivalent manner as that given for inorganic semiconductor band structure above. Amorphous materials have very high rates of scattering leading to a large Δp. Such materials no longer can be described through an energy-momentum relationship and therefore lack such band structure. This is the reason why silicon, an indirect bandgap material, becomes a direct bandgap material when amorphous. Large Δp also allows a small Δx, and charge carriers in amorphous materials are thus localized. Energy transport in organic semiconductors generally takes the form of hopping transport with the dominant mechanisms of transfer given below*.

2.1.2.1 Photon Reabsorption

Photon reabsorption is sometimes referred to as the cascade or trivial energy transfer process. In this process, fluorescence is emitted from the donor molecule and absorbed by the acceptor molecule.† This is a long-range interaction, generally important at lengths greater than 10 nm. The usual effect of this process is to increase the apparent exciton lifetime by up to a factor of 2. This is most important in photoluminescence (PL) measurements taken on the opposite side of the film from the excitation beam, as most light is absorbed near the illuminated surface and therefore emitted photons will have to travel through the entire film before being detected. This makes reabsorption more likely than when excitation and emission occur on the same surface. All PL measurements in this work were taken on the same surface as the illumination beam, meaning this is not a significant effect.

2.1.2.2 Förster Transfer

Förster or resonant energy transfer is a second mechanism of exciton transport. There are three energy regimes for Förster transfer, depending on the relative strength of the vibrational bandwidth of the acceptor electronic state ΔE and the strength of the interaction

*Some crystalline organic semiconductor materials such as PTCDA show evidence of band transport, but most materials do not, even when crystalline.

†The terminology of energy transfer refers to the originating molecule as the donor and the destination molecule as the acceptor. This is a different usage of these terms than we will see in Chapter 3.

between the donor and acceptor, J.[12] In practice, we deal only with the very-weak-coupling limit where $\Delta E > |J|$.

The original derivations of this transfer mechanism assumed coherent transfer mediated by the dipole-dipole interaction. In order for this assumption to hold, the acceptor-state lifetime must be long in comparison to $\hbar|J|^{-1}$. It was Förster who realized that this condition only applies in the rare strong-coupling case where $\Delta E << |J|$. In the common very-weak-coupling case, transfer is not coherent. The electronic state of the acceptor is strongly coupled to a large population of degenerate vibrational states at the same energy. This quickly disperses the energy of the acceptor state into the vibrational states, which can then easily relax to lower-energy vibrational states. This automatically causes dephasing of the acceptor state and introduces irreversability when the vibrational state relaxes.

Using this framework, the rate of energy transfer k_{ET} in the dipole approximation is [12]

$$k_{ET} = \frac{1}{\tau_D}\frac{1}{R^6}\left(\frac{3}{4\pi}\int \frac{c^4}{\omega^4 n_0^4} F_D(\omega)\sigma_A(\omega)d\omega\right) \tag{2.10}$$

where τ_D is the donor excited lifetime in the absence of energy transfer, R is the distance between donor and acceptor, n_0 is the index of refraction, $F_D(\omega)$ is the area-normalized fluorescence emission spectrum, and $\sigma_A(\omega)$ is the normalized acceptor absorption cross section in units of cm^2. The R^{-6} dependence arises from the dipole-dipole interaction between the molecules as the electrical near-field goes as R^{-3} and the induced dipole in the acceptor molecule also goes as R^{-3}. This holds for $R < \frac{\lambda}{2\pi n_0}$, hundreds of nm for visible light and typical organic indices of refraction of approximately 2. As interaction distances for Förster transfer are generally on the order of 1 to 10 nm for the systems considered, this relationship holds.

This still neglects several important parameters. Dipole-dipole interactions are inherently anisotropic; for crystalline materials this introduces a orientation factor[12]

$$f = \frac{3}{2}\left[\mu_D \cdot \mu_A - 3(\mu_d \cdot r)(\mu_A \cdot r)\right]^2 \tag{2.11}$$

where μ_D (μ_A) is the unit vector parallel to the donor (acceptor) transition dipole moment and r is the vector separating the two molecules. For an amorphous film with randomly oriented dipoles, $\sqrt{f} = 0.845\sqrt{2/3}$.[138] It is also more convenient to work with the observed donor lifetime τ instead of the natural lifetime τ_D, where $\tau = \Phi_F \tau_D$, where Φ_F is the fluorescence yield of the donor in the absence of the acceptor. We may now define the Förster transfer rate in terms of a characteristic distance $\bar{R}_0$, the donor acceptor distance at which transfer competes equally with all other paths for removal of energy from the donor

molecule:

$$K_{D\to A} = \frac{1}{\tau}\left(\frac{\bar{R}_0}{R}\right)^6 ; \bar{R}_0 = \frac{3\Phi_F f}{4\pi}\int \frac{c^4}{\omega^4 n_0^4} F_D(\omega)\sigma_A(\omega)d\omega) \tag{2.12}$$

A common acronym for Förster transfer in the literature is FRET, which originally was defined as "Fluorescence Resonance Energy Transfer." However, Förster does not involve fluorescence; under certain conditions, it may even be applied to energy transfer from triplet states to singlet states, which by definition cannot be fluorescence.[139] Despite the definition of Eq. 2.12 using the fluorescence yield Φ_F, no fluorescence is involved. The spectral overlap integral instead corresponds to a density of states overlap between the acceptor and donor. Therefore the acronym FRET now stands for Förster Resonance Energy Transfer".

Several aspects of FRET require caution in their use. For one, consider Förster's original definition for R_0:[139]

$$R_0^6 = \frac{9(ln(10))}{128\pi^5 N_A}\frac{f\Phi_F}{n_0^4}J \tag{2.13}$$

where N_A is Avogadro's number, and J is the overlap integral. It is important to note that this equation was misprinted in some of Förster's original papers as π^6 instead of π^5. This was later corrected by Förster, but the error has propagated through the literature and must be watched for.

Care must also be taken when calculating the spectral overlap integral J. As defined in Eq. 2.12, the overlap integral uses the normalized donor fluorescence emission spectra $F_D(\omega)$. Many sources in the literature do not define whether this is the *area-* or *peak-*normalized fluorescence. Obviously these will result in very different values for the overlap integral. The correct choice is to use the area-normalized fluorescence,[139] such that

$$\int F_D(\omega)d\omega = 1 \tag{2.14}$$

or

$$\int F_D(\lambda)d\lambda = 1 \tag{2.15}$$

depending on whether the fluorescence is defined with respect to frequency or wavelength, both equally valid if consistent definitions are used for all terms in the integral. Spectrofluorimeters generally possess some non-unity exit channel response function that can distort the measured fluorescence spectrum. Such spectra must be corrected for this effect before they can be used in Eq. 2.12 to avoid incorrect overlap integrals.

An additional error that has propagated through the literature is a factor of 9000 instead of 9 in the definition of Eq. 2.13.[139] This factor is not technically incorrect; it is often

included to convert units of dm^3 in the overlap integral into cm^3. The different definitions appearing in the literature can easily lead one into using the incorrect equation, resulting in more than a three times larger value for R_0. Care must be taken to ensure units are consistent on both sides of Eq. 2.13.

2.1.2.3 Dexter Transfer

The derivation of Förster transfer relies on dipole-dipole interactions between the donor and acceptor molecules. However, many excitonic states possess electric-dipole forbidden transitions which therefore cannot undergo Förster transfer. Such states include triplet excitons in materials with minimal spin-orbit coupling and materials with molecular symmetries that disallow dipole transitions such as the fullerene C_{60}. Excitons in these materials instead diffuse through higher multipole interactions or electron exchange. The transfer rate for electron exchange has been modeled for the important case of triplet-triplet energy transfer by Dexter as

$$K_{D\to A} = \frac{2\pi}{\hbar}|\beta_{DA}|^2 \int F_D(E)F_A(E)dE \tag{2.16}$$

where β_{DA} is the energy exchange interaction between materials, E is the energy, and $F_D(E)$ and $F_A(E)$ are the normalized phosphorescence spectrum of the donor and the normalized absorption of the acceptor molecule, respectively.

2.1.3 Exciton Diffusion

In practice, exciton diffusion in organic materials can be accurately modeled with the diffusion equation

$$\frac{\delta n(x,t)}{\delta t} = \frac{L_D^2}{\tau}\frac{\delta^2 n(x,t)}{\delta x^2} - \frac{n(x,t)}{\tau} + G(x,t) \tag{2.17}$$

where $n(x,t)$ is the exciton density as a function of time and position in the material, τ is the exciton lifetime, L_D is the exciton diffusion length, the average distance the exciton travels before recombining, and $G(x,t)$ is the exciton generation rate. Materials under steady-state illumination such as OPVs and many PL measurements use the steady-state (time independent) exciton diffusion equation:

$$0 = \frac{L_D^2}{\tau}\frac{\delta^2 n(x)}{\delta x^2} - \frac{n(x)}{\tau} + G(x) \tag{2.18}$$

This model of exciton transport is insensitive to the types of transport discussed in section 2.1.2.

Interfaces in organic stacks are represented by an appropriate choice of boundary conditions. There are three types: ideal blocking, where all excitons incident on the interface are reflected back into the layer; ideal quenching, where all excitons incident on the interface recombine; and non-ideal, where the interface has some behavior intermediate between ideal blocking and ideal quenching. The ideal boundary conditions are

$$\left.\frac{\delta n}{\delta x}\right|_{x=0} = 0 \tag{2.19}$$

for blocking and

$$n(0) = 0 \tag{2.20}$$

for quenching. A non-ideal interface can be characterized in terms of the density at the interface. For an ideal blocking interface, the exciton density at the interface will be a maximum, $n(0) = n_B$. A non-ideal interface will have some exciton density between n_B and the quenching density of 0, such that

$$n(0) = \phi n_B \tag{2.21}$$

where ϕ is the blocking efficiency.

For Eq. 2.18 to be valid, the material in question must be represented fully by L_D and τ. This requires that the material be essentially identical on the molecular scale; at most L_D and τ may vary with time or position. The steady-state diffusion equation is therefore unable to handle systems where the properties of individual molecules are important, or systems with a degree of randomness that cannot be modeled with an effective L_D or τ. Examples of such problems include simulations of exciton transport through organic layers with random disorder in the energy of individual molecules or diffusion through mixed conductor-insulator blends. Such problems are instead treated through Monte-Carlo simulations of exciton transport. This also allows for derivation from first principles of material parameters such as diffusivity instead of using fixed values.

The predominant method for calculating transition rates of excitons between molecules in an organic semiconductor is the Miller-Abrahams model. This was originally developed to model the hopping transport of charge carriers in deep-gap defect states in inorganic semiconductors, but may be applied to many types of hopping transport. The Miller-Abrahams model states that the transition rate W_{ij} from site i to site j is

$$W_{ij} = \nu_0 e^{-2(r_{ij}/b)} \begin{cases} e^{-(\epsilon_j - \epsilon_i)/k_B T}, & \epsilon_j > \epsilon_i \\ 1, & \epsilon_j < \epsilon_i \end{cases} \tag{2.22}$$

where ϵ_i and ϵ_j indicate the energy of site i and j, respectively, r_{ij} is the distance between the two sites, b is the localization radius of the charge carrier, $\nu_0 = A\overline{|\epsilon_i - \epsilon_j|}/\hbar$, A is a numerical constant, and $\overline{|\epsilon_i - \epsilon_j|}$ is the average energy spacing between sites i and j.

2.2 Photoluminescence

Luminescence is defined as the light emitted by an excited material, in addition to the black-body radiation expected at any temperature above absolute zero. This is inherently a non-equilibrium process where extra energy is provided to the material which re-equilibrates with its surroundings through the emission of radiation. The prefix of the term indicates the mechanism by which the energy is provided; common mechanisms include chemiluminescence, excitation through exothermic chemical reactions; thermoluminescence, the release of heat energy in the form of light; electroluminescence, the operating principle of OLEDs where light is generated by the recombination of injected charge carriers; and photoluminescence, where the material is excited by incident light and re-emits at a longer wavelength.

Luminescence is also distinguished by the characteristic timescale on which it occurs. Other varieties of non-equilibrium light emission from matter occur including scattering processes such as Raman or Brillouin scattering, reflected light, and Chrenkov radiation. However, these interactions occur on extremely short time scales, on the order of fs, and result in almost no energy transfer between the incident photon and the electronic system of the material. In contrast, luminescence requires the constituent atoms or molecules of the material to be excited to a higher electronic energy state. This gives luminescence a characteristic longer decay time, as electronic excited states have a lifetime of $> 10^{-10}$ s*.

In this work we focus on photoluminescence (PL). The first historical term used to describe PL was phosphorescence describing the long-term light emission of certain materials after the cessation of the exciting illumination. This was frequently observed in phophorus, leading to the name, but the modern usage of the term has nothing to do with the chemical composition of the emitting material. Later, the term fluorescence was developed to describe light emission which ceased immediately upon cessation of illumination. Similar to the origin of the term phosphorescence, fluorescence was first observed in fluorite, CaF_2.

Modern usage in organic materials distinguishes between phosphorescence and fluorescence based on the spin of the originating excited state, as discussed in section 2.1.1.

*The full range of lifetimes of luminescent electronic excited states is extremely broad, ranging from hundreds of ps to days. It is the lower limit that distinguishes luminescence from other interactions between light and matter.

Fluorescence is emitted by singlet states with a characteristic short ($\sim$ ns) lifetime due to the allowed optical transition between the excited and ground state. Phosphorescence is emitted by triplet states with a much longer (μs - minutes) lifetime due to the excited triplet to ground singlet ($T_1 \rightarrow S_0$) being optically disallowed. The two types of emission are generally separated in both lifetime and energy, allowing for independent measurements of both.

Organic and inorganic materials both exhibit PL. In covalently bonded materials such as most crystalline inorganic semiconductors, PL reflects the bulk characteristics of the material as its electronic states are an emergent property of the crystalline structure. In van der Waals bonded organics the individual molecules are isolated enough that the single-molecule properties determine the PL. Organic materials therefore have similar PL in solution and in solid films, although the effects of the local environment (solvents of different polarity or disorder in the solid film) lead to some differences.

The relative brightness of the luminescence of a material can be expressed in terms of the photoluminescence quantum yield or quantum efficiency $\Phi \leq 1$. This is defined as the ratio of emitted to absorbed photons. The value of Φ determines the sensitivity of the detectors needed. Materials used in OLEDs are generally highly efficient, with Φ approaching 1. Materials used in OPV tend to be very weak emitters, with Φ ranging from 0.01 to 10^{-6}.

The basic experimental setup of a PL measurement is shown in Fig. 2.3. Generally, monochromatic light is used to excite a sample, then the emitted luminescence is collected, passed through a monochromator, and measured. The excitation light source depends on the measurement and materials. Either laser illumination or light from a broad-spectrum source such as a Xe arc lamp passed through a monochromator is used, and the PL is measured under either time-resolved or steady-state conditions. Laser illumination is very spectrally pure and allows for extremely high excitation intensities. It also allows for extremely short (ps or less) excitation pulses which are necessary when measuring the singlet lifetimes of many materials, often $\leq$1 ns.

The main advantage to using an arc lamp or other incoherent light source is their broad spectrum. The spectrum of a Xe arc lamp runs from 250 nm to 1000 nm, allowing sample excitation over this entire range of wavelengths. This is difficult to match with a single laser, especially in steady-state. Incoherent light sources are often best suited for general-use systems where a wide range of materials with different excitation spectra may be measured, as well as for measurements that relay on measuring the PL at a wide range of excitation wavelengths, such as will be discussed in Chapter 4. They are also suited for measurements where intense excitation is not only unneeded but detrimental. Many organic materials

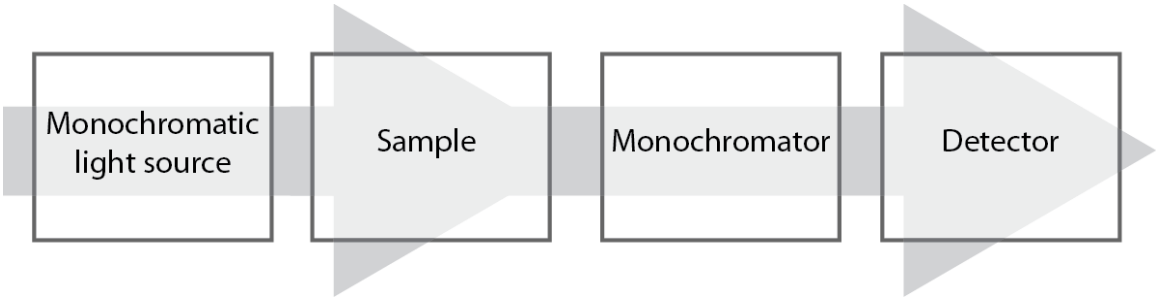

Figure 2.3: Basic setup for a PL measurement. Monochromatic light, either from a laser or an incoherent light source passed through a monochromator, is used to excite a sample. The light emitted by the sample is then passed through a monochromator and measured.

are damaged if too much radiative energy is dumped on them, leading to a change in the PL signal over time. Even stable materials can show nonlinear effects at high excitation intensities when exciton density becomes large enough, with higher-order exciton-exciton interactions leading to erroneously low measured values of the exciton lifetime.

Multiple sample configurations are also possible. One of the most common for highly-absorbing thin films is the front-illuminated, front-emission geometry where the excitation and emission beams are separated by 90° which allows the optics of each to be adjusted separately. A sample angle of 45° to the excitation beam is generally avoided to keep from reflecting the excitation light directly into the detector, but the sample can otherwise be freely rotated. In the extreme case, the sample may be placed perpendicular to the excitation light, allowing the film to waveguide emitted light into the detector. However, this can lead to distortions of the emitted PL spectrum as the sample can reabsorb portions of the emitted light.

One possible confounding factor with the use of monochromators for the excitation and emission beams is the presence of wavelength-doubled light. Most modern monochromators use diffraction gratings to spectrally separate the incident illumination which have higher-order peaks at integer multiples of the wavelength. This means a strong 300 nm peak, for example, will also be transmitted at lower intensity when the monochromator is set to 600 nm and 900 nm. This can be a problem when the emission is measured at an integer multiple of the excitation wavelength, as scattered excitation light can then overwhelm weak sample PL. Long-pass filters are often incorporated in the optical paths to screen out higher-order lower-wavelength light. Dielectric filters are preferred for this application as colored-glass filters can possess their own PL which can also swamp the sample PL signal. Even some transparent dielectric materials can exhibit low-level PL, as can substrate materials like quartz, and this must be tested when performing measurements on materials with

low Φ.

Detector choice also depends on the Φ of the material under study. High-intensity materials allow the use of multichannel detectors which can measure photon flux at multiple points in space at once. These usually take the form of linear or two-dimensional arrays of photosensitive detectors such as CCDs. Combined with a monochromator which spatially separates light of different wavelengths, this allows the simultaneous measurement of the entire emission spectra. Streak cameras are a further development of this idea where the emitted light from the sample under pulsed illumination is swept across a two-dimensional detector array. One axis of the array then corresponds to wavelength as described above, and the other corresponds to time, set by the speed of the sweep. This allows for examination of the spectral response of the material on times scales on the order of nanoseconds, difficult to perform with single channel detectors that can only measure one wavelength at a time.

Multichannel detectors have some limitations, however. The wavelength resolution of the detector is limited by the grating and the spacing of the detector elements which can be disadvantageous for some measurements. Multichannel detectors are also generally less sensitive than single-channel detectors such as photomultiplier tubes (PMTs) or avalanche photodiodes (APDs). These single-channel detectors are sensitive to individual photons, allowing for true photon counting. Single-channel detectors are therefore the most useful for measuring materials with extremely low Φ, which describes many of the materials used in OPVs. The tradeoff is that these measurements take longer to perform than with a multichannel detector as the detector must be scanned over each wavelength. The most sensitive single-channel detectors also tend to have long response times which prevent them from being used to measure sub-nanosecond PL lifetimes.

2.3 Charges

Here we discuss some of the physics governing charge transport through single layers of organic semiconductors. Charge recombination in organic devices is often intimately connected with the organic heterojunction and therefore is treated in Chapter 3.

As mentioned in Section 1.2, the mathematical description of charge transport in crystalline inorganic semiconductors relies on the periodic nature of the lattice. Particles traveling in a periodic potential can be modeled through the use of Bloch's theorem which states that the wavefunction of such a particle is

$$\Psi(r) = e^{ikr}u(r) \tag{2.23}$$

where Ψ is the total wavefunction of the charge, r is the position coordinate, k is the wavenumber, and u is a periodic function with the same period as the potential. Such a particle is delocalized with the wavefunction extending over all space. The physics of such materials is therefore an emergent property of the bulk material as delocalized electrons interact.

Organic semiconductors, especially amorphous organics, cannot be modeled through use of Bloch's theorem. The lack of a periodic potential due to molecular disorder means that charges are no longer delocalized and instead are generally considered to reside on a single molecule. Charge transport in organics proceeds through site-to-site hopping. This is very similar to exciton transport with one critical difference. Excitons are composed of an electron and a hole and are therefore net neutral. In contrast, free charges, electrons and holes, can be driven by an electric field within a device.

There are two models used to describe the hopping transport of charges in organic semiconductors. The first is the Miller-Abrahams model, similar to exciton transport. The Miller-Abrahams model states that the transition rate W_{ij} from site i to site j is:[140]

$$W_{ij} = \nu_0 e^{-2(r_{ij}/b)} \begin{cases} e^{-(\epsilon_j - \epsilon_i)/k_B T}, & \epsilon_j > \epsilon_i \\ 1, & \epsilon_j < \epsilon_i \end{cases} \tag{2.24}$$

where ϵ_i and ϵ_j indicate the energy of site i and j, respectively, r_{ij} is the distance between the two sites, b is the localization radius of the charge carrier, $\nu_0 = A\overline{|\epsilon_i - \epsilon_j|}/\hbar$, A is a numerical constant, and $\overline{|\epsilon_i - \epsilon_j|}$ is the average energy spacing between sites i and j. In the case of an applied electric field the site energies include an electrostatic energy term.

Amorphous organic materials possess both variation in the distance between molecules and variation in the relative energies of individual molecules due to changes in the local environment. This is incorporated into modeling of charge transport by allowing both r_{ij} and the energy of each site to vary, usually with a Gaussian distribution:

$$\rho\epsilon = (2\pi\sigma^2)^{-1/2} exp(-\frac{\epsilon^2}{2\sigma^2}) \tag{2.25}$$

where σ is an adjustable parameter which sets the width of the Gaussian and therefore the disorder. This technique has been used in Monte Carlo simulations of charge transport through organics, correctly displaying characteristic behaviors such as field dependence of mobility obeying the Poole-Frenkel law,[8] $\ln(\mu) \propto \sqrt{E}$.

An alternate method for calculating the rate of charge transfer in organic semiconductors revolves around Marcus theory,[141] originally developed to calculate the rates of outer-sphere electron transfer reactions.[142] Outer-sphere reactions such as these are defined

as a reaction in which an electron is transferred from one molecule to another without any chemical bonds being made or broken, and examples include photosynthesis, certain types of corrosion, and the oxidation of iron ions. Rudolph A. Marcus was awarded the Nobel Prize in Chemistry for this work in 1992.

Chemical reactions can all be expressed as the movement of the system along an energy surface from a local minimum at the initial state to a local minimum at the final state. Marcus showed that the entire system could be expressed as two harmonic oscillators relative to a single reaction coordinate, one representing the energy of the reactants plus the surrounding medium and the other representing the products plus the surrounding medium. The effects of the surrounding medium are vitally important to the theory as a molecule embedded in a dielectric will have a significantly different local environment if it is charged, polarizing the dielectric. Thermal energy, the driver of spontaneous reactions, can then be represented as random fluctuations in the reaction coordinate.

A sample reaction is shown in Fig. 2.4. This is an electron self-exchange reaction where the free energy of the initial and final states are equal. The intersection of the free energy curves is the point where the energy and reaction coordinate of the two systems are equal, and therefore defines the transitional state and activation energy of the reaction. Two important parameters in calculating the reaction rate are shown. The reorganization energy λ is the energy required to go from the equilibrium initial state to the final state. Physically this has two parts; the internal reorganization energy, the energy required to rearrange the molecules taking part in the reaction from their initial to final states; and the external reorganization energy, the energy needed to rearrange the surrounding medium, for example by polarizing surrounding molecules. The other parameter shown is H_{ab}, the electronic coupling matrix element between the initial and final state. This gives the splitting between the two states at their intersection, though in practice it is often neglected when calculating the activation energy of the reaction.

In organics, the rate of intermolecular hopping of charges according to Marcus theory is:[143]

$$k_{et} = \frac{2\pi}{\hbar} \frac{H_{ab}^2}{\sqrt{4\pi\lambda kT}} \exp\left(\frac{(\Delta G^0 + \lambda)^2}{4\lambda kt}\right) \tag{2.26}$$

where k is the Boltzmann constant, T is the temperature of the reaction, and ΔG^0 is the free energy difference between the initial and final state.

Marcus theory explains why organic semiconductors often have different electron and hole mobilities. These are inherently different physical processes; both have an uncharged molecule as one reactant, but one also has a molecule with an extra electron and the other a molecule with a missing electron. This can result in both a different internal reorganization

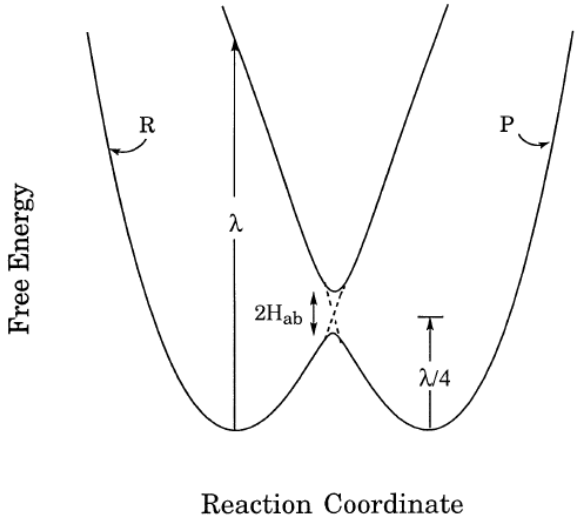

Figure 2.4: Diagram of a self-exchange reaction in Marcus theory. In this case the energy of the reactants (R) and products (P) are equal. A reaction with differing initial and final energies is represented by shifting one of the curves up or down in relation to the other. The reorganization energy, the energy required to go from the initial equilibrium state to the (non-interacting) product state is given by λ, and $2H_{ab}$ is the splitting of the energy curves at the intersection, calculated from the electronic coupling matrix element H_{ab}. Image is from.[142]

energy, as the internal energy states of the molecule will be different in the two situations, and a different external reorganization energy, as the medium reacts differently to a net positive and a net negative charge.

In practice, Marcus theory can be more difficult to use to model charge transport than Miller-Abrahams theory as it requires additional physical parameters to be known. The reorganization energy of organic molecules can be difficult to measure in organic thin films, and is required for calculation of the transfer rate. In addition, the external reorganization energy depends strongly on the external medium, which means that it will change if the molecule is in a solid film or in solution in a specific solvent.

CHAPTER 3

Physics of Organic Devices

All OPVs studied before 1985 relied on single organic layers, with dissociation occurring in the bulk of the material.[93] Such devices were extremely inefficient, often with PCE below 1%. Due to the high binding energy of excitons ($\sim$ 1 eV), charge generation from these devices was dependent on the applied bias, requiring high electric fields to show any reasonable amount of dissociation.

Tang in 1986 introduced the use of organic heterojunctions in OPVs.[93] Tang used two materials with offset energy levels to form a Type-II heterojunction (see Fig. 3.1) which provided the energy needed to dissociate excitons without external energy input. This results in as a field-independent dissociation rate.

Devices since then have been further improved by the introduction of Type-I heterojunctions used to confine excitons to the active layers and improve photocurrent yield. This confinement layer is known as a blocking layer.

In this chapter we examine the physics of multilayer structures such as those used in OPVs, as the importance of heterojunctions to device operation means that much of the physics involved in these devices arises from the behavior of multiple adjacent layers. This is an extension of Chapter 2, where we considered the physics of single organic layers in isolation. We begin with a brief discussion of the operation and characterization of OPVs, important as background for a deeper discussion of the physical properties of the devices that lead to these characteristics. We then discuss some of the loss mechanisms for current in devices, and methods for characterizing such losses. Finally, we examine the techniques used to calculate the standing optical field in a multilayer stack under illumination.

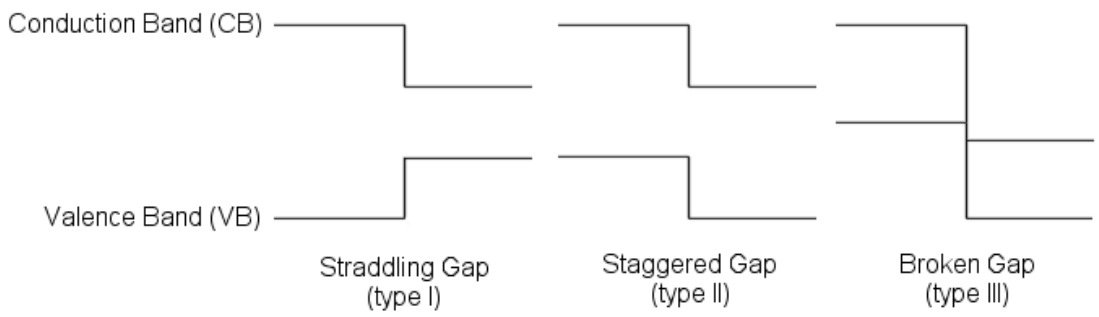

Figure 3.1: Energy level diagrams of the three types of heterojunction. OPVss make use of type I and type II heterojunctions.

3.1 OPV Operation

Four steps are required to go from light to extracted photocurrent in an OPVs, each with its own associated efficiency. These processes are, in order, absorption (A), exciton diffusion (ED), dissociation (CT, for the intermediate charge-transfer state), and extraction(CC, charge collection), each with its own associated physics. The total efficiency of the device can then be expressed as the product of these efficiencies, $\eta = \eta_A \eta_{ED} \eta_{CT} \eta_{CC}$.

3.1.1 Absorption

The first step of current generation is the absorption of light, where a photon is absorbed in the organic active layer and forms an exciton. There are several common limitations on the efficiency of this step. One is that, as discussed in Section 1.5.1, the thickness of the active layers is often limited due to high resistance, short exciton diffusion length, or other undesirable properties of the active materials. The mixed heterojunction is one technique used to increase the thickness of the active layers, but is still often limited by resistivity. Tandem devices, where two or more OPVs are stacked, can also be used to increase total absorption and, therefore, efficiency. New materials are also constantly being developed, with many groups searching for organic semiconductors that exhibit higher absorption, better charge conduction, and longer exciton diffusion length. Presently, however, the absorptive layers in OPVs are generally on the order of 10-100 nm, which is much thinner than the micron-thick absorption layers often seen in inorganic devices. Reasonable efficiencies are still possible due to the high absorption coefficient of organics on the order of 10^5 to 10^6 cm^{-1}, but room for improvement still exists.

Parasitic absorption in layers that do not generate photocurrent is also an issue in OPVs. Organic devices incorporate a range of materials in addition to the active layers, ranging

from protective layers to exciton confining layers to the contacts themselves. Although these materials are generally selected for transparency across the solar spectrum, some absorbing materials currently have no completely transparent replacement. An example of this is the common transparent electrode material ITO. In general the transparency of ITO can be increased by increasing the amount of oxygen in the oxide and by thinning the layer, but both of these also increase the resistance. There is therefore a trade-off between decreasing the parasitic absorption of the ITO (increasing η_A) and decreasing the series resistance of the device (increasing η_{CC}).

Absorption of a device can also be adjusted by altering the position of layers with respect to the standing optical wave within the device. As OPVs consist of a stack of thin dielectrics with a strongly reflecting metal contact on one end, interference effects are extremely important within the device.The first step in designing a device is then to place the active layers at the optical maxima, enhancing absorption. The calculation of the optical field is treated in depth in Section 3.5.

Organics have narrow absorption peaks, so a single device generally incorporates a red absorber and a blue-green absorber, with the red absorber placed farther from the reflecting metal electrode. It is then somewhat possible to place other layers in locations that minimize parasitic absorption. For example, transparency is somewhat less important for the blocking layer directly adjacent to the metal electrode, as there is an optical node at the surface of the electrode.

3.1.2 Exciton Diffusion

Once an exciton has been generated, it must diffuse to the heterojunction to be dissociated into free charge carriers. The physics of exciton diffusion is covered in depth in Section 2.1.3. Here we simply assume that organic semiconductors have an intrinsic exciton diffusion length L_D, defined as the average distance traveled before recombining. The exciton diffusion efficiency η_{ED} is then the percentage of excitons that reach a heterojunction before recombining.

The L_D is usually 10-20 nm for most OPV materials, and therefore limits the maximum thickness of a planar layer. The mixed heterojunction (see Section 1.5.1) does not have this problem, as the donor and acceptor are intimately blended so that all excitons are formed directly adjacent to a dissociating interface. Therefore $\eta_{ED} = 1$ for a mixed heterojunction.

3.1.3 Dissociation

Upon reaching a heterojunction, an exciton is dissociated into free charge carriers which can be extracted from the device as photocurrent. This occurs through the intermediary of a polaron-pair or CT state, where the hole and the electron in the exciton reside on molecules of different materials but are still weakly bound across the heterointerface. The lowest energy CT state (CT_1) has lower energy than either the free exciton or free charge, with a manifold of excited states of ascending energy.

Two theories exist for the exact mechanism of dissociation, as shown in Fig. 3.2. One states that the true intermediary of charge dissociation is a higher energy CT state, with CT_1 acting as a trap. In this view, dissociation is considered to be such a rapid process that it occurs before thermalization of the exciton to CT_1. The excess energy provided by the transition from the high-energy bound exciton state to the lower-energy "hot" CT state is what provides the energy to fully dissociate electron and hole.[144–146]

Transient absorption measurements have provided some evidence for this theory.[145,146] Transient absorption signals in organics have been detected on timescales shorter than those required for relaxation in the CT manifold, suggestive of dissociation occurring through the hot CT state. In this case, charge generation from CT_1 would be inefficient and highly field-dependent, evidence of a large energy gradient against dissociation from this state.

In practice, however, it is unclear whether the "hot" effects observed in transient absorption have any effect on actual device performance. The binding energy of CT_1 is also often unknown. The binding energy is $E_{CS} - E_{CT1} \leq kT$ (where E_{CS} is the energy of the separated charges, k is Boltzmann's constant, and T is the temperature), hence the thermal energy alone will be sufficient to dissociate the CT_1 state into free charges.

The alternate explanation for the mechanism of charge dissociation relies on this assumption. The work of Giebink, et al.,[147,148] among others, postulates that CT_1 serves as the intermediate state for charge dissociation, with negligible contribution from "hot" states. In this picture the free exciton transfers to the CT state and thermalizes to CT_1 before dissociating into free charge carriers.[149–151] In this case charge generation from the CT_1 state should be essentially external field independent.

Recent work by Vandewal et al. has shown that the the CT_1 state is an integral intermediate step in exciton dissociation, not a trap state.[152] This was accomplished through a comparison of the quantum yield of charge generation of selective excitation of the CT_1 state to that of exciton generation in the bulk donor and acceptor of an OPVs. If the CT_1 state is a necessary participant in the process of exciton dissociation, then charge generation from direct excitation of this state and from bulk excitation of the active materials should have identical efficiencies. In comparison, if the CT_1 state serves only as a trap and

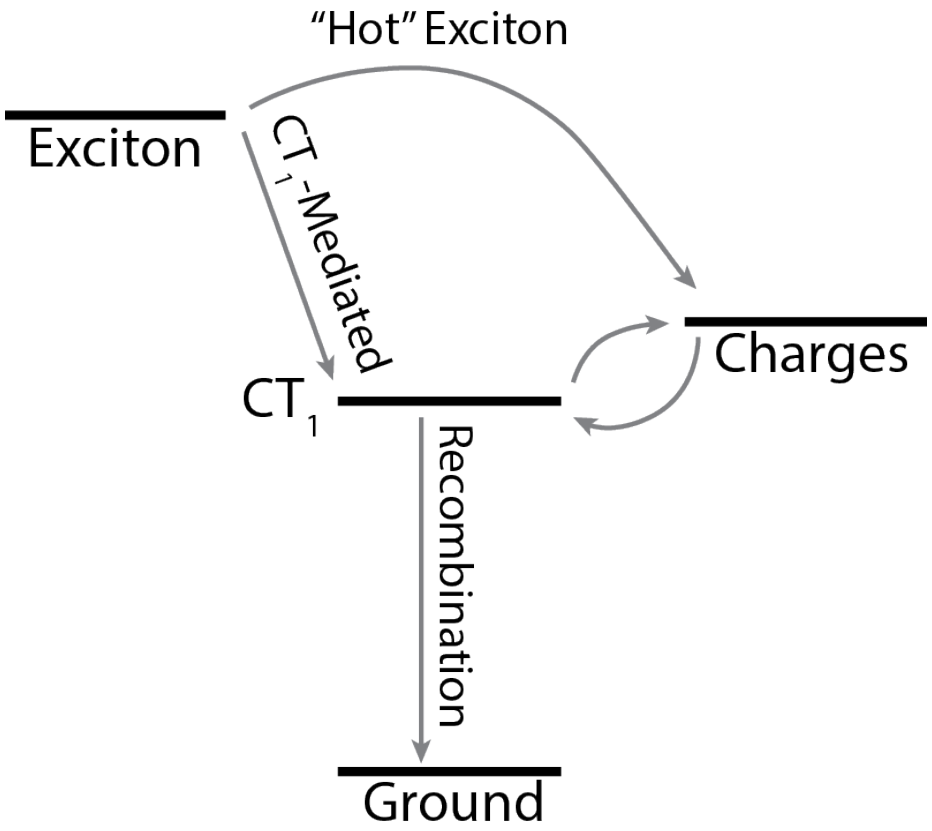

Figure 3.2: The two theorized pathways for exciton dissociation into free charges. In one (the "hot" exciton pathway) the excess energy of the exciton allows it to directly dissociate into charge carriers at the heterojunction, with the lowest-energy charge-transfer state (CT_1) serving only as a trap. In the other theory, the CT_1 state serves as an intermediary to the dissociation process. In this case thermal energy is enough to dissociate the weakly-bound CT_1 state into free charge carriers.

dissociation occurs through hot CT states, then selective excitation of the CT_1 state will only produce trapped excitons with no ability to access the higher-energy "hot" states, and photocurrent generation will be significantly less efficient than for bulk excitation. The role of CT_1 can therefore be determined by measuring the IQE of OPVs, the ratio of electrons out to photons absorbed in the active layer at each wavelength.

The IQE is determined from the EQE of the device, the wavelength-specific ratio of incident photons to extracted electrons. The EQE is defined as $EQE(E) = \eta_A(E)\eta_{ED}(E)\eta_{CT}(E)\eta_{CC}(E) = \eta_A(E)IQE(E)$, where E is the energy of the monochromatic incident light. The EQE and the absorptivity of the active layers of the device $\eta_A(E)$ must therefore be measured in order to calculate IQE.

This measurement is relatively simple in the energy regime of incident light where the bulk active layers strongly absorb. Measuring EQE is a standard characterization technique

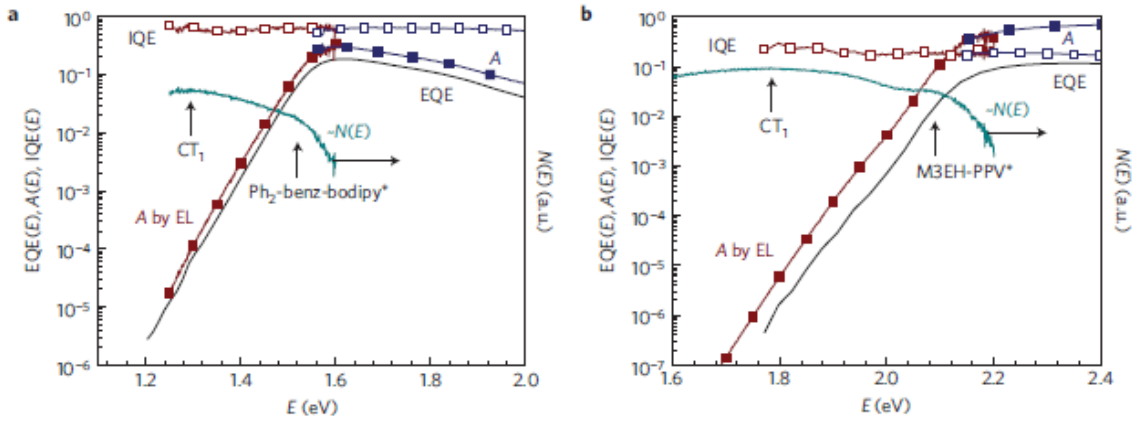

Figure 3.3: external quantum efficiency (EQE), internal quantum efficiency (IQE), and absorption ($A(E)$) for (a) a vacuum-processed Ph_2-benz-bodipy:C_{60} small-molecule device[153,154] and (b) a M3EH-PPV:CN-ether-PPV polymer:polymer device.[155] Figure is from[152]

.

for photovoltaics (see Section 3.2) and the absorption can be calculated either through direct measurements of the reflectivity of the device or by using ellipsometrically measured optical constants using transfer matrices to calculate the total absorption in the active layers at each wavelength. Measurements become significantly more difficult when attempting to detect the CT_1 state. It exists only at an interface instead of in the bulk and therefore has a significantly smaller total number of states.

The EQE of an OPVs can be measured through the use of lock-in techniques, which allows the low-noise detection of direct CT_1 excitation photocurrent, a factor of 10^5 smaller than the photocurrent of the device illuminated in the visible. (See Fig. 3.3). The equivalent absorptivity signal $\eta_A(E)$ is however too faint to measure with conventional reflective or ellipsometric techniques. Instead, the absorptivity is determined by measuring the inverse optical process; radiative decay from the CT_1 state to the ground state. If the population of excited states are in thermal equilibrium, the fraction of absorbed photons $\eta_A(E)$ at a given excitation energy is related to the fraction of emitted photons $N(E)$ by:[156,157]

$$\eta_A(E) \sim n(E)E^{-2}\exp\left(\frac{E}{kT}\right) \tag{3.1}$$

Vandewal et al. then used the measured electroluminescence and EQE of twelve different OPVs, including polymer/polymer, small molecule/fullerene and polymer/fullerene devices, and used this to determine the IQE from the visible to the infrared (IR).[152] Sample results are shown in Fig. 3.3. All devices exhibited flat IQE from the visible to the IR,

indicating that dissociation was just as efficient for excitons generated directly in the CT_1 state as it was for excitons generated in the bulk. Accordingly, charge dissociation in OPVs proceeds through the lowest energy state of the CT manifold and is relatively unaffected by "hot" excitonic processes.

3.1.4 Charge Collection

Once the exciton has been dissociated, the free charge carriers must be extracted through the layers of the device and out the electrodes as photocurrent. This is considered to be a highly efficient process in planar devices, with $\eta_{CC} \sim 1$, as the hole and electron cannot recombine once they leave the interface and are located on separate materials.. Charge collection in mixed devices can be more difficult, as the disordered nature of the heterojunction means that conductive pathways from some regions of the heterojunction can be narrow and torturous or even missing entirely. The presence of the heterojunction through the entire layer also means that charges which leave the interface can later encounter another interface where they can recombine with charges of the opposite polarity. The mechanism of recombination will be treated in further detail in 3.4.

3.2 OPV Characterization

There are two standard methods for characterizing the operation of a solar cell, the current-voltage (IV) characteristics and the EQE. IV characterization provides the overall efficiency of the device, while the EQE gives the response at each wavelength. The setup for each measurement is shown in Figure3.5.

IV measurements are taken both in the dark and under illumination with a simulated solar spectrum at a range of intensities. A NREL-traceable silicon photodetector with a known responsivity is used for intensity calibration and for correction of the mismatch between the simulated solar spectrum and the AM1.5G standard. A parameter analyzer is used to sweep the applied bias and measure the output current. Several parameters are then extracted from the data, as shown in Figure 3.4. The open-circuit voltage (V_{OC}) and short-circuit current (J_{SC}) correspond to the current and voltage at zero bias and zero current, respectively. The fill factor (FF) is defined as

$$FF = \frac{J_{max}V_{max}}{J_{SC}V_{SC}} \tag{3.2}$$

where J_{max} and V_{max} are the current and voltage where the power from the cell, $P = JV$,

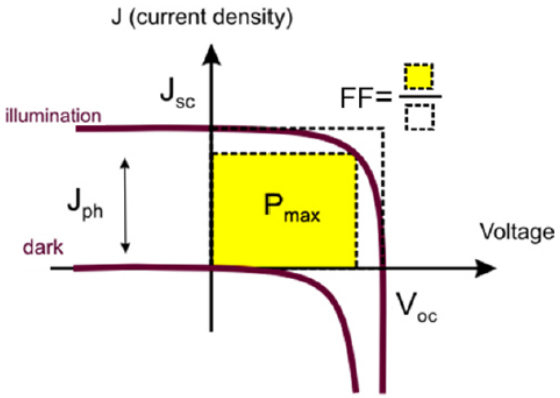

Figure 3.4: An example of a general IV characteristic for an organic device showing the extracted parameters. Image courtesy of Mark Thompson.

is a maximum. A FF $= 1$ corresponds to a perfectly square IV characteristic, while a FF of 0.25 corresponds to a resistor. The power conversion efficiency η_P is then defined as

$$\eta_P = \frac{J_{max}V_{max}}{P_0} = \frac{FF \cdot J_{SC}V_{OC}}{P_0} \tag{3.3}$$

where P_0 is the incident power on the cell.

The EQE is a measurement of the solar cell responsivity at each wavelength, given in units of output electrons per incident photon. The cell under test is illuminated with light from a Xe lamp, chopped and passed through a monochromator, and measured with a lock-in amplifier. The incident light is focused to underfill the cell, having an area smaller than that of the device. The incident power at each wavelength is measured with a NIST-traceable silicon photodetector with known responsivity. A solar simulator is not required as EQE measurements are performed with monochromatic light, but it is important to make sure that the the intensity of different regions of the illumination are similar. This may be checked by measuring white-light biased EQE, where the sample is flooded with constant illumination to provide a background level of charge carriers.

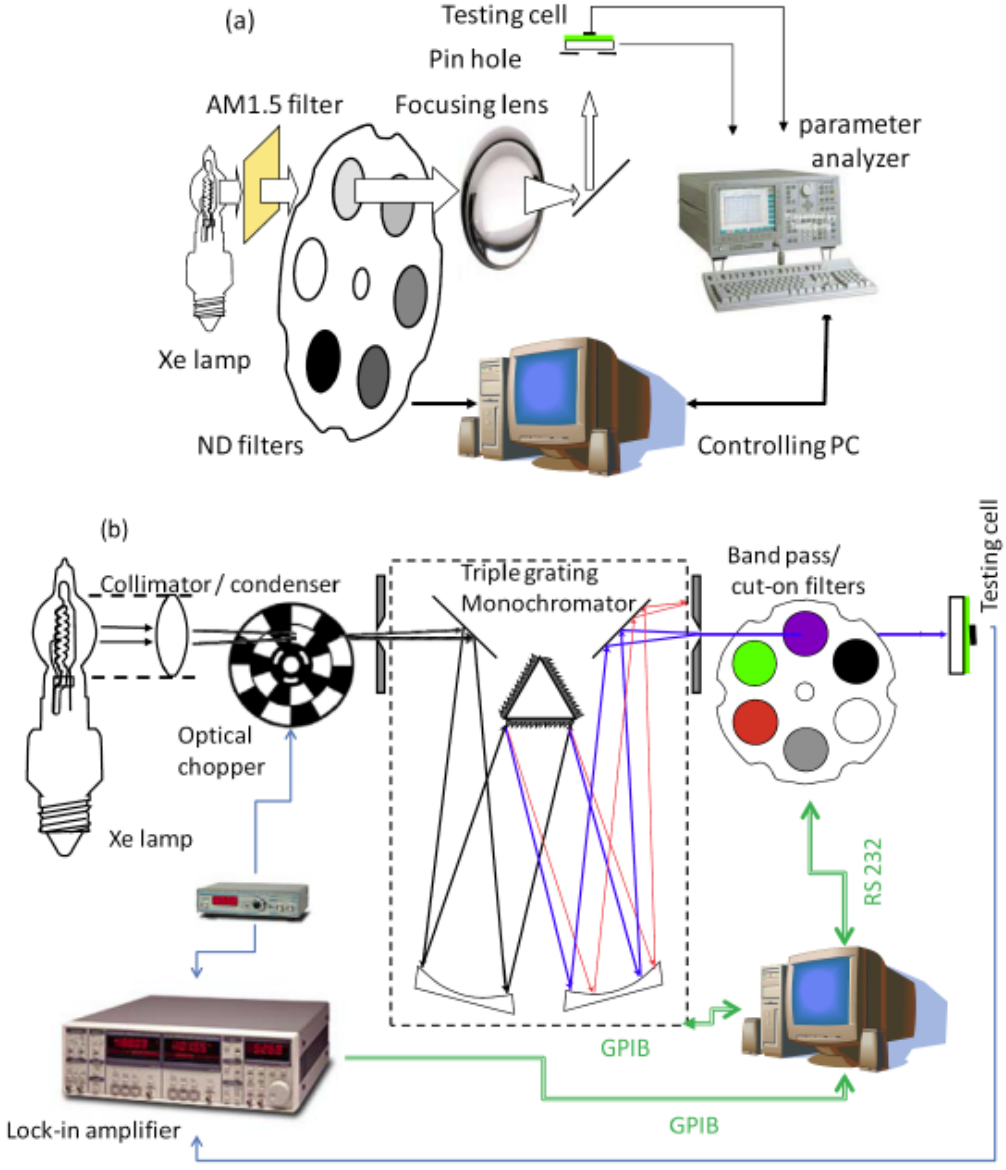

Figure 3.5: Experimental setup used to measure the (a)IV characteristics and (b)EQE of OPVs. Image courtesy of Fan Yang.

3.3 Theoretical Efficiency

For solar cells to become a solution to civilization's energy needs, they must be able to provide power at a competitive price with other methods. One factor in the price of solar power is the efficiency of the cells. It is therefore instructive to consider the maximum possible efficiency for solar cells. The seminal work for both ideal and real solar cells was performed by Shockley and Quiesser.[158]

Let us begin by considering the ideal case of a planar cell with no concentration made from a semiconductor with an inorganic-like bandgap energy E_g. We assume complete absorption of all photons with energy $E > E_g$ and complete transparency to all photons $E < E_g$. Furthermore, we assume perfect charge generation and extraction, such that every photon absorbed generates an electron of current. This corresponds to IQE $= 1$. The number of photons of frequency greater than $\nu_g = E_g/h$ per area per unit time, $Q_s(\nu_g, T_s)$ is then

$$Q_s(\nu_g) = \frac{2\pi}{c^2} \int_{\nu_g}^{\infty} N_{AM1.5}(\nu)\nu^2 d\nu \tag{3.4}$$

where $N_{AM1.5}$ is the AM1.5G solar spectrum. In this simple case, assuming a cell of area A, the output current is then $I = eAQ_s$, where e is the electron charge. Assuming thermalization of all charges, the current is extracted at the bandgap voltage $V = E_g/e$. The total power from the cell is then

$$P_{out} = IV = AQ_sE_g = hAQ_s\nu_g \tag{3.5}$$

The total efficiency is then

$$\eta = \frac{P_{out}}{P_s} = \frac{h\nu_g AQ_S}{P_s} \tag{3.6}$$

where P_s is calculated by a numeric integral of the AM1.5G solar spectrum in the same manner as Q_s is calculated.

Assuming the case of a spherical cell at absolute zero completely surrounded by a mathematically more tractable blackbody spectrum of $T_s = 6000K$ for the sun, Shockley and Queisser calculated a maximum theoretical efficiency of 44% at a bandgap of 1.1 eV.[158] This is the ultimate theoretical efficiency of a solar cell, but such a cell could never exist in practice due to the assumptions required. Shockley and Quiesser are therefore more well known for their further extension of this derivation to real devices, giving a maximum practical efficiency of 33.7% for a single-junction device with a bandgap of 1.3 eV.[158]

Several factors go into this further derivation. A real solar cell must operate at a non-zero temperature, meaning it will emit thermal radiation. For a perfect absorber such as

our theoretical solar cell, it is therefore thermodynamically required that it also be a perfect blackbody emitter at the same wavelengths, as input and output flux must be equal for an object in thermal equilibrium with its surroundings. As emitted radiation with energy $E > E_g$ must come from the recombination of holes and electrons in the device, some current will be lost in comparison to the ideal cell.

In total there are five processes which affect the steady-state population of holes and electrons: the generation of charge carriers by absorbed radiation, the radiative recombination of charge carriers, non-radiative recombination and generation of charge carriers, and extraction of charge carriers from the device as current. The steady-state current-voltage characteristics of the cell may then be derived by setting the sum of these contributions to zero.

Incorporating these corrections and using the correct AM1.5G solar spectrum gives the maximum theoretical efficiency for real devices of 33.7% for a single-junction device with a bandgap of 1.3 eV mentioned above.[158] The theoretical maximum efficiency for organic devices falls even below this value, as additional energy is lost to dissociate strongly-bound excitons. For a single-cell organic device with a driving energy for exciton dissociation from the interface charge-transfer state of $\Delta G_{CT} = -0.5$ eV, characteristic of current high-efficiency cells, the maximum efficiency is 22%.[106] As record efficiencies for OPVs are currently in the neighborhood of 12%, this still leaves plenty of room for improvement.

Multiple techniques have been proposed to exceed the Shockley-Queisser (SQ) limit. One of the most feasible is the use of multijunction cells, universally used in the highest-efficiency solar cells.[159–162] Such cells essentially consist of a stack of multiple solar cells each with a different absorption edge and therefore bandgap. Assuming the cells are connected in series, the combined cell then has the sum of the voltages of the individual cells and the lowest current of any individual cell. Optimized multijunction devices therefore balance the absorption of individual cells to equalize the current from each.

As presented above, a single cell is limited in efficiency by the trade-off between the total number of photons absorbed, giving the photocurrent, and the operating voltage of the cell. Multijunction cells have more flexibility to exceed both these limits. The individual cells with a lower energy bandgap than the optimum single cell are able to harvest additional low-energy photons that would otherwise be lost. And the higher-bandgap cells operate at a higher operating voltage than the optimal individual cell. In sum, this results in both better usage of the solar spectrum and better operating voltage. The maximum theoretical efficiency of a three-junction cell, the architecture most used in commercial devices, has been calculated to be 49%.[160] The maximally efficient device is that with infinitely many layers, each absorbing a single wavelength. This cell has been calculated to have a

maximum efficiency of 68%.[160]

Another technique considered to break the SQ limit is exciton fission.[163–165] Exciton fission occurs in organic semiconductors whose triplet energy is half or less that of its singlet energy. Singlets generated in these materials can then split into two triplet excitons. If used as a sensitizer on a conventional inorganic cell, these materials can drastically increase the energy harvest from short wavelength light, as the majority of the energy of the light would otherwise be lost when the electron thermalized down to the bandgap. Instead, singlet fission materials can generate two electrons for each high-energy photon, doubling the EQE in this portion of the spectrum and therefore increasing the output power of the device. Test devices have been demonstrated with greater than 100% EQE due to singlet fission, but a truly practical device has not yet been invented.

The least practical method for making solar cells exceed the SQ limit is to get a better sun. As presented above, the maximum possible efficiency for solar cells is intimately connected to the spectrum of the incident light. The bluer the light is, the higher the voltage a cell can operate at without a loss of photocurrent. Increasing the temperature of the sun and therefore shifting its blackbody spectrum more into the blue would therefore easily improve the efficiency of all single-junction solar cells. However, as of now, no feasible method has been proposed in the literature*.

3.4 Loss mechanisms

The are multiple loss pathways for excitons and charges during the photogeneration process given in Section 3.1. To make more efficient devices, it is important to understand loss mechanisms and the physics underlying their operation. A variety of techniques have therefore been developed to characterize the dominant loss mechanisms in OPVs, including transient photocurrent, charge extraction through linearly increasing voltage (CELIV), and intensity dependence of the photocurrent.

In this Section we cover some of the more common loss mechanisms in OPVs. We specifically examine processes that occur after the absorption of light in the active layers of OPVs. The efficiency of light absorption is generally calculated using the method of optical transfer matrices, which is covered in Section 3.5.

*The spectrum of the sun will also become redder as it ages, lowering the expected efficiency of all solar cells over the next several billion years. This is the least pressing issue facing OPVs.

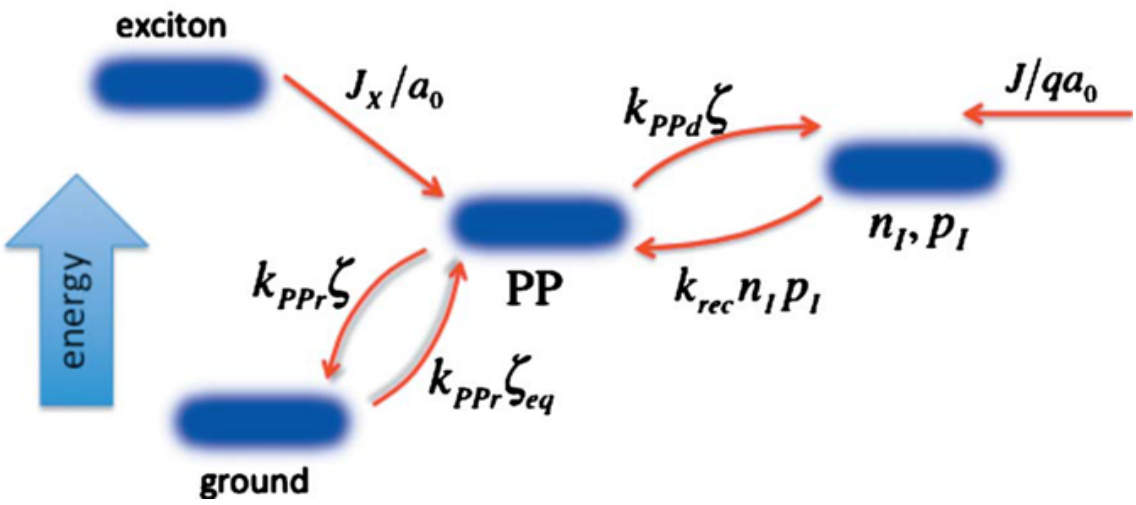

Figure 3.6: State diagram for the process of dissociation and geminate recombination at the organic heterojunction. Excitons diffuse with current density J_x to the interface and transfer to the polaron-pair (PP) or charge-transfer (CT) state with spatial extent a_0 and population ξ. This transfer is assumed to be unidirectional due to the large energy difference between the exciton and PP state. The exciton can then dissociate with rate constant k_{PPd} or recombine with rate constant k_{PPr}. Free charges at the interface (n_I for electrons and p_I for holes) are populated by the current density J and can recombine to the PP state with rate constant k_{rec}. The thermal equilibrium PP population ξ_{eq} is determined from detailed balance.

3.4.1 Geminate Recombination at the Heterojunction

Geminate recombination is defined as the recombination of two particles originating from the same precursor state.[166] In the case of charges in OPVs, this corresponds to the recombination of the electron and hole from the same exciton. The method of Giebink, et al[147,148] can be used to describe geminate recombination at the heterojunction in competition with the dissociation of the charge-transfer state as discussed in Section 3.1.3.

Giebink's analysis begins with the state diagram shown in Fig. 3.6. The recombination of the polaron-pair state in steady-state, assuming no traps at the interface, is given by

$$\frac{J_x}{a_0} - k_{PPr}(\xi - \xi_{eq}) - k_{PPd}\xi + k_{rec}n_I p_I = 0 \tag{3.7}$$

and the free carriers by

$$k_{PPd}\xi - k_{rec}n_I p_I + \frac{J}{qa_0} = 0 \tag{3.8}$$

where ξ is the PP density, J_x is the current density of excitons diffusing to the heterojunction, J is the charge current density in the device, q is the electron charge and a_0 is the average PP separation. The rates k_{PPd}, k_{PPr}, and k_{rec} correspond to the PP dissociation

rate, the PP recombination rate, and the free charge recombination rate respectively. The population ξ_{eq} is the thermal equilibrium population in the PP state, determined by detailed balance.[167]

Solving the above equations for the current from the heterojunction gives

$$J = qa_0 k_{rec} \frac{k_{PPr}}{k_{PPd} + k_{PPr}} \left(n_I p_I - \frac{k_{PPd}}{k_{PPd,eq}} n_{I,eq} p_{I,eq} \right) - qj_x \frac{k_{PPd}}{k_{PPd} + k_{PPr}}$$
$$= qa_0 k_{rec} \eta_{PPd} \left(n_I p_I - \frac{k_{PPd}}{k_{PPd,eq}} n_{I,eq} p_{I,eq} \right) - qj_x \eta_{PPd} \quad (3.9)$$

where Eq. 3.8 has been used to calculate ξ_{eq}, the thermal equilibrium value in the absence of bias or illumination, finding $\xi_{eq} = k_{rec} n_{I,eq} p_{I,eq} / k_{PPd,eq}$. This derivation assumes quasi-equilibrium. Here $\eta_{PPd} = k_{PPd}/(k_{PPd} + k_{PPr})$ is the PP dissociation probability.

Assuming detailed balance of the charge density adjacent to an injecting contact, the current-voltage characteristics of the organic heterojunction can then be derived. Assuming an ideality factor of 1, this is

$$J = J_{s0}(\exp(qV_a/k_bT) - \frac{k_{PPd}}{k_{PPd,eq}}) - q\eta_{PPd} J_x \quad (3.10)$$

where V_a is the applied bias and $J_{s)}$ is the dark current prefactor. The term on the right gives the photocurrent, which is proportional to the flux of excitons to the interface and the PP dissociation efficiency. Under forward bias $\frac{k_{PPd}}{k_{PPd,eq}} \approx 1$.

In practice, the disordered organic semiconductors used in OPVs have a broad density of states near the HOMO and LUMO energies. The tail of this density of states acts as traps, meaning that the trap-free assumption is generally violated. The derivation of the effects of traps on the organic heterojunction are as follows:

Assuming an exponential trap distribution in the acceptor with characteristic trap temperature $T_{t,A}$, the relationship between the trapped (n_t) and free (n) electron densities are given by

$$n_t \approx H_A \exp\left(\frac{E_{Fn} - E_{LUMO}}{k_b T_{t,A}} \right) = H_A \left(\frac{n}{N_{LUMO}} \right)^{1/l_A} \quad (3.11)$$

where H_A is the density of trap states at the acceptor LUMO, E_{Fn} is the electron quasi-Fermi energy in the acceptor, E_{LUMO} is the acceptor LUMO energy, and $l_A = T_{t,A}/T$. A similar relationship may be written for the trapped hole density p_t in the donor, with appropriate substitutions for the HOMO. Under the assumption that the trapped carrier density significantly exceeds the free carrier density, the expression for the current-voltage

characteristics of an OPVs becomes

$$J = J_{sD}[\exp(qV_a/n_D k_b T) - 1] + J_{sA}[\exp(qV_a/n_A k_b T) - 1] - q\eta_{PPd} J_x \tag{3.12}$$

for $k_{PPd} \leq k_{PPd,eq}$ under forward bias. Here J_{sD} and J_{sA} are the dark saturation currents from the donor and acceptor, respectively. Unlike the trap-free case, recombination between free electrons and holes is rare. Instead, recombination occurs primarily at trap states, with $k_{rec,n}$ and $k_{rec,P}$ describing the recombination at the heterojunction between a free electron in the acceptor n_I and a trapped hole in the donor p_{It} and vice versa. The ideality factors n_A and n_D are given by

$$n_A = \frac{l_A}{\delta_D(l_A - 1) + 1} \tag{3.13}$$

and

$$n_D = \frac{l_D}{\delta_A(l_D - 1) + 1} \tag{3.14}$$

where δ indicates the fraction of the potential dropped across the acceptor or donor layer.

In both the trap-free and the trap case, it can be seen that the photocurrent in a device will be directly dependent on η_{PPd}. Furthermore, the decrease in open-circuit voltage from its theoretical maximum goes as[148] $\ln(k_{PPr}/k_{PPd})$.

The difference that η_{PPd} makes to a device has been shown in studies of boron subphthalocyanine chloride (SubPc)/C_{60} and CuPc/C_{60} OPVs. The donor materials SubPc and CuPc have been widely studied, with CuPc shown to make consistently less efficient devices than SubPc. This is attributed to the lower V_{OC} in CuPc / C_{60} devices; calculations of the maximum V_{OC} have shown that devices at room temperature operate at approximately 0.3 V less than their theoretical maximum, while SubPc-based devices operate at their theoretical maximum under standard operating conditions.[147,148,168] Giebink et. al. used the method of intensity-modulated photocurrent spectroscopy (IMPS) to measure η_{PPd} by superimposing a small modulation onto the steady-state illumination incident on a photovoltaic and measuring the frequency-dependent complex response of the cell.

Equations 3.7 and 3.8 can be modified to incorporate a harmonic perturbation in the exciton current at frequency ω, $J_x \rightarrow J_x(1 + \delta e^{i\omega t})$. This assumes the exciton lifetime is small compared to ω^{-1}. Separating out the time-varying and steady-state components and keeping only the first-order terms allows for the derivation of the complex IMPS response,

$$\tilde{\Psi} = \frac{\eta_{PPd}(1 + i\omega\tau)}{1 + k_{rec} n_I \tau(1 - \eta_{PPd}) + 2i\omega\tau} \tag{3.15}$$

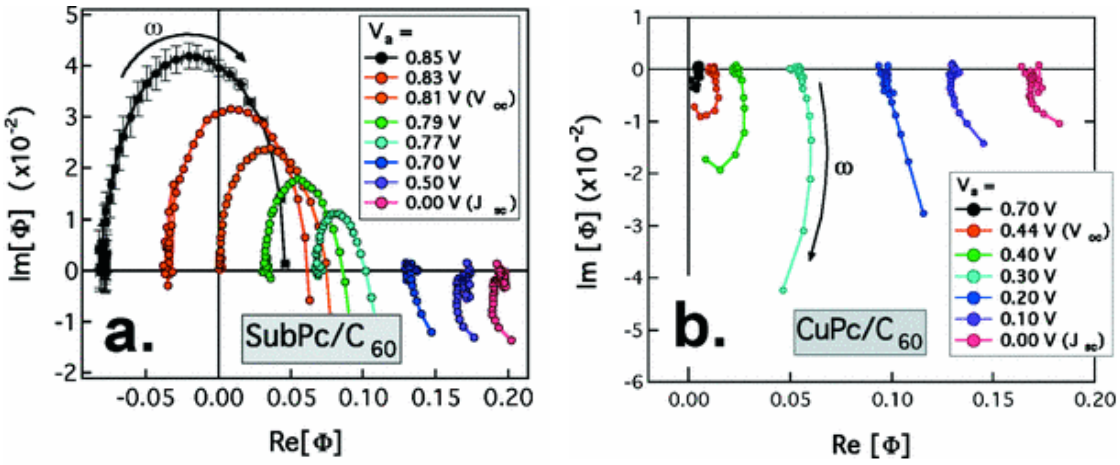

Figure 3.7: Cole-Cole representation of the the measured IMPS signal of a (a)SubPc/C_{60} cell and a (b)CuPc/C_{60} cell. The phase advance around open-circuit in the SubPc cell is due to bimolecular recombination of free charges at the heterojunction. In contrast, the lack of phase advance and the trend $|\tilde{\Psi}| \rightarrow 0|$ as the bias approaches V_{OC} in the CuPc device indicates that free carriers are lost to geminate recombination before dissociating, indicating significantly lower polaron-pair dissociation efficiency η_{PPd}. Image is modified from.[148]

where $\tau = RC$ is the time constant of the equivalent RC circuit formed by the layer bulk between the heterointerface and the contacts. Note that Eq. 3.15 predicts a transition from $\text{Im}(\tilde{\Psi}) < 0$ to $\text{Im}(\tilde{\Psi}) > 0$ for $k_{rec} n_I \tau (1 - \eta_{PPd}) > 1$. Assuming a roughly constant k_{rec}, τ, and η_{PPd}, an increase in the interfacial free carrier density n_I will cause a crossover from phase lag to phase advance IMPS data.

The measured IMPS data is shown in Fig. 3.7. As the SubPc device approaches V_{OC}, the transition from phase advance to phase lag predicted by Eq. 3.15 is observed. This is a sign of an increase in n_I, proof that SubPc/C_{60} heterojunctions exhibit efficient exciton dissociation even at V_{OC} where the internal field across the heterojunction is zero. The CuPc/C_{60} devices, in contrast, show no phase transition as $V \rightarrow V_{OC}$. This is a sign of low η_{PPd}, as it shows that a large number of charges are being lost to geminate recombination instead of dissociating and increasing n_I. This corresponds to a roughly 20-fold difference in recombination rate between the SubPc- and CuPc-based devices, which directly translates to a ~ 0.15 V decrease in V_{OC}.

It has previously been proposed that decreasing the electronic coupling between the donor and acceptor molecules at the interface decreases PP recombination.[169] The only molecules at the interface that participate in the recombination process are those within approximately a_0 of each other,[148] so spatially separating the donor and acceptor at the interface will decrease the recombination while still allowing dissociation to proceed. This

can be accomplished, for example, by introducing steric bulk to the donor and acceptor molecules or by creating disorder at the interface.

This has been shown in the recent work by Zimmerman, et al. on 2,4-bis[4-(N,N-diphenylamino) 2,6-dihydroxyphenyl] squaraine (DPSQ)/C_{60} devices.[89] The squaraine DPSQ is a solution processed material whose morphology can be altered in various ways through solvent annealing at different points in the deposition process of an OPVs. Zimmerman, et al. showed that they could create three types of devices, depending on whether they annealed the device before C_{60} deposition on top of the DPSQ layer, after C_{60} deposition, or not at all.

In the unannealed (as-cast) device, the bulk DPSQ was disordered while the bulk C_{60} was weakly ordered, as shown through X-ray diffraction (XRD) measurements. This resulted in a disordered heterointerface and a low k_{PPr}, leading to a high V_{OC}. However, the disorder of the bulk organic layers resulted in relatively poor charge and exciton conduction, leading to a low J_{SC}.

By annealing before C_{60} deposition, the DPSQ became crystalline. This templated the C_{60}, resulting in a crystalline C_{60} layer as well. The heterointerface between the two also was ordered and resulted in a high k_{PPr}, as shown by the decrease in V_{OC} from 0.94 ± 0.01 V in the as-cast devices to 0.86 ± 0.01 V in the pre-C_{60}-annealed devices. These devices showed an increase in J_{SC}, attributed to improved charge and exciton conduction due to the increased crystallinity of the layers.

Annealing after C_{60} deposition gave the best of both worlds. The C_{60} was found to confine the DPSQ, preventing the heterojunction morphology from changing and preserving the disorder of the as-cast device. This preserved the low k_{PPr} and high V_{OC} of the as-cast device. The bulk DPSQ was still found to undergo some crystallization, allowing for improved conduction and increase J_{SC}. This resulted in an improvement of PCE from $\eta_P = 3.6 \pm 0.2\%$ for the as-cast device to $\eta_P = 4.8 \pm 0.3\%$ for the post-C_{60}-annealed device. This was therefore a successful demonstration of the fact that interface disorder helps to reduced k_{PPr} and therefore geminate recombination, while bulk order improves the charge and exciton conduction process.

3.4.2 Nongeminate Recombination

The generation and transport of charges in an organic device can be described by the steady-state drift-diffusion equation

$$0 = D\frac{\partial^2 n_c(x)}{\partial x^2} + \mu\frac{\partial}{\partial x}(E(x)n_c(x)) + G(x) - k_{agg}n_c \tag{3.16}$$

where D is the diffusivity of charges, n_c is the charge concentration, μ is the mobility of charges, $E(x)$ is the electric field and $G(x)$ is the charge generation. Here k_{agg} represents the aggregate recombination processes in the device which may be a function of n_c or other parameters. Geminate recombination is not included in k_{agg}, as it occurs before the exciton dissociates into free charges, and therefore is included by an appropriate change to $G(x)$.

3.4.2.1 Monomolecular and Bimolecular Recombination

Non-geminate recombination is generally separated into two categories, bimolecular and monomolecular recombination. Bimolecular recombination is defined as any process which depends on the square of the charge density, such as recombination between free electrons and holes. Monomolecular recombination is defined as any process that depends linearly on the charge population, such as recombination between one species of trapped charge and one species of free charge. The rates for these processes may therefore be expressed as $k_{bi} = k_b n_c$ and $k_{mono} = k_m$ where k_b and k_m are the rate constants for bimolecular and monomolecular quenching respectively, with the exact values dependent on the device in question*. The relative magnitude of k_b and k_m then determines the range of values of n where each recombination process dominates.

The main factors influencing the charge density n_c in a given device are the illumination intensity and the applied bias. Illumination intensity determines the rate at which the heterojunction produces current and therefore the steady-state value of n_c. Applied bias sets the electric field across the device, which determines how quickly charges are extracted. As the bias approaches V_{OC} the total electric field falls to zero, resulting in slower and slower charge extraction and a larger and larger n_c.

The effects of altering the rate of bimolecular recombination is shown in Fig. 3.8. Current-voltage characteristics and responsivity with respect to illumination intensity are shown for two sets of devices, one with low bimolecular recombination thanks to a highly conductive BPhen:C_{60} buffer layer, and the other with high bimolecular recombination caused by a poorly-conducting neat BPhen buffer. The BPhen:C_{60} buffer is examined in much greater detail in chapter 6.

The most pronounced effect of high bimolecular recombination on the current-voltage characteristics is a decrease in fill factor. The current falls off more quickly as the internal field in the device decreases near V_{OC}. Bimolecular recombination also has a clearly visible effect on the responsivity of the devices with respect to illumination intensity. The responsivity R is defined as $R = J_{SC}/I$ and is expected to be constant for pure monomolecular

*Higher-order recombination processes exist, but are negligible in the regimes covered in this work. Auger recombination, a three-particle process, is one example of such higher-order recombination.

recombination and fall off linearly with increasing negative slope as the rate of bimolecular recombination increases.

Bimolecular and monomolecular recombination are primarily a problem in mixed heterojunctions. Photogenerated free charges in OPVs are spatially separated with electrons on the acceptor and holes on the donor. As the intrinsic charge population in organic semiconductors is extremely low, organic semiconductors are considered to be fully depleted during operation. Therefore charge recombination can only occur at the heterojunction between the donor and acceptor. In planar devices, charges are driven from the heterojunction by the internal field under operating conditions and have few chances to recombine. In mixed heterojunctions, however, charges generated within the mixed layer are always in close proximity to a heterointerface, due to the intimate blending of the donor and acceptor. It is therefore much more likely for a charge in a mixed heterojunction to encounter a heterointerface and recombine.

3.4.2.2 Exciton-Polaron Quenching

Exciton-polaron quenching is the process where an exciton transfers its energy to a free charge and recombines, with the free charge then relaxing to its initial excited state. This process occurs at a rate $k_{ex-pol} = k_{ep}n_{ex}$, where n_{ex} is the exciton density. This is technically neither a bimolecular or monomolecular recombination process as defined above, since the quenching scales quadratically with illumination intensity (as $n_e x$ also depends linearly on I) but linearly with n_c.

Exciton-polaron quenching is primarily a concern in planar layers, as it requires a large and spatially congruent population of both charges and excitons. Planar architectures possess a significant steady-state exciton population, as excitons in mixed heterojunctions form adjacent to a heterojunction and are dissociated almost instantly. Exciton-polaron quenching also affects the FF and responsivity of devices, as it is strongest when there is a large charge population like in bimolecular recombination.

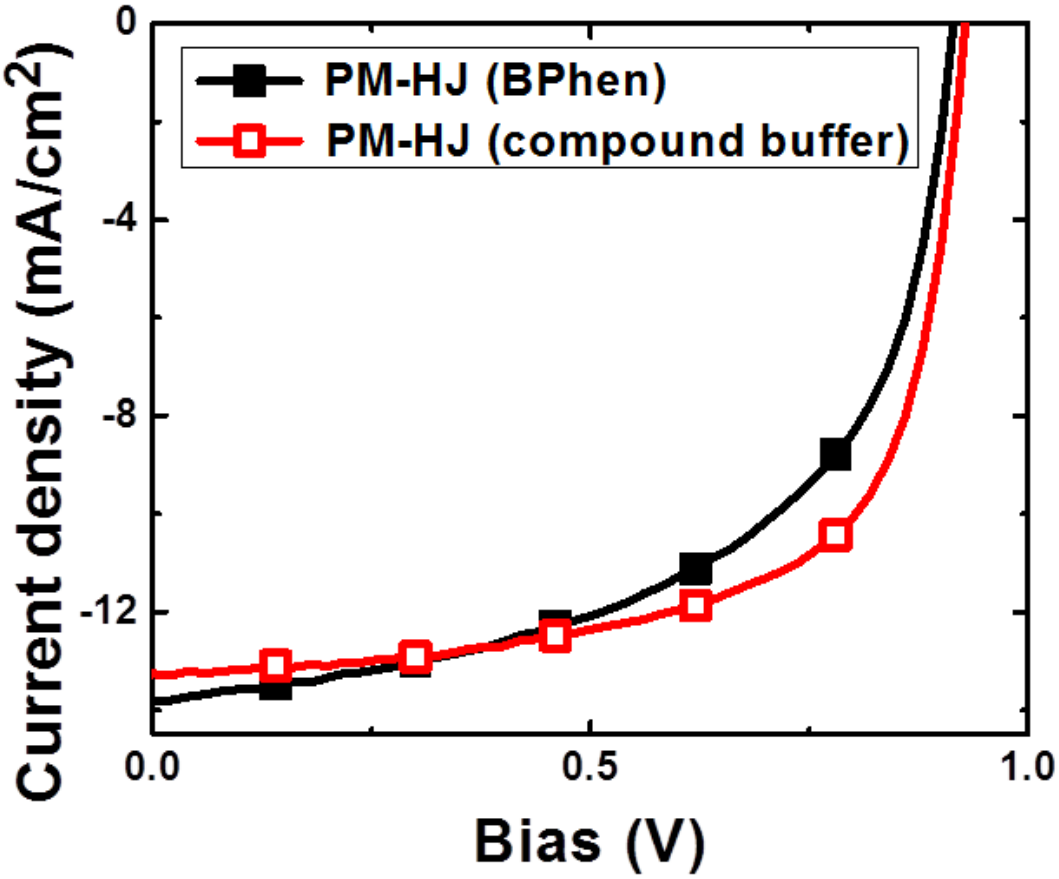

Figure 3.8: Comparisons of devices with different levels of bimolecular recombination. A BPhen:C_{60} compound buffer was used to enhance charge extraction and reduce bimolecular recombination in otherwise equivalent devices. Higher bimolecular recombination leads to a reduction in FF as shown in the IV characteristics, as the device will exhibit higher recombination and therefore reduced current as the applied bias is increased towards V_{OC}. Data is from[170]

3.5 Optical Modeling

To calculate the expected behavior of an optoelectronic device, we must first fully describe its interaction with light. This may be accomplished through the method of optical transfer matrices.

Let us begin by considering the case of two semi-infinite slabs of dielectric with a plane wave incident from the left, as shown in Fig 3.9. The boundary conditions that apply in this case are[171]

$$\epsilon_1 E_1^{\perp} = \epsilon_2 E_2^{\perp} \tag{3.17}$$

$$B_1^{\perp} = B_2^{\perp} \tag{3.18}$$

for the component of the electric and magnetic fields perpendicular to the surface and

$$E_1^{\parallel} = E_2^{\parallel} \tag{3.19}$$

$$\frac{1}{\mu_1} B_1^{\parallel} = \frac{1}{\mu_2} B_2^{\parallel} \tag{3.20}$$

for the parallel component.

Assuming normal incidence, plane waves propagating in the layers take the form

$$\left.\begin{aligned} \tilde{E}_{1,2}^{+,-} &= \tilde{E}_{01,2}^{+,-} e^{i(\pm k_{1,2} - \omega t)} \hat{x} \\ \tilde{B}_{1,2}^{+,-} &= \pm \tfrac{1}{\nu_{1,2}} \tilde{E}_{01,2}^{+,-} e^{i(\pm k_{1,2} - \omega t)} \hat{y} \end{aligned}\right\} \tag{3.21}$$

where 1 and 2 indicate the layer the wave is in and + and - indicate the direction of propagation of the wave. $\tilde{E}_0$ is the magnitude of the wave. Here we have made the substitution $B_0 = 1/\nu E_0$, where $\nu = c/n$ is the speed of the wave in the dielectric medium.

Normal incidence means there is no perpendicular component of the waves, leaving two boundary conditions:

$$\tilde{E}_{01}^{+} + \tilde{E}_{01}^{-} = \tilde{E}_{02}^{+} \tag{3.22}$$

and

$$\frac{1}{\nu_1}(\tilde{E}_{01}^{+} - \tilde{E}_{01}^{-}) = \frac{1}{\nu_2} \tilde{E}_{02}^{+} \tag{3.23}$$

assuming that μ for each layers is approximately μ_0, true for many dielectrics. These equations are then be solved for the outgoing amplitudes in terms of the incident amplitude

$$E_{01}^{-} = \left|\frac{n_1 - n_2}{n_1 + n_2}\right| E_{01}^{+} \tag{3.24}$$

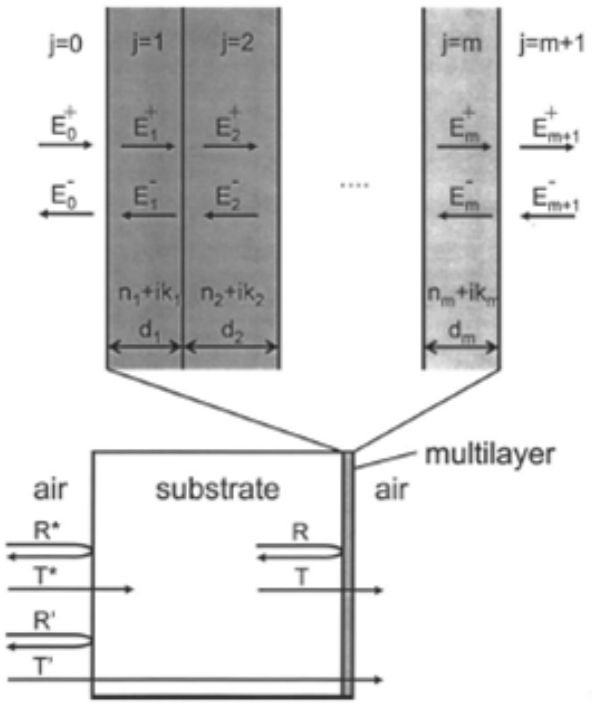

Figure 3.9: Setup of the dielectric stack considered in the optical transfer matrix method. The stack is deposited on a thick transparent substrate, which has incoherent reflections at the far interface that must be corrected for separately. Layers 0 and $m + 1$ are the transparent substrate and air, and are assumed to be semi-infinite in the derivation. Figure is from.[172]

$$E_{02}^{+} = (\frac{2n_1}{n_1 + n_2})E_{01}^{-} \tag{3.25}$$

This gives the well-known Fresnel reflection and transmission coefficients,

$$r = \frac{E_{01}^{-}}{E_{01}^{-}} = \frac{n_1 - n_2}{n_1 + n_2} \tag{3.26}$$

$$t = \frac{E_{02}^{+}}{E_{01}^{-}} = \frac{2n_1}{n_1 + n_2} \tag{3.27}$$

where the total reflection from the interface is then $R = r^2$ and the transmission is $T = (n_2/n_1)t^2$. Note that $R + T = 1$ as expected from conservation of energy.

We can generalize this to give the effect of an arbitrary dielectric stack using the method of Heavens'[173,174] as applied to organic devices by Peumans.[172] The architecture considered in shown in Figure 3.9. We begin by rearranging the previous result into matrix form and

replacing the numerical subscripts with i and j to denote arbitrary adjoining layers.

$$\begin{bmatrix} E_i^+ \\ E_i^- \end{bmatrix} = I_{ij} \begin{bmatrix} E_j^+ \\ E_j^- \end{bmatrix} = \begin{bmatrix} \frac{1}{t_{ij}} & \frac{r_{ij}}{t_{ij}} \\ \frac{r_{ij}}{t_{ij}} & \frac{1}{t_{ij}} \end{bmatrix} \begin{bmatrix} E_j^+ \\ E_j^- \end{bmatrix} \tag{3.28}$$

where r_{ij} and t_{ij} are the Fresnel reflection and transmission coefficients between the two layers. For normal incidence, these are defined as $r_{ij} = (n_i - n_j)/(n_i + n_j)$ and $t_{ij} = (2n_j)/(n_i + n_j)$.

We next employ a matrix to describe the propagation of a plane wave through each layer. This will induce a phase shift in the wave, given by

$$L_j = \begin{bmatrix} e^{-i\xi_j d_j} & 0 \\ 0 & e^{i\xi_j d_j} \end{bmatrix} \tag{3.29}$$

where $\xi = (2\pi/\lambda)n_j$ and d_j is the thickness of the layer.

We now have all the pieces we need to model a stack of m layers, assuming homogeneous and isotropic materials with optically flat interfaces. We start by assuming the stack is sandwiched between semi-infinite layers on either side. The electric field in the two layers $j = 0$ and $j = m + 1$ is then

$$\begin{bmatrix} E_0^+ \\ E_0^- \end{bmatrix} = S \begin{bmatrix} E_{m+1}^+ \\ E_{m+1}^- \end{bmatrix} \tag{3.30}$$

where

$$S = \begin{bmatrix} S_{11} & S_{12} \\ S_{21} & S_{22} \end{bmatrix} = \left(\prod_{n=1}^{m} I_{(n-1)n} L_n \right) \cdot I_{m(m+1)} \tag{3.31}$$

Then the reflection and transmission coefficients are $r = E_0^-/E_0^+ = S_{21}/S_{11}$ and $t = E_{m+1}^+/E_0^+ = 1/S_{11}$. Similar to the single-interface case, the total transmissivity and reflectivity of the multilayer stack is then $T = |t|^2 n_{m+1}/n_0$ and $R = |r|^2$.

We then calculate the electric field at any point within the dielectric stack by stepping back through the layers. Note that for a given layer j, the total multilayer transfer matrix is

$$S = S_j^- L_j S_j^+ \tag{3.32}$$

where

$$S_j^- = \left(\prod_{n=1}^{j-1} I_{(n-1)n} L_n \right) \cdot I_{(j-1)j} \tag{3.33}$$

and

$$S_j^+ = \left(\prod_{n=j+1}^{m} I_{(n-1)n} L_n \right) \cdot I_{m(m+1)} \tag{3.34}$$

We now calculate the electric field at the left interface of layer j propagating right and at the right interface propagating left,

$$\frac{E_j^+}{E_0^-} = t_j^+ = \frac{\frac{1}{S_{j11}^-}}{1 + \frac{S_{j12}^- S_{j21}^+}{S_{j11}^- S_{j11}^+} e^{i2\xi_j d_j}} \tag{3.35}$$

and

$$\frac{E_j^-}{E_0^+} = t_j^- = t_j^+ \frac{S_{j21}^+}{S_{j11}^+} e^{i2\xi_j d_j} \tag{3.36}$$

We then sum the electric fields propagating in opposite directions to obtain the total electric field at any point in the layer,

$$E_j(x) = E_j^+(x) + E_j^-(x) = (t_j^+ e^{i\xi_j x} + t_j^- e^{-i\xi_j x}) E_0^+ \tag{3.37}$$

Finally, we use this to calculate the time averaged absorbed power at any point in the layer,

$$Q_j(x) = \frac{4\pi c \epsilon_0 k_j n_j}{2\lambda} |E_j(x)|^2 \tag{3.38}$$

where ϵ_0 is the permittivity of free space and c is the speed of light.

Organic devices are generally fabricated on a transparent substrate with thickness much greater than the wavelength of the incident light. This introduces an incoherent reflection off the front surface which must be accounted for separately. This is done simply by subtracting the front surface reflection from the intensity of the incident light.

For normally incident light, polarization is irrelevant. Non-normal light may be accounted for by using the appropriate form of the Fresnel reflection and transmission coefficients. The polarization of the incident light also becomes important in the non-normal case, with different definitions of the coefficients for the two possible linear polarizations.

For s-polarized light, the Fresnel coefficients are defined as

$$r_s = \frac{\bar{n}_1 \cos\theta_1 - \bar{n}_2 \cos\theta_2}{\bar{n}_1 \cos\theta_1 + \bar{n}_2 \cos\theta_2} \tag{3.39}$$

$$t_s = \frac{2\bar{n}_1 \cos\theta_1}{\bar{n}_1 \cos\theta_1 + \bar{n}_2 \cos\theta_2} \tag{3.40}$$

and for p-polarized light

$$r_p = \frac{\bar{n}_1 \cos\theta_2 - \bar{n}_2 \cos\theta_1}{\bar{n}_1 \cos\theta_2 + \bar{n}_2 \cos\theta_1} \tag{3.41}$$

$$t_p = \frac{2\bar{n}_1 \cos\theta_1}{\bar{n}_1 \cos\theta_2 + \bar{n}_2 \cos\theta_1} \tag{3.42}$$

where $\bar{n}$ is the complex index, defined as $\bar{n} = n - ik$.

CHAPTER 4

Exciton Diffusion Length Measurement in Optically Thin Films

4.1 Background

A critical parameter required in the design of organic solar cells and other excitonic devices is the exciton diffusion length (L_D) of the active materials. This parameter, which describes the average distance an exciton travels before being lost to recombination, is useful in optimizing the exciton diffusion efficiency[172] (see Sec. 3.1). The optimal thickness for planar heterojunction active layers is approximately L_D, the best compromise between increased absorption from a thicker layer and improved exciton harvesting with a thinner layer. Similarly, the optimal grain size in mixed heterojunctions in on the order of L_D, which provides the largest, least resistive paths for charge conduction out of the heterojunction while still dissociating the majority of excitons. Design rules for other organic devices also rely on L_D, such as fluorescent/phosphorescent, triplet-managed organic white light emitting devices.[175]

One widely used method for measuring L_D uses the photoresponse of an organic thin-film Schottky diode.[176] A thin organic layer is sandwiched between two metal contacts, one ohmic and one rectifying, and illuminated through the ohmic contact with a range of wavelengths. The exciton distribution in the device is then considered to depend on the depth of optical penetration of the excitation light, with strongly absorbed wavelengths generating excitons very near the ohmic contact. As only the Schottky contact is able to generate photocurrent, the photocurrent spectrum is "out-of-phase" with the absorption, with the region of highest absorption corresponding to the lowest photocurrent. Ghosh and Feng used this technique to measure $L_D = 60$ Åfor merocyanine dyes. [176]

Schottky diode measurements of L_D have multiple issues. The metal-metal sandwich structure forms an optical cavity with strong interference effects, which can be difficult to characterize near the metal films.[177] This is problematic as the method requires a good

understanding of the exciton distribution profile and therefore the optical absorption in the organic film. Calculations of the optical field in the device are further complicated by the illumination through a thin metal layer, whose absorption can be enhanced due to surface plasmons. Metal layers deposited on organics can also penetrate tens of nanometers into the material,[178] which extends the region of exciton dissociation and leads to an overestimate of L_D. Further overestimates are caused by long-range energy transfer to the metal, which can occur over distances as large as 50 nm. Measurements of L_D using this technique often are above 100 nm, values which lack independent support.[179–181]

Alternative techniques for measuring L_D use PL measurements to avoid issues with metal layers. A common technique is thickness-dependent photoluminescence quenching (TD-PLQ), where the PL of different thicknesses of an organic layer by itself and adjacent to a quenching layer is measured. As the PL of an organic layer is directly proportional to the exciton population, the difference between the PL of the layers with and without the quenching material will saturate as the thickness of the organic layer exceeds L_D.[172,182,183] This technique is cumbersome, as it requires a large number of samples in order to extract L_D for a single material. Organic films also do not necessarily form continuous layers at extreme thinness, complicating the analysis. It has been shown that quenching layers do not necessarily fully quench when the layer thickness is on the order of L_D.[184] Different film thicknesses and films with and without the quenching layer will also have different optical excitation profiles due to interference, further complicating the measurement.[185]

A more recent highly accurate technique is spectrally-resolved photoluminescence quenching (SR-PLQ).[138] In SR-PLQ the PL from two identical organic films is compared, one capped with a blocking layer and one with a quencher. The PL is measured over a range of excitation wavelengths resulting in different excitation profiles in the material at differently-absorbed wavelengths and L_D is calculated from the ratio of the spectra of the two devices. Example exciton profiles for the two samples are shown in Fig. 4.1 for monochromatic illumination at a wavelength with high absorption in the sample ($\alpha = 0.4$ nm^{-1}) and the other at low absorption ($\alpha = 0.1$ nm^{-1}). For the strongly-absorbing film, the majority of excitons are generated adjacent to the front interface, resulting in a large difference in total exciton population between the blocking and quenching samples. The low-absorption case, in contrast, has exciton generation much farther into the film and therefore a much smaller difference between the two samples. As the PL signal is directly proportional to the total exciton population in the material, the difference between the blocking and quenching samples over a range of excitation wavelengths (and therefore a range of absorption strengths) gives L_D.

The method of SR-PLQ possesses multiple advantages over other techniques. It uses

only organic materials, much easier to model than metal layers. It only requires two samples, both of the same thickness. As morphology can vary with thickness, this allows for consistent samples and also avoids the issues with incomplete layers than can arise in TD-PLQ.

The advantages of SR-PLQ have allowed for measurements of many organic materials. One such measurement was Lunt et al's systematic examination of the change in L_D with crystallinity in PTCDA films.[186] The difference in L_D between crystalline and amorphous films of single materials such as tetracene[164,187–190] had been previously measured, but there had not been an examination of L_D over the full range from amorphous to crystalline. This was at least partially due to the difficulty in preserving the same degree of crystallinity that would have been required for the large number of samples used in TD-PLQ, whereas the active layer in the samples required for SR-PLQ was deposited in one growth on adjacent substrates, ensuring uniformity. This work showed a linear increase in L_D with the extent of crystalline order in the film, with L_D increasing to its single-crystal value for crystal sizes above $20L_D$.

The technique of SR-PLQ does, however, possess some disadvantages. It requires the organic films tested to be optically thick at all excitation wavelengths (i.e. where the absorption coefficient $\alpha(\lambda) > d$, the film thickness), which in the initial work required film thicknesses of 200-600 nm.[138] This can be wasteful of expensive organics and is impractical for materials that cannot be made sufficiently thick such as many solvent-processed materials (see Section 1.4.2.1). This includes many solution-processed materials such as squaraine-based donors, where d is limited by their solubility and processing constraints.[191,192]

In this work, we address this disadvantage by extending the use of SR-PLQ to organic films of arbitrary optical thickness. By calculating the spatial dependence of the optical field in thin films and using it along with the steady-state exciton diffusion equation, we show that the diffusion lengths from relatively thin films ($<$100 nm) can be unambiguously determined, allowing for the study of a large range of materials heretofore inaccessible using conventional SR-PLQ. Furthermore, this technique allows for the measurement of diffusion lengths in films whose thickness is comparable to that used in an optimized device, thus eliminating uncertainties due to dependencies of L_D on d. Indeed, we show that subphthalocyanines exhibit such a dependence which has, to our knowledge, not been previously observed.

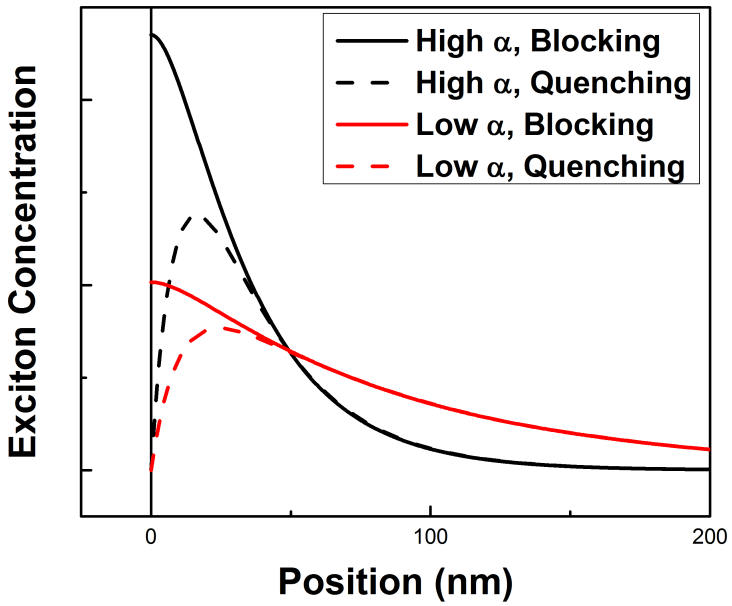

Figure 4.1: Example exciton profiles for a sample with either a blocking (perfectly reflects excitons) or quenching (destroys excitons) interface at $x = 0$. Two cases are simulated using the steady-state exciton diffusion equation for an exponentially decaying illumination profile, high-absorption ($\alpha = 0.4$ nm^{-1}) and low-absorption ($\alpha = 0.1$ nm^{-1}). The quenching boundary condition decreases the exciton population within $2L_D$, creating a larger difference in total exciton population between the blocking and the quenching case for the high-absorption case where most excitons are generated near the front interface. As the PL signal is directly proportional to the total exciton population in the layer, the ratio of the PL signals η from the two layers over a range of excitation wavelengths λ has the relation $\eta(\lambda) = \frac{\alpha(\lambda)}{cos(\theta_R)} L_D + 1$ where the absorption α has been corrected for the angle of refraction of the light θ_R in the material.

4.2 Theory

The technique of SR-PLQ is based on the steady-state diffusion equation,

$$L_D^2 \frac{\delta^2 n}{\delta x^2} - n + \tau G(x) = 0 \tag{4.1}$$

where $n(x)$ is the exciton density distribution, τ is the exciton lifetime, and $G(x) = \frac{\lambda}{hc} Q$ is the exciton generation profile, $Q(x)$ is the time-averaged absorbed optical power in the active layer, λ is the excitation wavelength, h is Planck's constant, and c is the speed of light.

In conventional SR-PLQ, the active layer is optically thick at all wavelengths, eliminating the effects of optical interference from reflections from the back surface. The active

layer is then represented as a semi-infinite layer with the edge at $x = 0$ and the exciton generation profile becomes

$$G(x) = \frac{I_0 \alpha}{cos(\theta_R)} exp\left(-\frac{\alpha x}{cos(\theta_R)}]\right) \tag{4.2}$$

where I_0 is the incident light intensity and θ_R is the refracted angle of light in the active layer. Then Eq. 4.1 is solved for the case of a blocking ($\frac{\delta n}{\delta x}|_{x=0} = 0$) or a quenching ($n(x) = 0$) interface to calculate the exciton density. As the PL signal from a layer is directly proportional to the total exciton concentration in the layer, we then calculate the ratio of the two signals η:

$$\eta(\lambda) = \frac{\int n_B(x)dx}{\int n_Q(x)dx} = \frac{PL_B}{PL_Q} = \frac{\alpha(\lambda)}{cos(\theta_R)} L_D + 1 \tag{4.3}$$

where n_B and n_Q are the exciton density distribution in the active layer with a blocking or quenching interface, respectively, and PL_B and PL_Q are the PL signals from an organic layer capped with a blocker or quencher, respectively. As the PL signal from an organic layer is directly proportional to the total exciton population in the layer, the ratio of the PL signals cancels out the constant of proportionality and is therefore equal to the ratio of the total exciton population in the layers. This also cancels out a large number of other possibly difficult-to-measure constants, such as τ, I_0, the PL quantum yield Φ_F, and the spectrofluorimeter monochromator and detector response functions. The ratio is then graphed with respect to absorption and fit to Eq. 4.3, with example data shown in Fig. 4.2.

To extend SR-PLQ to optically thin layers the optical field $E(x)$ throughout the two layers is calculated using the method of optical transfer matrices (Sec. 3.5). The time-averaged absorbed power $Q(x) = (2c\epsilon_0 kn/\lambda)|E(\lambda, x)|^2)$ is then used to numerically solve Eq. 4.1 for the blocking and quenching sample and calculate $\eta(\lambda)$. The ratio is then fit to PL data using L_D as the free parameter.

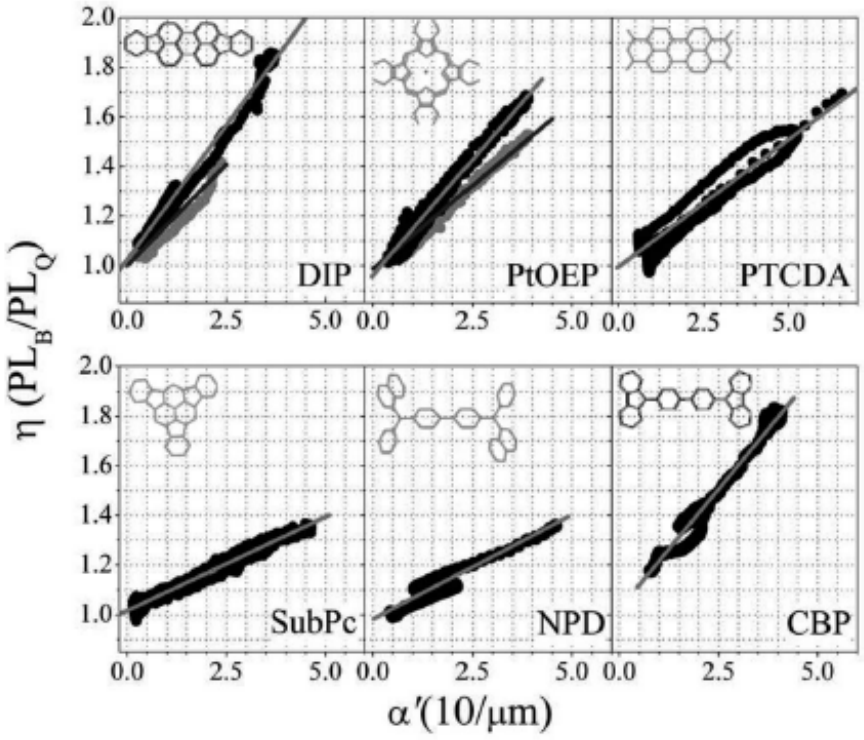

Figure 4.2: Data for SR-PLQ for six different organic molecules. The PL from a layer of material capped with a blocker or a quencher was measured to calculate the ratio η, which was plotted with respect to the material absorption coefficient α at the excitation wavelength. Lines are fit to the equation $\eta = \frac{\alpha(\lambda)}{cos(\theta_R)} L_D + 1$ to extract the diffusion length L_D from the slope of the line. Here $cos(\theta_R)$ is a correction for the non-normal incidence of the excitation light, where θ_R is the angle of refraction of excitation light in the active material. Figure is from.[138]

4.3 Experiment

Both solution- and vapor-deposited thin films were studied. The solution processed squaraines were prepared as follows: 2-[4-(N,N-diisobutylamino)-2,6-dihydroxyphenyl]-4-(4-diphenyliminio)-2,5-dien-1-ylidene-3-oxocyclobut-1-en-1-olate (ASSQ), 2-[4-(N,N-diphenylamino)-2,6-dihydroxyphenyl]-4-(4-diphenyliminio)-2,5-dien-1-ylidene-3 oxocyclobut-1-en-1-olate (DPASQ), and 2-[4-(N-phenyl-N-1-naphthylamino)-2,6-dihydroxyphenyl]-4-[(4-(N-phenyl-N-1-naphthyliminio)-2,6-dihydroxyphenyl)-2,5-dien-1-ylidene]-3-oxocyclobut-1-en-1-olate (1-NPSQ) were dissolved in chloroform and then spin-coated onto silicon (Si) or quartz substrates at 1000 revolutions per minute (RPM) in an ultrapure nitrogen ambient ($<$10 ppm O2, $<$0.1 ppm H_2O). Also, the acceptor, PTCDA, and the donor, SubPc were deposited on these same substrates via thermal evaporation in high vacuum (chamber base pressure $< 10^{-7}$ Torr). The samples were simultaneously

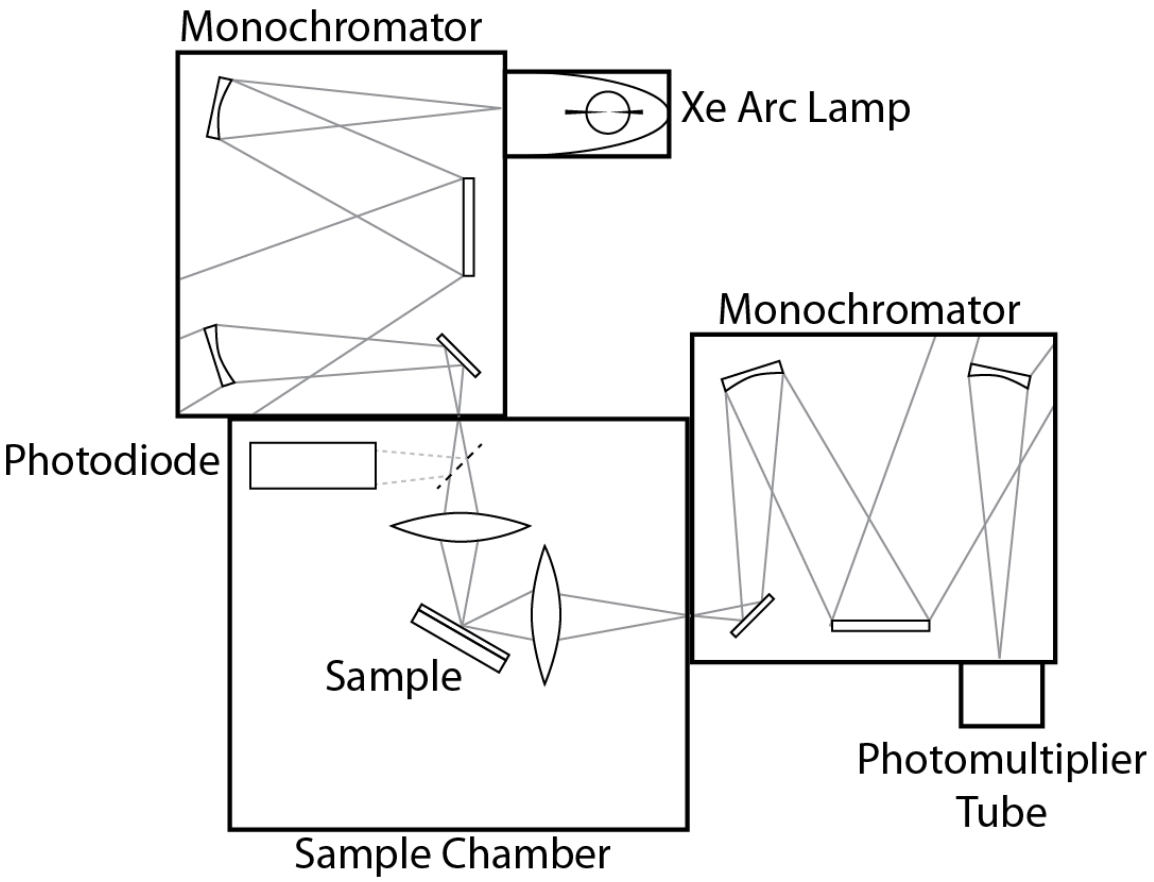

Figure 4.3: Experimental setup for PL measurement.

fabricated in pairs: one was capped with an exciton blocking layer of bathocuproine (BCP) and the other with a quenching layer of C_{60}. The photoluminescence excitation spectra of the samples were measured using a PTI QuantaMaster spectrofluorometer at an incident angle of $\theta = 30$ in a high purity N_2 atmosphere to prevent atmospheric degradation of the films with the experimental setup shown in Fig. 4.3. The samples were illuminated through the capping layer as shown by the experimental set-up in Fig. 4.4, inset. All optical constants and thicknesses employed were measured using a variable angle spectroscopic ellipsometer.

4.4 Results

An example photoluminescence excitation (PLE) spectrum for a 60 nm thick SubPc film on quartz capped with an 8 nm thick C_{60} or BCP layer, is shown in Fig. 4.4a. Multiple PLE scans were taken for each sample and then averaged to obtain the mean and error. The

wavelength-dependent ratio, $\eta(\lambda)$, is calculated, and is fit to these data using L_D as the free parameter.

Fits to data from several films are shown in Figs. 4.4b (60 nm thick SubPc) and Fig. 4.5 (lines), with all L_D obtained provided in Table 4.1. The reduced thickness control and increased surface roughness of DPASQ and ASSQ deposited via spin coating from solution necessitated up to a 15% adjustment of d from its ellipsometrically measured value to achieve the best fit to the small interference fringes that are apparent in the spectra of 1-NPSQ and PTCDA in Fig. 4.5.

The normalization procedure for SR-PLQ for an optically thick sample is given by Eq. 4.3. As seen in Fig. 4.6, an optically thick, 300 nm SubPc sample displays the linear behavior predicted by Eq. 4.3. However, the 60 nm sample cannot be adequately fit using this simple procedure due to optical field variations that differ from a purely exponential decay as assumed in SR-PLQ. Indeed, near their transparency regions, data in even optically thick samples deviates from a linear function requiring that data in such regions be discarded. However, in the thin film method, all data can be included in the fit as long as only a single excitonic species is excited across the wavelength region of interest.

To determine the accuracy of the thin film technique, we compared the results of fitting the data to Eq. 4.1 to conventional SR-PLQ in Eq. 4.3 for optically thick samples of 300 nm of SubPc. Our method yields $L_D = 22.7 \pm 0.9$ nm, compared to 16.4 ± 0.3 nm calculated using SR-PLQ in Fig. 4.6. The difference between the two values is due to the differing reflectance and transmission of the BCP or C_{60} capping layers. Equation 4.3 assumes that there are no optical effects from the capping layers, with SR-PLQ attempting to account for illumination through these layers by applying a correction to η calculated from the Fresnel transmission and reflection coefficients of the respective thin films. To determine if this adjustment is successful, a set of devices was simulated with and without capping layers. It is found that the simulated devices with capping layers showed the same discrepancy between our modeled L_D and that found based on conventional SR-PLQ. However, without capping layers, both methods were in good agreement. This suggests that the optical effects of the capping layers are must be considered even in conventional SR-PLQ to eliminate systematic errors introduced by assuming the capping layers affect $E(\lambda, 0)$ identically. The thin film method avoids this error due to its dependence on an exact calculation of the field throughout the entire sample.

Previous reports have indicated that diffusion lengths as small as 8 nm have been obtained for SubPc.[182,193] It is likely that the nearly three-fold larger value obtained here is due to elimination of exposure to atmosphere in our experiments. Indeed, such exposure can result in a significant decrease in PL intensity after only a few seconds. For example, it has

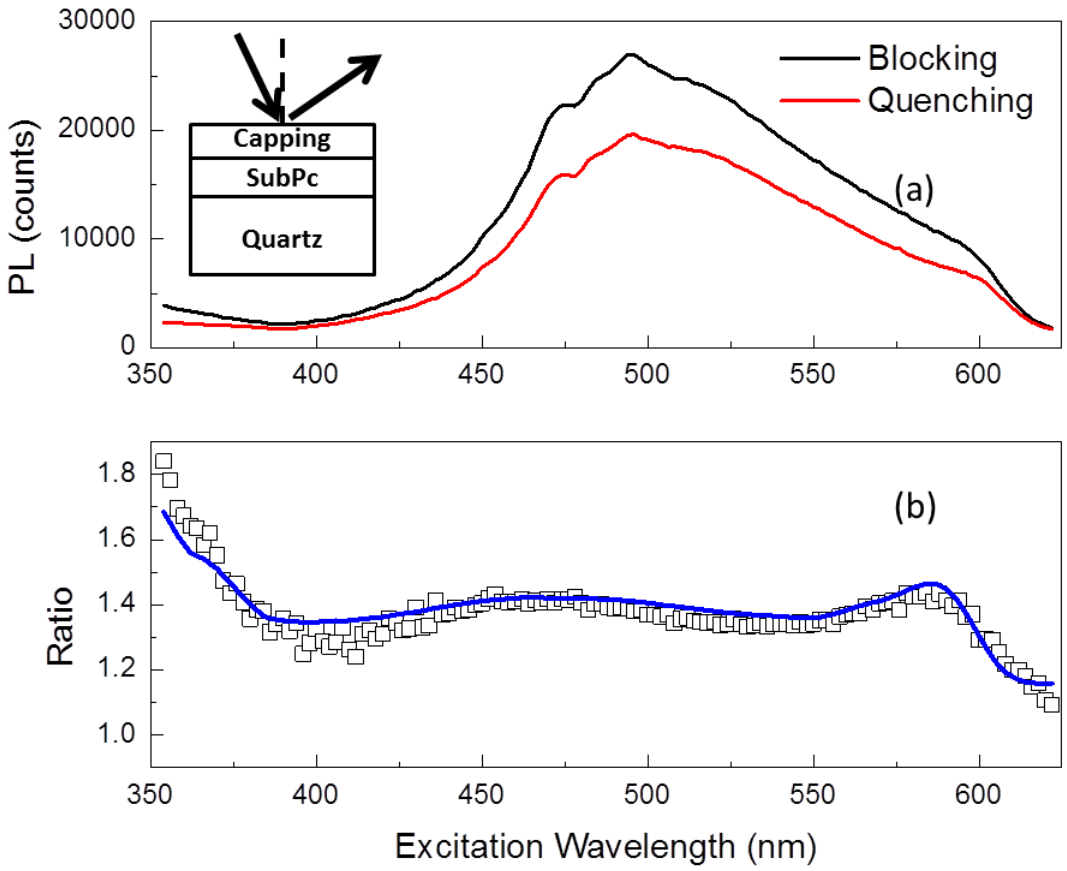

Figure 4.4: Example data for a $d = 60$ nm thick SubPc sample capped with 8 nm of BCP and C_{60}. At $d = 60$ nm, the sample is optically thick between wavelengths of $\lambda = 510$ and 610 nm, and is optically thin outside of this range. (a) Averaged photoluminescence excitation (PLE) spectra for SubPc capped by either a blocking (BCP) or quenching (C60) layer. Inset: Sample structure and experimental configuration . Samples were excited at $\theta = 30$ and the PLE was detected at 60 from normal (b) Ratio of the PLE intensity for the blocked to the quenching sample. The solid line is a fit to this data with a diffusion length of $L_D = 12$ nm.

also recently been reported that L_D = 28 nm for SubPc measured in a high-purity nitrogen atmosphere, using a similar optical model to fit the quenching efficiency of a SubPc-C_{60} interface.[194]

Note also that for PTCDA, we obtain $L_D = 9.3 \pm 0.8$ nm, in agreement with the previously reported value of 10.4 ± 1.0 nm.[182]

Measurement of L_D as a function of SubPc thickness indicate a decrease in diffusion length with decreasing d, as listed in Table 4.1. Typical SubPc thicknesses employed in OPVs are between 10 and 13 nm, which is considerably less than $L_D = 22.7 \pm 0.9$ nm for optically thick (i.e. 300 nm) films of SubPc.[195,196] For planar layers, the optimal layer thickness is expected to be slightly larger than L_D. In this context, L_D approaches a value

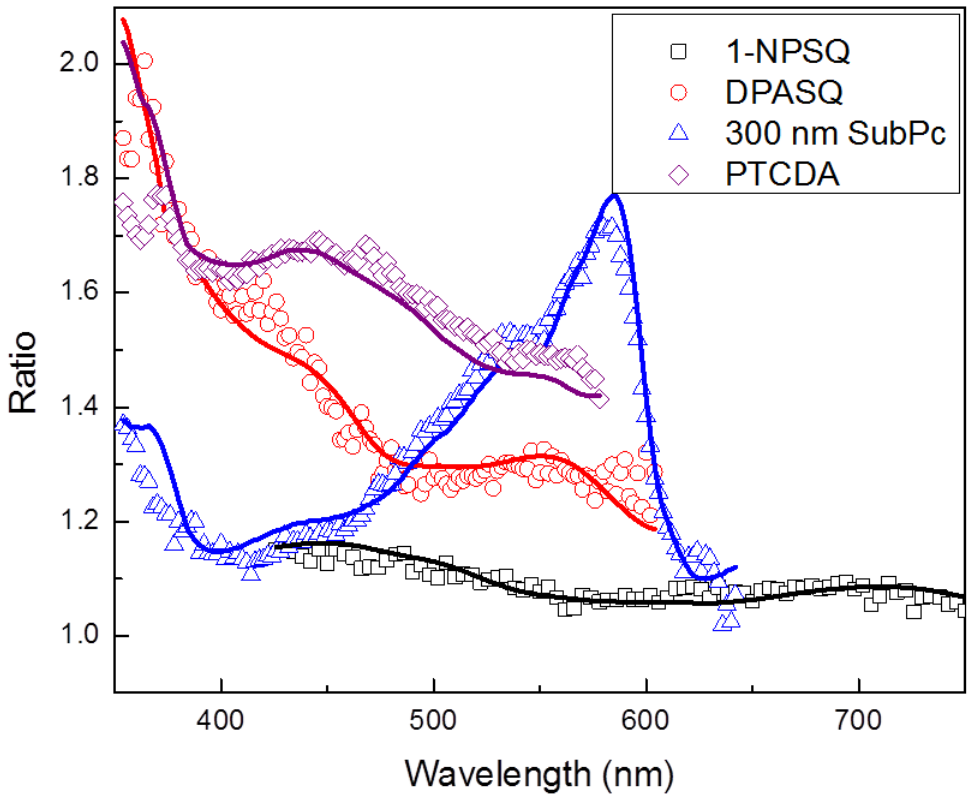

Figure 4.5: Experimental photoluminescence excitation spectra and fits for $d = 30$ nm thick PTCDA, 80 nm thick 1-NPSQ , 300 nm thick SubPc, and 73 nm thick DPASQ films. Photoluminescence was measured at wavelengths of 740 nm, 805 nm, 700 nm, and 720 nm for PTCDA, 1-NPSQ, SubPc, and DPASQ respectively.

closer to the optical device thickness as sample thickness decreases, although more study is needed to determine if this is a real effect due to the large error.

Finally, we obtain $L_D = 2.9 \pm 0.8$ nm for 1-NPSQ, another donor material used in efficient small molecule OPVs.[192] This value is for as-cast samples, while layers used in devices are typically thermally annealed, which has been shown to increase surface roughness, order and the diffusion length, resulting in a highly entangled, nanocrystalline heterojunction solar cell structure.[186] However, even unannealed, planar devices employing this donor show a high efficiency. More investigation is required to determine the mechanisms that result in high efficiency, even in the presence of such a short diffusion length.

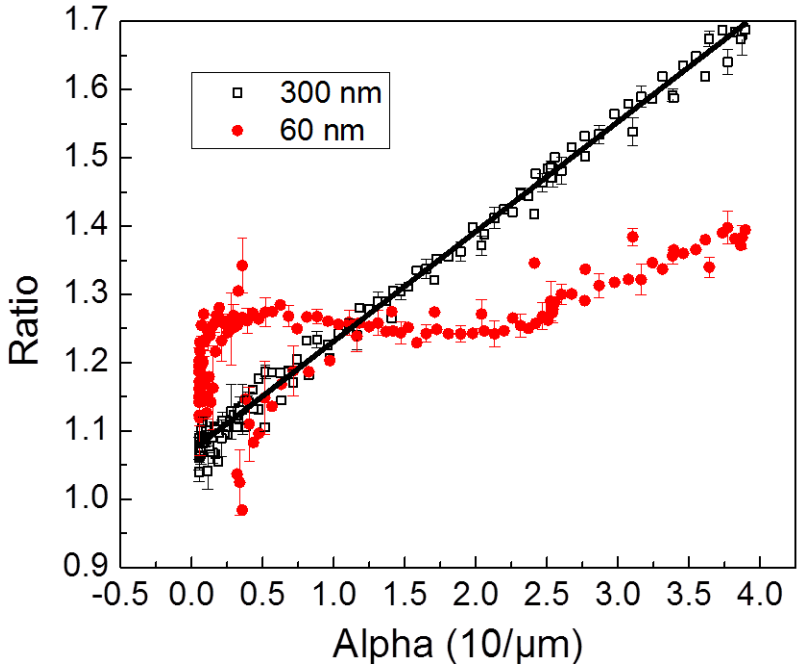

Figure 4.6: A comparison of the ratio of the intensity of photoluminescence for 60 and 300 nm thick samples of SubPc with a blocking vs. a quenching layer cap (η). The optically thick (300 nm) sample is linear for all values of absorption coefficient, α, measured over the wavelength domain from 354 nm to 660 nm, while the thinner (60 nm) sample does not follow the linear function anticipated for conventional SR-PLQ. Both sets of data have been corrected for reflection and absorption of the BCP and C_{60} capping layers. The solid line indicates a fit to the thick film sample yielding a diffusion length of 16.1 nm.

Material	Thickness (nm)	L_D (nm)
ASSQ	70	11 ± 0.6
DPASQ	73	10.7 ± 0.2
1-NPSQ	80	2.9 ± 0.8
PTCDA	30	9.3 ± 0.8
SubPc	300	22.7 ± 0.9
SubPc	154	15.5 ± 1.5
SubPc	103	19.2 ± 1.6
SubPc	80	17.3 ± 2.2
SubPc	60	16.2 ± 1.4

Table 4.1: Diffusion lengths of several archetype small molecular weight thin film materials. The solution-processed squaraine (*SQ) materials could not be deposited in films thicker than 80 nm and were therefore unable to be measured using conventional SR-PLQ.

4.5 Conclusion

In summary, we have demonstrated the application of SR-PLQ to optically thin organic films based on an exact modeling of the optical field throughout a layered sample composed of both the film under study and the quenching or blocking cap layer. This extension of conventional SR-PLQ allows for the study of solvent-processed materials such as squaraine and subphthalocyanine donors, and acceptor materials, which have been used in efficient organic solar cell structures. The method also allows the accurate determination of the dependence of L_D on layer thickness such as observed in SubPc, for films whose thickness is comparable to that used in practical device structures.

CHAPTER 5

Exciton Diffusion in Fullerenes

Two independent and direct measurements of exciton transport in the fullerene C_{60} unambiguously indicate that singlets, and not triplets as often claimed, are responsible for energy transport and ultimately charge generation in organic photovoltaic cells. The singlet exciton diffusion length, L_D, was measured using fits to the external quantum efficiency of planar heterojunction photovoltaics, and via C_{60} fluorescence, giving values of 32 $\pm$ 2 nm and 36 $\pm$ 2 nm, respectively. The surprisingly long exciton diffusion length in C_{60} is a result of its molecular symmetry that results in quantum mechanical selection rules strongly prohibiting singlet recombination, as opposed to the past assumption that the diffusion is due to long-lived triplets generated by spin-orbit coupling. Further, the measured diffusion length of C_{60} is used to determine the relative differences between the highest occupied molecular orbital to lowest unoccupied molecular orbital energy gaps of C_{60} and the closely-matched, analogous fullerene, C_{70}. We find that the C_{60} energy gap is 18 $\pm$ 5 meV wider than C_{70}. To perform these measurements, we develop methods to treat exciton populations at interfaces with a range of blocking or quenching characteristics, including diffusion between materials with identical energy gaps.

5.1 Background

Absorption of a photon in an organic semiconductor results in the formation of a bound electron-hole pair, or exciton. Organic photovoltaic (OPV) cells require that the exciton dissociate into free charges at a donor-acceptor interface,[172] in contrast to inorganic semiconductors where charge is directly generated by a band-to-band excitation without an intermediate excitonic state.[197] The exciton diffusion length,[172] corresponding to the characteristic distance travelled prior to its recombination, is therefore a critical parameter of all organic semiconductors, and that strongly influences the performance of OPV cells. It depends on both the microscopic and macroscopic natures of optically active organic

materials,[186] and ultimately the design of devices themselves.[138,198]

The fullerene, C_{60}, commonly used in OPVs has been shown to have a relatively long exciton diffusion length of L_D 40 nm, compared to many other donors and acceptors whose L_D typically ranges between 5 nm and 10 nm.[138] There are two competing theories for the origin of this exceptionally long L_D, that both agree on the importance of molecular symmetries in C_{60} in forbidding optical transitions from the lowest energy singlet (total spin quantum number S=0) exciton state.[199,200] The C_{60} molecule consists of 60 carbon atoms arranged in 12 five-membered rings and 20 six-membered rings. There are 1812 possible isomers of this structure, but the most stable and only one observed obeys the isolated pentagons rule, where each five-membered ring is completely surrounded by six-member rings.[199] This molecular configuration belongs to the icosahedral (Ih) symmetry group, resulting in dipole-forbidden transitions from the lowest energy singlet level.

The primary differences in the theories for how the dipole-forbidden transitions lead to the long L_D lies in the exciton spin symmetry.[172,174,197] Photogenerated excitons are primarily antisymmetric singlets, but can transfer to spin-symmetric triplet states (S=1) via intersystem crossing. Then the forbidden optical transition might increase the intersystem crossing (ISC) rate, resulting in a large triplet population that is expected to have a large L_D due to their lifetimes on the order of milliseconds or longer. However, no systematic evidence for a larger L_D for singlets compared to triplets has been reported.[138,201] Alternatively, the forbidden transition may simply result in an increase in the singlet lifetime without involving ISC.

The ambiguity in the source of energy transport in C_{60} arises from the difficulties presented by the very low oscillator strength of the singlet transition. That is, singlet diffusion lengths are often accurately determined by characterizing the PLE fluorescence spectrum generated by singlet recombination.[138,198] However, due to the forbidden singlet dipole transition, C_{60} has extremely weak PL except at low temperatures[202–204] or high excitation intensities,[204,205] rendering these techniques impractical. Early attempts to determine the L_D of the fullerenes have therefore required the indirect approach of modeling OPV performance either by fitting the device EQE[172,174] or by inserting thin exciton blocking layers into the C_{60}.[206] More recently, measurements employing time-resolved microwave conductance[197] and transient absorption in C_{60}/zinc phthalocyanine (ZnPc) nanostructures[207] have resulted in reports of L_D varying from 7 nm to 40 nm in C_{60}. However, neither of these techniques can be used to clarify the spin symmetry of the excitation. Furthermore, the large range in measured diffusion lengths has been attributed to variations in material purity and crystallinity of samples prepared in different laboratories, leading to increased ambiguity in the interpretation of the results.[172]

In this work we study exciton diffusion in C_{60} by two independent methods. A spin-independent L_D measurement is extracted from fits to the EQE spectrum of C_{60} incorporated in C_{60}/tetraphenyldibenzoperiflanthene (DBP)[100] planar heterojunction photovoltaic cells, giving 32 $\pm$ 2 nm.[172,174] The very low intensity room-temperature steady-state C_{60} fluorescence is also used to unambiguously measure the singlet exciton diffusion length L_D = 36 $\pm$ 2 nm through the sensitive technique of spectrally-resolved photoluminescence quenching (SR-PLQ).[138,198] Agreement between these measurements show that the source of photocurrent in C_{60} layers is the singlet exciton. The properties of C_{60} are further examined using the related fullerene,[208] C_{70}, as a fluorescent probe layer placed in contact with C_{60}. Excitons freely diffuse between C_{70} and C_{60} due to the close match between their HOMO and LUMO energies.[209] The reduced symmetry of C_{70} gives rise to differences in the absorption spectra and emission intensity compared with C_{60}, allowing for their selective excitation and emission.[199,200] Then, SR-PLQ is used once again to treat exciton diffusion between these materials with different L_D and exciton lifetime, τ. From these data, we infer that the energy gap of C_{60} is 18 $\pm$ 5 meV larger than C_{70}.

These measurements have required the development of analytical tools to treat the effects of a variety of interfaces on exciton diffusion. Most treatments of exciton diffusion exclusively treat ideal blocking or quenching interfaces, whereby excitons are perfectly reflected back into the material, or are quenched with unity efficiency.[138,172,174,198] Here we extend the analysis to consider the effects of partially blocking or quenching interfaces, as well as extending these techniques to treat exciton diffusion between materials with identical HOMO-LUMO energy gaps but different L_D and τ. We have further developed methods to treat the effect of small ($\sim kT$, where k is the Boltzmann constant and T is the temperature) energy gap differences on exciton diffusion between such materials.

5.2 Theory

The measurement of L_D via SR-PLQ is based on the steady-state exciton diffusion equation:

$$0 = \frac{L_D^2}{\tau}\frac{\partial^2 n(x)}{\partial x^2} - \frac{n(x)}{\tau} + G(x) \tag{5.1}$$

where n is the exciton density generated by the incident PL pump beam, and $G(x)$ is their generation rate. Ideal blocking and quenching interfaces of the material under study are represented by the boundary conditions[138] of $\frac{\partial n}{\partial x}\big|_{x=0} = 0$ and $n(0) = 0$, respectively. The diffusion equation is solved for the case of two identical, semi-infinite layers with either a blocking or a quenching boundary condition at $x = 0$, excited by an exponentially decaying

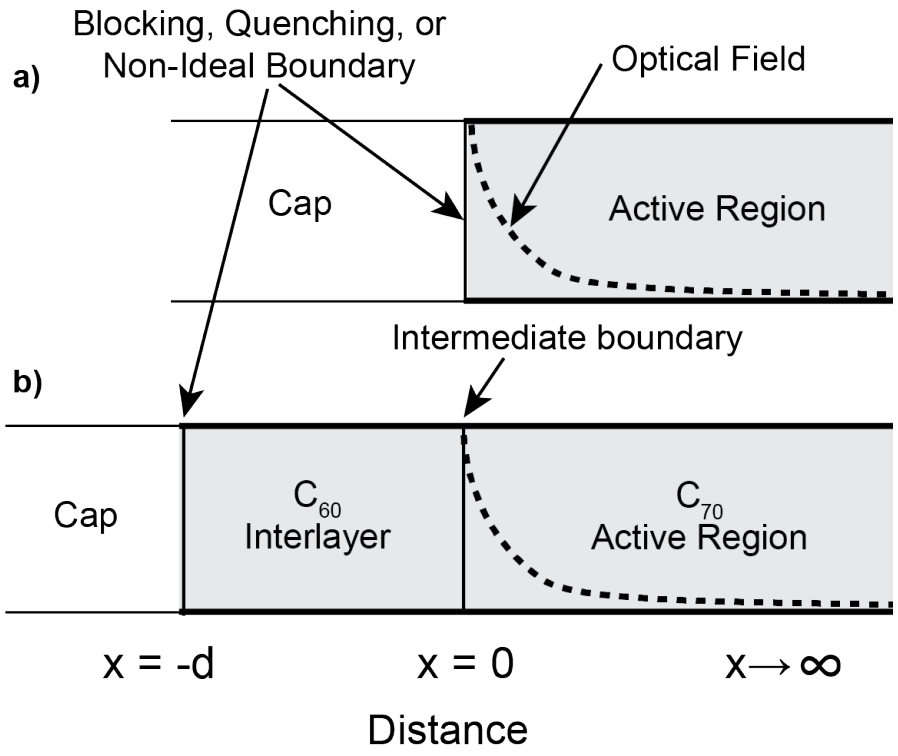

Figure 5.1: Layering schemes and boundary conditions used in modeling (a) spectrally-resolved photoluminescence quenching (SR-PLQ) and blocking efficiency measurements, and (b) C60 interlayer measurements.

optical field following $G(x) = exp(-\alpha x)$ (see Fig. 5.1a). The ratio of the total exciton population in the two samples is:[138]

$$\eta(\lambda) = \frac{\int_0^\infty n_B(x)dx}{\int_0^\infty n_Q(x)dx} = \alpha`(\lambda)L_D + 1 \tag{5.2}$$

where $\alpha`$ is the absorption coefficient of the material at wavelength, λ, corrected for the angle of refraction, θ_r, in the layer, and the subscript B (Q) indicates a blocking (quenching) layer capping the material under test. Since the PL intensity of a layer is directly proportional to its exciton population, η is also the ratio of the PL of two identical layers with blocking or quenching boundary conditions. Then L_D is calculated by fitting η over a range of λ.

To use C_{70} as a fluorescence sensitizer for C_{60}, the case of diffusion across an interface between these two materials with identical HOMO and LUMO levels but different L_D and τ must be considered. We assume a semi-infinite layer of material 1 (C_{70}) with an interlayer

(thickness, d) of material 2 (C_{60}) separating it from a blocking or quenching boundary, as shown in Fig. 5.1b. The interface between the materials is located at $x = 0$, and the other side of the interlayer is at $x = -d$. We further assume that layer 1 is luminescent while layer 2 is transparent and non-luminescent. In this case, the boundary conditions between the two materials are:

$$\frac{L_{D1}^2}{\tau_1}\frac{\partial n_1}{\partial x}\,|_{x=0} = \frac{L_{D2}^2}{\tau_2}\frac{\partial n_2}{\partial x}\bigg|_{x=0} \tag{5.3}$$

$$n_1(0) = n_2(0) \tag{5.4}$$

Equation 5.3 can be re-written as:

$$\frac{L_{D1}}{L_{D2}}\xi\frac{\partial n_1}{\partial x}\bigg|_{x=0} = \frac{\partial n_2}{\partial x}\bigg|_{x=0} \tag{5.5}$$

where $\xi = \frac{L_{D2}/L_{D1}}{\tau_2/\tau_1}$. These boundary conditions can be used to solve Eq. 5.1 for a relationship analogous to Eq. 5.2 that can be fit to yield L_{D2}. Calculating η for a blocking or a quenching boundary at $x = -d$ gives:

$$\eta(\lambda) = \left(\frac{\alpha_1{\text{`}}L_{D1}\xi}{\xi + \tanh(L_{D2}/d)} + 1\right) / \left(\frac{\alpha_1{\text{`}}L_{D1}\xi}{\xi + \coth(L_{D2}/d)} + 1\right) \tag{5.6}$$

This reduces to Eq. 5.2 in the limit of $d = 0$, and to $\eta \to 1$ for $d \to \infty$.

The number of fitting parameters in Eq. 5.6 can be reduced by a direct measurement of the ratio, ξ. This requires a method to treat non-ideal blocking or quenching interfaces, such as the boundary between two fullerenes (C_{60} and C_{70}) where both the exciton population and its first derivative are non-zero. For this, we introduce the relative blocking efficiency, ϕ:

$$n(0) = \phi n_B \tag{5.7}$$

where, as above, n_B is the exciton density at the interface with an ideal blocking layer. Thus, $\phi = 1$ for a perfectly blocking interface and $\phi = 0$ for a perfect quencher. Solving Eq. 5.2 using two non-ideal blockers (1 and 2) gives:

$$\eta = \frac{\phi_1\alpha{\text{`}}L_D + 1}{\phi_2\alpha{\text{`}}L_D + 1} \tag{5.8}$$

It is possible to measure L_D separately with Eq. 5.2, and to determine ϕ_2 by using an ideal blocker or quencher, allowing ϕ_1 of an arbitrary layer to be calculated from η.

The exciton population at a non-ideal interface can also be expressed in terms of ξ, which is calculated based on a direct measurement of ϕ. For an interface between two

materials with identical HOMO and LUMO energies at $x = 0$, where material 1 is a finite layer with a blocking boundary condition at $x = -d$ and uniform generation rate $G(x) = G_0$, while material 2 is a semi-infinite layer with no absorption (and hence, $G = 0$), the population at the interface using Eqs. 5.3 and 5.4 is:

$$n(0) = \frac{\tau_1}{L_{D1}^2} G_0 \left[1 - \frac{1}{\xi \tanh(d/L_{D1}) + 1} \right] \tag{5.9}$$

The population in material 1 for a perfectly blocking interface is:

$$n_B(0) = \frac{\tau_1}{L_{D1}^2} G_0 \tag{5.10}$$

. Substituting Eqs. 5.9 and 5.10 into Eq. 5.7 and assuming $d > 2L_{D1}$, then:

$$\phi = \frac{\xi}{\xi + 1} \tag{5.11}$$

If L_{D2} is unknown, it can be obtained using Eq. 5.6.

Once L_{D2} is determined (i.e. using SR-PLQ if it is luminescent), this method can be further extended to examine differences between the HOMO-LUMO energy gaps of the two materials. For example, when the energy gap in one material differs by approximately energy kT, the heterojunction between the materials becomes slightly blocking. Excitons incident on the interface from the smaller energy gap material will have a reduced probability of transfer as given by the Miller-Abrahams model[140,210] (Eq. 2.24). The total exciton distribution in the two materials is calculated by taking a weighted average of solutions to Eq. 5.1 for a perfectly blocking interface, and a perfectly energy matched interface based on $P_{1\to2}$. The new exciton distribution is then used in Eq. 5.6, allowing the ratio to be fit to the heterojunction energy offset.

5.3 Experiment

All samples used were deposited by vapor deposition in high vacuum ($< 10^{-6}$ torr), with fullerenes and DBP source materials purified once via vacuum thermal gradient sublimation prior to use. Samples for SR-PLQ measurements used structure A in Table 5.1. Samples for the C_{60} interlayer measurements used structure B, and the blocking efficiency measurements used structure C. The 20 nm thick C_{60} layer in structure C was required to prevent interactions between excitons in C_{70} and the top surface of the C_{60} layer. The luminescent layer was deposited simultaneously in all three samples. BPhen was used as an ex-

Structure	Active Layer	Interlayer	Cap
A	310 nm C_{60}	None	8 nm BPhen (Bl)
			8 nm NPD (Q)
B	80 nm C_{70}	8/13/15 nm C_{60}	8 nm BPhen (Bl)
			8 nm NPD (Q)
C	80 nm C_{70}	None	8 nm BPhen (Bl)
			8 nm NPD (Q)
			20 nm C_{60} (Non-Ideal)

Structure	Anode	Anode Blocker	Donor	Acceptor	Cathode Blocker	Cathode
D	ITO	10 nm MoOx	10 nm DBP	40 nm C_{60}	10 nm BPhen	100 nm Ag

Table 5.1: Structures used for (A) spectrally-resolved photoluminescence quenching, (B) C_{60} interlayer, and (C) blocking efficiency measurements (blocking (Bl) and quenching (Q) layers indicated). Structure (D) is an OPV.

citon blocker and N,N-Di-[(1-naphthyl)-N,N-diphenyl]-1,1-biphenyl)-4,4-diamine (NPD) was the exciton quencher.

The OPV used structure D in Table 5.1. The device area of 1 mm^2 was defined by a shadow mask during metal cathode deposition. The EQE was measured as previously reported.[89] Fits to the EQE were performed using the method of Peumans, et al.[172] on the C_{60} in its absorption range of λ=380 nm to 520 nm. The PL measurements were taken in a high purity N2 atmosphere using a PTI QuantaMaster spectrofluorometer at a pump incidence angle of $\theta = 30$. The PL intensity was measured at 60 from normal at $\lambda = 750$ nm for C_{60} and $\lambda = 685$ nm for C_{70}. Fits to the PL data were performed by calculating η via Eq. 5.1, with $G(x)$ obtained via the transfer matrix method.[198] All optical constants and thicknesses were measured using a variable angle spectroscopic ellipsometer.

5.4 Results

The EQE spectrum of a planar DBP/C_{60} OPV (structure D) is shown in Fig. 5.2 (inset). A fit to the EQE in the region of C_{60} absorption[172] yields L_D = 32 $\pm$ 2 nm. The SR-PLQ measurements of C_{60} (structure A) give L_D = 36 $\pm$ 2 nm, with sample PLE data shown in Fig. 5.2. Fits to the ratio of these data using Eq. 5.2 are shown in Fig. 5.3 (circles). The PL emission was measured at $\lambda = 750$ nm, corresponding to C_{60} fluorescence.[209] No room-temperature phosphorescence expected at $\lambda = 825$ nm[209] was observed, indicating that triplet excitons were not observed.

The diffusion length was also measured using a C_{60} interlayer on C_{70} (structure B), and

was found to be L_D=20 $\pm$ 2 nm. This smaller value suggests there is a difference between the HOMO-LUMO energy gaps (Δ_{EHL}) of the two fullerenes. Fitting the ratio of the data in Fig. 5.4 using Eq. 5.6 and 2.24, and L_D = 36 nm gives $\Delta_{EHL} = 18 \pm 5$ meV (Fig. 5.3), with C_{60} have the wider energy gap. Also, for C_{70}, we find that $L_D = 10 \pm 1$ nm (Fig. 5.3), consistent with previous reports,[211] and the blocking efficiency of C_{60} on C_{70} was ϕ = 62 $\pm$ 6%, using data from structure C in Fig. 5.5 along with Eq. 5.8. This corresponds to ξ = 1.6 $\pm$ 0.4.

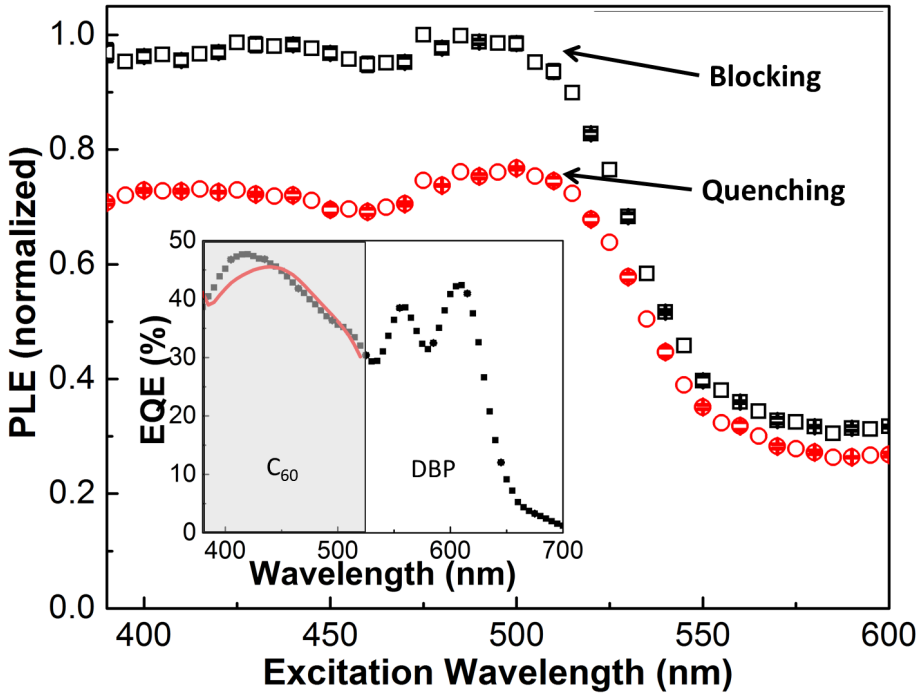

Figure 5.2: Photoluminescence excitation (PLE) data for 310 nm thick C60 layers. The C_{60} was were capped with a blocking BPhen, or a quenching NPD layer. Samples were excited at 30 from normal incidence, and emission detected at $\theta = 60$ at $\lambda = 750$ nm. Inset: External quantum efficiency (EQE) (squares) for the OPV structure D. The shaded area indicates the range of C_{60} absorption, and the remainder the range of DBP absorption. Solid line is a fit to the C_{60} response of EQE, giving a diffusion length of $L_D = 32 \pm 2$ nm

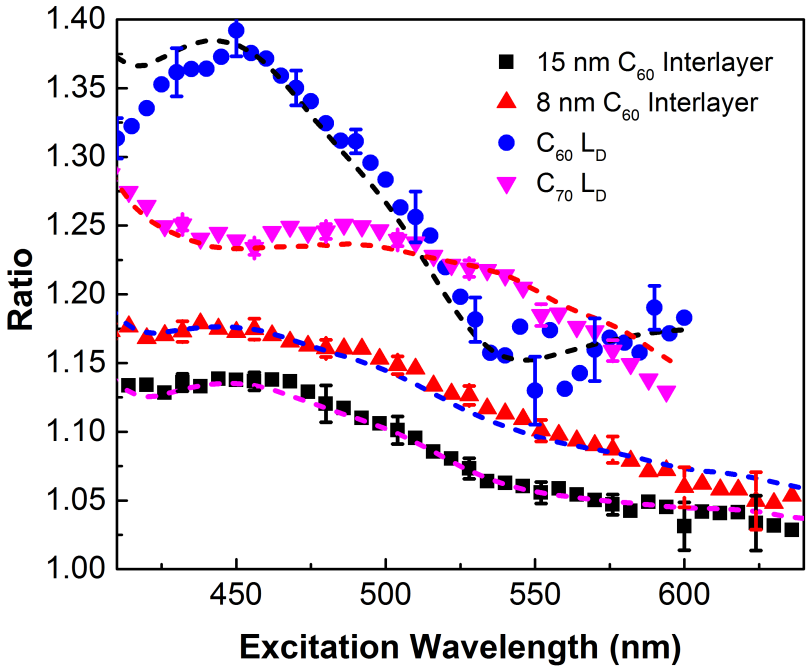

Figure 5.3: Ratio of PLE spectral intensities ($\eta(\lambda)$) and fits using theory in text. Spectrally-resolved photoluminescence quenching (SR-PLQ) was used to fit the data from C_{60} (circles) and C_{70} (downwards-pointing triangles) films, giving $L_D = 36 \pm 2$ nm and $L_D = 10 \pm 2$ nm, respectively. C_{60} interlayers of 8 nm (upwards-pointing triangles) and 15 nm (squares) were fit using intermediate boundary conditions at the interface between the fullerenes, giving $L_D = 20 \pm 2$ nm for both.

5.5 Discussion

The diffusion lengths measured for C_{60} based on EQE and SR-PLQ are consistent with previous measurements by Peumans[172] and Qin.[206] Since the spin-independent EQE measurement and the SR-PLQ measurement that depends only on the optical generation of emissive singlets agree, we conclude that photocurrent due to absorption in the C_{60} layer in OPVs primarily originates from singlet excitons. Note, too that our measured value for L_D disagrees with recent measurements of singlets by Lane et al[207] and Fravventura et al.[197] Using time-resolved microwave conductance, Fravventura observed L_D = 7.1 $\pm$ 0.5 nm, but also concluded that singlet excitons were the primary carrier of photoexcitation. Lane reported L_D = 10 $\pm$ 4 nm in C_{60}/zinc phthalocyanine (ZnPc) nanostructures. The discrepancies between these values are attributed to differences in C_{60} crystallinity and purity, as previously noted.[172] Also, the very short diffusion lengths in these studies contradict considerable work on OPV cells. This suggests that singlet recombination in samples with uncertain purity may occur through defects, hence circumventing the strict quantum mechanical selection rules arising from the C_{60} molecular symmetry.

The importance of purity to the diffusion length of C_{60} is supported by measurements made in our own work on different batches of C_{60} of varying purity. Devices using C_{60} with L_D = 36 $\pm$ 2 nm yielded the highest efficiencies, suggesting high purity. In contrast, devices made with a separate source batch of C_{60} from the same supplier showed significantly reduced efficiency, with measurements of L_D of the lower-efficiency C_{60} giving L_D = 20 $\pm$ 2 nm. All source materials used in this study were purified using thermal gradient sublimation as above, but reduced purity in the starting material nevertheless results in a 45% reduction in L_D, indicating the limitations to purification of materials with various qualities. Indeed, it has been shown that contamination can lead to C_{60} oligomerization and oxidation, with such reaction products having a significantly reduced τ, and hence L_D compared to pure source materials.[68]

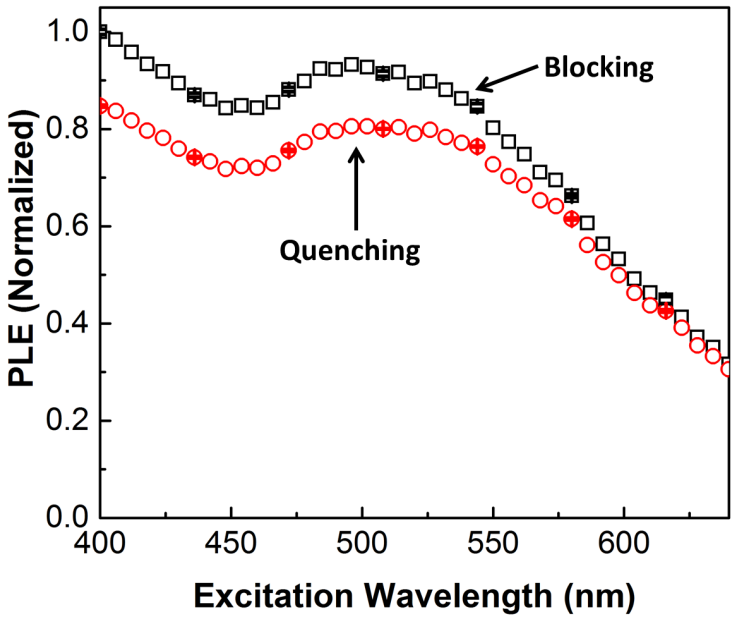

Figure 5.4: Photoluminescence excitation (PLE) spectral intensity of an 8 nm thick C_{60} interlayer between an 80 nm thick C_{70} and an 8 nm thick blocking (BPhen) or quenching (NPD) cap layer. Samples were excited at $\theta = 30$ from normal, and the PLE was detected at 60 from normal. Emission was measured at $\lambda = 685$ nm, corresponding to the peak of the C_{70} singlet exciton absorption.

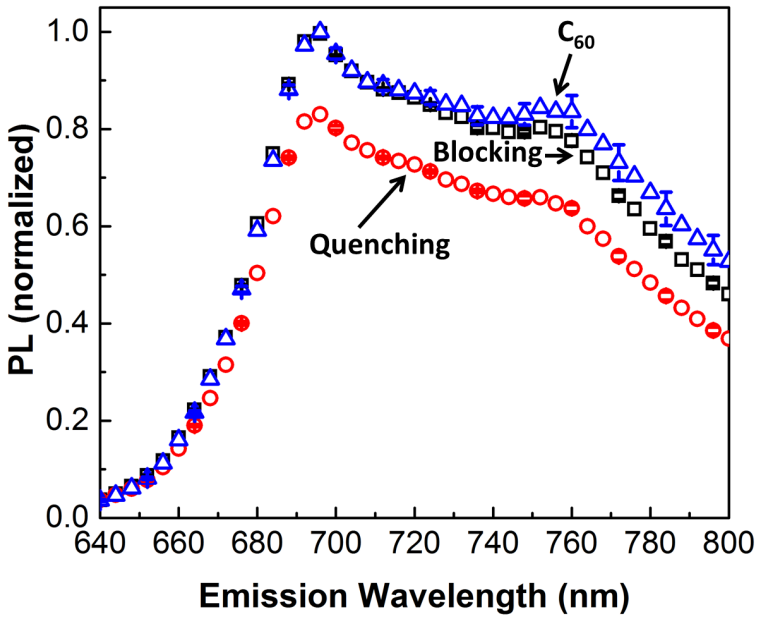

Figure 5.5: Photoluminescence (PL) spectra used to calculate the C_{60} exciton blocking efficiency by C_{70}, yielding $\phi = 62 \pm 6\%$. Samples were comprised of a 80 nm thick C_{70} layer capped with an 8 nm thick blocking (BPhen) or quenching (NPD) layer, or a 20 nm thick C_{60} cap. Samples were excited at $\lambda = 540$, where C_{70} has strong absorption and C_{60} does not.

5.6 Conclusion

In conclusion, we found that the source of the energy transport in optically-excited C_{60} films originates from the generation of singlet excitons. Measurements made using fits to the EQE of OPVs and those using spin-dependent SR-PLQ measurements give L_D = 32 $\pm$ 2 nm and L_D = 36 $\pm$ 2 nm, respectively. We have extended the application of SR-PLQ by employing C_{70} as a fluorescent sensitizer for C_{60}. This led to measurements of the energy offset between the two materials, where we found that the HOMO-LUMO energy gap of C_{60} is 18 $\pm$ 5 meV greater than for C_{70}. We have also developed techniques to include the effects of partially blocking or quenching interfaces on exciton diffusion between materials with only minor differences in HOMO-LUMO energy gaps, but with different L_D and τ. These techniques expand the class of structures that can be used to accurately determine these fundamental materials parameters, such as devices incorporating partially blocking buffer layers such as molybdenum oxide (MoOx).

CHAPTER 6

Surprisingly High Conductivity and Efficient Exciton Blocking in Fullerene:Wide-Energy-Gap Small Molecule Mixtures

6.1 Effects of Mixed Buffer in Devices

Exciton confinement in the active regions of OPVs provided by a blocking layer between the cathode and electron acceptor is a necessary element for achieving high solar power conversion efficiency. The blocker serves four functions: (i) confinement of excitons within the active layer to prevent quenching at the organic/cathode interface,[212,213] (ii) prevention of damage to the acceptor layer during the deposition of the cathode,[213,214] (iii) provision of a transparent spacer to optimize the optical field distribution within the active layer,[215] and (iv) promotion of efficient charge extraction following exciton dissociation in the active region. Multiple types of blockers have been developed, with the major differences being the mechanism for charge conduction. The most effective means for achieving confinement is the double heterojunction,[172] where a cathode-side organic buffer layer forms a blocking, nested (Type I) heterojunction with the acceptor. A wide, highest occupied molecular orbital (HOMO)-lowest unoccupied MO (LUMO) energy gap material such as BCP[212,213] or BPhen[216,217] with a LUMO energy significantly smaller than that of the acceptor layer can transfer charge through defect states induced during metal deposition.[172] Materials such as 3,4,9,10 perylenetetracarboxylic bisbenzimidazole (PTCBI) and 1,4,5,8-napthalene-tetracarboxylic-dianhydride (NTCDA) conduct electrons along LUMOs that align with those of the acceptor.[191] In contrast, tris-(acetylacetonato) ruthenium(III) [$Ru(acac)_3$] and related compounds with very shallow HOMO levels conduct holes from the cathode that recombine with electrons from the acceptor layer at the buffer/acceptor interface.[218,219]

The recently developed mixed buffer[170,220] that is comprised of an electron conducting

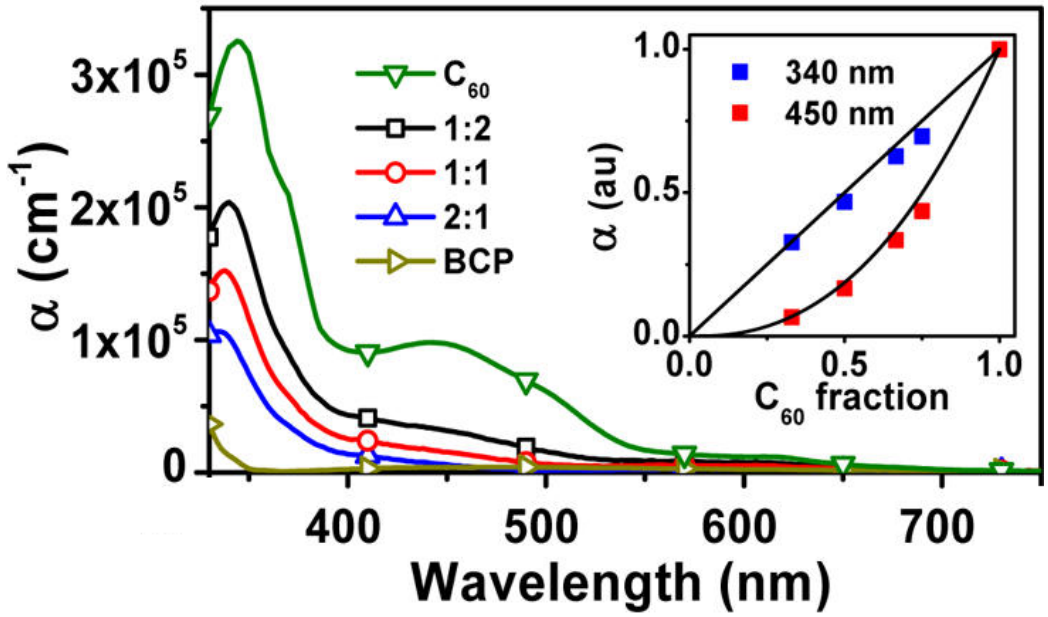

Figure 6.1: Absorption of various C_{60}':BCP blends. Inset: Absorption at the Frenkel absorption peak (340 nm) and the CT peak (450 nm). Frenkel absorption corresponding to an exciton on a single C_{60} molecule drops off linearly with concentration, while CT absorption drops off with power-law dependence with an exponent of 2.7 ± 0.1. This implies that the formation of the CT excitons involves two to three molecules, in agreement with previous studies.[209,221] Figure adapted from[220]

fullerene (e.g. C_{60}) blended into a wide HOMO-LUMO energy gap material such as BPhen or BCP uses a fourth mechanism. The fullerene provides conductive pathways through the wide gap, insulating material which, in turn, blocks (or filters) excitons. This leads to improved charge transport compared to pure wide energy gap materials while still maintaining most of the blocking characteristic of such materials.

Transparency is also required in a good buffer material. Absorption in C_{60} above 400 nm is due to a CT exciton, with the first allowed Frenkel transition occurring at 340 nm.[209] The absorption of CT excitons falls off superlinearly with dilution, as it requires multiple C_{60} molecules in proximity to form. As shown in Fig. 6.1, the 1:1 buffer is nearly transparent above 400 nm. The Frenkel peak falls off linearly, as expected from a single-molecule exciton, while the CT absorption at 450 nm falls off with power law dependence x^m, where x is the C_{60} volume fraction and $m = 2.7 \pm 0.1$ (Fig. 6.1 inset). This indicates that absorption into the CT exciton involves two to three molecules, and that dilution of C_{60} is sufficient to render it transparent enough to serve as a buffer material.

Initial work in devices focused on the effects of the mixed buffer in planar structures. The performance of devices using a 1:1 BCP:C_{60} mixed buffer was compared to pure layers

of the conventional blockers BCP[222] or PTCBI[89] as well as to layers of the compound buffer capped with a thin layer of either BCP or PTCBI.[191] Active layers in these devices were composed of DPSQ and C_{60} (Fig. 6.2 (a)), with the DPSQ spincoated on the substrate and all other layers deposited through VTE. The devices were then solvent-vapor annealed after deposition of the C_{60} but before deposition of the buffer layer.[89]

The current-voltage characteristics of the devices are shown in Fig. 6.2(b) with the device parameters given in Table 6.1. The mixed buffer alone had equivalent efficiency to the pure buffer devices ($4.8 \pm 0.2\%$ for all three), while adding a thin layer of a pure buffer on top of the mixed buffer resulted in higher efficiency devices. That is $PCE = 5.3 \pm 0.2\%$ and $PCE = 5.0 \pm 0.2\%$ for a top layer of PTCBI and BPhen, respectively. The top layer of pure buffer protects the C_{60} in the mixed buffer from being damaged by the deposition of the metal electrode.

The improvement in the DPSQ/C_{60} planar devices is attributed to a reduction in exciton-polaron quenching[223] in the neat C_{60} active layer. It has been previously shown that large-energy gap conductors such as BCP have poor conductivity, leading to charge pile-up at the C_{60}/BCP interface.[220,224] The resulting large charge population in the C_{60} then quenches excitons, reducing photocurrent.

The mixed buffer serves to reduce exciton-polaron quenching by spatially segregated excitons and polarons. Excitons have a difficult time diffusing into the mixed buffer, as they cannot transfer to the high-energy gap material. The mixed buffer therefore has a smaller density of sites which excitons can hop to, encouraging diffusion back into the active layer. In contrast to neutral excitons, free charges experience a driving force from the internal field of the device that pushes them into the conductive pathways of C_{60} in the buffer. Charges therefore easily migrate into the mixed buffer, reducing the steady-state charge population in the active layer and therefore the amount of exciton-polaron quenching. This explains the improvement in photocurrent from 7.6 ± 0.2 mA/cm^2 and 7.1 ± 0.2 mA/cm^2 in the pure PTCBI and BCP devices, respectively, to 8.1 ± 0.2 mA/cm^2 and 8.3 ± 0.2 mA/cm^2 in the mixed buffer capped with PTCBI and BCP devices, respectively.

The effects of the mixed buffer on charge extraction was further examined through the use of biased EQE. Negative bias across an OPV enhances charge extraction, so the ratio of the EQE taken at 0 V and at negative bias provides a relative measure of the efficiency of charge extraction. As seen in Fig. 6.2(c), the large difference in the pure buffer devices between 0 V and -1 V bias is a clear signal of poor charge extraction, while the optimized mixed buffer device remains almost constant with bias indicating much more efficient charge extraction.

The difference in ratio between long and short wavelengths in biased EQE is then a

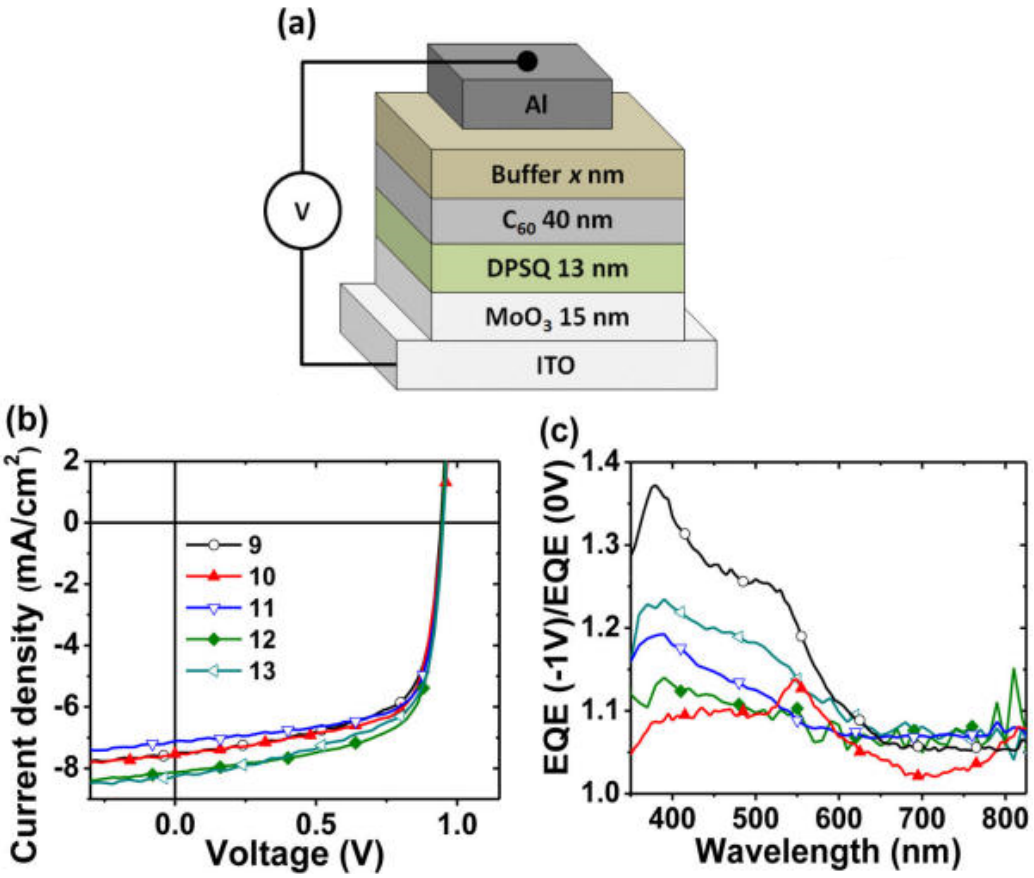

Figure 6.2: Performance of planar heterojunction DPSQ/C_{60} devices using the structure shown in (a). Buffers used were: (9) 10 nm BCP; (10) 10 nm BCP:C_{60}; (11) 10 nm PTCBI; (12) 10 nm 10 nm BCP:C_{60} / 5 nm PTCBI; (13) 10 nm BCP:C_{60} / 5 nm BCP. (b) Current-voltage characteristics of devices under one sun, AM1.5G illumination. (c) Ratio of EQE of devices at -1 V bias to its value at 0 V bias for devices with architectures as in (b). Figure adapted from[220]

characteristic sign of exciton-polaron quenching in the C_{60} layer in the pure buffer devices. The acceptor C_{60} absorbs mostly in the blue while the donor DPSQ absorbs in the red. Shorter-wavelength illumination then primarily measures the effect of the mixed buffer on the C_{60} exciton population, while longer-wavelength illumination measures the effect on the DPSQ exciton population. Devices incorporating BCP show the largest difference between long and short wavelengths, a sign of the expected exciton-polaron quenching in C_{60} caused by the poor charge transport characteristics of the BCP. The mixed buffer/PTCBI device, in contrast, was almost flat with bias, indicating that the combination of the mixed buffer with the good conductor PTCBI almost completely eliminated exciton-polaron quenching. Even the mixed buffer device incorporating a pure BCP layer showed improvement over the pure BCP device, showing that the mixed buffer helps to spatially segregate charges and excitons.

Device	J_{sc} (mA/cm^2)	V_{OC} (V)	FF	PCE (%)
9	7.5 ± 0.2	0.95 ± 0.1	0.65 ± 0.1	4.8 ± 0.2
10	7.6 ± 0.2	0.95 ± 0.1	0.66 ± 0.1	4.8 ± 0.2
11	7.1 ± 0.2	0.95 ± 0.1	0.71 ± 0.1	4.8 ± 0.2
12	8.1 ± 0.2	0.95 ± 0.1	0.68 ± 0.1	5.3 ± 0.2
13	8.3 ± 0.2	0.95 ± 0.1	0.64 ± 0.1	5.0 ± 0.2

Table 6.1: Device characteristics of planar DPSQ/C_{60} devices with varying buffers. Buffers used were: (9) 10 nm BCP; (10) 10 nm BCP:C_{60}; (11) 10 nm PTCBI; (12) 10 nm 10 nm BCP:C_{60} / 5 nm PTCBI; (13) 10 nm BCP:C_{60} / 5 nm BCP.

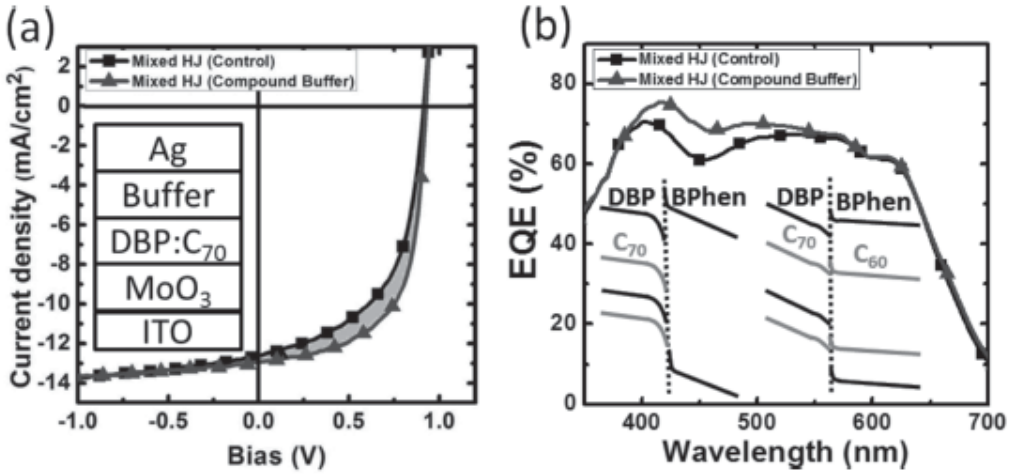

Figure 6.3: Performance of mixed heterojunction DBP/C_{60} devices using the structure shown in (a), inset. a) Spectrally-corrected current-voltage characteristics under 1 sun AM1.5G illumination. Shaded region indicates the difference in FF between the two cells. b) EQE spectra fore the two cells. b), inset: Diagrams of energy levels at the DBP:C_{70}/buffer interface, with the neat BPhen buffer on the right and the mixed buffer on the left. Figure adapted from[170]

The mixed buffer has also been tested in mixed heterojunction devices, with the current-voltage characteristics and EQE shown in Fig. 6.3.* As can be seen, the mixed buffer led to an improvement in both FF and J_{SC}.

Unlike in the planar devices, the improvement in mixed heterojunctions cannot be attributed to a reduction in exciton-polaron quenching. All excitons in a mixed heterojunction are generated adjacent to the heterojunction and therefore dissociate almost instantly, meaning the steady-state exciton population is essentially zero.[100] As the rate of exciton-polaron quenching follows $n \cdot n_c$, where n is the exciton density and n_c is the charge density

*These devices used BPhen as the wide-energy gap material instead of the BCP used in planar devices. The two materials are chemically similar and had equivalent results in devices, with the switch to BPhen occurring because of its reduced tendency to crystallize in comparison to BCP.

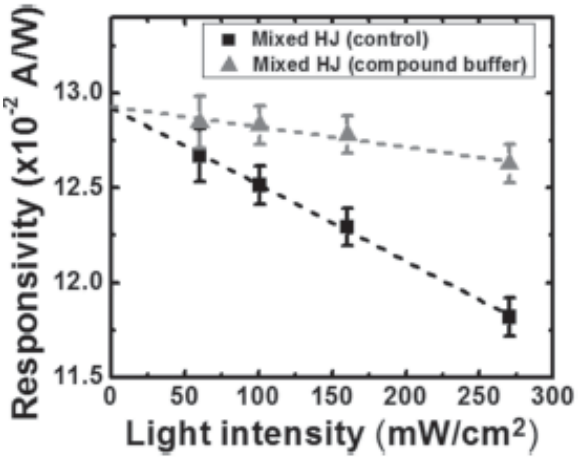

Figure 6.4: Responsivity vs. illumination intensity for the DBP:C_{70} cells using either a pure BPhen layer (control) or the mixed buffer. Dashed lines indicate linear fits according to bimolecular recombination theory. Figure is from[170]

(see section 3.4.2.2), the effect is negligible.

The improved device characteristics in mixed heterojunctions are instead attributed to a reduction in bimolecular recombination.[225,226] Previous studies have shown that energy bending occurs at the fullerene/BPhen interface, leading to charge pile-up at the interface and a large potential drop (Fig. 6.3(b), left inset). This leads to a reduced field across the heterojunction, increasing the charge extraction time and therefore the residence time for holes and electrons in the mixed heterojunction. This allows more time for the free charge carriers to recombine, reducing the photocurrent. This effect is most pronounced as the applied bias is increased towards V_{OC}, reducing the internal field. The higher conductivity of the mixed buffer results in improved charge extraction from the mixed heterojunction, causing less charge pile-up and therefore a smaller potential drop at the interface (Fig. 6.3(b), left inset). This in turn leads to reduced bimolecular quenching and the improved device characteristics shown in Fig. 6.3 (a) and (b).

The role of bimolecular recombination is further investigated by examining the responsivity of the mixed heterojunction cells $R = J_{SC}/I$ with respect to illumination intensity I. Both cells display a monotonic decrease in R with I, with the control cell decreasing from $R = (12.7 \pm 0.4) \cdot 10^{-2}$ A/W at $I = 0.6$ sun to $R = (11.8 \pm 0.3) \cdot 10^{-2}$ A/W at $I = 2.7$ suns. The mixed buffer cell, in contrast, showed a decrease of only 0.002 A/W over the same intensity range (Fig. 6.4). In general, $J_{SC} = J_G - J_{MM} - J_{BM}$, where J_G is the photogenerated current and J_{MM} and J_{BM} are the current lost to monomolecular and bimolecular recombination, respectively. Both J_G and J_{MM} are linearly proportional to I while $J_{BM} \propto \beta I^2$, where β is a constant. Device responsivity therefore goes as

$R = J_{SC}/I = R_0 - \beta I$, where R_0 is the device responsivity in the absence of bimolecular recombination. Linear fits to this equation (Fig. 6.4, dashed lines) show both devices to have the same $R_0 = 12.9$ A/W, implying they have the same responsivity in the absence of bimolecular recombination. However, β for the control cell is four times larger than that of the mixed buffer cell, showing that bimolecular recombination is reduced by an equivalent amount in the mixed buffer cell. The enhanced conductivity of the mixed buffer results in approximately a 50% decrease in both hole and electron population in the mixed heterojunction, resulting in less current lost to bimolecular recombination and therefore a higher FF and J_{SC}.

New applications for the mixed buffer continue to be developed. It has been used in highly-efficient planar-mixed DBP/C_{70} devices,[170] improving the efficiency from $7.1 \pm 0.3\%$ with a pure BPhen layer to $8.1 \pm 0.4\%$. It has also been shown to serve as a good intermediate buffer layer between the two cells of a tandem device, being more transparent than the PTCBI previously used for that purpose. Given the broad application of the mixed buffer, a deeper physical understanding is desired and will be covered in the following sections.

6.2 Monte Carlo Simulation of Mixed Buffer Properties

Further attempts to understand the reasons for the mixed buffer's effectiveness begin with Monte Carlo simulations of charge and exciton transport through the layer. The simulations represent the physical structure of the BPhen:C_{60} mixed buffer as a 3-D random distribution of available (C_{60}) and unavailable (BPhen) sites for transport on an isoenergetic cubic lattice, adjacent to a layer of pure C_{60}. The edges of the simulated region perpendicular to the C_{60} / mixed buffer interface obey periodic boundary conditions, while the boundary conditions of the remaining interface of the C_{60} and mixed buffer layers vary between the exciton and charge simulations. A characteristic portion of the simulated region is shown in Fig. 6.5, inset.

Simulations of exciton transport use a blocking condition for the back C_{60} interface and a semi-infinite layer of mixed buffer. Excitons were randomly generated in the pure C_{60} film and allowed to diffuse in a random walk through nearest-neighbor hopping. Each exciton was run through 2000 steps before the final position was recorded, with exciton-exciton interactions neglected. Any exciton that attempts to transfer onto a BPhen molecule instead remains in place for that step. The final positions of the excitons are then summed and displayed with respect to position along the C_{60} / mixed buffer interface normal.

Sample results from the Monte Carlo simulations are shown in Fig. 6.5. For a junction

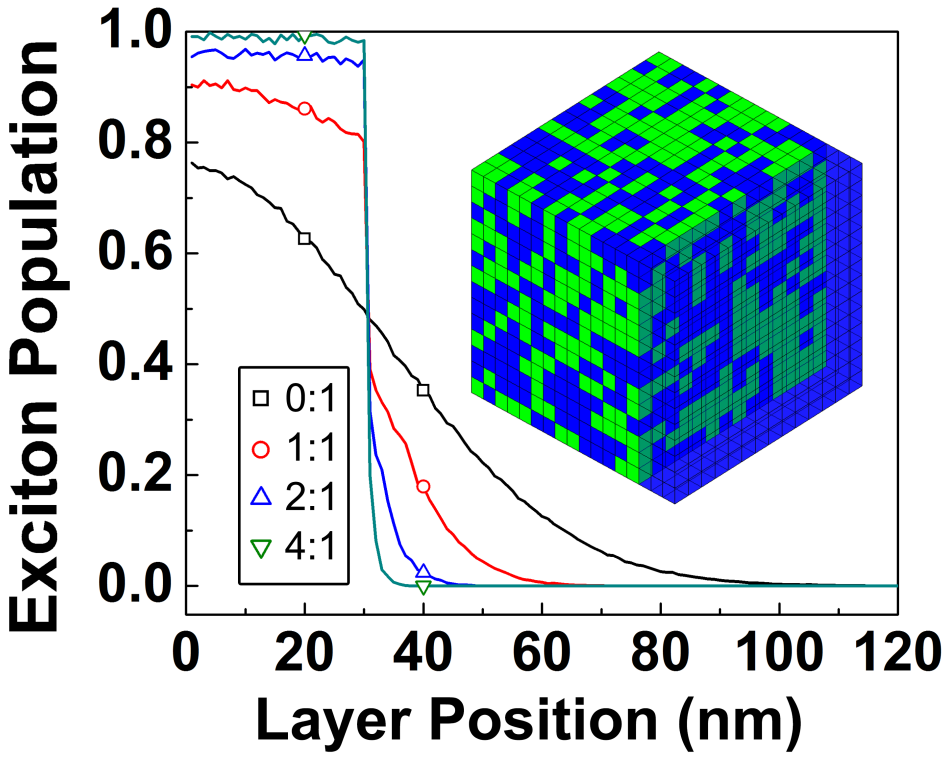

Figure 6.5: 3-D Monte Carlo simulation of exciton diffusion from neat C_{60} into BPhen:C_{60} blend layer. The neat C_{60} (0:1) blocks 50% of the excitons, the 1:1 ratio blocks approximately 81%, the 2:1 ratio blocks $\sim 95\%$, and the 4:1 ratio blocks $\sim 98\%$ of the excitons. The blocking efficiency is defined as the ratio of the exciton population at the interface to the population expected for an ideal blocking layer, and all data are normalized to this value. Inset: 3D illustration of the 1:1 mixed layer used in the simulation. Green denotes BPhen, blue is C_{60}. The neat C_{60} acceptor layer is shown as the semi-transparent region on the front right edge of the blend.

between two materials with equal site densities, the final population at the interface is half way between a perfect blocker and a perfect quencher (i.e. zero population at the interface) and corresponds to 50% blocking. In the case of a 1:1 mixture of BPhen:C_{60}, which corresponds to the case of a Frenkel exciton of C_{60} approaching an evenly mixed buffer, the mixed layer is 81% efficient at blocking excitons.. For a 4:1 mixture of blocking to transport sites, which corresponds to a CT exciton approaching a 1:1 C_{60}:BPhen mixture, the interface is 98% blocking, showing that a seemingly porous interconnected mixed layer can indeed act as an efficient exciton blocking layer.

Charge transport simulations examined the transit time of charges through the mixed buffer. Charges were injected into the pure C_{60} layer and allowed to diffuse through random walk nearest-neighbor hopping until they were collected on the far side of the mixed buffer

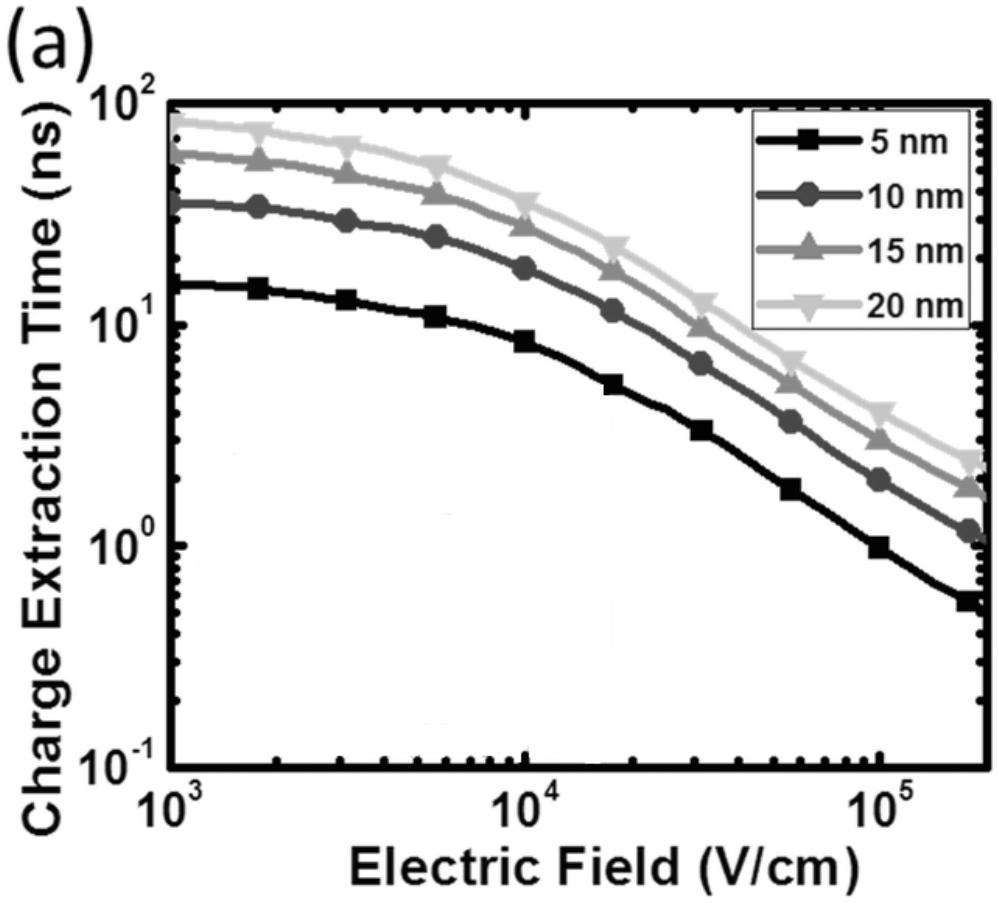

Figure 6.6: 3-D Monte Carlo simulation of charge transport through a BPhen:C_{60} blend layer. Data shows the median charge extraction time with respect to applied electric field for several thicknesses of the 1:1 mixed buffer.

and their transit time recorded. The Miller-Abrahams approximation (Eq. 2.24) was used to weight the relative hopping probabilities for different directions under an applied electric field and charge-charge interactions were neglected. The median transit time for charges under a range of applied electric fields passing through a layer with a given mixing fraction was then used to calculate the mobility of the layer from the relationship between extraction time and applied electric field, normalized by setting the zero-field mobility of electrons in the neat C_{60} layer to the experimental value of $5.1 \cdot 10^{-2}$ cm^2 / V $\cdot$ s.[227]

Results are shown in Fig. 6.6. For the 1:1 mixed buffer, used in devices, the model predicts an effective mobility of $4.7 \cdot 10^{-3}$ cm^2 / V $\cdot$ s, only one order of magnitude less than that of pure C_{60}. This is in comparison to the significantly lower mobility of $1.9 \cdot 10^{-5}$ cm^2 / V $\cdot$ s for pure BPhen.[228] The relatively low mobility of BPhen then leads to the charge

pile-up at the buffer / active layer interface that promotes quenching.

6.3 Experimental Characterization

In this section, we quantitatively investigate the physical mechanisms of conduction and exciton blocking by the compound blocker using a combination of photoluminescence (PL) quenching,[138,198] transient photocurrent,[229–231] resistivity, conductive atomic force microscopy (conductive-tip atomic force microscopy (cAFM)) and x-ray diffraction (XRD) measurements. We find that the compound buffer is greater than the sum of its parts, with the C_{60} and BPhen contributing to the current transport and exciton blocking characteristics of the buffer to a degree that is strikingly greater than their mixing fraction would suggest. A 1:1 (by volume) BPhen:C_{60} mixed buffer blocks 84±5% of the excitons incident from the active layer, which is only a slight decrease from that of a neat BPhen layer. The resistance of the compound buffer remains more than an order of magnitude lower than pure BPhen even at a very high (¿80%) BPhen fractions, implying that nanoscale phase segregation in the C_{60} allows it to conduct charges over the entire range of mixing fractions.[232–236] Electron transport through the compound buffer is non-dispersive, which is qualitatively different from conduction through neat BPhen. The improved charge transport properties of the compound buffer combined with efficient blocking characteristics leads to the increased efficiency for both planar and mixed active layer OPVs.

The exciton population in an organic semiconductor is modeled using the steady-state diffusion equation[172] (Eq. 2.18). This equation is the basis of spectrally-resolved photoluminescence quenching (SR-PLQ),[138,198] a method to measure the L_D of a photoluminescent material. This technique uses two identical films of the material, one capped with a blocking layer (with boundary condition $\frac{\partial n}{\partial x}|_{x=0} = 0$) and the other with a quenching layer (with $n(0) = 0$). For an exponentially decaying $G(x)$ in the absorbing layer, the ratio, η, of the photoluminescence of the optically pumped sample capped with a blocking (B) layer to that with a quenching (Q) layer is: [138,198]

$$\eta(\lambda) = \frac{PL_B}{PL_Q} = \alpha\prime(\lambda)L_D + 1 \tag{6.1}$$

where $\alpha\prime = \frac{\alpha}{cos(\theta_r)}$ is the absorption coefficient of the active region at wavelength λ, corrected for the propagation angle, θ_r, in the layer as measured from normal incidence. The slope of η vs. $\alpha\prime$ in Eq. 6.1 gives the exciton diffusion length. This method has been extended to optically thin films through the use of transfer matrices to calculate $G(x)$.[198]

For a perfectly quenching interface, $n(0) = n_Q = 0$, whereas for a perfect blocker,

$n_0 = n_B$. Intermediate between these extremes is the non-ideal interface characterized by its blocking efficiency, ϕ, such that $n_{NI} = \phi \cdot n_B$, where n_{NI} is the exciton density at the non-ideal interface. In this case, Eq. (2) becomes:

$$\eta(\lambda) = \frac{PL_{NI}}{PL_Q} = \phi\alpha\prime(\lambda)L_D + 1 \tag{6.2}$$

Here, $\phi = 1$ for a perfectly blocking interface and $\phi = 0$ for a perfect quencher. If L_D is known, ϕ can be directly measured. If the PL from three different samples capped with a blocker, a quencher, and a non-ideal blocking/quenching layer is measured, then both ϕ for the non-ideal blocker and L_D for the luminescent material can be independently determined.

Traditional descriptions of charge transport in semiconductors assume that the hopping time of a carrier is small compared to its transit time through the material. A narrow charge packet injected into one side of a film will then travel at a constant velocity characterized by the carrier mobility with a time-dependent Gaussian spread in the packet as predicted by the central limit theorem. In contrast, dispersive transport occurs when the hopping time is on the order of the transit time so a small number of hops can drastically change the transit time for a given charge.[237,238] The central limit theorem is therefore no longer applicable, as it requires a large number of independent random events, and the spread in the charge packet becomes non-Gaussian. Dispersive transport is characterized by a time-dependent mobility that is generally lower than for the case of non-dispersive transport.

The current response in the dispersive limit where charges are injected with a delta- or step-function shape is:

$$I(t) \propto \begin{cases} t^{-(1-\beta)}, & t < t_c \\ t^{-(1+\beta)}, & t \geq t_c \end{cases} \tag{6.3}$$

where t_c is the transit time across the layer, and β is an empirical factor in the domain $\{0, 1\}$. This behavior is in contrast to the exponential decay of the current as expected for non-dispersive transport.

In the mixed conductor (C_{60})/insulator (BPhen) blends, it is useful to determine whether or not there is phase separation that will affect the conductive properties of the material. For this purpose, we examine the distribution of the current based on its autocorrelation function, a method that is useful in identifying spatial order. For a 2-D current map of current density, $j(r)$, the autocorrelation function is defined as:[239–241]

$$C(r) = \int j(r\prime)j(r\prime + r)dr\prime \tag{6.4}$$

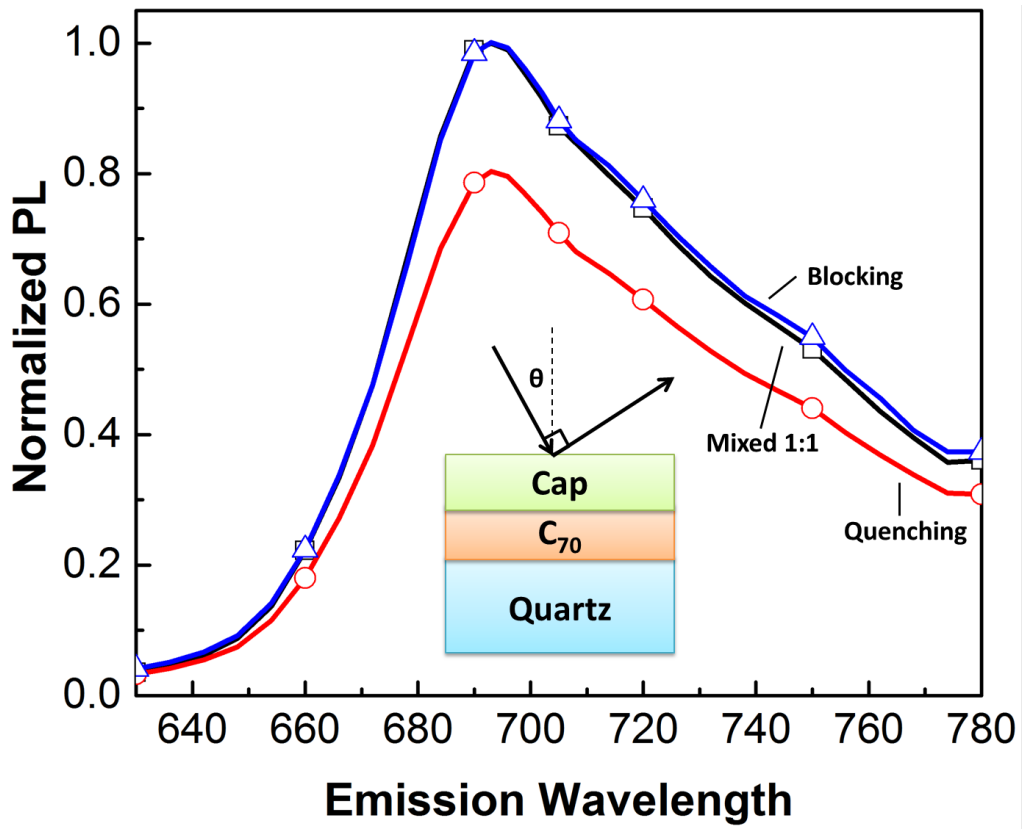

Figure 6.7: photoluminescence (PL) intensity from an 80 nm thick C_{70} layer capped with an 8 nm thick layer of BPhen (exciton blocking), 8 nm thick NPD (quenching), or a 20 nm thick 1:1 BPhen:C_{60} compound buffer. The blocking efficiency, ϕ, is calculated from the PL intensity relative to the blocking and quenching caps. Although the compound buffer sample PL overlaps that of the blocking sample, it corresponds to $\phi = 84 \pm 5\%$ instead of 100% due differing optical fields in the two samples. Inset: Sample structure used for PL measurements. Samples were excited at a wavelength of 540 nm, at an incidence angle θ=30° and measured at θ=60°.

Here, r is the separation between any two points in the image. In a completely random distribution, $C(r)$ is a constant independent of separation. The autocorrelation function may, therefore, be used to look for phase segregation in a current map of a conductor-insulator blend such as used in the compound buffer.

All materials were deposited by thermal evaporation in high vacuum (base pressure $< 10^{-7}$ torr), with DBP[100] and the fullerenes purified once by vacuum thermal gradient sublimation.[172] For PL measurements, films were grown on quartz substrates with all deposition rates and thicknesses monitored with a quartz crystal microbalance. Layer thicknesses and optical constants of the thin films were measured by ellipsometry. The sample structure was quartz/C_{70} (80 nm)/cap layer, where the cap was either a BPhen (8 nm) blocker, an NPD (8 nm) quenching layer, or a C_{60}:BPhen mixed buffer (20 nm). Excitons freely

diffuse between the identical energy levels of the two fullerenes,[209] but C_{70} has a longer wavelength absorption cutoff than C_{60} due to its reduced molecular symmetry,[199].[199,200] The sample is excited at $\lambda = 540$ nm where C_{60} has minimal absorption, resulting in a step function excitation profile within the C_{70}, decreasing to zero at the interface with C_{60}.

The C_{70} for all samples with various cap layers was simultaneously deposited to ensure consistency. The C_{70} PL was monitored at the emission peak wavelength of $\lambda = 685$ nm for several minutes prior to data acquisition in a N2 atmosphere to check for degradation. Samples were illuminated through the capping layer at an incident angle of $\theta = 30°$, and PL was collected at 90° to the excitation beam, also through the cap. Data were fit to the PL ratios obtained from Eq. 2.18 using optical transfer matrices to account for interference effects and the absorption of the various layers.

The OPVs have the structure: glass / ITO / MoOx (10 nm) / DBP:C_{60} 1:8 (54 nm) / buffer / Ag (100 nm), where the buffer is either 8 nm BPhen or 10 nm BPhen:C_{60}/5 nm BPhen. Prior to film deposition, the glass/ITO substrates were cleaned in a sequence of detergent in deionized water, acetone and isopropanol for 10 min each, followed by ultraviolet-ozone exposure for 10 min. The 2 mm^2 device area was defined by the intersection of patterned ITO on the substrate and by the Ag cathode deposited through a shadow mask. Devices were encapsulated in a glass/epoxy/glass package in a high purity N_2 atmosphere to protect them from atmospheric exposure during transient photocurrent measurements.

Device efficiency was measured as described previously.[100] The transient photocurrent was obtained with a Textronix TDS 3054B oscilloscope using a 50 Ω termination, and excited by a Thorlabs $\lambda = 530$ nm light emitting diode driven by 100 s pulses from an impedance-matched HP 8114A pulse generator. The pulse duration was sufficiently long to allow the device to reach steady-state.

Samples used for measuring film resistivity consisted of an array of devices with the structure glass/ITO/100 nm Ag/10 nm PTCBI/100 nm buffer /10 nm BPhen/120 nm Al. The 1 mm diameter circular devices were defined by deposition of the Al cathode through a shadow mask. Also, PTCBI was placed beneath the Ag contact due to its deep LUMO energy.[191] Current-voltage characteristics were measured in a high purity N_2 atmosphere. The voltage was scanned in both the forward and reverse directions and no evidence for hysteresis was observed. Resistivity was calculated from the ohmic region between ± 0.15 V.

Layers of the mixed C_{60}:BPhen buffer used for cAFM were deposited on a glass substrate coated with ITO and a 10 nm polyethylenimine, ethoxylated (PEIE) film to provide an electron injecting contact. The cAFM measurements were obtained using an Asylum

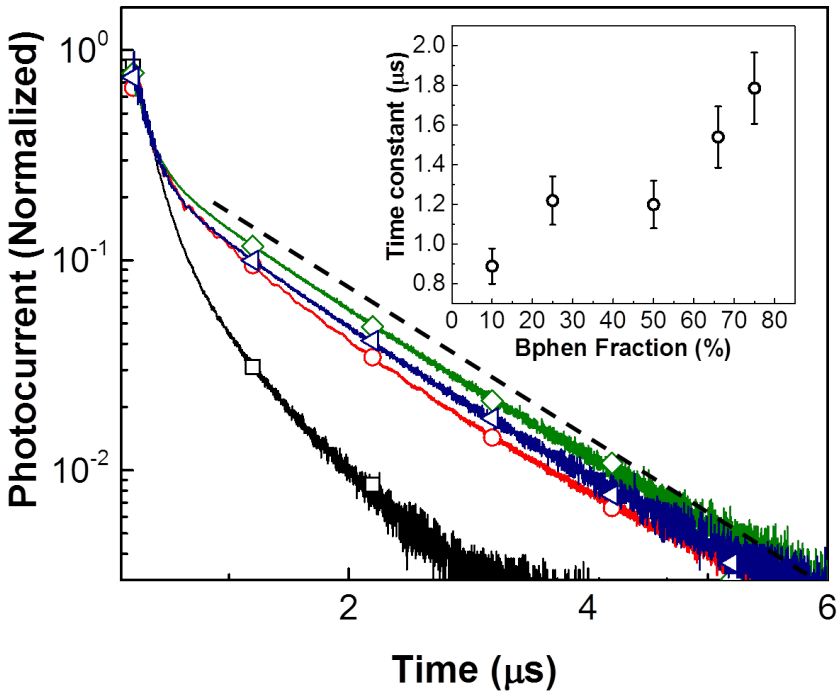

Figure 6.8: Photocurrent vs. time (t) of an ITO / 10 nm MoOx / 54 nm DBP:C_{60} 1:8 / buffer / 100 nm Ag organic photovoltaic (OPV) cell following the end of a 530 nm wavelength optical pulse. The buffer was either an 8 nm thick BPhen, or a 10 nm thick compound buffer capped with 5 nm BPhen to protect the underlying layer from damage during metal deposition. Current for the neat BPhen buffer (black squares) follows t^{-2}, indicative of dispersive transport. All compound buffer BPhen fractions (25%, blue triangles; 50%, green diamonds; 90%, red circles) show an exponential decay transient (indicated by the dashed line as a guide to the eye), suggesting dispersive transport. Inset: Time constants of exponential transient photocurrent decay versus BPhen fraction.

Research MFP-3D stand-alone AFM under ultrapure Ar. A Pt-Ir 5-coated atomic force microscopy (AFM) probe (Nanosensors, ATEC-CONTPt, spring constant 0.2 N/m) was used as the top electrodes for contact-mode measurements, allowing for simultaneous determination of both topography and current. The contact force was ∼10 nN. X-ray diffraction data were obtained in the Bragg-Brentano configuration for 200 nm thick organic layers deposited on sapphire substrates. Data were recorded in 0.04° steps at 30 s/degree.

Example scans for SR-PLQ measurements are shown in Fig. 6.7 for the structure in Fig. 6.7, inset. The data were used to calculate ϕ using Eq. 6.2, and compared to those predicted by previously-reported Monte-Carlo simulations of exciton transport in the compound buffer[220] (see Table 1). We find that neat C_{60} has $\phi = 50 \pm 2\%$ (consistent with absorption only in C_{70} due to the pump at $\lambda = 540$ nm) compared with 100% for BPhen.

% BPhen	Predicted Blocking Efficiency (%)	Blocking Efficiency ϕ Relative to Blocker (%)	Blocking Efficiency ϕ Relative to Quencher (%)
0	50	50 ± 2	46 ± 2
25	63	76 ± 3	69 ± 11
50	81	84 ± 5	82 ± 5
66	95	87 ± 4	87 ± 4
100	100	–	–
NPD	0	–	–

Table 6.2: Comparison of simulated and measured exciton blocking characteristics of the mixed buffer. Pure BPhen and NPD are assumed to be a perfect blocker and quencher, respectively.

A linear interpolation of these two points suggests that 1:1 BPhen:C_{60} would have ϕ = 75%, in contrast to $\phi = 84 \pm 5\%$ observed. Other mixing ratios display the same disproportionately high blocking efficiency. This is explained as follows: The exciton diffuses via a random walk between nearest-neighbor molecules. A BPhen molecule acts as a blocking site in the lattice that prohibits exciton transfer. At the interface between the neat fullerene and the compound buffer, there are therefore only a limited number of possible transfer sites in the buffer compared to sites in the bulk fullerene, efficiently blocking excitons. This is consistent with the physical picture used in Monte Carlo simulations of exciton diffusion into the mixed buffer,[220] and the simulated values match our experimental results in Table 1.

Transient photocurrent measurements are shown in Fig. 6.8. Devices using the compound buffer have qualitatively different characteristics compared to those with a neat BPhen buffer, which showed an inverse power law relationship $I(t) \propto t^{-2}$, corresponding to $\beta = 1$ in Eq. 6.3. This is characteristic of dispersive transport.[237,238] Photocurrent transients from all devices with the compound buffer exhibited exponential decay with time, indicative of non-dispersive transport, with time constants shown in Fig. 6.8 inset.

The PCE at 1 sun AM 1.5G illumination for the OPV used in the transient photocurrent measurements is shown in Fig. 6.9 (inset). Devices were 6.6 $\pm$ 0.1% efficient from 1:4 BPhen:C_{60} to 3:1 BPhen:C_{60}, decreasing to 5.9 $\pm$ 0.1% at $> 9:1$ BPhen:C_{60}. The decrease in PCE is due to a reduction in fill factor (FF) from 61% to 57%.

As shown in Fig. 6.9, the resistivity of the compound buffer gradually increases with BPhen fraction, with a sharp jump seen at 100% BPhen as the film becomes insulating. The resistivity of 100% BPhen of $6 \pm 1 \cdot 10^{11}\ \Omega \cdot$cm matches literature values.[242] Just as BPhen has a disproportionate effect on the exciton blocking characteristics of the buffer, C_{60} has a similarly pronounced effect on its charge transport properties. Even at 9:1 BPhen:C_{60}, the

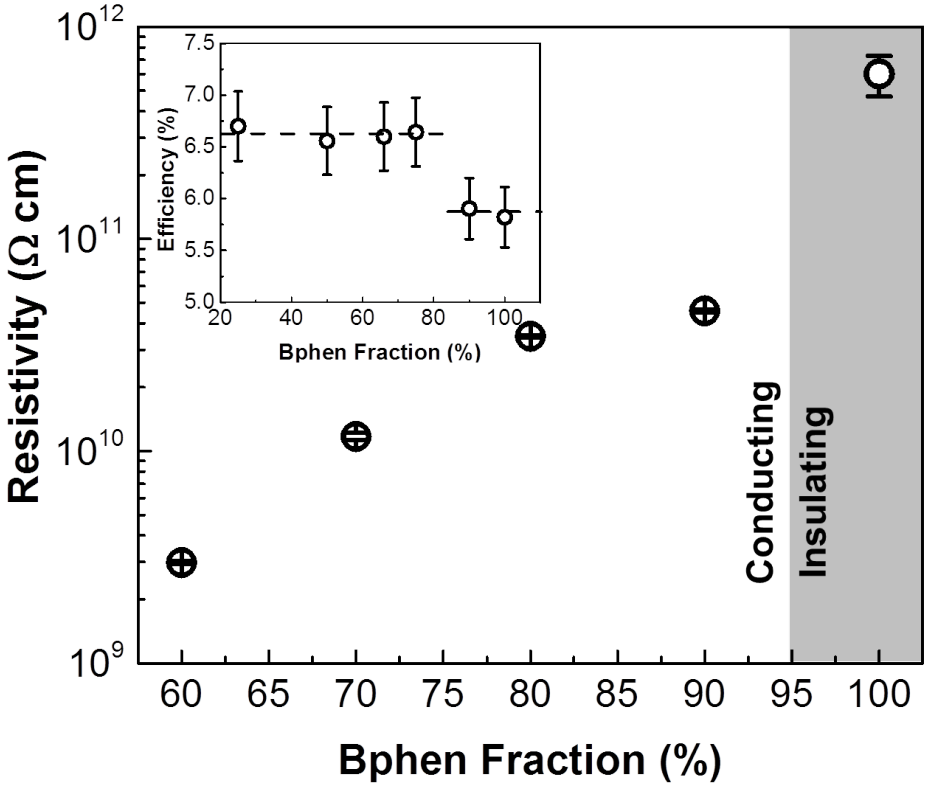

Figure 6.9: Resistivity as a function of BPhen fraction in a 100 nm thick C_{60}:BPhen mixed layer. The resistitivity only increases sharply when all C_{60} is eliminated from the layer, suggesting that the C_{60} forms conductive paths even at 90% BPhen. Inset: Power conversion efficiency of OPVs under 1 sun AM1.5G illumination vs. BPhen fraction in a C_{60}:BPhen buffer. Device efficiency was roughly constant from 20% to 80% BPhen, showing the buffer had efficient exciton blocking and charge extraction over this entire range. Device efficiency decreases at ¿ 80% BPhen, primarily due to a decrease in fill factor from 61±1% to 57±1% due to reduced charge extraction efficiency.

resistance of the buffer is an order of magnitude less than neat BPhen, and the conduction is non-dispersive. This indicates that C_{60} undergoes nanoscale phase segregation that allows it to form conductive paths even at very high BPhen concentrations. This is further supported by the constant efficiency of OPV devices under 1 sun AM1.5G illumination employing the buffers with mixtures ranging from 1:3 BPhen:C_{60} to 4:1 BPhen:C_{60}, as shown in the inset of Fig. 6.9.

2-D current maps of the compound buffer with varying blend ratios obtained by cAFM at an applied bias of -1.0 V are shown in Fig. 6.10. For the 1:2 C_{60}:BPhen buffer the current density data is analyzed using Eq. 6.4. Autocorrelation of the current density vs distance was constant, indicative of a random distribution of conductor and insulator as

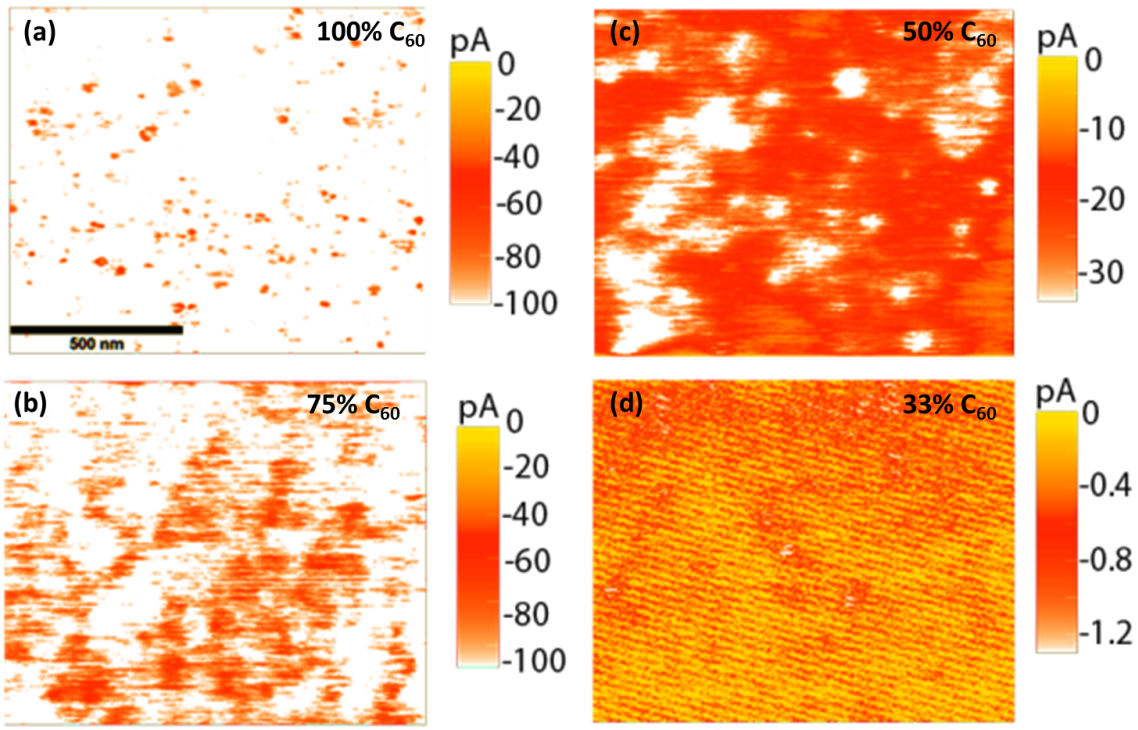

Figure 6.10: conductive-tip atomic force microscopy (cAFM) images of C_{60}:BPhen blends, with (a)100 vol.%, (b) 75 vol.%, (c) 50 vol.%, and (d) 33 vol.% C_{60}, taken at -1.0 V tip bias. The 100% C_{60} samples (a) show only small areas of reduced conduction. As the BPhen concentration is increased, patches of the film become increasingly insulating, until at 33 vol.% C_{60}, conduction occurs only in isolated regions. This change from widespread to isolated conduction is accompanied by a 100X decrease in current.

shown in Fig. 6.11, inset. The transition from conducting C_{60} to mostly insulating BPhen is apparent in Fig. 6.10. The neat C_{60} sample shows bulk conductivity, with only isolated patches of slightly $(20-40\%)$ decreased current. Layers with larger BPhen concentrations show increasingly larger insulating areas, with the 1:2 C_{60}:BPhen mixture showing both a maximum current of 100 times less than pure C_{60}, and conduction only through isolated regions. Layers with lower concentrations of C_{60} were too insulating to be imaged. Phase segregation, if it exists therefore occurs on scales below the cAFM instrument resolution of 10 nm.

We further examined the nanostructure of the mixed buffer using XRD, with scans of three BPhen:C_{60} mixtures shown in Fig. 6.11. Neat C_{60} exhibits peaks corresponding to diffraction from the (002), and (112) crystal planes, with a domain size of 20 nm calculated from the peak Scherer broadening.[243] For 1:1 C_{60}:BPhen, a small peak corresponding to the (112) crystal plane is still visible. The broadened peak indicates that the C_{60} domains

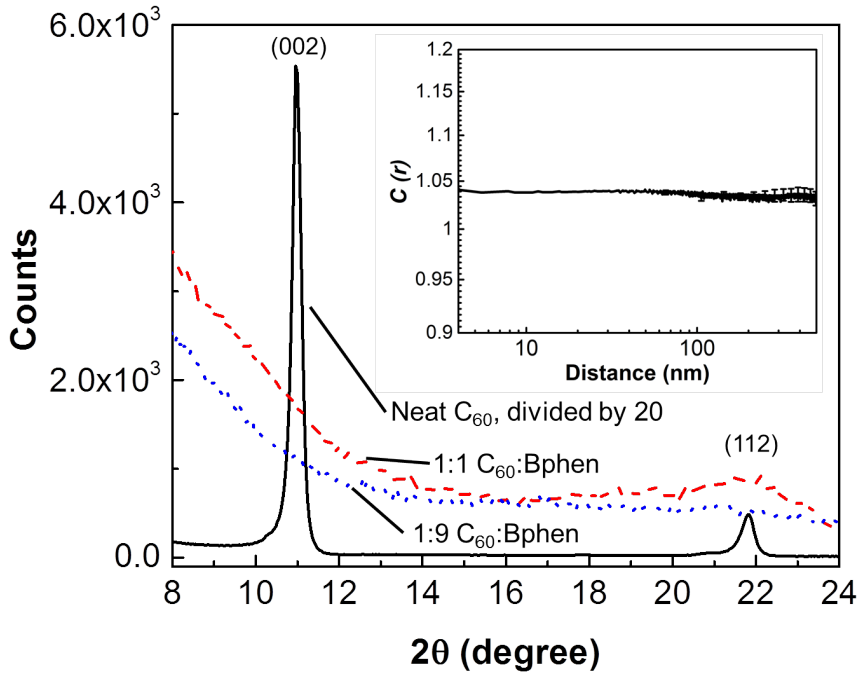

Figure 6.11: X-ray diffraction pattern of 200 nm thick C_{60} (black line, data divided by 20), 1:1 BPhen:C_{60} (red dashed line), and 9:1 BPhen:C_{60} (blue dotted line) films on sapphire substrate taken in the Bragg-Brentano configuration using the Cu-K line. Peaks from the (002) and (112) crystal planes are visible for the neat C_{60} film, with peak widths corresponding to a domain size of 20 ± 1 nm. The 1:1 BPhen:C_{60} compound buffer shows a smaller and wider (112) peak, corresponding to a 3 ± 1 nm domain size. No crystallinity was observed in the 9:1 BPhen:C_{60} buffer. Inset: Averaged values of the current autocorrelation function $C(r)$ vs. distance r of three, 2 m x 1 m 2:1 BPhen:C_{60} conductive-tip AFM images taken at 3 V bias. The magnitude of C(r) is constant over two orders of magnitude of distance, from which we infer a random distribution of BPhen and C_{60} at all length scales. The cAFM spatial resolution is 10 nm.

are only 3 ± 1 nm, which is too small to be imaged by cAFM. When the C_{60} was further diluted in the 1:9 BPhen:C_{60} sample, no XRD peaks are observed. We attribute this to the small quantity of C_{60} that cannot result in observable peaks at our instrumental resolution, although their absence does not rule out the possibility of small-scale phase segregation.

Improved charge extraction through the compound buffer explains the improvement in both mixed and planar heterojunction devices. It has been previously shown that planar heterojunctions with a neat BPhen layer exhibit charge pile-up at the buffer-acceptor interface, resulting in a high steady-state charge density in the active layers, and hence a high rate of exciton-polaron quenching.[224] Exciton-polaron quenching is not present in mixed donor-acceptor heterojunctions due to the drastically reduced exciton concentration, but

inefficient charge extraction in such devices leads to increased bimolecular recombination and a similar loss in device efficiency.[170]

Percolation theory has been extensively applied to understanding the conductivity of disordered conductor-insulator composites.[232–236] The transition point from insulator to conductor is dependent on the crystal structure, with the close-packed BPhen:C_{60} structures expected to have a conducting threshold of $\sim$20% C_{60} concentration.[244–247] Surprisingly, we observe no such threshold in either the transient photocurrent or resistance measurements. This suggests that C_{60} undergoes nanoscale phase segregation when mixed in BPhen, which allows it to form conductive pathways even at extremely low concentrations. As discussed above, autocorrelation analysis of the cAFM scans of the compound buffer shows no ordering, suggesting that phase segregation occurs on a smaller scale than the instrument resolution of 10 nm, which is consistent with the XRD measurements in Fig. 6.11.

For a layer of finite thickness, the threshold concentration for conduction follows:

$$p_c - p_c(L) = AL^{-1.14} \tag{6.5}$$

where p_c is the critical conductor fraction for an infinitely thick layer, $p_c(L)$ is the critical fraction for a layer thickness of L and lattice constant a (assuming a cubic molecular arrangement) $a = 1.1$ nm for[200] C_{60}. Also, A is an empirical constant. For the 10 nm thick compound buffer used in transient photocurrent measurements, $L \sim 9$ Å, and $L \sim 91$ Åfor the 100 nm thick layer used in resistivity measurements. The lack of a transition point at high BPhen concentration is therefore attributed to either nanoscale phase segregation of C_{60}, or large A. For thin layers used in our OPVs, either explanation suggests a high conductivity of the mixed buffer across almost the entire range (80% BPhen) of mixing fractions.

In conclusion, we have examined charge and exciton transport through a compound fullerene:BPhen buffer. We find that BPhen has a disproportionate effect on the exciton blocking characteristics of the buffer for a given mixing ratio. For example, 1:1 BPhen:C_{60} buffer was found to block 84$\pm$5% of incident excitons instead of the 75% expected from a linear interpolation between 0% and 100% BPhen, and other mixing fractions showed a similarly pronounced blocking effect. Indeed, C_{60} was also found to have a disproportionate effect on charge conduction, with non-dispersive transport observed even in 1:9 C_{60}:BPhen layers, which is qualitatively different from the dispersive transport observed for neat BPhen. Furthermore, the lack of a percolative phase transition suggests small-scale phase segregation of C_{60} creates conductive pathways even in the 1:9 compound

buffer. In combination, these characteristics indicate that the compound buffer can improve efficiency for a range of OPV architectures, as has been demonstrated in both planar and mixed heterojunction devices.

CHAPTER 7

Conclusions and Future Work

The field of organic semiconductors has made great strides forward since the turn of the millennium. However, compared to inorganic semiconductors, much work remains to bring it to maturity. This work lies both in the realm of device and materials engineering and in basic physical understanding of the principles of operation.

A primary challenge facing the field today is a better understanding of the atomic-level morphology of devices. Inorganic semiconductors have long been able to use a range of techniques such as scanning electron microscopy (SEM) and transmission electron microscopy (TEM) to observe the atomic lattice itself, which has allowed researchers to understand the relationship between novel processing techniques and the basic structure of their materials. It has also allowed a fundamental understanding of the purity and crystallinity of inorganic semiconducting materials, as dislocations and impurities in the lattice can be directly observed.

These methods do not work nearly as well for organic semiconductors. TEM relies on differences in atomic weight to show contrast between materials; this is difficult to achieve in organics, as both components of most blends are composed of similar light elements. In the BPhen:C_{60} blends analyzed in chapter 6, for example, the two molecules are both composed primarily of carbon, with BPhen having an additional two nitrogen molecules. These blend layers therefore appeared as a single undifferentiated film under TEM.

Organics are also significantly more fragile than inorganics, which rules out the remaining methods that work so well for inorganics. High-energy electron beams such as those used in TEM or SEM can easily damage organics during measurement, changing the observed morphology. This further reduces the contrast possible with these methods.

Other techniques such as AFM can be used to measure the surface of organics., but AFM cannot distinguish between different organic materials and therefore cannot truly characterize blend layers. The method of cAFM can distinguish between organics in certain blends, but it has a relatively low resolution, on the order of 10 nm, and cannot see

atomic-level structure. Techniques such as AFM are also unsuitable for looking at organic blends in cross-section, required if a truly three-dimensional picture of the structure is to be acquired*.

To truly understand the effects of different processing techniques on layer morphology, and to clarify our understanding of the mixed layers that are used in nearly all highly-efficient devices today, new techniques must therefore be developed to image organics with molecule-level resolution. It is unclear as of yet what these techniques will be. They will have to avoid damaging the fragile organic films and allow the three-dimensional imaging of device-equivalent layers.

A more promising recent technique relies on endohedral fullerenes to dramatically improve contrast in TEM images of organic blends.[248–250] Endohedral fullerenes are fullerenes which incorporate additional atoms, ions, or molecules inside the spherical hollow fullerene. By incorporating heavy atom complexes into the fullerene, in this case lutetitum complexes (Lu_3N), high contrast is seen between the fullerene and the donor material in mixed heterojunctions.This has allowed for full three-dimensional imaging of mixed fullerene:P3HT heterojunctions, showing the location of the fullerene, the polymer, and a blend phase composed of both.

However, the broader applicability of this technique remains in question. The fullerene used was C_{80}, not the more commonly used C_{60} or C_{70}, and it is unclear whether lutetium complexes could be incorporated into the smaller fullerenes. Furthermore, it is as of yet unclear whether the incorporation of the lutetium complex changes the chemical properties or deposition behavior of the fullerenes, which would also change the morphology of the heterojunction. A technique capable of imaging the hollow fullerene is therefore desirable, which would also possess the ability to image hopefully-arbitrary blends of materials.

Another problem which remains to be solved is a better understanding of the behavior of excitons at interfaces. In chapters 5 and 6, we presented a method for measuring the blocking efficiency of a given interface relative to an ideal blocker or quencher. However, the blocker and quencher were simply assumed to be ideal. A method for measuring the absolute blocking or quenching characteristic of an interface remains elusive.

The work of Giebink, et al. (see section 3.4.1) was an important advance in understanding the physics of dissociation at the organic heterojunction,[147,148] but further work remains. The effects of specific energy difference at the heterojunction still remains unclear. What is the minimum separation between the HOMO of the acceptor and the LUMO

*To further complicate matters, it is difficult just to fabricate an organic cross-section. Amorphous organics do not cleave along a crystal plane like silicon does, meaning that simple mechanical cleaving of the substrate may not generate a usable sample. Techniques to cut a cross-section such as focused ion beam (FIB) milling or chemical etching bear a high possibility of damaging the fragile organics.

of the acceptor required for efficient dissociation? How do things change as the energy difference increases and decreases? What energy offset is best for efficient devices, and how does this change based on material properties?

Many future advances in OPV are likely to come from materials advances, working in concert with the deeper understanding of organic semiconductor physics discussed here. The field lacks a highly efficient NIR absorber which would allow for the harvesting of the solar spectrum past approximately 900 nm. This is a lack that can only be addressed by the development of new materials.

Significant effort is also going towards finding acceptor materials that give comparable efficiency to the fullerenes C_{60} and C_{70}. Efficient series tandem OPV require that each sub-cell generate equal photocurrent, most easily achieved when each subcell absorbs a separate part of the solar spectrum. Currently, tandem devices incorporating three or four heterojunctions must have duplicate fullerene layers due to the small selection of efficient acceptor materials. A wider range of materials would therefore allow for greater flexibility in tandem design.

A fullerene replacement would be also be attractive for reducing the cost of OPV. The spherical structure of the fullerenes is currently impossible to synthesize with conventional chemical techniques. Instead, fullerenes are manufactured through the controlled combustion of hydrocarbons in conditions optimized to produce fullerene soot. This is an improvement over the previous low-volume method of laser or electrical ablation of a carbon filament, but still is relatively high-cost compared to bulk chemical synthesis.

In summary, organic devices have made great advances in recent years, both in engineering of efficient devices and in understanding of the physics underlying the materials themselves. Indeed, OPV hover on the cusp of commercializability. Advances in materials and device engineering hold the promise of letting OPV finally find a place in the market.

APPENDIX A

Thermal Properties of Organic Light-Emitting Diodes

The high efficiency, large color gamut, and ease of manufacture of organic light-emitting diodes (OLEDs) have led to their practical application in flat panel displays.[251] More recently, large-area white OLEDs have also been found suitable for lighting applications, with devices already exceeding the efficiency of fluorescent panels.[252,253] However, the lifetime of OLEDs operated at the surface luminance required for lighting (3000 cd/m^2 or higher) is sensitive to temperature, with 1.65x longer lifetime for a decrease of 10K.[254] Accurate methods for modeling and designing temperature-tolerant device structures and luminaires, therefore, are needed.

Here, we apply a recently introduced matrix method to quantify one-dimensional heat-transfer from the active region of a multi-layer, packaged OLED by fully describing the effects of conduction, convection and radiation. In an extension of previous work,[255] we employ an analytical treatment for the effects of convection, allowing for an accurate determination of the packaged device thermal properties using no undetermined, free parameters. With this method, we describe approaches to minimizing the temperature increase in high-brightness OLEDs that are of particular interest in solid-state lighting applications.

A.1 Theory

As described previously,[255,256] the transmission matrix approach employs Laplace transforms of the heat transfer equations. The solution to these equations through a single layer are represented using:

$$\begin{bmatrix} \hat{T}_{i+1} \\ \hat{Q}_{i+1} \end{bmatrix} = \begin{bmatrix} cosh(\theta_i) & Z_i sinh(\theta_i) \\ \frac{sinh(\theta_i)}{Z_i} & cosh(\theta_i) \end{bmatrix} \begin{bmatrix} \hat{T}_i \\ \hat{Q}_i \end{bmatrix} = \begin{bmatrix} A_i & B_i \\ C_i & D_i \end{bmatrix} \begin{bmatrix} \hat{T}_i \\ \hat{Q}_i \end{bmatrix} = [T(\theta_i)] \begin{bmatrix} \hat{T}_i \\ \hat{Q}_i \end{bmatrix} \quad \text{(A.1)}$$

where $\hat{T}_i(s)$ and $\hat{Q}_i(s)$ are the Laplace transforms of the temperature and heat flux across the i^{th} layer; $\theta_i = L_i\sqrt{C_i s/K_i}$ is the operational propagation constant, K_i is the thermal conductivity of the film, C_i is its volumetric heat capacity, L_i is the layer thickness, $Z_i = \sqrt{1/(K_i C_i s)}$ is the characteristic impedance, and A_i, B_i, C_i, and D_i are matrix elements that can be approximated by polynomial expansions in the Laplace variable, s. Multiple layers are handled in one of two ways: a series of layers are treated as the product of the transmission matrices for the several films, while layers placed in parallel, or parallel heat channels such as conduction and thermal radiation, are treated by assuming that the incident heat flux splits between the two independent channels with no flow between them. This gives the final matrix as the sum of the channels:

$$\begin{bmatrix} \hat{Q}_1 \\ \hat{Q}_2 \end{bmatrix} = \sum_i \begin{bmatrix} \hat{Q}_{1i} \\ \hat{Q}_{2i} \end{bmatrix} = \sum_i \begin{bmatrix} A_i/B_i & -1/B_i \\ 1/B_i & -A_i/B_i \end{bmatrix} \begin{bmatrix} \hat{T}_1 \\ \hat{T}_2 \end{bmatrix} \tag{A.2}$$

The parallel and series channels are then combined to model heat transfer through arbitrary, multilayer, one-dimensional systems. Full OLED modeling also requires the inclusion of interface resistance[257] and the treatment of radiation and conduction as parallel heat transfer paths.

Previous work treated convective transfer from the device surface as an additional conductive layer whose thickness was used as a free parameter to match the model predictions to the measured data, thereby limiting its predictive capabilities. Here, we model convection using Newtons Law of Cooling,[258,259] $Q_{\text{conv}} = h\Delta T$, where h is the convective heat transfer coefficient of the ambient, and ΔT is the temperature difference between the surface and ambient. For forced convection, h is a constant, while it is temperature-dependent for natural convection.[259] Now, Q_{conv} is derived from the Nusselt number, Nu whose form depends on the thermal environment and experimental geometry. For our analysis, we consider only the case of convection in the laminar flow regime from the upper surface of a heated, horizontally positioned packaged OLED. In this case,[258] $Nu = hL/K_{amb} = 0.54Ra^{1/4}$, where L is the characteristic length of the system, K_{amb} is the thermal conductivity of the convective medium, and Ra is the Rayleigh number. Other orientations and geometries may be considered by inserting the appropriate expression for Nu. The Rayleigh number is then defined for a given convective medium, in our case air, as:

$$Ra = \frac{C_P \rho^2 g \beta (\Delta T) L^3}{\mu K_{amb}} \tag{A.3}$$

where C_P is the heat capacity at constant pressure of the convective medium, ρ is its density, μ the viscosity, g is the acceleration due to gravity, and β is the gas volume expansion

Material	Density (kg/m^3)	Volume Expansion (1/K)	Viscosity (kg/m · s)	ΔT (K)
Air	1.18	$3.35 \cdot 10^{-3}$	$1.85 \cdot 10^{-5}$	6
Rayleigh Number	$9.0 \cdot 10^3$			
Nusselt Number (Horizontal Plate)	5.3			

Table A.1: Rayleigh and Nusselt numbers at 25.5°C

coefficient. From the foregoing, we find that $Q \sim \Delta T^{5/4}$, which renders the Laplace transform of this equation mathematically intractable. However, the temperature rise for the devices studied is only $5-10$K even under the highest intensity operating conditions.[254,255] This small temperature change allows us to set the Rayleigh number to a constant, thereby linearizing Newtons Law of Cooling and greatly simplifying the analysis. The parameters used to calculate this term and the values of Ra and Nu are provided in Table A.1. Applying this assumption for a simulated input power of 1 kW/m^2, we find that the device reaches a steady-state temperature of approximately 85°C. If we then change the Rayleigh number by two orders of magnitude in the model, the steady-state temperature changes by only 2%, indicating that the model is largely insensitive to these changes.

Combining the analytical treatment of convection with the matrix method allows us to derive an expression for the device operating temperature, T_{in}, in terms of the input heat flux, Q_{in}, the heat transfer coefficient h, and the transmission matrix elements to yield:

$$T_{in} = -\frac{B_T^2\left(h + \frac{A_T}{B_T}\right)Q_{in}}{1 - B_T^2\left(h + \frac{A_T}{B_T}\right)\left(\frac{A_B}{B_B} + \frac{A_T}{B_T}\right)} \tag{A.4}$$

where $A_{T,B}$ and $B_{T,B}$ denote matrix elements corresponding to heat transfer through the top (T) and bottom (B) device surfaces (see Fig. A.1).

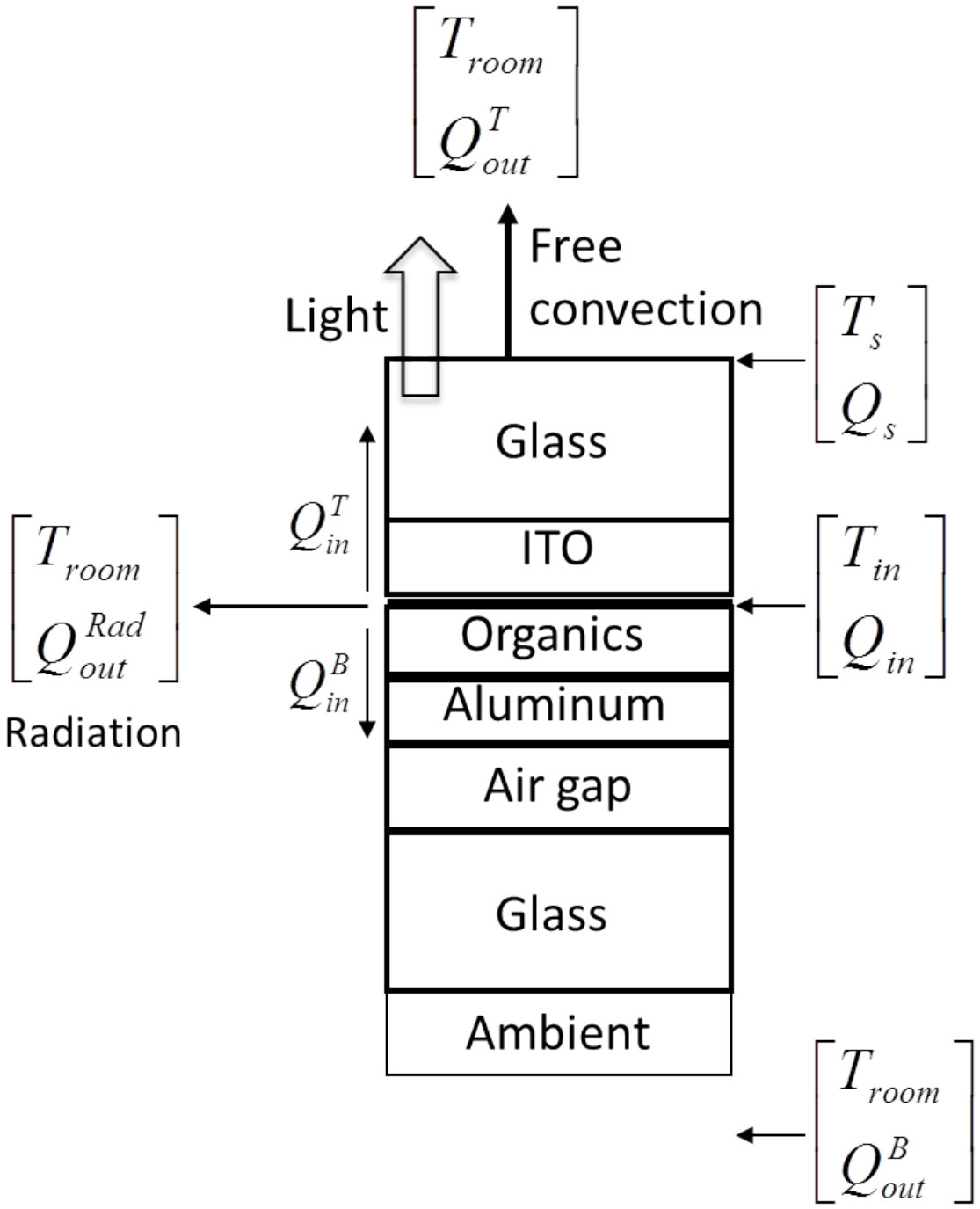

Figure A.1: Device structure of an OLED. Heat, Q_{in}, is input in the organic emission layer and then splits to flow toward the top, Q_{in}^{T}, and bottom, Q_{in}^{B}, device surfaces. T_{in} is then the temperature of the active layer, T_S and Q_S are the temperature and heat flow through the top device surface, T_{room} is the ambient temperature, and Q_{out}^{T}, Q_{out}^{B}, and Q_{out}^{Rad} are the heat fluxes due to convection at the top surface, conduction at the bottom surface, and radiation, respectively.

A.2 Results and Discussion

We tested the model using a 25 cm^2, glass-encapsulated, green phosphorescent OLED (Universal Display Corp, Ewing, NJ) whose structure is shown schematically in Fig. A.1. Its layer thicknesses and material thermal constants are given in Table A.2. Current density-vs.-voltage ($J-V$) characteristics were obtained using a Keithley 2400 source meter, while optical characteristics were measured using a calibrated reference detector. Thermal surface image measurements (Fig. A.2, inset) were taken with a non-contact infrared camera (FLIR A325) inside a box with a black interior to eliminate stray reflections and to provide a stable thermal environment. Previous work has shown that the temperature difference between the upper surface and the organic EML is negligible.[255] Hence, we can assume that the thermal image temperature is the same as that of the EML. The input thermal power was calculated from the total input electrical power and the measured output optical power,[255] Q_{opt}, using: $Q_{in} = JV - Q_{opt}$. During thermal measurements, the devices were suspended several millimeters above an optical table held at ambient temperature. The gap between the table (which acted as an ambient heat sink) and the device was too narrow to allow for convection, and hence was treated as an additional thermally conductive layer.

The OLED surface temperature was measured as a function of time at several different current densities after the onset of a current step at $t = 0$ and then compared to model calculations, as shown in Fig. A.2. The model is defined by only the thermal parameters of the various layers and the geometry of the setup (see Table A.1). The operating currents at the highest intensities result in a surface luminance of ~ 3000 cd/m^2, with an external quantum efficiency of approximately 19% at all current densities studied.

The accuracy of the model suggests that it can be useful in designing devices with optimized thermal characteristics. In Fig. A.3 we plot the fraction of heat dissipation (ξ) via conduction through the bottom device surface vs. the total heat loss, as a function of thickness of the layers (i.e. the glass package cap, squares; or the internal air gap between cap and cathode, circles) between the emission region and the conductive bottom surface. The simulations were performed for a constant input power of 114 W/m^2 that is applied at $t = 0$. Arrows in Fig. A.3 correspond to thicknesses of the measured device. The discrepancy between heat dissipation through the two surfaces can be partly explained by the device structure, as shown below, and partly through the different heat transfer mechanisms through the top and bottom surfaces.

Changing the glass cap thickness does not substantially change ξ. It is apparent that heat is primarily dissipated via conduction in the packaged device, and that natural convection to the ambient is a comparatively inefficient heat removal pathway. The efficiency of heat

Layer	Thickness (mm)	Heat Capacity at Constant Pressure ($10^2 \cdot$ J/kg $\cdot$ K)	Thermal Conductivity (W/K·m)	Reference
Glass	0.7	8.2	1.3	[260, 261]
ITO	$1 \cdot 10^{-3}$	3.4	5.0	[255]
Organic Active Region	$1 \cdot 10^{-4}$	17	0.2	[255]
Aluminum	$1 \cdot 10^{-4}$	9.0	250	[260]
Air (internal gap)	1.9	10	0.026	[260]

Table A.2: Thermal constants and layer thicknesses used in model

removal through the top surface of the device is, therefore, limited by convection which is not readily adjusted through changes in device architecture. Forced convection could increase the cooling efficiency, albeit at the risk of increasing lighting fixture cost and complexity.

The bottom device surface also has potential for increased heat extraction via conduction to the ambient. The glass cap and the internal air gap thickness have large effects on heat transfer, as they are by far the thickest layers. Using the same assumptions as in Fig. A.3, we modeled the effect of changes in the thickness of these layers on device heating, with the results shown in Fig. A.4a. We find that the thicknesses of the glass layers do not have a significant effect on the steady-state temperature. Instead, the thickness of the glass determines the thermal equilibration rate following the onset of device heating. In contrast, the internal air gap (Fig. A.4b) presents the most significant bottleneck to heat transfer. For the thinnest air layers considered, (0.1 mm), there is almost no heating predicted for the device at 3000 cd/m^2. This corresponds to a larger percentage of heat being removed through conduction via the bottom surface, as seen in Fig A.3, suggesting that optimal device architectures can operate at room temperature; a highly promising result for the future commercialization of OLEDs for lighting applications.

When the internal air gap limits thermal diffusion, the gap between the bottom surface of the device and the heat-sink must also contribute to device heating. Indeed, we found that the thickness of the air gap has a significant effect on operating temperature, as predicted by the model. Also, the device showed a temperature rise of approximately 1.5°C when attached directly to a Cu heat-sink. This indicates the existence of an internal heat-transfer bottleneck due to the internal air gap.

While simulations were performed for a green phosphorescent OLED (PHOLED), lighting applications require white PHOLEDs. Nevertheless, we can extend the analysis

to white PHOLEDs using data of Levermore et al.[254] There, an input power of 489 W/m^2 resulted in a brightness of 3000 cd/m^2, as compared to the input electrical power of 132 W/m^2 for the green devices. If we assume analogous identical device active organic layer thicknesses structure with an equivalent percentage of input electrical power dissipated as heat, then this device gives a steady-state temperature of 47.8°C . Levermore reported a heat rise of approximately 10°C , which suggests different heat sinking or output optical characteristics from our device.

In summary, we have extended the transmission matrix method for modeling heat transfer in OLEDs, providing a full analytical treatment that includes free convection, conduction and radiation. The model accurately predicts the thermal profile of OLEDs while providing an understanding of the factors that determine device operating temperature. In particular, we find that the internal air gap between the package lid and substrate provides the largest impedance to heat transfer, and that elimination of this gap allows operation at near ambient temperature even at high brightness. Further optimization of the thermal performance of OLEDs and other photonic devices can be obtained using the methods presented.

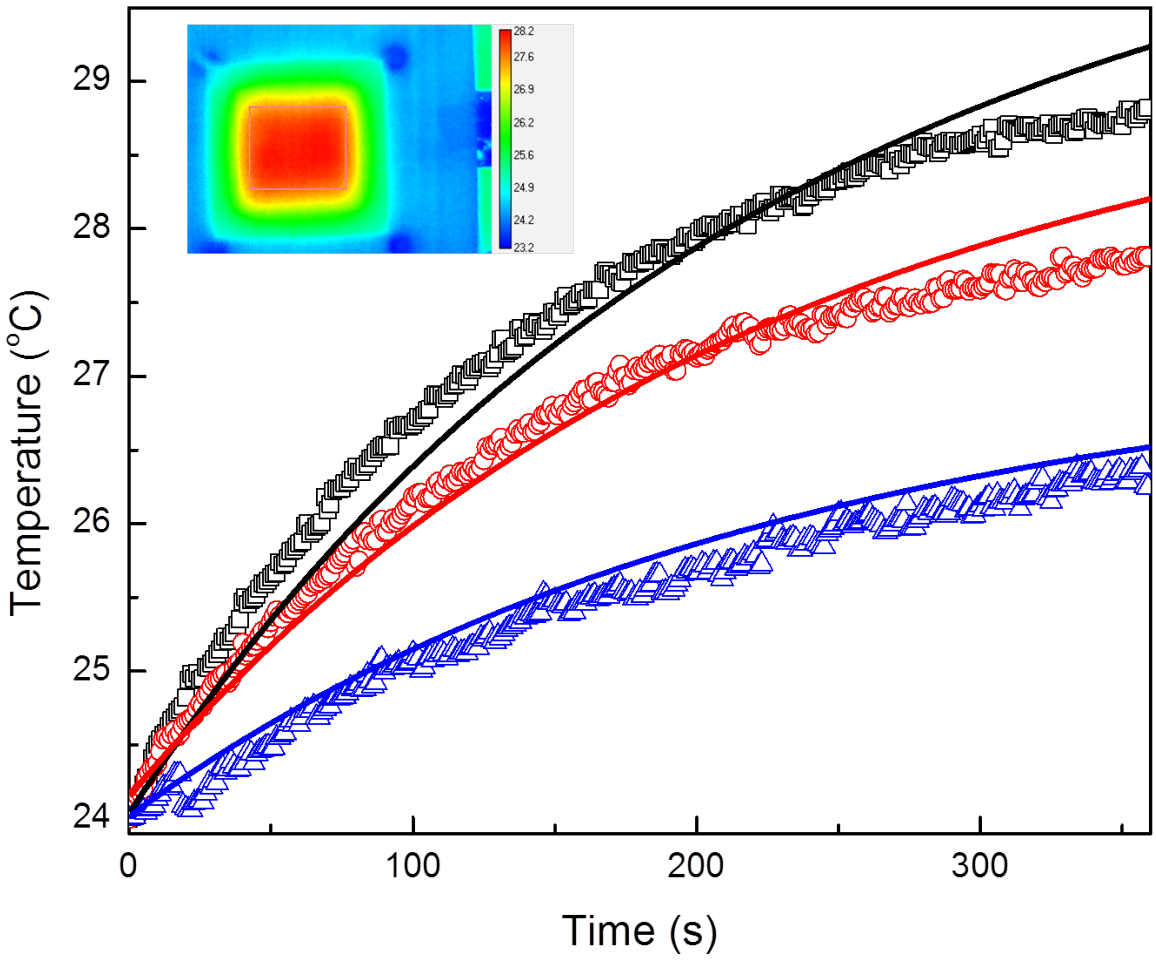

Figure A.2: Measured temperature of a 25 cm^2 green phosphorescent OLED at several different input current densities (points), compared to model predictions (lines). Data are taken at current densities of 2 mA/cm^2 (triangles), 3 mA/cm^2 (circles), and 4 mA/cm^2 (squares), with the current turned on at time $t = 0$. Inset: Thermal image of an OLED after 6 min following the onset of a 3 mA/cm^2 current step. Current was injected along the entire perimeter of the device, which minimized contact heating and provided a uniform thermal profile. The box in the figure shows the area which was averaged to obtain the device temperature.

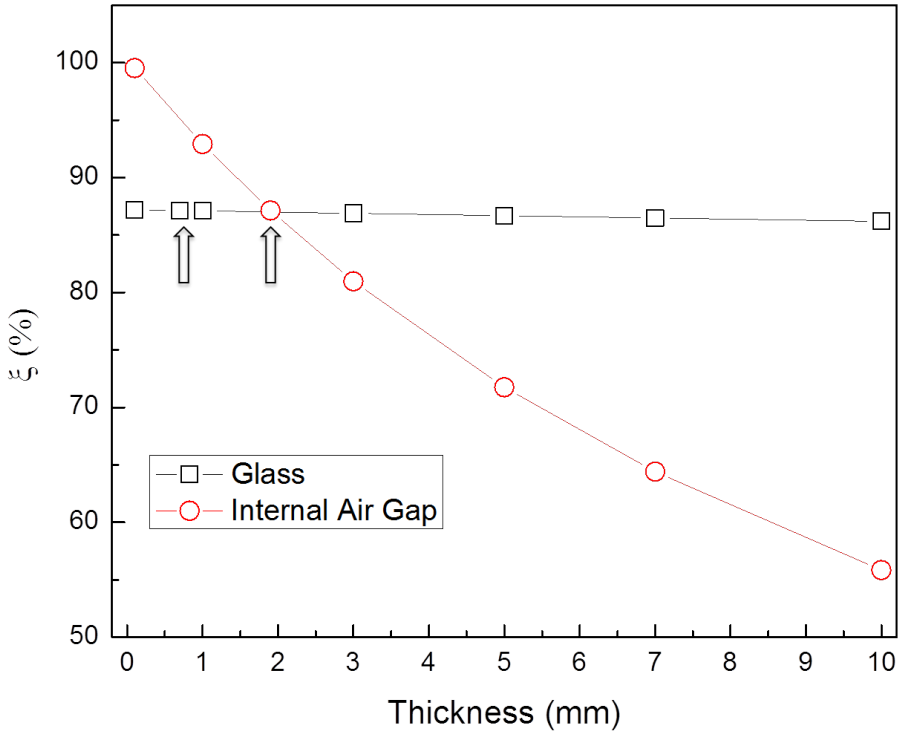

Figure A.3: Calculated fraction (ξ) of steady-state heat dissipated at a thermal input power of 114 W/m2 via conduction through the bottom device surface vs. thickness of the glass cap and substrate layers (squares) and the internal air gap (circles). Arrows indicate values for the layers in the experimental device in Table A.1 and Fig. A.2. The operating conditions correspond to a luminance of 3000 cd/m^2. The largest fraction of generated heat is dissipated through conduction, with the thickness of the internal air gap presenting significant thermal impedance to heat transfer. The steady-state device temperature increases as the fraction of heat dissipated through conduction decreases, as this is the most efficient heat transfer pathway. The efficiency of convective and radiative cooling will increase somewhat as the device temperature increases, as these depend on the difference between the device and ambient, but not enough to fully compensate.

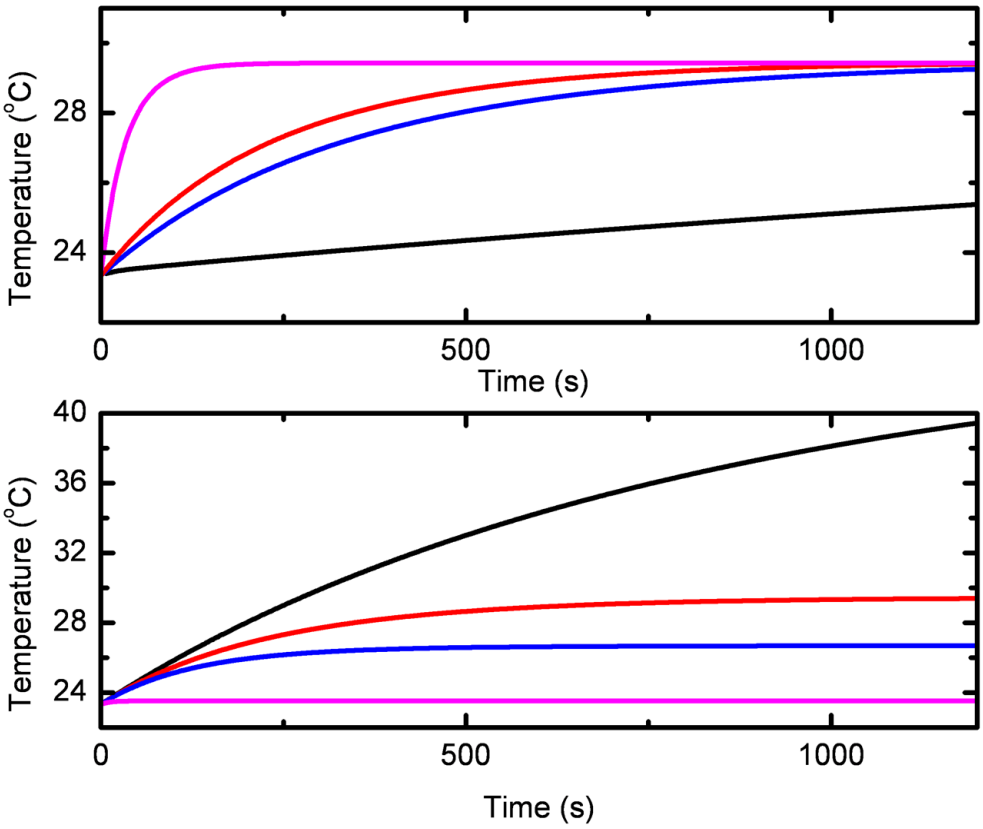

Figure A.4: a) Effects of thickness of the glass substrate and cap layers. From top to bottom, lines correspond to individual layer thicknesses of 0.1, 0.7 (actual thickness), 1.0, and 10 mm. Variation in glass thickness changes the rate of thermal equilibration, but does not significantly affect the ultimate equilibrium temperature. The 10 mm simulation did not reach equilibrium in the time scale shown here, but should not have a significantly different steady-state temperature. b) Effects of changing the encapsulated air gap thickness. From top to bottom, lines correspond to a thickness of 10, 1.9 (actual thickness), 1.0, and 0.1 mm. For the thinnest layers, there is no significant heating of the device. Devices were modeled for an input thermal power of 114 W/m^2, assumed to be turned on at time $t = 0$.

APPENDIX B

Nonideal Behavior in Carbon Nanotube p-n Junctions

THE ability to fabricate ultraclean, nearly defect free, suspended carbon nanotubes (CNTs) has enabled several interesting phenomena to be observed, including nonadiabatic behavior (i.e., breakdown of the BornOppenheimer approximation),[262] mode selective electron-phonon coupling (leading to negative differential resistance and nonequilibrium phonon populations) ,[263] gate-controllable modulation of Raman intensity ,[264,265] and a possible structural phase transition.[264,266,267] These effects are not seen in substrate-supported nanotubes, and the elimination of substrate interactions, defects, and surface contaminants is essential to their observation .[268] While diode-like rectification has been achieved in CNT p-n junctions formed by chemical doping ,[269,270] polymer coating ,[271] impurities ,[272] asymmetric contacts ,[273,274] and intramolecular junctions ,[275] p-n junctions can also be formed by electrostatic gating [276–279] that enables doping of nanotubes without introducing defects, impurities, or surface contaminants. These imperfections can scatter electrons, increase electronhole recombination, create subbandgap states, and ultimately lead to nonideal diode behavior.

Several studies have focused on CNTs lying on a substrate and/or on densely packed CNT films .[271,280,281] Residue from lithographic processing and imperfections induced at the nanotube-substrate interface perturb the 1-D conducting carbon nanotube as the electrons experience random fluctuations in potential along the tube length .[268] Electrostatically doped p-n junctions in suspended CNTs have shown ideality factors, $n \approx 1$, suggesting the near absence of charge recombination during transport .[277,279] Current annealing has been shown to remove adsorbates, further improving the ideality factor .[282] However, most of these studies have been limited to fixed gate voltages and relatively small bias voltages across the nanotube ($< |0.2V|$). The many-body theory has predicted that the bandgaps and exciton binding energies in semiconducting CNTs will significantly decrease with doping due to dynamic screening by acoustic plasmons .[283] This bandgap reduction is approxi-

mately ten times larger than in bulk semiconductors at the same doping level (~ 800 meV for densities of $\rho = 0.6$ holes or electrons per nanometer), however, this phenomenon has up to this point gone largely unstudied.

In this study, we study CNT p-n junction diodes under relatively large applied bias voltages over a broad range of electrostatic doping conditions imposed by two isolated gate electrodes, as illustrated in Fig. B.1(a). A two-diode model is developed to explain the nonidealities in current versus voltage (IV) behavior observed at high bias. This model includes bandgap bandgap renormalization (BGR), which is particularly important under high electrostatic doping. The IV characteristics are also taken under illumination to further elucidate the charge-carrier dynamics at the p-n junction.

Samples are fabricated by etching a 4-μm wide, 500-nm deep trench in a Si/SiO_2/Si_3N_4 substrate, as described previously.[262] Two 1-μm wide and 35-nm thick Pt/W gate electrodes (30 nm Pt/5 nm W adhesion layer) separated by 2 μm are deposited on the bottom of the trench, as shown schematically in Fig. B.1(a). Source and drain electrodes with the same Pt/W thicknesses are patterned lithographically on each side of the trench. The CNTs are then grown by chemical vapor deposition at 850°C with Fe and Mo catalysts using argon bubbled through ethanol for 10 min. Fig. B.1(c) is an SEM image of the device with a dashed line indicating where the CNT typically grows. The diameters of the CNTs are typically 1.2 ± 0.1 nm. Current annealing is performed in argon at $V_{bias} = \pm 1.5$ V. We only select single suspended CNTs based on the empirical F rule [284] for our measurement. The IV characteristics are taken both in the dark and under illumination using a variable output power, $\lambda = 532$ nm wavelength diode-pumped solid-state laser. The laser is focused to an approximately 0.5 μm diameter spot, and the power of the laser spot incident on the nanotube ranged from 20 to 200 μW. Complete photovoltage and photocurrent maps are provided in the Supplemental Materials in Fig. S5.

Fig. B.2 shows the dark IV characteristics of the device taken at various gate voltages. In the weak gating regime [see Fig. B.2(a)], an S shape curve is observed, indicating two back-to-back diodes. At larger applied gate voltages [see Fig. B.2(b) and (c)], nearly ideal diode behavior is observed at low bias voltages as previously reported, however, nonideal diode behavior can be seen at bias voltages > 0.2 V. A two-diode model (described later) is used to fit the experimental data, as shown by the solid lines in Fig. B.2(a), (b), and (c).

To understand the device behavior, we assume a model comprising two back-to-back diodes, as illustrated in the band diagram of Fig. B.1(b). Here, the diode labeled "con" corresponds to the Pt-contact Schottky barrier diode, and "cnt" represents the electrostatically doped p-n junction. These two diodes have different turn-on voltages under forward bias, thereby limiting the current at high voltage. We represent the tunneling current in the

device with a pair of shunt resistances, R_P^{con} and R_P^{cnt}, also shown in Fig. B.1(c). Thus, the current through the device can be written as

$$I = I_0^{con}\left(\exp\left(\frac{-qV^{con}}{kT}\right) - 1\right) + \left(\frac{V^{con}}{R_P^{con}}\right) = I_0^{cnt}\left(\exp\left(\frac{-qV^{cnt}}{kT}\right) - 1\right) + \left(\frac{V^{cnt}}{R_P^{cnt}}\right) \quad \text{(B.1)}$$

where V^{con} and V^{cnt} are the voltages dropped across the reverse- and forward-biased diodes, respectively, and I_0^{con} and I_0^{cnt} are their respective reverse saturation currents. Hence, the total voltage is $V = V^{con} + V^{cnt}$. We solve (1) for V, to obtain

$$V = I\left(R_P^{con} + R_P^{cnt}\right) + I_0^{con}R_P^{con} - V_{th}\cdot W\left(\frac{I_0^{con}R_P^{con}}{V_{th}}\exp\left(\frac{\left(I + I_0^{con}\right)R_P^{con}}{V_{th}}\right)\right) - I_0^{con}R_P^{cnt} + V_{th}\cdot W\left(\frac{I_0^{cnt}R_P^{cnt}}{V_{th}}\exp\left(\frac{\left(I + I_0^{cnt}\right)R_P^{cnt}}{V_{th}}\right)\right) \quad \text{(B.2)}$$

The thermal voltage is $V_{th} = kT/q$, where k is Boltzmann's constant, T is the temperature, q is the electron charge, and W is the Lambert W-function,[285,286] defined as the solution to F. The W-function is introduced to allow for exact analytical solutions of (2). Typical values for I_0 and R_P are 0.5 nA and 0.7 GΩ, respectively.

Fig. B.3 shows the reverse saturation currents (I_0^{con} and I_0^{cnt}) and equivalent tunneling resistances (R_P) plotted versus gate voltage for the Schottky and p-n diodes, respectively. Here, R_P, decreases exponentially with the square root of the gate voltage, and hence, bandgap, as shown in Fig. B.3(b). Interestingly, the reverse saturation current increases with doping, which is the opposite of expectations for conventional diffusion-limited diodes .[287] This is due to BGR, which results in a decrease in bandgap with increased doping due to dynamical screening mediated by acoustic plasmons .[283] This effect is considerably stronger in CNTs than in conventional semiconductors due to the 1-D confinement of carriers.

To relate the reverse saturation current to doping, we start with the CNT conduction band density of states [279,288]

$$D\left(E, E_c\right) = D_0\frac{E}{\sqrt{E^2 - E_c^2}}, E > E_c \quad \text{(B.3)}$$

where E_c is the energy of the conduction band minimum and D_0 is the effective density of states at the conduction band minimum. From the density of states, we calculate the

minority carrier density in the doped regions [289]

$$n_p = D_0 e^{-\frac{E_a}{kT}} \int_0^\infty \frac{E + E_c}{\sqrt{E^2 + 2E_c E}} e^{-\frac{E}{kT}} dE \tag{B.4}$$

where E_a is equal to the energy difference between the conduction band minimum and the Fermi energy in the P-doped region $(E_c - E_{F,p})$. The integral is solved for a conduction band minimum energy of 300 meV. The reverse saturation current is expressed as [3]

$$I_0 = qD_{\text{iff}} \left(n_p + p_n\right) / \sqrt{D_{\text{iff}}\tau} \tag{B.5}$$

where D_{iff} is the diffusion coefficient and τ is the minority carrier lifetime. Substituting (4) into (5) gives

$$I_0 = (0.12\text{eV})\, D_0 q \sqrt{\frac{D_{\text{iff}}}{\tau}} e^{-\frac{E_a}{kT}} \tag{B.6}$$

where the factor of 0.12 eV is obtained from the numerical solution of (4). By measuring the temperature dependence of I_0, it is possible to extract both E_a and τ. The diffusion coefficient D_{iff} is calculated from the Einstein relation using a mobility of $2 \cdot 10^4$ cm^2 / V·s.[290] We find that $\tau = 0.10 \pm 0.02$ ns, assuming that D_{iff}, D_0, and τ are doping independent. This value is similar to recent observations of time-resolved photoluminescence .[291] Here, E_a is doping dependent and spans a range from $0.250.18$ eV, as shown in Fig. B.4.

Spataru and Leonard used many-body simulations to understand the shift in bandgap due to BGR, determining that the change of the bandgap, $\Delta E_{gap} \propto \sqrt{\rho}$.[283] Assuming that the change in E_a is proportional to the BGR, we can write $E_a = E_a^0 - A\Delta E_{gap}$, where E_a^0 is the activation energy in the undoped nanotube and A is a fitting parameter. For a Fermi level in the middle of the bandgap in the undoped nanotube, $E_a^0 = \frac{1}{2} E_{gap}$, yielding

$$E_a = \frac{E_{gap}}{2} - B\sqrt{\rho} \tag{B.7}$$

where B is a fitting parameter and ρ is calculated from the capacitance between the nanotube and the gate electrodes. Approximating the CNT as an infinite conducting cylinder over a conducting plane, we obtain $\rho = 0.05$ dopants/nm·V, which is comparable to previous reports .[292] Using our values for E_a, we find the nanotubes have a zero-bias bandgap of approximately 600 meV.

The temperature-dependent data exhibit characteristics similar to that of two back-to-back p-n diodes, rather than one p-n diode and one Schottky diode. This is likely due to local doping of the CNT by the metallic contact causing the formation of a second, internal p-n junction instead of a standard Schottky contact, labeled as contact diode in Fig.

B.1(b). This phenomenon has been previously observed in spatially resolved photocurrent measurements .[293] Other devices measured in this study showed a more pronounced asymmetry between the two diodes, with one exhibiting typical p-n rectifying characteristics, and the other showing a minimal change with temperature, characteristic of a tunneling Schottky contact.

In conclusion, we have found that suspended carbon nanotube p-n junction diodes exhibit nearly ideal behavior for small bias voltages. At higher bias, the metalsemiconductor contacts limit current injection, resulting in a back-to-back diode characteristic with the P-doped side having an ohmic contact and the n-doped side having a Schottky contact with the underlying Pt electrodes. The parallel tunneling resistance also significantly influences current at high bias. Our model of the doping dependence of the reverse saturation current, parallel resistance, and open-circuit voltage provide evidence for the theoretically predicted BGR by dynamic screening by acoustic plasmons in carbon nanotubes.

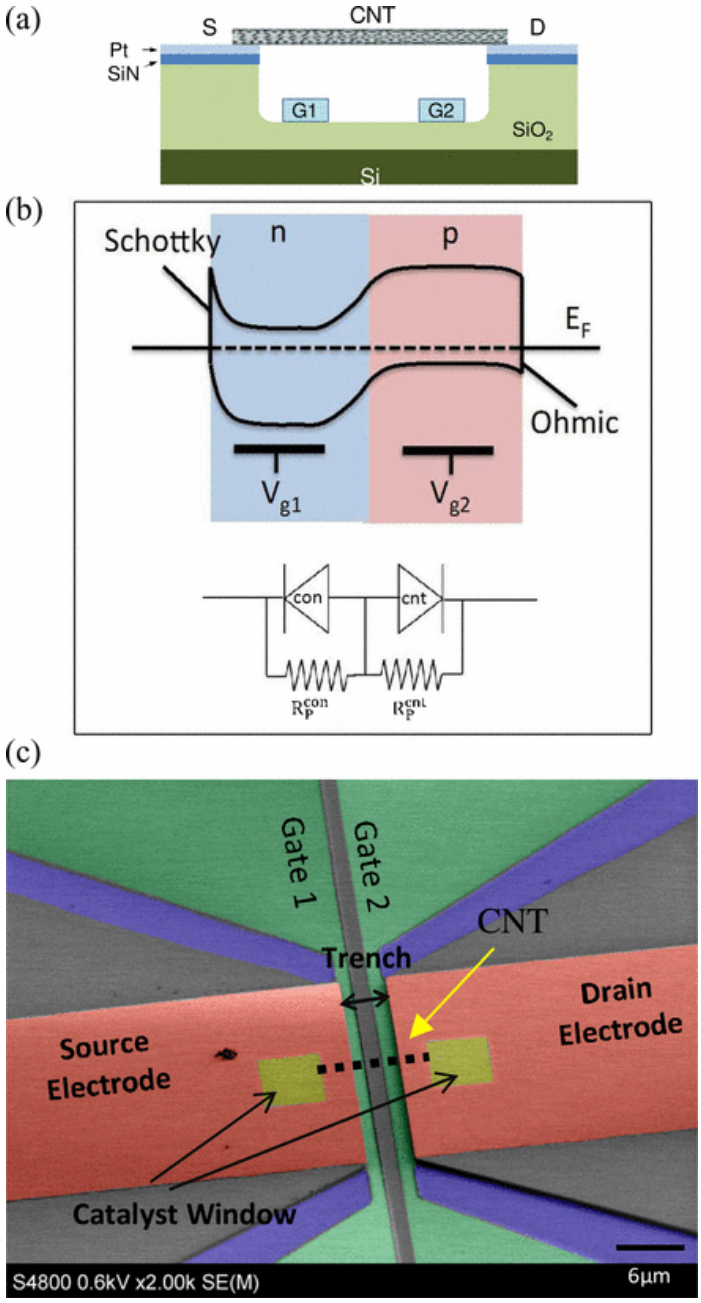

Figure B.1: (a) Schematic diagram of the dual-gate device geometry. (b) Equilibrium diode band diagram where the gate voltages are $V_{g1} > 0$ V and $V_{g2} < 0$ V, and the device equivalent circuit represented by two diodes in opposite directions. Here, E_F is the Fermi energy and R_P^{con} and R_P^{cnt} are the shunt resistances of the Schottky and p-n junctions, respectively. (c) Colorized SEM image of the dual-gate device geometry.

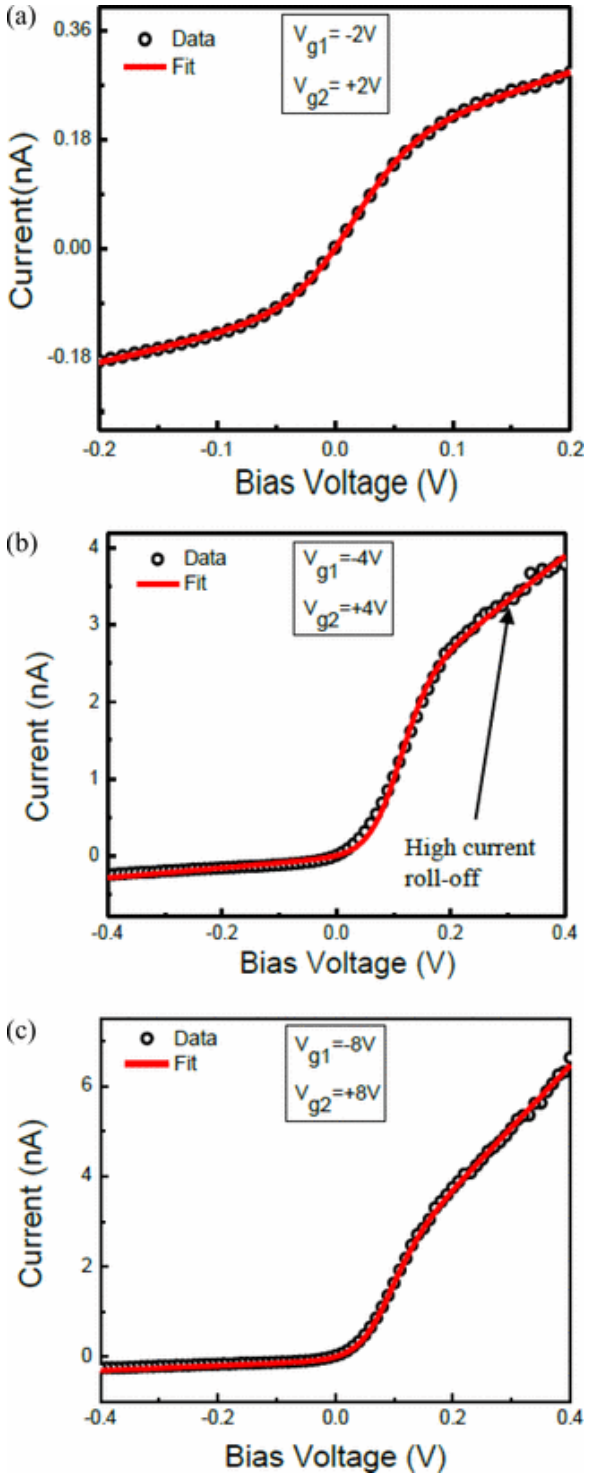

Figure B.2: Typical IV bias characteristics of an electrostatically doped p-n junction CNT taken at various gate voltages showing nonideal behavior at high bias (> 0.2 V). The fits to the data (red lines) follow the theory outline in the text.

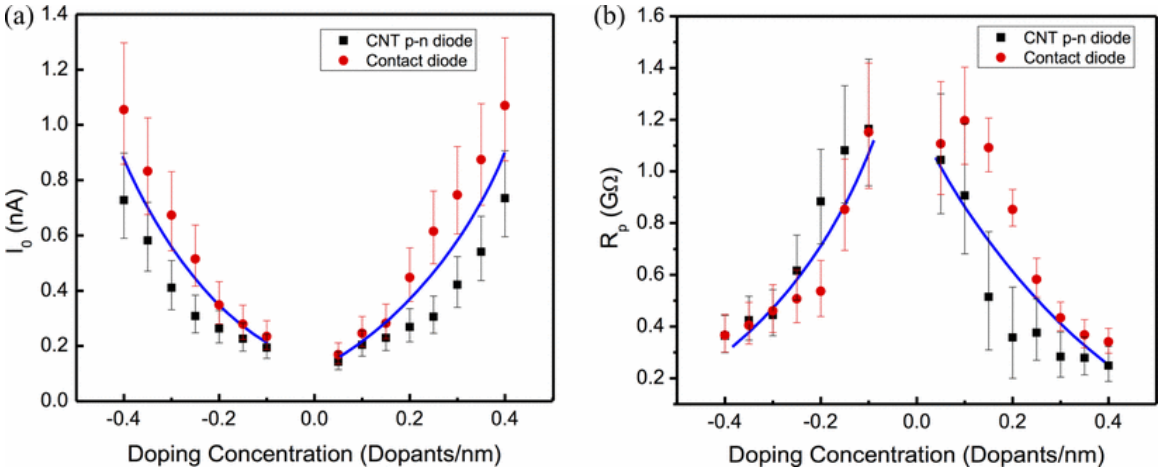

Figure B.3: Dependence of (a) reverse saturation current and (b) parallel resistance on doping ($V_{g1} = -V_{g2}$). Lines are added as guides to the eye.

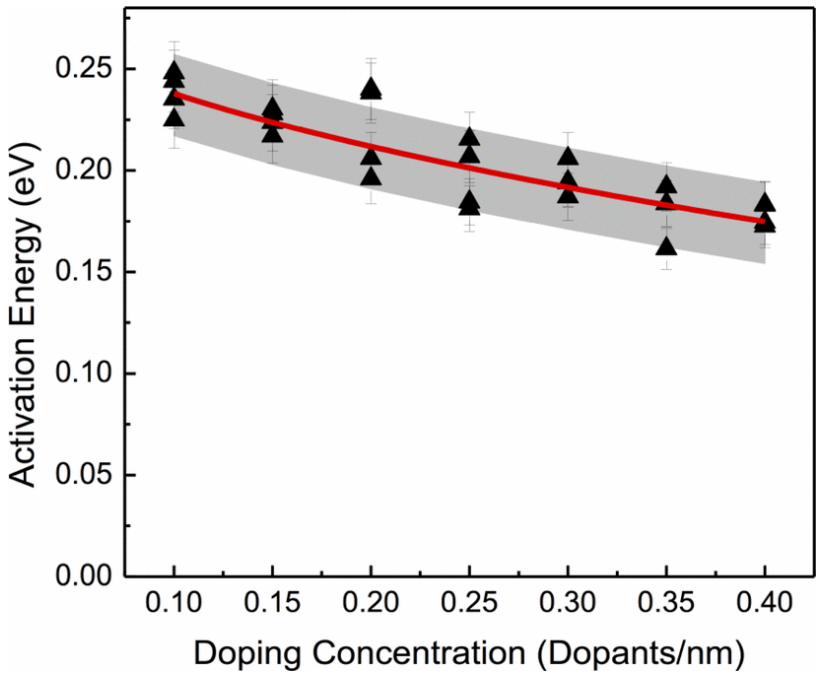

Figure B.4: Relationship between E_a and doping, fit (line) to a square-root dependence on the doping. This gives a bandgap of 600 $\pm$ 40 meV, with error given by the shaded region.

Bibliography

[1] S. L. Seager and M. R. Slabaugh, *Chemistry for Today: General, Organic, and Biochemistry*. Belmont, CA: Cengage Learning, 5 edition ed., Jan. 2004.

[2] C. Kittel, *Introduction to Solid State Physics*. Hoboken, NJ: Wiley, 8 edition ed., Nov. 2004.

[3] S. M. Sze and K. K. Ng, *Physics of Semiconductor Devices*. Hoboken, N.J: Wiley-Interscience, 3 edition ed., Oct. 2006.

[4] R. Eisberg and R. Resnick, *Quantum Physics of Atoms, Molecules, Solids, Nuclei, and Particles*. New York: John Wiley & Sons, 2nd edition ed., 1985.

[5] N. Karl, "Charge carrier transport in organic semiconductors," *Synthetic Metals*, vol. 133134, pp. 649–657, Mar. 2003.

[6] N. Tessler, Y. Preezant, N. Rappaport, and Y. Roichman, "Charge Transport in Disordered Organic Materials and Its Relevance to Thin-Film Devices: A Tutorial Review," *Advanced Materials*, vol. 21, pp. 2741–2761, July 2009.

[7] V. Coropceanu, J. Cornil, D. A. da Silva Filho, Y. Olivier, R. Silbey, and J.-L. Bredas, "Charge transport in organic semiconductors," *Chemical Reviews*, vol. 107, pp. 926–952, Apr. 2007. WOS:000245600000002.

[8] H. Bassler, "Charge Transport in Disordered Organic Photoconductors - a Monte-Carlo Simulation Study," *Physica Status Solidi B-Basic Research*, vol. 175, pp. 15–56, Jan. 1993. WOS:A1993KL45000001.

[9] R. Hilborn, "Einstein Coefficients, Cross-Sections, F Values, Dipole-Moments, and All That," *American Journal of Physics*, vol. 50, no. 11, pp. 982–986, 1982. WOS:A1982PN99500009.

[10] S. R. Forrest, "The path to ubiquitous and low-cost organic electronic appliances on plastic," *Nature*, vol. 428, pp. 911–918, Apr. 2004.

[11] R. S. Muller, T. I. Kamins, and M. Chan, *Device Electronics for Integrated Circuits*. New York, NY: Wiley, 3 edition ed., Oct. 2002.

[12] M. Pope and C. E. Swenberg, *Electronic Processes in Organic Crystals and Polymers*. Oxford University Press, 1999.

[13] F. Gutmann and L. Lyons, *Organic Semiconductors*. Huntington, N.Y: Krieger Pub Co, Aug. 1983.

[14] G. Gu, P. E. Burrows, S. Venkatesh, S. R. Forrest, and M. E. Thompson, "Vacuum-deposited, nonpolymeric flexible organic light-emitting devices," *Optics Letters*, vol. 22, pp. 172–174, Feb. 1997.

[15] J.-S. Park, H. Chae, H. K. Chung, and S. I. Lee, "Thin film encapsulation for flexible AM-OLED: a review," *Semiconductor Science and Technology*, vol. 26, p. 034001, Mar. 2011.

[16] A. B. Chwang, M. A. Rothman, S. Y. Mao, R. H. Hewitt, M. S. Weaver, J. A. Silvernail, K. Rajan, M. Hack, J. J. Brown, X. Chu, L. Moro, T. Krajewski, and N. Rutherford, "Thin film encapsulated flexible organic electroluminescent displays," *Applied Physics Letters*, vol. 83, pp. 413–415, July 2003.

[17] Z. Liu, J. Li, and F. Yan, "Package-Free Flexible Organic Solar Cells with Graphene top Electrodes," *Advanced Materials*, vol. 25, pp. 4296–4301, Aug. 2013.

[18] Y. Galagan, J.-E. J.M. Rubingh, R. Andriessen, C.-C. Fan, P. W.M. Blom, S. C. Veenstra, and J. M. Kroon, "ITO-free flexible organic solar cells with printed current collecting grids," *Solar Energy Materials and Solar Cells*, vol. 95, pp. 1339–1343, May 2011.

[19] A. Sugimoto, H. Ochi, S. Fujimura, A. Yoshida, T. Miyadera, and M. Tsuchida, "Flexible OLED displays using plastic substrates," *IEEE Journal of Selected Topics in Quantum Electronics*, vol. 10, pp. 107–114, Jan. 2004.

[20] J. J. Wortman and R. A. Evans, "Young's Modulus, Shear Modulus, and Poisson's Ratio in Silicon and Germanium," *Journal of Applied Physics*, vol. 36, pp. 153–156, Jan. 1965.

[21] J. M. Torres, N. Bakken, C. M. Stafford, J. Li, and B. D. Vogt, "Thickness dependence of the elastic modulus of tris(8-hydroxyquinolinato)aluminium," *Soft Matter*, vol. 6, pp. 5783–5788, Nov. 2010.

[22] C.-J. Chiang, S. Bull, C. Winscom, and A. Monkman, "A nano-indentation study of the reduced elastic modulus of Alq3 and NPB thin-film used in OLED devices," *Organic Electronics*, vol. 11, pp. 450–455, Mar. 2010.

[23] G. Chen, H. Sasabe, Z. Wang, X.-F. Wang, Z. Hong, Y. Yang, and J. Kido, "Co-Evaporated Bulk Heterojunction Solar Cells with >6.0% Efficiency," *Advanced Materials*, vol. 24, pp. 2768–2773, May 2012.

[24] A. K. K. Kyaw, X. W. Sun, C. Y. Jiang, G. Q. Lo, D. W. Zhao, and D. L. Kwong, "An inverted organic solar cell employing a sol-gel derived ZnO electron selective layer and thermal evaporated MoO3 hole selective layer," *Applied Physics Letters*, vol. 93, p. 221107, Dec. 2008.

[25] P. Servati and A. Nathan, "Orientation-dependent strain tolerance of amorphous silicon transistors and pixel circuits for elastic organic light-emitting diode displays," *Applied Physics Letters*, vol. 86, p. 033504, Jan. 2005.

[26] A. Jedaa and M. Halik, "Toward strain resistant flexible organic thin film transistors," *Applied Physics Letters*, vol. 95, p. 103309, Sept. 2009.

[27] P. Mach, S. J. Rodriguez, R. Nortrup, P. Wiltzius, and J. A. Rogers, "Monolithically integrated, flexible display of polymer-dispersed liquid crystal driven by rubber-stamped organic thin-film transistors," *Applied Physics Letters*, vol. 78, pp. 3592–3594, June 2001.

[28] E. Menard, M. A. Meitl, Y. Sun, J.-U. Park, D. J.-L. Shir, Y.-S. Nam, S. Jeon, and J. A. Rogers, "Micro- and nanopatterning techniques for organic electronic and optoelectronic systems," *Chemical Reviews*, vol. 107, pp. 1117–1160, Apr. 2007.

[29] A. L. Briseno, M. Roberts, M.-M. Ling, H. Moon, E. J. Nemanick, and Z. Bao, "Patterning Organic Semiconductors Using Dry Poly(dimethylsiloxane) Elastomeric Stamps for Thin Film Transistors," *Journal of the American Chemical Society*, vol. 128, pp. 3880–3881, Mar. 2006.

[30] J. Park and P. T. Hammond, "Multilayer Transfer Printing for Polyelectrolyte Multilayer Patterning: Direct Transfer of Layer-by-Layer Assembled Micropatterned Thin Films," *Advanced Materials*, vol. 16, pp. 520–525, Mar. 2004.

[31] J. A. DeFranco, B. S. Schmidt, M. Lipson, and G. G. Malliaras, "Photolithographic patterning of organic electronic materials," *Organic Electronics*, vol. 7, pp. 22–28, Feb. 2006.

[32] C. D. Mller, A. Falcou, N. Reckefuss, M. Rojahn, V. Wiederhirn, P. Rudati, H. Frohne, O. Nuyken, H. Becker, and K. Meerholz, "Multi-colour organic light-emitting displays by solution processing," *Nature*, vol. 421, pp. 829–833, Feb. 2003.

[33] M. Bafleur, A. Munoz-Yague, and A. Rocher, "Microtwinning and growth defects in GaAs MBE layers," *Journal of Crystal Growth*, vol. 59, pp. 531–538, Oct. 1982.

[34] G. W. Smith, A. J. Pidduck, C. R. Whitehouse, J. L. Glasper, and J. Spowart, "Real-time laser-light scattering studies of surface topography development during GaAs MBE growth," *Journal of Crystal Growth*, vol. 127, pp. 966–971, Feb. 1993.

[35] P. Calvert, "Inkjet Printing for Materials and Devices," *Chemistry of Materials*, vol. 13, pp. 3299–3305, Oct. 2001.

[36] H. Minemawari, T. Yamada, H. Matsui, J. Tsutsumi, S. Haas, R. Chiba, R. Kumai, and T. Hasegawa, "Inkjet printing of single-crystal films," *Nature*, vol. 475, pp. 364–367, July 2011.

[37] M. Hermenau, M. Riede, K. Leo, S. A. Gevorgyan, F. C. Krebs, and K. Norrman, "Water and oxygen induced degradation of small molecule organic solar cells," *Solar Energy Materials and Solar Cells*, vol. 95, pp. 1268–1277, May 2011.

[38] A. Seemann, T. Sauermann, C. Lungenschmied, O. Armbruster, S. Bauer, H. J. Egelhaaf, and J. Hauch, "Reversible and irreversible degradation of organic solar cell performance by oxygen," *Solar Energy*, vol. 85, pp. 1238–1249, June 2011.

[39] N. Grossiord, J. M. Kroon, R. Andriessen, and P. W. M. Blom, "Degradation mechanisms in organic photovoltaic devices," *Organic Electronics*, vol. 13, pp. 432–456, Mar. 2012.

[40] Y. Zhang, J. Lee, and S. R. Forrest, "Tenfold increase in the lifetime of blue phosphorescent organic light-emitting diodes," *Nature Communications*, vol. 5, Sept. 2014.

[41] M. A. Baldo, M. E. Thompson, and S. R. Forrest, "Phosphorescent materials for application to organic light emitting devices," *Pure and Applied Chemistry*, vol. 71, pp. 2095–2106, Nov. 1999. WOS:000088200100012.

[42] J. Meiss, K. Leo, M. K. Riede, C. Uhrich, W.-M. Gnehr, S. Sonntag, and M. Pfeiffer, "Efficient semitransparent small-molecule organic solar cells," *Applied Physics Letters*, vol. 95, no. 21, p. 213306, 2009.

[43] R. Koeppe, D. Hoeglinger, P. Troshin, R. Lyubovskaya, V. Razumov, and N. Sariciftci, "Organic Solar Cells with Semitransparent Metal Back Contacts for Power Window Applications," *ChemSusChem*, vol. 2, no. 4, pp. 309–313, 2009.

[44] R. R. Sndergaard, M. Hsel, and F. C. Krebs, "Roll-to-Roll fabrication of large area functional organic materials," *Journal of Polymer Science Part B: Polymer Physics*, vol. 51, pp. 16–34, Jan. 2013.

[45] F. C. Krebs, T. Tromholt, and M. Jrgensen, "Upscaling of polymer solar cell fabrication using full roll-to-roll processing," *Nanoscale*, vol. 2, pp. 873–886, June 2010.

[46] F. C. Krebs, "All solution roll-to-roll processed polymer solar cells free from indium-tin-oxide and vacuum coating steps," *Organic Electronics*, vol. 10, pp. 761–768, Aug. 2009.

[47] Y. Galagan, I. G. de Vries, A. P. Langen, R. Andriessen, W. J. H. Verhees, S. C. Veenstra, and J. M. Kroon, "Technology development for roll-to-roll production of organic photovoltaics," *Chemical Engineering and Processing: Process Intensification*, vol. 50, pp. 454–461, May 2011.

[48] F. C. Krebs, S. A. Gevorgyan, and J. Alstrup, "A roll-to-roll process to flexible polymer solar cells: model studies, manufacture and operational stability studies," *Journal of Materials Chemistry*, vol. 19, pp. 5442–5451, July 2009.

[49] C. J. Lawrence, "The mechanics of spin coating of polymer films," *Physics of Fluids (1958-1988)*, vol. 31, pp. 2786–2795, Oct. 1988.

[50] Y. Yao, J. Hou, Z. Xu, G. Li, and Y. Yang, "Effects of Solvent Mixtures on the Nanoscale Phase Separation in Polymer Solar Cells," *Advanced Functional Materials*, vol. 18, pp. 1783–1789, June 2008.

[51] F. Machui, S. Langner, X. Zhu, S. Abbott, and C. J. Brabec, "Determination of the P3ht:PCBM solubility parameters via a binary solvent gradient method: Impact of solubility on the photovoltaic performance," *Solar Energy Materials and Solar Cells*, vol. 100, pp. 138–146, May 2012.

[52] M. Drees, K. Premaratne, W. Graupner, J. R. Heflin, R. M. Davis, D. Marciu, and M. Miller, "Creation of a gradient polymer-fullerene interface in photovoltaic devices by thermally controlled interdiffusion," *Applied Physics Letters*, vol. 81, pp. 4607–4609, Dec. 2002.

[53] R. Pandey and R. J. Holmes, "Graded DonorAcceptor Heterojunctions for Efficient Organic Photovoltaic Cells," *Advanced Materials*, vol. 22, pp. 5301–5305, Dec. 2010.

[54] C. Girotto, B. P. Rand, S. Steudel, J. Genoe, and P. Heremans, "Nanoparticle-based, spray-coated silver top contacts for efficient polymer solar cells," *Organic Electronics*, vol. 10, pp. 735–740, July 2009.

[55] J. Krantz, T. Stubhan, M. Richter, S. Spallek, I. Litzov, G. J. Matt, E. Spiecker, and C. J. Brabec, "Spray-Coated Silver Nanowires as Top Electrode Layer in Semitransparent P3ht:PCBM-Based Organic Solar Cell Devices," *Advanced Functional Materials*, vol. 23, pp. 1711–1717, Apr. 2013.

[56] T. Pompe, A. Fery, S. Herminghaus, A. Kriele, H. Lorenz, and J. P. Kotthaus, "Submicron Contact Printing on Silicon Using Stamp Pads," *Langmuir*, vol. 15, pp. 2398–2401, Mar. 1999.

[57] Y. Sun, M. Shtein, and S. R. Forrest, "Direct patterning of organic light-emitting devices by organic-vapor jet printing," *Applied Physics Letters*, vol. 86, p. 113504, Mar. 2005.

[58] M. S. Arnold, G. J. McGraw, S. R. Forrest, and R. R. Lunt, "Direct vapor jet printing of three color segment organic light emitting devices for white light illumination," *Applied Physics Letters*, vol. 92, p. 053301, Feb. 2008.

[59] G. J. McGraw, D. L. Peters, and S. R. Forrest, "Organic vapor jet printing at micrometer resolution using microfluidic nozzle arrays," *Applied Physics Letters*, vol. 98, p. 013302, Jan. 2011.

[60] A. Manuelli, A. Knobloch, A. Bernds, and W. Clemens, "Applicability of coating techniques for the production of organic field effect transistors," in *2nd International IEEE Conference on Polymers and Adhesives in Microelectronics and Photonics, 2002. POLYTRONIC 2002*, pp. 201–204, 2002.

[61] Y.-H. Chang, S.-R. Tseng, C.-Y. Chen, H.-F. Meng, E.-C. Chen, S.-F. Horng, and C.-S. Hsu, "Polymer solar cell by blade coating," *Organic Electronics*, vol. 10, pp. 741–746, Aug. 2009.

[62] P. Schilinsky, C. Waldauf, and C. J. Brabec, "Performance Analysis of Printed Bulk Heterojunction Solar Cells," *Advanced Functional Materials*, vol. 16, pp. 1669–1672, Sept. 2006.

[63] I.-K. Ding, J. Melas-Kyriazi, N.-L. Cevey-Ha, K. G. Chittibabu, S. M. Zakeeruddin, M. Grtzel, and M. D. McGehee, "Deposition of hole-transport materials in solid-state dye-sensitized solar cells by doctor-blading," *Organic Electronics*, vol. 11, pp. 1217–1222, July 2010.

[64] C. J. Brabec and J. R. Durrant, "Solution-Processed Organic Solar Cells," *MRS Bulletin*, vol. 33, pp. 670–675, July 2008.

[65] N. A. Azarova, J. W. Owen, C. A. McLellan, M. A. Grimminger, E. K. Chapman, J. E. Anthony, and O. D. Jurchescu, "Fabrication of organic thin-film transistors by spray-deposition for low-cost, large-area electronics," *Organic Electronics*, vol. 11, pp. 1960–1965, Dec. 2010.

[66] C. Girotto, B. P. Rand, J. Genoe, and P. Heremans, "Exploring spray coating as a deposition technique for the fabrication of solution-processed solar cells," *Solar Energy Materials and Solar Cells*, vol. 93, pp. 454–458, Apr. 2009.

[67] S. M. Menke, W. A. Luhman, and R. J. Holmes, "Tailored exciton diffusion in organic photovoltaic cells for enhanced power conversion efficiency," *Nature Materials*, vol. 12, pp. 152–157, Feb. 2013. WOS:000314627000023.

[68] Q. Burlingame, X. Tong, J. Hankett, M. Slootsky, Z. Chen, and S. R. Forrest, "Photochemical origins of burn-in degradation in small molecular weight organic photovoltaic cells," *Energy & Environmental Science*, vol. 8, pp. 1005–1010, Mar. 2015.

[69] X. Tong, N. Wang, M. Slootsky, J. Yu, and S. R. Forrest, "Intrinsic burn-in efficiency loss of small-molecule organic photovoltaic cells due to exciton-induced trap formation," *Solar Energy Materials and Solar Cells*, vol. 118, pp. 116–123, Nov. 2013.

[70] L. Wang, D. Li, Y. Hu, and C. Jiang, "Realization of uniform large-area pentacene thin film transistor arrays by roller vacuum thermal evaporation," *Journal of Vacuum Science & Technology A*, vol. 29, p. 041510, July 2011.

[71] F. Yang, M. Shtein, and S. R. Forrest, "Controlled growth of a molecular bulk heterojunction photovoltaic cell," *Nature Materials*, vol. 4, pp. 37–41, Jan. 2005.

[72] M. A. Baldo, V. G. Kozlov, P. E. Burrows, S. R. Forrest, V. S. Ban, B. Koene, and M. E. Thompson, "Low pressure organic vapor phase deposition of small molecular weight organic light emitting device structures," *Applied Physics Letters*, vol. 71, pp. 3033–3035, Nov. 1997.

[73] M. Baldo, M. Deutsch, P. Burrows, H. Gossenberger, M. Gerstenberg, V. Ban, and S. Forrest, "Organic Vapor Phase Deposition," *Advanced Materials*, vol. 10, pp. 1505–1514, Dec. 1998.

[74] D. Pisignano, L. Persano, M. F. Raganato, P. Visconti, R. Cingolani, G. Barbarella, L. Favaretto, and G. Gigli, "Room-Temperature Nanoimprint Lithography of Non-thermoplastic Organic Films," *Advanced Materials*, vol. 16, pp. 525–529, Mar. 2004.

[75] C. Clavijo Cedeo, J. Seekamp, A. P. Kam, T. Hoffmann, S. Zankovych, C. M. Sotomayor Torres, C. Menozzi, M. Cavallini, M. Murgia, G. Ruani, F. Biscarini, M. Behl, R. Zentel, and J. Ahopelto, "Nanoimprint lithography for organic electronics," *Microelectronic Engineering*, vol. 6162, pp. 25–31, July 2002.

[76] L. J. Guo, "Nanoimprint Lithography: Methods and Material Requirements," *Advanced Materials*, vol. 19, pp. 495–513, Feb. 2007.

[77] G. De Luca, W. Pisula, D. Credgington, E. Treossi, O. Fenwick, G. M. Lazzerini, R. Dabirian, E. Orgiu, A. Liscio, V. Palermo, K. Mllen, F. Cacialli, and P. Samor, "Non-conventional Processing and Post-processing Methods for the Nanostructuring of Conjugated Materials for Organic Electronics," *Advanced Functional Materials*, vol. 21, pp. 1279–1295, Apr. 2011.

[78] R. W. I. de Boer, M. E. Gershenson, A. F. Morpurgo, and V. Podzorov, "Organic single-crystal field-effect transistors," *Physica Status Solidi a-Applied Research*, vol. 201, pp. 1302–1331, May 2004. WOS:000221705700015.

[79] R. R. Lunt, J. B. Benziger, and S. R. Forrest, "Growth of an Ordered Crystalline Organic Heterojunction," *Advanced Materials*, vol. 19, pp. 4229–4233, Dec. 2007.

[80] W. H. Lee, D. H. Kim, J. H. Cho, Y. Jang, J. A. Lim, D. Kwak, and K. Cho, "Change of molecular ordering in soluble acenes via solvent annealing and its effect on field-effect mobility," *Applied Physics Letters*, vol. 91, p. 092105, Aug. 2007.

[81] Y. Kim, S. A. Choulis, J. Nelson, D. D. C. Bradley, S. Cook, and J. R. Durrant, "Device annealing effect in organic solar cells with blends of regioregular poly(3-hexylthiophene) and soluble fullerene," *Applied Physics Letters*, vol. 86, p. 063502, Feb. 2005. WOS:000227355200073.

[82] G. Wei, R. R. Lunt, K. Sun, S. Wang, M. E. Thompson, and S. R. Forrest, "Efficient, Ordered Bulk Heterojunction Nanocrystalline Solar Cells by Annealing of Ultrathin Squaraine Thin Films," *Nano Letters*, vol. 10, pp. 3555–3559, Sept. 2010.

[83] K. C. Dickey, J. E. Anthony, and Y.-L. Loo, "Improving organic thin-film transistor performance through solvent-vapor annealing of solution-processable triethylsilylethynyl anthradithiophene," *Advanced Materials*, vol. 18, pp. 1721–+, July 2006. WOS:000239181300017.

[84] F.-C. Chen, C.-J. Ko, J.-L. Wu, and W.-C. Chen, "Morphological study of P3ht:PCBM blend films prepared through solvent annealing for solar cell applications," *Solar Energy Materials and Solar Cells*, vol. 94, pp. 2426–2430, Dec. 2010.

[85] P. Peumans, S. Uchida, and S. R. Forrest, "Efficient bulk heterojunction photovoltaic cells using small-molecular-weight organic thin films," *Nature*, vol. 425, pp. 158–162, Sept. 2003.

[86] J. J. Dittmer, R. Lazzaroni, P. Leclre, P. Moretti, M. Granstrm, K. Petritsch, E. A. Marseglia, R. H. Friend, J. L. Brdas, H. Rost, and A. B. Holmes, "Crystal network formation in organic solar cells," *Solar Energy Materials and Solar Cells*, vol. 61, pp. 53–61, Feb. 2000.

[87] J. C. Conboy, E. J. C. Olson, D. M. Adams, J. Kerimo, A. Zaban, B. A. Gregg, and P. F. Barbara, "Impact of Solvent Vapor Annealing on the Morphology and Photophysics of Molecular Semiconductor Thin Films," *The Journal of Physical Chemistry B*, vol. 102, pp. 4516–4525, June 1998.

[88] D. Placencia, W. Wang, R. C. Shallcross, K. W. Nebesny, M. Brumbach, and N. R. Armstrong, "Organic Photovoltaic Cells Based On Solvent-Annealed, Textured Titanyl Phthalocyanine/C60 Heterojunctions," *Advanced Functional Materials*, vol. 19, pp. 1913–1921, June 2009.

[89] J. D. Zimmerman, X. Xiao, C. K. Renshaw, S. Wang, V. V. Diev, M. E. Thompson, and S. R. Forrest, "Independent Control of Bulk and Interfacial Morphologies of Small Molecular Weight Organic Heterojunction Solar Cells," *Nano Letters*, vol. 12, pp. 4366–4371, Aug. 2012.

[90] G. Li, V. Shrotriya, J. Huang, Y. Yao, T. Moriarty, K. Emery, and Y. Yang, "High-efficiency solution processable polymer photovoltaic cells by self-organization of polymer blends," *Nature Materials*, vol. 4, pp. 864–868, Nov. 2005.

[91] G. Wei, S. Wang, K. Renshaw, M. E. Thompson, and S. R. Forrest, "Solution-Processed Squaraine Bulk Heterojunction Photovoltaic Cells," *ACS Nano*, vol. 4, pp. 1927–1934, Apr. 2010.

[92] G. Wei, S. Wang, K. Sun, M. E. Thompson, and S. R. Forrest, "Solvent-Annealed Crystalline Squaraine: PC70bm (1:6) Solar Cells," *Advanced Energy Materials*, vol. 1, pp. 184–187, Mar. 2011.

[93] C. W. Tang, "Twolayer organic photovoltaic cell," *Applied Physics Letters*, vol. 48, pp. 183–185, Jan. 1986.

[94] C. Deibel and V. Dyakonov, "Polymerfullerene bulk heterojunction solar cells," *Reports on Progress in Physics*, vol. 73, p. 096401, Sept. 2010.

[95] M. Riede, T. Mueller, W. Tress, R. Schueppel, and K. Leo, "Small-molecule solar cellsstatus and perspectives," *Nanotechnology*, vol. 19, p. 424001, Oct. 2008.

[96] G. Li, R. Zhu, and Y. Yang, "Polymer solar cells," *Nature Photonics*, vol. 6, pp. 153–161, Mar. 2012.

[97] V. I. Arkhipov, E. V. Emelianova, and H. Bssler, "Hot Exciton Dissociation in a Conjugated Polymer," *Physical Review Letters*, vol. 82, pp. 1321–1324, Feb. 1999.

[98] M. Tong, N. E. Coates, D. Moses, A. J. Heeger, S. Beaupr, and M. Leclerc, "Charge carrier photogeneration and decay dynamics in the poly(2,7-carbazole) copolymer PCDTBT and in bulk heterojunction composites with ${\text{PC}}_{70}\text{BM}$," *Physical Review B*, vol. 81, p. 125210, Mar. 2010.

[99] C.-C. Chen, W.-H. Chang, K. Yoshimura, K. Ohya, J. You, J. Gao, Z. Hong, and Y. Yang, "An Efficient Triple-Junction Polymer Solar Cell Having a Power Conversion Efficiency Exceeding 11%," *Advanced Materials*, vol. 26, no. 32, pp. 5670–5677, 2014.

[100] X. Xiao, J. D. Zimmerman, B. E. Lassiter, K. J. Bergemann, and S. R. Forrest, "A hybrid planar-mixed tetraphenyldibenzoperiflanthene/C70 photovoltaic cell," *Applied Physics Letters*, vol. 102, p. 073302, Feb. 2013.

[101] M. Granstrm, K. Petritsch, A. C. Arias, A. Lux, M. R. Andersson, and R. H. Friend, "Laminated fabrication of polymeric photovoltaic diodes," *Nature*, vol. 395, pp. 257–260, Sept. 1998.

[102] G. Yu, J. Gao, J. Hummelen, F. Wudl, and A. Heeger, "Polymer Photovoltaic Cells - Enhanced Efficiencies Via a Network of Internal Donor-Acceptor Heterojunctions," *Science*, vol. 270, pp. 1789–1791, Dec. 1995. WOS:A1995TK47600035.

[103] N. Li and S. R. Forrest, "Tilted bulk heterojunction organic photovoltaic cells grown by oblique angle deposition," *Applied Physics Letters*, vol. 95, p. 123309, Sept. 2009.

[104] J. Xue, B. P. Rand, S. Uchida, and S. R. Forrest, "A Hybrid PlanarMixed Molecular Heterojunction Photovoltaic Cell," *Advanced Materials*, vol. 17, pp. 66–71, Jan. 2005.

[105] A. Mishra and P. Buerle, "Small Molecule Organic Semiconductors on the Move: Promises for Future Solar Energy Technology," *Angewandte Chemie International Edition*, vol. 51, pp. 2020–2067, Feb. 2012.

[106] N. C. Giebink, G. P. Wiederrecht, M. R. Wasielewski, and S. R. Forrest, "Thermodynamic efficiency limit of excitonic solar cells," *Physical Review B*, vol. 83, p. 195326, May 2011.

[107] J. Adams, G. D. Spyropoulos, M. Salvador, N. Li, S. Strohm, L. Lucera, S. Langner, F. Machui, H. Zhang, T. Ameri, M. M. Voigt, F. C. Krebs, and C. J. Brabec, "Air-processed organic tandem solar cells on glass: toward competitive operating lifetimes," *Energy & Environmental Science*, vol. 8, pp. 169–176, Dec. 2014.

[108] R. Sherman, "Carbon Dioxide Snow Cleaning," *Particulate Science and Technology*, vol. 25, pp. 37–57, Jan. 2007.

[109] R. Sherman, J. Grob, and W. Whitlock, "Dry surface cleaning using CO2 snow," *Journal of Vacuum Science & Technology B*, vol. 9, pp. 1970–1977, July 1991.

[110] R. Sherman, D. Hirt, and R. Vane, "Surface cleaning with the carbon dioxide snow jet," *Journal of Vacuum Science & Technology A*, vol. 12, pp. 1876–1881, July 1994.

[111] N. Wang, J. D. Zimmerman, X. Tong, X. Xiao, J. Yu, and S. R. Forrest, "Snow cleaning of substrates increases yield of large-area organic photovoltaics," *Applied Physics Letters*, vol. 101, p. 133901, Sept. 2012.

[112] M. Pope, H. P. Kallmann, and P. Magnante, "Electroluminescence in Organic Crystals," *The Journal of Chemical Physics*, vol. 38, pp. 2042–2043, Apr. 1963.

[113] C. W. Tang and S. A. VanSlyke, "Organic electroluminescent diodes," *Applied Physics Letters*, vol. 51, pp. 913–915, Sept. 1987.

[114] Y. Hamada, H. Kanno, T. Tsujioka, H. Takahashi, and T. Usuki, "Red organic light-emitting diodes using an emitting assist dopant," *Applied Physics Letters*, vol. 75, pp. 1682–1684, Sept. 1999.

[115] M. A. Baldo, C. Adachi, and S. R. Forrest, "Transient analysis of organic electrophosphorescence. II.\quad{}Transient analysis of triplet-triplet annihilation," *Physical Review B*, vol. 62, pp. 10967–10977, Oct. 2000.

[116] A. Endo, M. Ogasawara, A. Takahashi, D. Yokoyama, Y. Kato, and C. Adachi, "Thermally Activated Delayed Fluorescence from Sn4+Porphyrin Complexes and Their Application to Organic Light Emitting Diodes A Novel Mechanism for Electroluminescence," *Advanced Materials*, vol. 21, pp. 4802–4806, Dec. 2009.

[117] Q. Zhang, J. Li, K. Shizu, S. Huang, S. Hirata, H. Miyazaki, and C. Adachi, "Design of Efficient Thermally Activated Delayed Fluorescence Materials for Pure Blue Organic Light Emitting Diodes," *Journal of the American Chemical Society*, vol. 134, pp. 14706–14709, Sept. 2012.

[118] S. Y. Lee, T. Yasuda, H. Nomura, and C. Adachi, "High-efficiency organic light-emitting diodes utilizing thermally activated delayed fluorescence from triazine-based donoracceptor hybrid molecules," *Applied Physics Letters*, vol. 101, p. 093306, Aug. 2012.

[119] Y. Sun and S. R. Forrest, "Enhanced light out-coupling of organic light-emitting devices using embedded low-index grids," *Nature Photonics*, vol. 2, pp. 483–487, Aug. 2008.

[120] M. Slootsky and S. R. Forrest, "Full-wave simulation of enhanced outcoupling of organic light-emitting devices with an embedded low-index grid," *Applied Physics Letters*, vol. 94, p. 163302, Apr. 2009.

[121] J. Frischeisen, D. Yokoyama, A. Endo, C. Adachi, and W. Brtting, "Increased light outcoupling efficiency in dye-doped small molecule organic light-emitting diodes with horizontally oriented emitters," *Organic Electronics*, vol. 12, pp. 809–817, May 2011.

[122] S. Reineke, F. Lindner, G. Schwartz, N. Seidler, K. Walzer, B. Lssem, and K. Leo, "White organic light-emitting diodes with fluorescent tube efficiency," *Nature*, vol. 459, pp. 234–238, May 2009.

[123] P. Sorokin and J. Lankard, "Stimulated Emission Observed from an Organic Dye Chloro-Aluminum Phthalocyanine," *Ibm Journal of Research and Development*, vol. 10, no. 2, pp. 162–&, 1966. WOS:A19667564200007.

[124] V. G. Kozlov, V. Bulovic, P. E. Burrows, and S. R. Forrest, "Laser action in organic semiconductor waveguide and double-heterostructure devices," *Nature*, vol. 389, pp. 362–364, Sept. 1997. WOS:A1997XX67500046.

[125] Y. Zhang and S. R. Forrest, "Existence of continuous-wave threshold for organic semiconductor lasers," *Physical Review B*, vol. 84, p. 241301, Dec. 2011.

[126] Z. Zhao, O. Mhibik, M. Nafa, S. Chnais, and S. Forget, "High brightness diode-pumped organic solid-state laser," *Applied Physics Letters*, vol. 106, p. 051112, Feb. 2015.

[127] S. Chnais and S. Forget, "Recent advances in solid-state organic lasers," *Polymer International*, vol. 61, pp. 390–406, Mar. 2012.

[128] M. Slootsky, Y. Zhang, and S. R. Forrest, "Temperature dependence of polariton lasing in a crystalline anthracene microcavity," *Physical Review B*, vol. 86, p. 045312, July 2012.

[129] V. G. Kozlov, V. Bulovi, and S. R. Forrest, "Temperature independent performance of organic semiconductor lasers," *Applied Physics Letters*, vol. 71, pp. 2575–2577, Nov. 1997.

[130] G. Ramos-Ortiz, C. Spiegelberg, N. Peyghambarian, and B. Kippelen, "Temperature dependence of the threshold for laser emission in polymer microlasers," *Applied Physics Letters*, vol. 77, pp. 2783–2785, Oct. 2000.

[131] Z. Bao, A. J. Lovinger, and A. Dodabalapur, "Organic fieldeffect transistors with high mobility based on copper phthalocyanine," *Applied Physics Letters*, vol. 69, pp. 3066–3068, Nov. 1996.

[132] D. Gundlach, Y. Lin, T. Jackson, S. Nelson, and D. Schlom, "Pentacene organic thin-film transistors-molecular ordering and mobility," *IEEE Electron Device Letters*, vol. 18, pp. 87–89, Mar. 1997.

[133] M. M. Somoza, "English: Depiction of Franck Condon principle in absorption and fluorescence.," May 2006.

[134] I. Pelant and J. Valenta, *Luminescence Spectroscopy of Semiconductors*. Oxford ; New York: Oxford University Press, 1 edition ed., Mar. 2012.

[135] G. G. Guilbault, ed., *Practical Fluorescence, Second Edition*. New York: CRC Press, 2 edition ed., Oct. 1990.

[136] J. S. Townsend, *A Modern Approach to Quantum Mechanics*. University Science Books, Jan. 2000.

[137] J. J. Sakurai, *Modern Quantum Mechanics*. Reading, Mass: Addison Wesley, 1 edition ed., Sept. 1993.

[138] R. R. Lunt, N. C. Giebink, A. A. Belak, J. B. Benziger, and S. R. Forrest, "Exciton diffusion lengths of organic semiconductor thin films measured by spectrally resolved photoluminescence quenching," *Journal of Applied Physics*, vol. 105, no. 5, p. 053711, 2009.

[139] S. E. Braslavsky, E. Fron, H. B. Rodrguez, E. S. Romn, G. D. Scholes, G. Schweitzer, B. Valeur, and J. Wirz, "Pitfalls and limitations in the practical use of Frster's theory of resonance energy transfer," *Photochemical & Photobiological Sciences*, vol. 7, no. 12, p. 1444, 2008.

[140] I. I. Fishchuk, D. Hertel, H. Bssler, and A. K. Kadashchuk, "Effective-medium theory of hopping charge-carrier transport in weakly disordered organic solids," *Physical Review B*, vol. 65, p. 125201, Mar. 2002.

[141] R. A. Marcus, "Electron transfer reactions in chemistry. Theory and experiment," *Reviews of Modern Physics*, vol. 65, pp. 599–610, July 1993.

[142] Brookhaven National Laboratory. and United States., *Marcus equation*. No. 9 p., Washington, D.C. : Oak Ridge, Tenn.: United States. Dept. of Energy. Office of Energy Research ; distributed by the Office of Scientific and Technical Information, U.S. Dept. of Energy, 1998. bibtex: BrookhavenNationalLaboratory.1998.

[143] B. C. Lin, C. P. Cheng, Z.-Q. You, and C.-P. Hsu, "Charge Transport Properties of Tris(8-hydroxyquinolinato)aluminum(III): Why It Is an Electron Transporter," *Journal of the American Chemical Society*, vol. 127, pp. 66–67, Jan. 2005.

[144] H. Ohkita, S. Cook, Y. Astuti, W. Duffy, S. Tierney, W. Zhang, M. Heeney, I. McCulloch, J. Nelson, D. D. C. Bradley, and J. R. Durrant, "Charge Carrier Formation in Polythiophene/Fullerene Blend Films Studied by Transient Absorption Spectroscopy," *Journal of the American Chemical Society*, vol. 130, pp. 3030–3042, Mar. 2008.

[145] A. A. Bakulin, A. Rao, V. G. Pavelyev, P. H. M. v. Loosdrecht, M. S. Pshenichnikov, D. Niedzialek, J. Cornil, D. Beljonne, and R. H. Friend, "The Role of Driving Energy and Delocalized States for Charge Separation in Organic Semiconductors," *Science*, vol. 335, pp. 1340–1344, Mar. 2012.

[146] G. Grancini, M. Maiuri, D. Fazzi, A. Petrozza, H.-J. Egelhaaf, D. Brida, G. Cerullo, and G. Lanzani, "Hot exciton dissociation in polymer solar cells," *Nature Materials*, vol. 12, pp. 29–33, Jan. 2013.

[147] N. C. Giebink, G. P. Wiederrecht, M. R. Wasielewski, and S. R. Forrest, "Ideal diode equation for organic heterojunctions. I. Derivation and application," *Physical Review B*, vol. 82, p. 155305, Oct. 2010.

[148] N. C. Giebink, B. E. Lassiter, G. P. Wiederrecht, M. R. Wasielewski, and S. R. Forrest, "Ideal diode equation for organic heterojunctions. II. The role of polaron pair recombination," *Physical Review B*, vol. 82, p. 155306, Oct. 2010.

[149] P. Parkinson, J. Lloyd-Hughes, M. B. Johnston, and L. M. Herz, "Efficient generation of charges via below-gap photoexcitation of polymer-fullerene blend films investigated by terahertz spectroscopy," *Physical Review B*, vol. 78, p. 115321, Sept. 2008.

[150] J. Lee, K. Vandewal, S. R. Yost, M. E. Bahlke, L. Goris, M. A. Baldo, J. V. Manca, and T. V. Voorhis, "Charge Transfer State Versus Hot Exciton Dissociation in PolymerFullerene Blended Solar Cells," *Journal of the American Chemical Society*, vol. 132, pp. 11878–11880, Sept. 2010.

[151] T. G. J. van der Hofstad, D. Di Nuzzo, M. van den Berg, R. A. J. Janssen, and S. C. J. Meskers, "Influence of Photon Excess Energy on Charge Carrier Dynamics in a Polymer-Fullerene Solar Cell," *Advanced Energy Materials*, vol. 2, pp. 1095–1099, Sept. 2012.

[152] K. Vandewal, S. Albrecht, E. T. Hoke, K. R. Graham, J. Widmer, J. D. Douglas, M. Schubert, W. R. Mateker, J. T. Bloking, G. F. Burkhard, A. Sellinger, J. M. J. Frchet, A. Amassian, M. K. Riede, M. D. McGehee, D. Neher, and A. Salleo, "Efficient charge generation by relaxed charge-transfer states at organic interfaces," *Nature Materials*, vol. advance online publication, Nov. 2013.

[153] R. Gresser, M. Hummert, H. Hartmann, K. Leo, and M. Riede, "Synthesis and Characterization of Near-Infrared Absorbing Benzannulated Aza-BODIPY Dyes," *Chemistry A European Journal*, vol. 17, pp. 2939–2947, Mar. 2011.

[154] J. Meiss, F. Holzmueller, R. Gresser, K. Leo, and M. Riede, "Near-infrared absorbing semitransparent organic solar cells," *Applied Physics Letters*, vol. 99, p. 193307, Nov. 2011.

[155] C. Yin, M. Schubert, S. Bange, B. Stiller, M. Castellani, D. Neher, M. Kumke, and H.-H. Hrhold, "Tuning of the Excited-State Properties and Photovoltaic Performance in PPV-Based Polymer Blends," *The Journal of Physical Chemistry C*, vol. 112, pp. 14607–14617, Sept. 2008.

[156] P. Wurfel, "The chemical potential of radiation," *Journal of Physics C: Solid State Physics*, vol. 15, p. 3967, June 1982.

[157] P. Wrfel, *Physics of Solar Cells: From Basic Principles to Advanced Concepts*. Weinheim: Wiley-VCH, 1 edition ed., Mar. 2009.

[158] W. Shockley and H. J. Queisser, "Detailed Balance Limit of Efficiency of p-n Junction Solar Cells," *Journal of Applied Physics*, vol. 32, no. 3, p. 510, 1961.

[159] A. S. Brown and M. A. Green, "Detailed balance limit for the series constrained two terminal tandem solar cell," *Physica E: Low-dimensional Systems and Nanostructures*, vol. 14, pp. 96–100, Apr. 2002.

[160] A. D. Vos, "Detailed balance limit of the efficiency of tandem solar cells," *Journal of Physics D: Applied Physics*, vol. 13, p. 839, May 1980.

[161] F. Meillaud, A. Shah, C. Droz, E. Vallat-Sauvain, and C. Miazza, "Efficiency limits for single-junction and tandem solar cells," *Solar Energy Materials and Solar Cells*, vol. 90, pp. 2952–2959, Nov. 2006.

[162] C. C. Grosjean and A. D. Vos, "On the upper limit of the energy conversion efficiency in tandem solar cells," *Journal of Physics D: Applied Physics*, vol. 14, p. 883, May 1981.

[163] D. N. Congreve, J. Lee, N. J. Thompson, E. Hontz, S. R. Yost, P. D. Reusswig, M. E. Bahlke, S. Reineke, T. V. Voorhis, and M. A. Baldo, "External Quantum Efficiency Above 100% in a Singlet-Exciton-FissionBased Organic Photovoltaic Cell," *Science*, vol. 340, pp. 334–337, Apr. 2013.

[164] R. R. Alfano, S. L. Shapiro, and M. Pope, "Fission rate of singlet excitons in a tetracene crystal measured with picosecond laser pulses," *Optics Communications*, vol. 9, pp. 388–391, Dec. 1973.

[165] T. C. Berkelbach, M. S. Hybertsen, and D. R. Reichman, "Microscopic theory of singlet exciton fission. I. General formulation," *The Journal of Chemical Physics*, vol. 138, no. 11, p. 114102, 2013.

[166] C. Deibel and A. Wagenpfahl, "Comment on Interface state recombination in organic solar cells," *Physical Review B*, vol. 82, p. 207301, Nov. 2010.

[167] T. Kirchartz, J. Mattheis, and U. Rau, "Detailed balance theory of excitonic and bulk heterojunction solar cells," *Physical Review B*, vol. 78, p. 235320, Dec. 2008.

[168] B. P. Rand, D. P. Burk, and S. R. Forrest, "Offset energies at organic semiconductor heterojunctions and their influence on the open-circuit voltage of thin-film solar cells," *Physical Review B*, vol. 75, p. 115327, Mar. 2007.

[169] M. D. Perez, C. Borek, S. R. Forrest, and M. E. Thompson, "Molecular and Morphological Influences on the Open Circuit Voltages of Organic Photovoltaic Devices," *Journal of the American Chemical Society*, vol. 131, pp. 9281–9286, July 2009.

[170] X. Xiao, K. J. Bergemann, J. D. Zimmerman, K. Lee, and S. R. Forrest, "Small-Molecule Planar-Mixed Heterojunction Photovoltaic Cells with Fullerene-Based Electron Filtering Buffers," *Advanced Energy Materials*, pp. n/a–n/a, 2013.

[171] D. J. Griffiths, *Introduction to Electrodynamics*. Prentice Hall, 1999.

[172] P. Peumans, A. Yakimov, and S. R. Forrest, "Small molecular weight organic thin-film photodetectors and solar cells," *Journal of Applied Physics*, vol. 93, no. 7, p. 3693, 2003.

[173] O. S. Heavens, *Optical Properties of Thin Solid Films*. Courier Dover Publications, 1991.

[174] L. A. A. Pettersson, L. S. Roman, and O. Ingans, "Modeling photocurrent action spectra of photovoltaic devices based on organic thin films," *Journal of Applied Physics*, vol. 86, pp. 487–496, July 1999.

[175] Y. Sun, N. C. Giebink, H. Kanno, B. Ma, M. E. Thompson, and S. R. Forrest, "Management of singlet and triplet excitons for efficient white organic light-emitting devices," *Nature*, vol. 440, pp. 908–912, Apr. 2006.

[176] A. K. Ghosh and T. Feng, "Merocyanine organic solar cells," *Journal of Applied Physics*, vol. 49, pp. 5982–5989, Dec. 1978.

[177] S.-B. Rim and P. Peumans, "The effects of optical interference on exciton diffusion length measurements using photocurrent spectroscopy," *Journal of Applied Physics*, vol. 103, p. 124515, June 2008.

[178] A. C. Drr, F. Schreiber, M. Kelsch, H. D. Carstanjen, H. Dosch, and O. H. Seeck, "Morphology and interdiffusion behavior of evaporated metal films on crystalline diindenoperylene thin films," *Journal of Applied Physics*, vol. 93, pp. 5201–5209, May 2003.

[179] V. Bulovi and S. R. Forrest, "Excitons in crystalline thin films of 3,4,9,10-perylenetetracarboxylic dianhydride studied by photocurrent response," *Chemical Physics Letters*, vol. 238, pp. 88–92, May 1995.

[180] D. Kurrle and J. Pflaum, "Exciton diffusion length in the organic semiconductor diindenoperylene," *Applied Physics Letters*, vol. 92, p. 133306, Mar. 2008.

[181] N. Matsusue, S. Ikame, Y. Suzuki, and H. Naito, "Charge-carrier transport and triplet exciton diffusion in a blue electrophosphorescent emitting layer," *Journal of Applied Physics*, vol. 97, p. 123512, June 2005.

[182] A. Haugeneder, M. Neges, C. Kallinger, W. Spirkl, U. Lemmer, J. Feldmann, U. Scherf, E. Harth, A. Ggel, and K. Mllen, "Exciton diffusion and dissociation in conjugated polymer/fullerene blends and heterostructures," *Physical Review B*, vol. 59, p. 15346, June 1999.

[183] B. A. Gregg, J. Sprague, and M. W. Peterson, "Long-Range Singlet Energy Transfer in Perylene Bis(phenethylimide) Films," *The Journal of Physical Chemistry B*, vol. 101, pp. 5362–5369, July 1997.

[184] R. C. Powell and Z. G. Soos, "Singlet exciton energy transfer in organic solids," *Journal of Luminescence*, vol. 11, pp. 1–45, Sept. 1975.

[185] S. R. Scully and M. D. McGehee, "Effects of optical interference and energy transfer on exciton diffusion length measurements in organic semiconductors," *Journal of Applied Physics*, vol. 100, pp. 034907–034907–5, Aug. 2006.

[186] R. R. Lunt, J. B. Benziger, and S. R. Forrest, "Relationship between Crystalline Order and Exciton Diffusion Length in Molecular Organic Semiconductors," *Advanced Materials*, vol. 22, pp. 1233–1236, Mar. 2010.

[187] G. Vaubel and H. Kallmann, "Diffusion Length and Lifetime of Triplet Excitons and Crystal Absorption Coefficient in Tetracene Determined from Photocurrent Measurements," *Physica Status Solidi*, vol. 35, no. 2, pp. 789–&, 1969. WOS:A1969E256300027.

[188] W. Hofberger and H. Bassler, "Diffusion of Triplet Excitons in Amorphous Tetracene," *Physica Status Solidi B-Basic Research*, vol. 69, no. 2, pp. 725–730, 1975. WOS:A1975AH64000047.

[189] J. Kalinowski, "Quenching of Delayed Fluorescence at Tetracene Crystal Aqueous Electrode Interface," *Journal of Luminescence*, vol. 11, no. 5-6, pp. 393–402, 1976. WOS:A1976BV14200011.

[190] J. Aladekomo, S. Arnold, and M. Pope, "Triplet Exciton Diffusion and Double Photon Absorption in Tetracene," *Physica Status Solidi B-Basic Research*, vol. 80, no. 1, pp. 333–340, 1977. WOS:A1977DA63700038.

[191] B. E. Lassiter, G. Wei, S. Wang, J. D. Zimmerman, V. V. Diev, M. E. Thompson, and S. R. Forrest, "Organic photovoltaics incorporating electron conducting exciton blocking layers," *Applied Physics Letters*, vol. 98, p. 243307, June 2011.

[192] G. Wei, X. Xiao, S. Wang, K. Sun, K. J. Bergemann, M. E. Thompson, and S. R. Forrest, "Functionalized Squaraine Donors for Nanocrystalline Organic Photovoltaics," *ACS Nano*, vol. 6, no. 1, pp. 972–978, 2011.

[193] W. A. Luhman and R. J. Holmes, "Investigation of Energy Transfer in Organic Photovoltaic Cells and Impact on Exciton Diffusion Length Measurements," *Advanced Functional Materials*, vol. 21, pp. 764–771, Feb. 2011.

[194] H. . Gommans, D. Cheyns, T. Aernouts, C. Girotto, J. Poortmans, and P. Heremans, "ElectroOptical Study of Subphthalocyanine in a Bilayer Organic Solar Cell," *Advanced Functional Materials*, vol. 17, pp. 2653–2658, Oct. 2007.

[195] K. L. Mutolo, E. I. Mayo, B. P. Rand, S. R. Forrest, and M. E. Thompson, "Enhanced Open-Circuit Voltage in Subphthalocyanine/C60 Organic Photovoltaic Cells," *Journal of the American Chemical Society*, vol. 128, pp. 8108–8109, June 2006.

[196] X. Tong, B. E. Lassiter, and S. R. Forrest, "Inverted organic photovoltaic cells with high open-circuit voltage," *Organic Electronics*, vol. 11, pp. 705–709, Apr. 2010.

[197] M. C. Fravventura, J. Hwang, J. W. A. Suijkerbuijk, P. Erk, L. D. A. Siebbeles, and T. J. Savenije, "Determination of Singlet Exciton Diffusion Length in Thin Evaporated C60 Films for Photovoltaics," *The Journal of Physical Chemistry Letters*, vol. 3, pp. 2367–2373, Sept. 2012.

[198] K. J. Bergemann and S. R. Forrest, "Measurement of exciton diffusion lengths in optically thin organic films," *Applied Physics Letters*, vol. 99, no. 24, p. 243303, 2011.

[199] G. Orlandi and F. Negri, "Electronic states and transitions in C-60 and C-70 fullerenes," *Photochemical & Photobiological Sciences*, vol. 1, pp. 289–308, May 2002. WOS:000176893800001.

[200] J. W. Arbogast, A. P. Darmanyan, C. S. Foote, F. N. Diederich, R. L. Whetten, Y. Rubin, M. M. Alvarez, and S. J. Anz, "Photophysical properties of sixty atom carbon molecule (C60)," *The Journal of Physical Chemistry*, vol. 95, pp. 11–12, Jan. 1991.

[201] Y. Shao and Y. Yang, "Efficient Organic Heterojunction Photovoltaic Cells Based on Triplet Materials," *Advanced Materials*, vol. 17, no. 23, pp. 2841–2844, 2005.

[202] W.-C. Hung, C.-D. Ho, C.-P. Liu, and Y.-P. Lee, "Laser-Induced Fluorescence and Phosphorescence of C60 Isolated in Solid Ne," *The Journal of Physical Chemistry*, vol. 100, pp. 3927–3932, Jan. 1996.

[203] C. Reber, L. Yee, J. McKiernan, J. I. Zink, R. S. Williams, W. M. Tong, D. A. A. Ohlberg, R. L. Whetten, and F. Diederich, "Luminescence and absorption spectra of carbon (C60) films," *The Journal of Physical Chemistry*, vol. 95, pp. 2127–2129, Mar. 1991.

[204] E.-j. Shin, J. Park, M. Lee, D. Kim, Y. Doug Suh, S. Ik Yang, S. Min Jin, and S. Keun Kim, "Temperature-dependent photoluminescence study of C60 and C70," *Chemical Physics Letters*, vol. 209, pp. 427–433, July 1993.

[205] V. Capozzi, G. Casamassima, G. F. Lorusso, A. Minafra, R. Piccolo, T. Trovato, and A. Valentini, "Optical spectra and photoluminescence of C60 thin films," *Solid State Communications*, vol. 98, pp. 853–858, June 1996.

[206] D. Qin, P. Gu, R. S. Dhar, S. G. Razavipour, and D. Ban, "Measuring the exciton diffusion length of C60 in organic planar heterojunction solar cells," *physica status solidi (a)*, vol. 208, no. 8, pp. 1967–1971, 2011.

[207] P. A. Lane, P. D. Cunningham, J. S. Melinger, G. P. Kushto, O. Esenturk, and E. J. Heilweil, "Photoexcitation Dynamics in Films of C60 and Zn Phthalocyanine with a Layered Nanostructure," *Physical Review Letters*, vol. 108, p. 077402, Feb. 2012.

[208] R. Pandey, Y. Zou, and R. J. Holmes, "Efficient, bulk heterojunction organic photovoltaic cells based on boron subphthalocyanine chloride-C70," *Applied Physics Letters*, vol. 101, p. 033308, July 2012.

[209] S. Kazaoui, N. Minami, Y. Tanabe, H. J. Byrne, A. Eilmes, and P. Petelenz, "Comprehensive analysis of intermolecular charge-transfer excited states in C_{60} and C_{70} films," *Physical Review B*, vol. 58, pp. 7689–7700, Sept. 1998.

[210] A. Miller and E. Abrahams, "Impurity Conduction at Low Concentrations," *Physical Review*, vol. 120, pp. 745–755, Nov. 1960.

[211] B. E. Lassiter, J. D. Zimmerman, A. Panda, X. Xiao, and S. R. Forrest, "Tandem organic photovoltaics using both solution and vacuum deposited small molecules," *Applied Physics Letters*, vol. 101, p. 063303, Aug. 2012.

[212] D. F. OBrien, M. A. Baldo, M. E. Thompson, and S. R. Forrest, "Improved energy transfer in electrophosphorescent devices," *Applied Physics Letters*, vol. 74, pp. 442–444, Jan. 1999.

[213] G. Parthasarathy, C. Adachi, P. E. Burrows, and S. R. Forrest, "High-efficiency transparent organic light-emitting devices," *Applied Physics Letters*, vol. 76, pp. 2128–2130, Apr. 2000.

[214] V. Bulovi, P. Tian, P. E. Burrows, M. R. Gokhale, S. R. Forrest, and M. E. Thompson, "A surface-emitting vacuum-deposited organic light emitting device," *Applied Physics Letters*, vol. 70, pp. 2954–2954, June 1997.

[215] S. E. Burns, N. Pfeffer, J. Grner, M. Remmers, T. Javoreck, D. Neher, and R. H. Friend, "Measurements of optical electric field intensities in microcavities using thin emissive polymer films," *Advanced Materials*, vol. 9, pp. 395–398, May 1997.

[216] M. Y. Chan, C. S. Lee, S. L. Lai, M. K. Fung, F. L. Wong, H. Y. Sun, K. M. Lau, and S. T. Lee, "Efficient organic photovoltaic devices using a combination of exciton blocking layer and anodic buffer layer," *Journal of Applied Physics*, vol. 100, p. 094506, Nov. 2006. WOS:000242041500109.

[217] N. Wang, J. Yu, Y. Zang, J. Huang, and Y. Jiang, "Effect of buffer layers on the performance of organic photovoltaic cells based on copper phthalocyanine and C-60," *Solar Energy Materials and Solar Cells*, vol. 94, pp. 263–266, Feb. 2010. WOS:000274291300024.

[218] B. P. Rand, J. Li, J. Xue, R. J. Holmes, M. E. Thompson, and S. R. Forrest, "Organic Double-Heterostructure Photovoltaic Cells Employing Thick Tris(acetylacetonato)ruthenium(III) Exciton-Blocking Layers," *Advanced Materials*, vol. 17, pp. 2714–2718, Nov. 2005.

[219] C. K. Renshaw, C. W. Schlenker, M. E. Thompson, and S. R. Forrest, "Reciprocal carrier collection in organic photovoltaics," *Physical Review B*, vol. 84, p. 045315, July 2011.

[220] A. N. Bartynski, C. Trinh, A. Panda, K. Bergemann, B. E. Lassiter, J. D. Zimmerman, S. R. Forrest, and M. E. Thompson, "A Fullerene-Based Organic Exciton Blocking Layer with High Electron Conductivity," *Nano Letters*, vol. 13, pp. 3315–3320, July 2013.

[221] E. L. Shirley, L. X. Benedict, and S. G. Louie, "Excitons in solid ${\mathrm{C}}_{60}$," *Physical Review B*, vol. 54, pp. 10970–10977, Oct. 1996.

[222] P. Peumans, V. Bulovi, and S. R. Forrest, "Efficient photon harvesting at high optical intensities in ultrathin organic double-heterostructure photovoltaic diodes," *Applied Physics Letters*, vol. 76, pp. 2650–2652, May 2000.

[223] J. M. Hodgkiss, S. Albert-Seifried, A. Rao, A. J. Barker, A. R. Campbell, R. A. Marsh, and R. H. Friend, "Exciton-Charge Annihilation in Organic Semiconductor Films," *Advanced Functional Materials*, vol. 22, pp. 1567–1577, Apr. 2012.

[224] B. Verreet, P. E. Malinowski, B. Niesen, D. Cheyns, P. Heremans, A. Stesmans, and B. P. Rand, "Improved cathode buffer layer to decrease exciton recombination in organic planar heterojunction solar cells," *Applied Physics Letters*, vol. 102, p. 043301, Jan. 2013.

[225] A. K. K. Kyaw, D. H. Wang, V. Gupta, W. L. Leong, L. Ke, G. C. Bazan, and A. J. Heeger, "Intensity Dependence of CurrentVoltage Characteristics and Recombination in High-Efficiency Solution-Processed Small-Molecule Solar Cells," *ACS Nano*, vol. 7, pp. 4569–4577, May 2013.

[226] L. J. A. Koster, V. D. Mihailetchi, and P. W. M. Blom, "Bimolecular recombination in polymer/fullerene bulk heterojunction solar cells," *Applied Physics Letters*, vol. 88, p. 052104, Jan. 2006.

[227] B. P. Rand, J. Xue, S. Uchida, and S. R. Forrest, "Mixed donor-acceptor molecular heterojunctions for photovoltaic applications. I. Material properties," *Journal of Applied Physics*, vol. 98, p. 124902, Dec. 2005.

[228] M. A. Khan, W. Xu, K. ul Haq, Y. Bai, X. Y. Jiang, Z. L. Zhang, W. Q. Zhu, Z. L. Zhang, and W. Q. Zhu, "Electron mobility of 4,7-diphyenyl-1,10-phenanthroline estimated by using space-charge-limited currents," *Journal of Applied Physics*, vol. 103, p. 014509, Jan. 2008.

[229] W. Tress, S. Corvers, K. Leo, and M. Riede, "Investigation of Driving Forces for Charge Extraction in Organic Solar Cells: Transient Photocurrent Measurements on Solar Cells Showing S-Shaped CurrentVoltage Characteristics," *Advanced Energy Materials*, vol. 3, no. 7, pp. 873–880, 2013.

[230] R. A. Street, "Localized state distribution and its effect on recombination in organic solar cells," *Physical Review B*, vol. 84, p. 075208, Aug. 2011.

[231] C. R. McNeill, I. Hwang, and N. C. Greenham, "Photocurrent transients in all-polymer solar cells: Trapping and detrapping effects," *Journal of Applied Physics*, vol. 106, p. 024507, July 2009.

[232] V. I. Roldughin and V. V. Vysotskii, "Percolation properties of metal-filled polymer films, structure and mechanisms of conductivity," *Progress in Organic Coatings*, vol. 39, pp. 81–100, Nov. 2000.

[233] N. Xie, W. Shao, L. Feng, L. Lv, and L. Zhen, "Fractal Analysis of Disordered ConductorInsulator Composites with Different Conductor Backbone Structures near Percolation Threshold," *The Journal of Physical Chemistry C*, vol. 116, pp. 19517–19525, Sept. 2012.

[234] Z. Rubin, S. A. Sunshine, M. B. Heaney, I. Bloom, and I. Balberg, "Critical behavior of the electrical transport properties in a tunneling-percolation system," *Physical Review B*, vol. 59, pp. 12196–12199, May 1999.

[235] M. B. Heaney, "Measurement and interpretation of nonuniversal critical exponents in disordered conductorinsulator composites," *Physical Review B*, vol. 52, pp. 12477–12480, Nov. 1995.

[236] R. Viswanathan and M. B. Heaney, "Direct Imaging of the Percolation Network in a Three-Dimensional Disordered Conductor-Insulator Composite," *Physical Review Letters*, vol. 75, pp. 4433–4436, Dec. 1995.

[237] G. Pfister and H. Scher, "Dispersive (non-Gaussian) transient transport in disordered solids," *Advances in Physics*, vol. 27, no. 5, pp. 747–798, 1978.

[238] H. Scher and E. W. Montroll, "Anomalous transit-time dispersion in amorphous solids," *Physical Review B*, vol. 12, pp. 2455–2477, Sept. 1975.

[239] S. R. Forrest and T. A. W. Jr, "Long-range correlations in smoke-particle aggregates," *Journal of Physics A: Mathematical and General*, vol. 12, p. L109, May 1979.

[240] D. A. Weitz, M. Y. Lin, and C. J. Sandroff, "Colloidal aggregation revisited: New insights based on fractal structure and surface-enhanced Raman scattering," *Surface Science*, vol. 158, pp. 147–164, July 1985.

[241] T. Cleary, R. Samson, and J. W. Gentry, "Methodology for Fractal Analysis of Combustion Aerosols and Particle Clusters," *Aerosol Science and Technology*, vol. 12, pp. 518–525, Jan. 1990.

[242] T. Earmme and S. A. Jenekhe, "Improved electron injection and transport by use of baking soda as a low-cost, air-stable, n-dopant for solution-processed phosphorescent organic light-emitting diodes," *Applied Physics Letters*, vol. 102, p. 233305, June 2013.

[243] W. Krtschmer, L. D. Lamb, K. Fostiropoulos, and D. R. Huffman, "Solid C60: a new form of carbon," *Nature*, vol. 347, pp. 354–358, Sept. 1990.

[244] X. Xu, J. Wang, J.-P. Lv, and Y. Deng, "Simultaneous analysis of three-dimensional percolation models," *Frontiers of Physics*, vol. 9, pp. 113–119, Feb. 2014. arXiv: 1310.5399.

[245] M. J. Powell, "Site percolation in randomly packed spheres," *Physical Review B*, vol. 20, pp. 4194–4198, Nov. 1979.

[246] S. C. van der Marck, "Calculation of Percolation Thresholds in High Dimensions for FCC, BCC and Diamond Lattices," *International Journal of Modern Physics C*, vol. 09, pp. 529–540, June 1998.

[247] C. D. Lorenz and R. M. Ziff, "Universality of the excess number of clusters and the crossing probability function in three-dimensional percolation," *Journal of Physics A: Mathematical and General*, vol. 31, pp. 8147–8157, Oct. 1998. arXiv: cond-mat/9806224.

[248] R. B. Ross, C. M. Cardona, F. B. Swain, D. M. Guldi, S. G. Sankaranarayanan, E. Van Keuren, B. C. Holloway, and M. Drees, "Tuning Conversion Efficiency in Metallo Endohedral Fullerene-Based Organic Photovoltaic Devices," *Advanced Functional Materials*, vol. 19, no. 14, pp. 2332–2337, 2009.

[249] R. B. Ross, C. M. Cardona, D. M. Guldi, S. G. Sankaranarayanan, M. O. Reese, N. Kopidakis, J. Peet, B. Walker, G. C. Bazan, E. Van Keuren, B. C. Holloway, and M. Drees, "Endohedral fullerenes for organic photovoltaic devices," *Nature Materials*, vol. 8, pp. 208–212, Mar. 2009.

[250] J. D. Roehling, K. J. Batenburg, F. B. Swain, A. J. Moul, and I. Arslan, "Three-Dimensional Concentration Mapping of Organic Blends," *Advanced Functional Materials*, vol. 23, no. 17, pp. 2115–2122, 2013.

[251] C. Adachi, M. Baldo, M. Thompson, and S. Forrest, "Nearly 100% internal phosphorescence efficiency in an organic light-emitting device," *Journal of Applied Physics*, vol. 90, pp. 5048–5051, Nov. 2001. WOS:000171918700023.

[252] B. W. D'Andrade, J. Esler, C. Lin, V. Adamovich, S. Xia, M. S. Weaver, R. Kwong, and J. J. Brown, "Realizing white phosphorescent 100 lm/W OLED efficacy," *Proceedings of SPIE*, vol. 7051, pp. 70510Q–70510Q–5, Aug. 2008.

[253] B. . D'Andrade and S. . Forrest, "White Organic LightEmitting Devices for Solid-State Lighting," *Advanced Materials*, vol. 16, pp. 1585–1595, Sept. 2004.

[254] P. A. Levermore, A. B. Dyatkin, Z. Elshenawy, H. Pang, J. Silvernail, E. Krall, R. C. Kwong, R. Ma, M. S. Weaver, J. J. Brown, X. Qi, and S. R. Forrest, "Phosphorescent OLEDs for High Efficacy Long Lifetime Solid State Lighting," *Journal of Photonics for Energy*, vol. In press, 2012.

[255] X. Qi and S. R. Forrest, "Thermal analysis of high intensity organic light-emitting diodes based on a transmission matrix approach," *Journal of Applied Physics*, vol. 110, pp. 124516–124516–11, Dec. 2011.

[256] Pipes, Louis A., "Matrix analysis of heat transfer problems," *Journal of the Franklin Institute*, vol. 263, pp. 195–206, Mar. 1957.

[257] Y. Jin, A. Yadav, K. Sun, H. Sun, K. P. Pipe, and M. Shtein, "Thermal boundary resistance of copper phthalocyanine-metal interface," *Applied Physics Letters*, vol. 98, p. 093305, Mar. 2011.

[258] T. L. Bergman, A. S. Lavine, D. P. DeWitt, and F. P. Incropera, *Introduction to Heat Transfer*. Wiley, 6 ed., June 2011.

[259] R. H. S. Winterton, "Newton's law of cooling," *Contemporary Physics*, vol. 40, no. 3, pp. 205–212, 1999.

[260] W. M. Haynes, ed., *CRC Handbook of Chemistry and Physics, 95th Edition*. CRC Press, 95 edition ed., June 2014.

[261] M. Baesso, J. Shen, and R. Snook, "Time-resolved thermal lens measurement of thermal diffusivity of sodalime glass," *Chemical Physics Letters*, vol. 197, pp. 255–258, Sept. 1992.

[262] A. W. Bushmaker, V. V. Deshpande, S. Hsieh, M. W. Bockrath, and S. B. Cronin, "Direct Observation of Born-Oppenheimer Approximation Breakdown in Carbon Nanotubes," *Nano Letters*, vol. 9, pp. 607–611, Feb. 2009. WOS:000263298700017.

[263] A. W. Bushmaker, V. V. Deshpande, M. W. Bockrath, and S. B. Cronin, "Direct observation of mode selective electron-phonon coupling in suspended carbon nanotubes," *Nano Letters*, vol. 7, pp. 3618–3622, Dec. 2007. WOS:000251581600013.

[264] A. W. Bushmaker, V. V. Deshpande, S. Hsieh, M. W. Bockrath, and S. B. Cronin, "Large Modulations in the Intensity of Raman-Scattered Light from Pristine Carbon Nanotubes," *Physical Review Letters*, vol. 103, p. 067401, Aug. 2009. WOS:000268809300070.

[265] R. Dhall, S.-W. Chang, Z. Liu, and S. B. Cronin, "Pronounced electron-phonon interactions in ultraclean suspended carbon nanotubes," *Physical Review B*, vol. 86, p. 045427, July 2012. WOS:000306508600006.

[266] V. V. Deshpande, B. Chandra, R. Caldwell, D. S. Novikov, J. Hone, and M. Bockrath, "Mott Insulating State in Ultraclean Carbon Nanotubes," *Science*, vol. 323, pp. 106–110, Jan. 2009. WOS:000262104100050.

[267] S.-W. Chang, R. Dhall, M. Amer, K. Sato, R. Saito, and S. Cronin, "Evidence for structural phase transitions and large effective band gaps in quasi-metallic ultraclean suspended carbon nanotubes," *Nano Research*, vol. 6, pp. 736–744, Oct. 2013. WOS:000325819000005.

[268] M. R. Amer, A. Bushmaker, and S. B. Cronin, "The Influence of Substrate in Determining the Band Gap of Metallic Carbon Nanotubes," *Nano Letters*, vol. 12, pp. 4843–4847, Sept. 2012. WOS:000308576000070.

[269] K. Esfarjani, A. A. Farajian, Y. Hashi, and Y. Kawazoe, "Electronic and transport properties of N-P doped nanotubes," *Applied Physics Letters*, vol. 74, pp. 79–81, Jan. 1999. WOS:000077791800027.

[270] J. Kong, J. Cao, H. J. Dai, and E. Anderson, "Chemical profiling of single nanotubes: Intramolecular p-n-p junctions and on-tube single-electron transistors," *Applied Physics Letters*, vol. 80, pp. 73–75, Jan. 2002. WOS:000173029000025.

[271] Y. X. Zhou, A. Gaur, S. H. Hur, C. Kocabas, M. A. Meitl, M. Shim, and J. A. Rogers, "p-channel, n-channel thin film transistors and p-n diodes based on single wall carbon nanotube networks," *Nano Letters*, vol. 4, pp. 2031–2035, Oct. 2004. WOS:000224514800041.

[272] R. D. Antonov and A. T. Johnson, "Subband population in a single-wall carbon nanotube diode," *Physical Review Letters*, vol. 83, pp. 3274–3276, Oct. 1999. WOS:000083133200043.

[273] Z. Wang, H. Xu, Z. Zhang, S. Wang, L. Ding, Q. Zeng, L. Yang, T. Pei, X. Liang, M. Gao, and L.-M. Peng, "Growth and Performance of Yttrium Oxide as an Ideal High-kappa Gate Dielectric for Carbon-Based Electronics," *Nano Letters*, vol. 10, pp. 2024–2030, June 2010. WOS:000278449200009.

[274] L. Yang, S. Wang, Q. Zeng, Z. Zhang, T. Pei, Y. Li, and L.-M. Peng, "Efficient photovoltage multiplication in carbon nanotubes," *Nature Photonics*, vol. 5, pp. 673–677, Nov. 2011. WOS:000296706100011.

[275] Z. Yao, H. W. C. Postma, L. Balents, and C. Dekker, "Carbon nanotube intramolecular junctions," *Nature*, vol. 402, pp. 273–276, Nov. 1999. WOS:000083813700043.

[276] C.-H. Liu, C.-C. Wu, and Z. Zhong, "A Fully Tunable Single-Walled Carbon Nanotube Diode," *Nano Letters*, vol. 11, pp. 1782–1785, Apr. 2011. WOS:000289341500069.

[277] J. U. Lee, "Photovoltaic effect in ideal carbon nanotube diodes," *Applied Physics Letters*, vol. 87, pp. 073101–073101–3, Aug. 2005.

[278] J. U. Lee, P. P. Gipp, and C. M. Heller, "Carbon nanotube p-n junction diodes," *Applied Physics Letters*, vol. 85, pp. 145–147, July 2004.

[279] J. U. Lee, "Band-gap renormalization in carbon nanotubes: Origin of the ideal diode behavior in carbon nanotube p-n structures," *Physical Review B*, vol. 75, p. 075409, Feb. 2007. WOS:000244533400095.

[280] Y. F. Li, R. Hatakeyama, J. Shishido, T. Kato, and T. Kaneko, "Air-stable p-n junction diodes based on single-walled carbon nanotubes encapsulating Fe nanoparticles," *Applied Physics Letters*, vol. 90, p. 173127, Apr. 2007.

[281] S. Wang, Z. Zhang, L. Ding, X. Liang, J. Shen, H. Xu, Q. Chen, R. Cul, Y. Li, and L.-M. Peng, "A doping-free carbon nanotube CMOS inverter-based bipolar diode and ambipolar transistor," *Advanced Materials*, vol. 20, pp. 3258–+, Sept. 2008. WOS:000259205400012.

[282] A. Malapanis, E. Comfort, and J. U. Lee, "Current-induced cleaning of adsorbates from suspended single-walled carbon nanotube diodes," *Applied Physics Letters*, vol. 98, p. 263108, June 2011.

[283] C. D. Spataru and F. Leonard, "Tunable Band Gaps and Excitons in Doped Semiconducting Carbon Nanotubes Made Possible by Acoustic Plasmons," *Physical Review Letters*, vol. 104, p. 177402, Apr. 2010. WOS:000277210600048.

[284] E. Pop, D. Mann, J. Cao, Q. Wang, K. E. Goodson, and H. J. Dai, "Negative differential conductance and hot phonons in suspended nanotube molecular wires," *Physical Review Letters*, vol. 95, p. 155505, Oct. 2005. WOS:000232443400039.

[285] A. Ortiz-Conde, F. J. G. Sanchez, and J. Muci, "Exact analytical solutions of the forward non-ideal diode equation with series and shunt parasitic resistances," *Solid-State Electronics*, vol. 44, pp. 1861–1864, Oct. 2000. WOS:000165065100021.

[286] A. Ortiz-Conde and F. J. Garca Snchez, "Extraction of non-ideal junction model parameters from the explicit analytic solutions of its IV characteristics," *Solid-State Electronics*, vol. 49, pp. 465–472, Mar. 2005.

[287] D. Neamen, *An Introduction to Semiconductor Devices*. Boston, Mass. u.a.: McGraw-Hill Science/Engineering/Math, Jan. 2005.

[288] J. W. Mintmire and C. T. White, "Universal density of states for carbon nanotubes," *Physical Review Letters*, vol. 81, pp. 2506–2509, Sept. 1998. WOS:000076073100027.

[289] J. M. Marulanda and A. Srivastava, "Carrier density and effective mass calculations in carbon nanotubes," *Physica Status Solidi B-Basic Solid State Physics*, vol. 245, pp. 2558–2562, Nov. 2008. WOS:000261088100028.

[290] T. Durkop, S. A. Getty, E. Cobas, and M. S. Fuhrer, "Extraordinary mobility in semiconducting carbon nanotubes," *Nano Letters*, vol. 4, pp. 35–39, Jan. 2004. WOS:000188233200007.

[291] A. Hoegele, C. Galland, M. Winger, and A. Imamoglu, "Photon antibunching in the photoluminescence spectra of a single carbon nanotube," *Physical Review Letters*, vol. 100, p. 217401, May 2008. WOS:000256585500046.

[292] A. Malapanis, D. A. Jones, E. Comfort, and J. U. Lee, "Measuring Carbon Nanotube Band Gaps through Leakage Current and Excitonic Transitions of Nanotube Diodes," *Nano Letters*, vol. 11, pp. 1946–1951, May 2011. WOS:000290373000016.

[293] Y. H. Ahn, A. W. Tsen, B. Kim, Y. W. Park, and J. Park, "Photocurrent Imaging of pn Junctions in Ambipolar Carbon Nanotube Transistors," *Nano Lett.*, vol. 7, no. 11, pp. 3320–3323, 2007.